UNIVERSITY OF CALIFORNIA, SAN DIEGO

Electromagnetic Imaging of the Crust and Upper Mantle across the Continental Margin in Central California

A dissertation submitted in partial satisfaction of the
requirements for the degree
Doctor of Philosophy

in

Earth Sciences

by

Brent David Wheelock

Committee in charge:

Steven Constable, Chair
Kerry Key, Co-Chair
Steven Cande
Thomas O'Neil
Robert Parker
David Stegman

2012

The dissertation of Brent David Wheelock is approved, and it is acceptable in quality and form for publication on microfilm:

_____

_____

_____

_____

_____
Co-Chair

_____
Chair

University of California, San Diego

2012

DEDICATION

To my parents, Dorinda and Donald, and my sister, Alicia.

EPIGRAPH

Just because you feel it doesn't mean it's there.

—Thom Yorke

TABLE OF CONTENTS

LIST OF FIGURES

ACKNOWLEDGEMENTS

First, I thank my advisor Steven Constable who first introduced me to the world of applied geophysics in an undergraduate class which he taught on the subject. During the course, he invited me aboard the Research Vessel New Horizon for a five day cruise off the coast of San Diego to test new marine electromagnetic equipment. I happily accepted a chance for adventure and I have been hooked on marine electromagnetic geophysics ever since. Steven was instrumental in convincing me to pursue a higher degree in geophysics, and to do so at Scripps. I am extremely grateful for the opportunities he has presented me every step of the way. He has taken me on research cruises and to scientific conferences all over the world. I have been lucky to be a part of a research group, which, under his leadership, has defined itself as a world leader in marine electromagnetic geophysics. My research and professional development have benefitted greatly from his exceptional wisdom. The decision to come to Scripps to pursue a doctorate degree has been one of the most rewarding decisions of my life, and I would never have made it had I not met Steven Constable. I thank my thesis co-chair, Kerry Key. Having followed similar paths leading up to working with the Scripps Marine EM research group, he has been an inspiration to me throughout my time here. His well-placed insight and skepticism have helped me countless times in the course of my research. I greatly appreciate our frequent conversations, scientific and otherwise. I thank Robert Parker, a member of my thesis committee, for his tutelage and collaboration. The non-linear world of electromagnetic geophysics can turn murky very quickly, and he has brought much desired clarity to it. His influence is profound in my work as a scientist, and I am grateful to have been able to learn from and work with him directly. I thank the other members of my thesis committee: Steven Cande, Thomas O'Neil, and David Stegman. Their advice and comments about my work have made a positive contribution to this dissertation.

I thank my colleagues in Germany, particularly Michael Becken and Oliver Ritter. I enjoyed working in the field with them installing and maintaining land magnetotelluric (MT) instruments in central California. They have been extremely generous in providing me both the processed land data from central California and their interpretations of them, far in

advance to publishing either. My dissertation benefitted greatly from open communication with them and their student Kristina Tietze about both the land and marine MT studies in central California.

Thanks go to Jacques Lemire, John Souders, Chris Armerding, Jake Perez, and Cambria Berger whose hard work in preparing the instruments, and executing the cruise offshore central California provided me the excellent dataset upon which this dissertation is based. You all have been great friends and made work onshore and offshore a whole lot of fun.

My fiancée, Katherine, has filled my life with happiness over the last few years. Without her love and support, the completion of this dissertation would have been far more difficult. I thank her for generously taking up the responsibilities that I had neglected during the final stages of writing. I thank my parents, Donald and Dorinda, for giving me a solid foundation in life, and inspiring me to make the best of it. I thank them for their commitment to my education, which made this dissertation possible. I also thank them and my sister Alicia, for their love and encouragement throughout my life.

Many thanks go to my friends and colleagues at Scripps Institution of Oceanography. I thank Karen Weitemeyer and David Myer, once the senior students in the EM lab, for pulling me up to speed during my first few years in the group. I thank my officemate, Andrew Barbour, for providing useful advice ranging from typesetting, to figure aesthetics, to statistics, to ale selection. He and other geophysics students including, Brenden Crowell, Chris Takeuchi, Samer Naif, Dylan Connell, John Blum, and Daniel Brothers are thanked for making my time in graduate school lively and entertaining.

Funding for the research presented in this dissertation was provided by the UC Ship Funds Program, and by the Seafloor Electromagnetic Methods Consortium at Scripps Institution of Oceanography. I thank all of these sponsors. Without their dedication to advancing marine electromagnetic research, my work would not have been possible.

Chapter 5, in part, derives from material published in the Geophysical Journal International. Parker, Robert L.; Wheelock, Brent, Blackwell Publishing Ltd., 2012. The dissertation author was the secondary investigator and author of this paper. The remainder of the text of Chapter 5 is currently being prepared for submission for publication of the

material. Wheelock, Brent. The dissertation author was the primary investigator and author of this material.

VITA

2006	B. S. in Physics w/ Specialization in Earth Sciences *cum laude*, University of California, San Diego
2006-2012	Research Assistant, Scripps Institution of Oceanography, University of California, San Diego
2012	Ph. D. in Earth Sciences, Scripps Institution of Oceanography, University of California, San Diego

PUBLICATIONS

Parker, R. L. and Wheelock, B., "Fourier domain calculation of terrain effects in marine MT", *The Geophysical Journal International*, vol. 189, pp 240-50, 2012.

ABSTRACT OF THE DISSERTATION

Electromagnetic Imaging of the Crust and Upper Mantle across the Continental Margin in Central California

by

Brent David Wheelock
Doctor of Philosophy in Earth Sciences

University of California San Diego, 2012

Steven Constable, Chair

Electromagnetic methods, particularly magnetotelluric (MT) sounding, are often used to detect fluids in the crust and upper mantle. Recently, MT studies on land have focused on the deep structure of the San Andreas fault (SAF) in central California. One of these studies found a region of high conductivity, interpreted as a local abundance of pore fluid, southwest of the fault at depths corresponding to the lower crust and upper mantle. The study also identified a change in the connection of this deep conductor to the root of the SAF as their measurements moved along the strike of the fault. It was proposed that a change in access of fluids to the deep extension of the fault, as evidenced by the modeled resistivity of the region, is responsible for the observed change in behavior of both earthquakes and non-volcanic tremor along the central Californian segment of the SAF.

As an effort to extend knowledge of the resistivity structure into the offshore environment of central California, as well as to better constrain the interpretations made onshore, the Marine Electromagnetic Research Group at the Scripps Institution of Oceanography collected marine MT and controlled-source electromagnetic (CSEM) data there. Our single profile of data extends an existing profile of land data. In this dissertation I interpret both profiles of MT data, land and marine, jointly. Inversions of the amphibious dataset produce a resistivity model that is similar to previous results. However, upon closer inspec-

tion it was found that the marine data and the land data solicit antithetical structures. I suspected this to be caused by distortion from bathymetry that varies in three dimensions (3D), which is a problem because our 2D models assume that the earth is uniform in the horizontal dimension perpendicular to our profile. Few numerical methods exist to calculate the effects of 3D bathymetry in the necessary detail, so I improved upon an established thin-sheet technique to allow for higher resolution models. With this method I estimated how the effects of 3D bathymetry along our profile deviate from those predicted by an analogous 2D model. The effects are significant relative to the data errors used in inversion. As a test, I created synthetic data from both 2D and 3D bathymetric models, and invert them with a 2D inversion algorithm. Surprisingly, the inversion of 2D data did not recover the simple model used to create the synthetic data. Anomalous structures were introduced that weakly resembled those found in the models derived from actual data. Inversion of the 3D data made matters worse; the same artifacts found with 2D data became more extreme and their resemblance to the features in the results from actual data was enhanced. I concluded that the results from applying the established 2D inversion scheme on the actual data cannot be trusted, as is likely the case for the work on the same data that was previously published by others. The thin-sheet modeling suggests that future interpretations must at least take into account the known 3D bathymetric variations that occur off our profile.

Chapter 1

Introduction

The segment of the San Andreas fault (SAF) passing through central California has generated renewed interest with the discovery of non-volcanic tremor near the town of Cholame [Nadeau and Dolenc, 2005], the first observation of this phenomenon on a strike-slip fault. Non-volcanic tremors are long duration seismic signals originating near prominent faults that lack clear P- and S-wave arrivals, implying a different underlying mechanism than the double-couple mechanism that explains conventional earthquakes. The physics of tremor generation remain unclear and represent an emergent area of research. Clusters of tremor episodes have been located in a zone adjacent to Cholame, the northern limit of a locked section of the SAF [Nadeau and Guilhem, 2009]. These episodes were found to originate at depths between 15 and 30 km, below the zone where most earthquakes occur and within the ductile lower crust. Nadeau and Guilhem [2009] found that the tremor rate in Cholame was insensitive to normal stress changes induced by nearby earthquakes, which was interpreted as evidence for high pore fluid pressures in the zones generating tremor. The abundance and distribution of pore fluids at depths associated with non-volcanic tremor can be estimated with the deep electromagnetic imaging method of magnetotellurics (MT), which is particularly sensitive to the enhancement in electrical conductivity that fluids bring to rock.

There is a large body of MT work performed along the central Californian segment

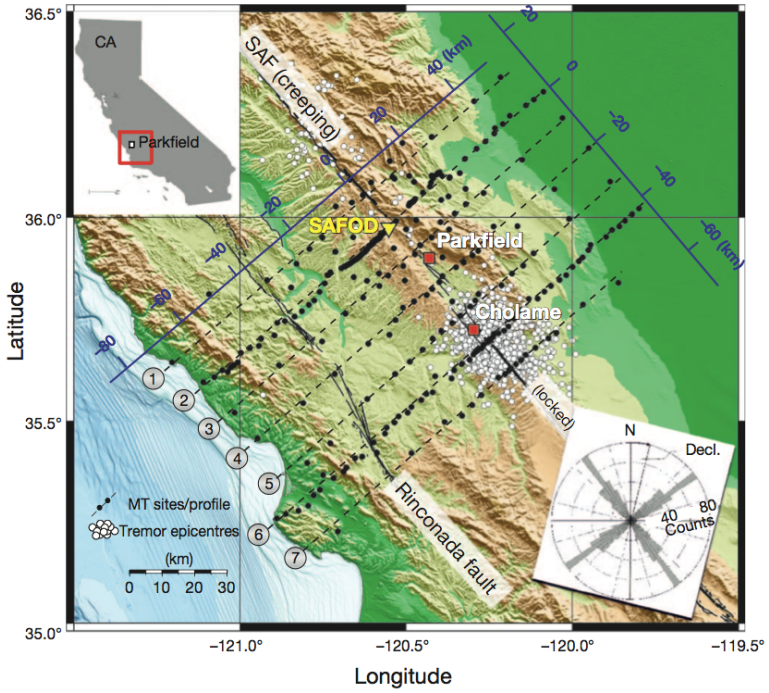

Figure 1.1: Map of the magnetotelluric survey of the central San Andreas fault from Becken et al. [2011]. Black dots show magnetotelluric stations along the 7 profiles. The inset rose-diagram depicts geoelectric strike estimates (similar to those found in Chapter 3), which are consistent with the orientation of the SAF.

of the SAF [e.g., Unsworth et al., 1997, 1999, 2000, Bedrosian et al., 2004, Unsworth and Bedrosian, 2004, Becken et al., 2008b, 2011]. In this dissertation, we focus on the most recent and most extensive of these studies. The work presented in Becken et al. [2011] began with the collection of 7 parallel profiles of MT data, each about 130 km in length and oriented perpendicularly to the regional trend of the SAF (see Figure 1.1). The southern-most profile crosses the SAF south of Cholame. The other profiles are separated by about 10 km along the strike of the SAF, in a northwestern progression. The northwestern-most profile crosses the SAF 10 km from the drill hole of the San Andreas Fault Observatory at Depth (SAFOD) [e.g. Hickman et al., 2004].

The published interpretation of these data derives from a suite of 2D inversion models, one for each of the 7 profiles [Becken et al., 2011], although results from 3D inversion are in preparation (personal communication with Kristina Tietze at the German Research Center for Geosciences, Potsdam). The main result from the 2D inversions is the appearance in each of the inversion models of a large anomalously-conductive body (1-10 Ωm), 30-40 km southwest of the SAF, residing at a depths below 15 km (see Figue 1.2). The character of this anomalous region changes from profile to profile. In the southeastern profiles, near Cholame and crossing the locked portion of the SAF, the large conductive body is electrically isolated from the deep root of the SAF by a highly-resistive bounding region. The profiles that lie northwest of Parkfield, toward the creeping section of the fault, develop a sub-vertical corridor of elevated conductivity, electrically connecting the deep conducting zone to the root of the SAF. In the northwestern-most profile, the anomalous body is about a factor of 10 less conductive than in the other profiles, though a connection to the deep extent of the SAF remains. Becken et al. [2011] interpreted the large conductive anomaly offset to the southwest from the SAF as evidence of saline aqueous fluids in the pore space of the lower crust and upper mantle. The emergence of a low-resistivity linkage between this body and the deep root of the SAF spatially correlates with lower tremor amplitudes in the lower-crust, and what has been independently-inferred as a mechanically weak upper-crust. Becken et al. [2011] propose that an increase in the supply of fluids, sourced from the deep reservoir (the conductive body to the southwest), can explain both phenomena. They suggest that the excess fluids, either through frictional weakening due to

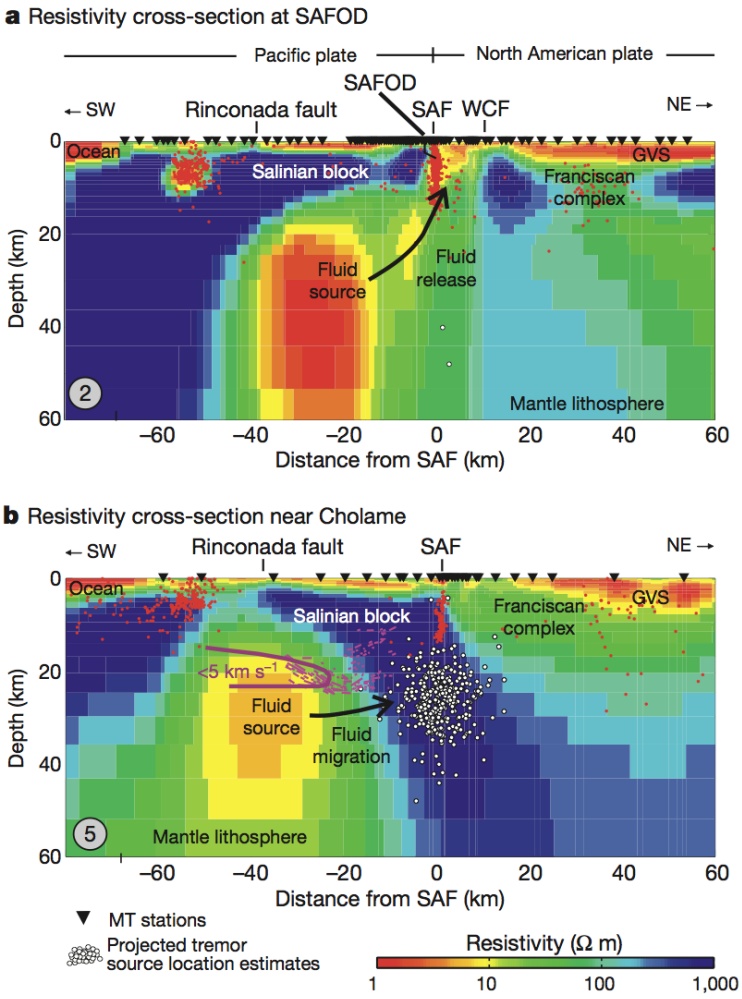

Figure 1.2: Figure 2 from Becken et al. [2011]. Two resistivity cross-sectional models from 2D inversions of two of the profiles of data: (**a**) profile 2, northwest near SAFOD, and (**b**) profile 5, southwest near Cholame. White dots indicate locations of tremor episodes. Thick purple line shows a 5 km/s seismic low-velocity contour and thin purple lines trace high seismic reflectivity, both interpreted from Trehu and Wheeler [1987]. WCF, Waltham canyon fault; GVS, Great Valley sequence.

mineral hydration, or the reduction of fault-normal stress by high fluid pressures, weaken the seismogenic upper crust northwest of Parkfield; hence, the SAF exhibits creeping behavior there. Also, the pathway by which these fluids reach the upper crust is inferred to represent mechanically weak material in the lower crust where tremors originate. A weak lower crust is more accommodating to fluid flow, whereas a mechanically strong lower crust is likely to allow fluid pressures to build to the point of brittle failure. They cite brittle failure due to fluid over-pressurization in the otherwise ductile deformation regime of the lower crust as the mechanism for tremor production. Thus, in the northwest where there is a low-resistivity, i.e. weaker, lower-crust, over-pressurization is less likely, so tremor amplitudes are subdued. In contrast, the southwestern profiles exhibit high-resistivity in the lower crust separating the fluid reservoir (conductive body) from the deep root of the SAF, enabling over-pressurization, brittle failure, and, consequently, larger tremor amplitudes.

It is highly plausible that the lower crust and upper mantle in central California is a significant source of hydrous fluids. The western boundary of the North American plate has witnessed subduction for at least the past 180 million years. The most recent episode of subduction off the coast of California involved the Farallon plate. By 24 Ma, the Farallon had fragmented into multiple smaller plates as offset segments of the Pacific-Farallon spreading center obliquely intersected the trench. One of these microplates, known as the Monterey plate, continued to subduct eastward beneath central California until around 19 Ma. By that time, the Monterey plate had become surrounded by Pacific-North American shear zones, to the point where it was compelled to take on the northwestern motion of the Pacific plate. A residual portion of the Monterey plate that was captured by the Pacific plate remains visible in the seafloor magnetic anomalies off the coast of central California [Lonsdale, 1991]. Subducting plates transport large volumes of water into the forearc crust and mantle in the form of free water in the pore spaces of sediments and upper oceanic crust, as well as bound water in hydrous minerals in the lower crust and uppermost mantle. During the shallow stage of subduction, increasing pressure reduces porosity and expels the free water. As the subducting plate moves deeper and is heated by the surrounding mantle, a succession of dehydration reactions occur as various hydrous minerals are moved out of their stability fields. These reactions can continue to release

water in the slab up to depths of around 200 km [Hyndman and Peacock, 2003]. Depending on where this water is released, it either enters the overlying forearc crust, the overlying forearc mantle, or the ocean by flow through faults in the accretionary prism.

The goal of this dissertation is to extend into the marine environment one of the profiles (profile 5 in Figures 1.1 & 1.2) of terrestrial MT data collected in central California. There are many reasons for doing this, but in this dissertation I will focus on two. First, if the large conductive body is associated with a fluid reservoir, a question that naturally arises is how it relates to the regional history of subduction. Land and marine active-seismic studies have imaged the subducted Monterey plate beneath the continental shelf of central California, and indicate that it extends beneath the continental crust as far east as the San Andreas fault [e.g. Trehu and Wheeler, 1987, Miller et al., 1992, Howie et al., 1993, Lafond and Levander, 1995, Bleibinhaus et al., 2007]. Yet no comparable model for the electrical conductivity of this offshore region exists. Such a model would provide the information necessary to link the large, lower-crustal conductor found onshore to fluids or hydrated minerals associated with the underplated ocean crust that extends offshore. Second, the large, deep conductive body southwest of the SAF discovered by Becken et al. [2011] lies close to the coastal edge of their data profiles. The resistivity structure of the adjacent continental margin is not constrained by terrestrial data and we investigate whether this freedom might cause trade-offs in the inverse process that artificially introduce such anomalous structures as were found. An expansion of data coverage into the ocean, to the west of the large conductive body, should help discern whether that body is required to exist. In the forthcoming chapters, I discuss the collection and processing of a profile of marine magnetotelluric data from offshore central California, and jointly interpret it with profile 5 of the terrestrial data from Becken et al. [2011].

Chapter 2

Data Collection offshore Estero Bay

In the months between November 2008 and January 2009 we conducted a marine magnetotelluric (MT) and controlled-source electromagnetic (CSEM) survey along a profile line approximately perpendicular to the central Californian coast at Estero Bay (the better known Morro Bay is a smaller bay within Estero Bay). The intent was to image the conductivity structure of the continental margin from the surface, through the crust, and down into the upper mantle, to a maximum depth approaching 100 km. The survey location was chosen purposefully to extend a previously acquired terrestrial MT dataset in central California [Becken et al., 2008b, 2011]. The terrestrial dataset is from a large MT array consisting of seven profiles, each of which began at the coast and extended inland to the western edge of the San Joaquin Valley (Figure 2.1). These profiles are oriented perpendicularly to the San Andreas fault (SAF), which is remarkably straight in central California and strikes at approximately N 43° W. The southernmost profile is centered about 20 km southeast along the SAF from the town of Cholame. From there, the profiles are arranged in an evenly-spaced progression northwestward along the strike of the SAF. The northernmost profile is centered about 10 km northwest along the SAF from the San Andreas Fault Observatory at Depth (SAFOD). Becken et al. [2011] detected a large lower

crust/upper mantle zone of elevated conductivity approximately 50 km west of the SAF, and approximately 20 km east of the coast in all profiles (see Chapter 1). Their data coverage ended at the coast, and hence so did their conductivity models. The terrestrial dataset left open questions about the origin of the conductor west of the SAF and its relationship to the geology of the continental margin to the west of it. We sought to answer some of these questions, among others, by collecting and interpreting electromagnetic (EM) data seaward of the coast, nearly collinear with one of these preexisting terrestrial profiles. The interpretation in later chapters will involve an amphibious dataset, consisting of one profile of the terrestrial data combined with the profile of marine data described here. Although both marine MT and marine CSEM data were collected as a part of this experiment, and both data types are described in this chapter, the remainder of the dissertation deals only with the MT data.

2.1 Experimental Design

The plan for this experiment was to collect 38 marine sites of MT and CSEM data by way of two separate trips on marine research vessels. The first trip was to deploy the marine EM receivers and to transmit with the controlled-source along the profile line. Then, the receivers were left on the seafloor to collect broadband MT data until the second trip during which all the receivers were recovered from the seafloor.

2.1.1 Deployment

The deployment leg of the experiment took place on the R/V New Horizon between November 15$^{\text{th}}$ and November 22$^{\text{nd}}$, 2008. During this leg of the experiment we deployed 38 seafloor receivers over a 187 km line starting 23 km from the shore of Estero Bay and extending 93 km past the base of the continental shelf (Figure 2.1). The receiver spacing was 3.5 km for the shallowest 29 sites, 7 km for the next 7 progressively deeper sites, and 15 km for the deepest 2 sites. To make the most of the fixed number of available instruments, the receiver spacing was made tight over the continental shelf and slope where we intended to image near-surface structure with higher resolution, and looser out in the abyssal plain where

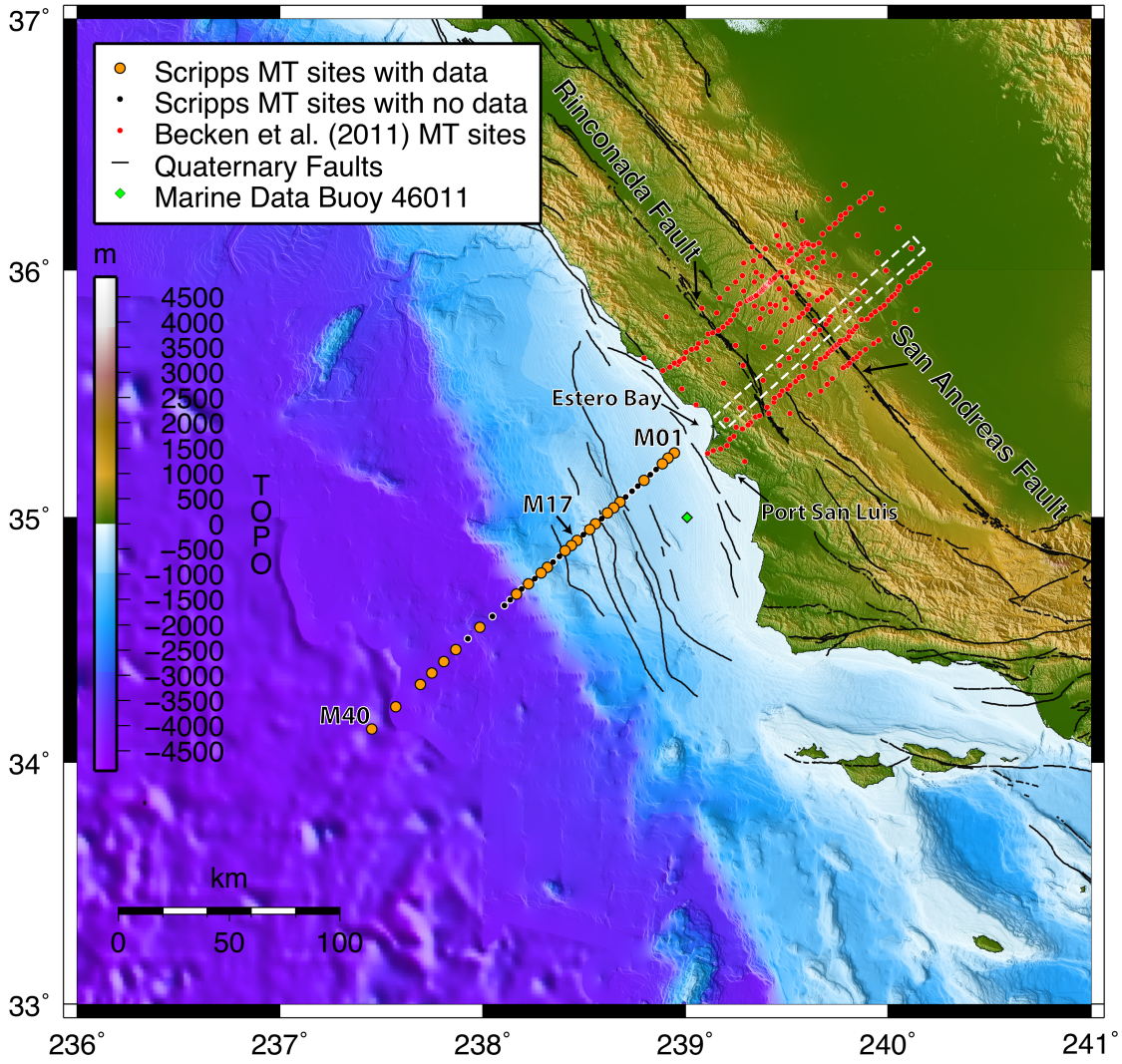

Figure 2.1: A map of the survey layout. Symbols depict instrument sites which were deployed to collect MT and CSEM data during the marine experiment as well as the land sites of MT data collected by Becken et al. [2011]. The white, dashed box encloses the terrestrial sites of MT data which will be interpreted along with the marine sites of MT data in the course of this dissertation. The 15 sites which failed to collect any data were spread quite evenly along our marine survey line. The marine data buoy 46011 provided spectral wave density data utilized in Chapter 3.

less resolution was desired; the most seaward sites served predominantly for constraining the coast effect (see Chapter 4). This survey collected a single profile of data with the expectation that the overall geo-electric structure would be predominantly two-dimensional (2D) (varying exclusively along the profile and with depth). The survey line is oriented at N 47° E, the same orientation as that of the terrestrial data profiles. The goal with this orientation was to make the survey lines perpendicular to the predominant 2D strike in the area. The SAF trends approximately N 43° W in this area of central California, perpendicular to our survey line. Most of the geologic structures in central California are elongated parallel to the SAF. Thus, the most likely direction for the axis of uniform conductivity in a 2D model is also N 43°W. The coast and continental shelf, although not entirely linear, trend roughly N 35° W so that our profile line is nearly perpendicular to these large features as well.

The receivers were deployed starting with the near-shore sites and moving toward the deep ocean sites. Between the deployment of each receiver, the ship followed a slight zig-zagged path between sites to allow for acoustic ranging along two linearly-independent horizontal directions. The independent sets of acoustic travel times from ship to receiver enable a non-linear inversion for the full 3D location of the receiver on the seafloor.

For the CSEM data the Scripps Undersea Electromagnetic Source Instrument (SUESI) was deployed and towed just above the seafloor near the profile of receivers. The transmitter tow began with a 15 km run-in from the deep-ocean end of the line. The tow line was parallel to the line of receivers but shifted a quarter mile to the south; the shift was intended to resolve ambiguity in the transmitter location in the cross-profile dimension, but came at a the cost of diminished electrical coupling with the seafloor near the receivers. The run-out of the tow was only 5 km on the shallow end of the receiver line. During the tow, we used SUESI's interrogating acoustic unit and a transponder relay on its antenna's tail to acquire a range between SUESI, the antennae tail, and the receivers as they were passed along the tow. Since the seafloor receiver locations are predetermined by interrogations from the ship during deployment, this additional web of acoustic travel times provides constraints on the transmitter position and orientation during the tow.

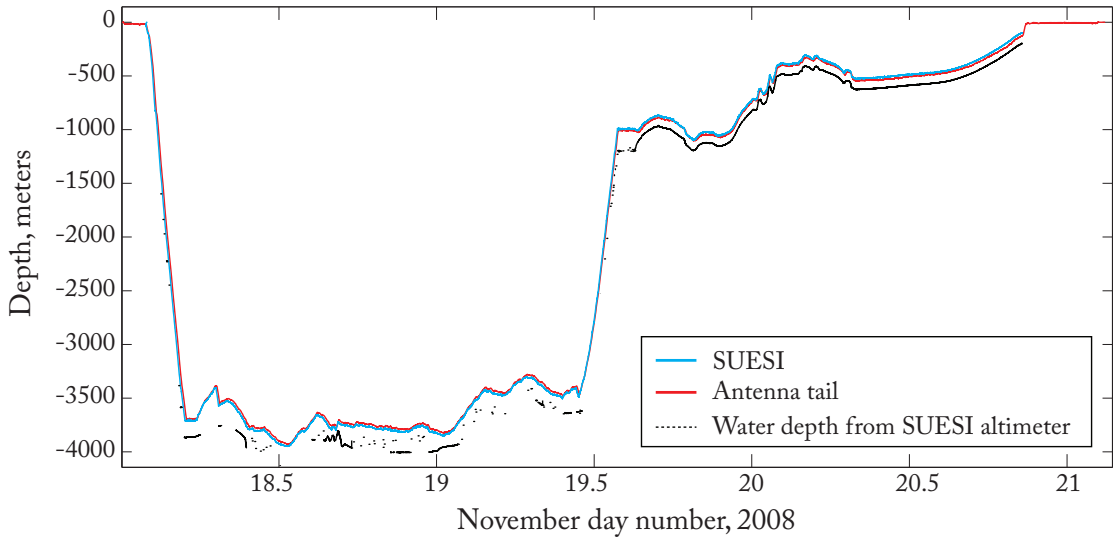

Figure 2.2: Water depth profile of the CSEM tow. SUESI depth, and antenna tail depth plotted along with pseudo-bathymetry calculated by the sum of SUESI's depth, and altimeter readings.

2.1.2 Recovery

After deployment and the CSEM tow, the receivers were left on the seafloor for a total of 6 weeks to maximize the opportunity to collect repetitions of long period MT signal. The recovery leg of the experiment took place on the R/V Robert Gordon Sproul between January 3rd and January 9th, 2009. We returned to the survey site in a smaller vessel to locate and recover the receivers. Before releasing an instrument from the seafloor, we again drove the ship in a zig-zag pattern over each site while gathering more acoustic range data, thereby increasing the accuracy of the estimated seafloor location of each instrument.

2.2 Survey Parameters

The SUESI transmitter operated at 200 A current on a 162 m dipole for a source dipole moment of 32.4 kAm. An attempt was made to carry out the CSEM tow at a flying height of 100 m above the seafloor. Due to the large variations in bathymetry along the towline, 100 m was chosen as a safer alternative to the usual 50 m height, despite the

sacrifice in seafloor coupling (Figure 2.2). We were unable to hold the 100 m height for the entire tow. On the deeper end of the our line, where water depths were greater than 4 km, over 5,600 m of 0.680 wire was trailing behind the ship in order to reach a flying height of 150 m. With so much payout, the winch controlling the wire was near its load limit and the chief engineer of the R/V New Horizon required that no more wire be paid out. Once the tow climbed up the continental shelf, the amount of wire-out fell below 1000 m and the winch returned to its normal performance. From that point onward in the tow, we were able to hold the tow package at 100m above the seafloor. In Figure 2.2, note the antenna tail flew slightly higher than SUESI in the deep water, but then reversed to flying below the SUESI in the shallow water; this is likely due to the fact that the tow cable was being hauled-in throughout the shallow water section. Also, notice that there were very few reliable altimeter readings in the deep ocean, a result of SUESI being towed more than 200 m above the seafloor, the maximum measurable height for the altimeter.

The waveform used for the SUESI transmissions was a compact, broadband, binary waveform developed by Myer et al. [2011]. The single free parameter for this waveform is the pattern's duration, which determines the fundamental frequency of the output. A 4 s duration was chosen for this experiment which set the lowest CSEM frequency to 0.25 Hz (Figure 2.3). This binary waveform spreads more power into the harmonics than would a simple square wave of the same fundamental frequency. The trade-off is a loss of power at the fundamental frequency. However, the fundamental, being the lowest frequency, is the least attenuated by the seawater. So one can usually afford the loss of power in the fundamental frequency in favor of more power at higher frequencies.

The seafloor receivers were configured to measure the electric and magnetic fields in two orthogonal directions in the horizontal plane relative to the instrument. If the instrument settled on the seafloor with any tilt, the sensor would no longer be measuring purely the horizontal fields. To alert us to this possibility, electronic compasses on the receivers provide measurements of horizontal orientation as well as tilt and roll angles of the instrument in its seafloor position. Although the SIO EM receivers can be configured to measure the vertical electric field, no vertical field sensors were installed during this experiment.

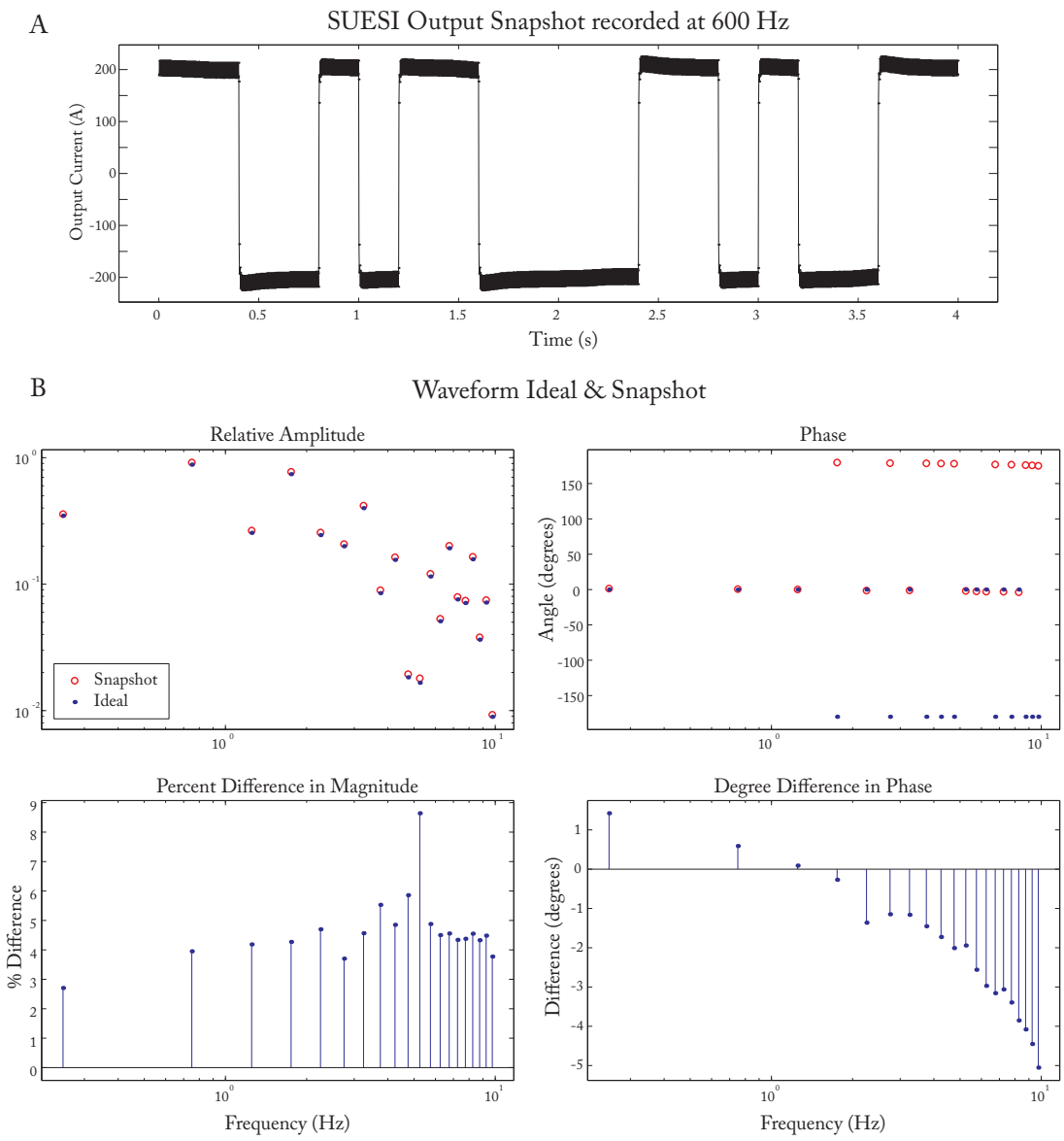

Figure 2.3: Transmitted Waveform. A) snapshot of the 4 second waveform pattern during transmission. The average output current is seen to dither around 200 A, and the actual transmitted waveform deviates slightly from the ideal rectangular shape. B) the amplitude and phase spectra of the recorded snapshot compared with the idealized binary sequence. Percent differences between these two are plotted below.

2.3 Instrument Performance

Instrument performance for this cruise represents an anomalous amount of data loss (approximately 40%) compared to the average rate over the preceding three cruises for the Scripps Marine EM lab (approximately 1%). Of 38 deployed receivers, all were retrieved from the seafloor, but only 23 had any usable data. The reason for this lies behind the experiment's extreme demands on receiver endurance. The six week deployment required a reconfiguration of the data logger's power supply, which enabled more than the usual number of batteries to be strung together. The development and installation of the new power supply was performed only a couple of weeks before this experiment; the instrument fleet had only just been retrieved from an experiment in the Gulf of Mexico, which took place during the late summer of 2008. With the reconfiguration, the battery capacity was nearly doubled, and a new diode board was used to connect the extra batteries, in parallel, to the data logger circuitry. The locus of failure was between two traces on the diode board that were manufactured too close together, and shorted-circuited upon powering-up in nearly 2 out of 5 instruments. Pressed for time, we had only been able to test a few of these new diode boards before sending them out to sea. Unfortunately, the few that had been tested ahead of time in the lab turned out to be good, leaving the faulty boards undetected. This loss of data, due to a minor change in equipment, underscores the experimental nature of research. The continuous advancement of technology is invariably met with the occasional setback. Luckily, the incidence of instrument failure was spread somewhat evenly along the survey line; no one area is severely diminished in data density relative to the rest, and the overall intended aperture of the profile was sustained (see Figure 2.1).

Of the instruments that did not have shorted batteries, the data recovery was good. Four of these instruments had problem channels. One instrument, (instrument name Croc, site M14) had a magnetic channel with amplitudes nearly an order of magnitude less than those of its other magnetic channel and those of magnetic channels from adjacent instruments. Further investigation of this instrument led to the discovery of a single incorrect resistor on the amplifier board which depressed that particular amplifier's voltages. Another instrument, (Cuscus, site M15) had an electric channel which was dead for most

of the deployment except, strangely, for a few days in the middle (November 30, 2008 - December 3, 2008) suggesting a connector problem with the electrode. Two other instruments (Occie, site M22, and Cocky, site M38) each had one bad E channel which had no recoverable data. The aforementioned problems exclude these sites from the ensuing MT analysis because uninterrupted data records for all four channels (E_x, E_y, B_x, & B_y) are needed. However, problem sites that retain some working channels may contain some useful CSEM information. In summary, of the deployed 38 sites of marine MT data, 19 sites are used in the MT analysis throughout this dissertation.

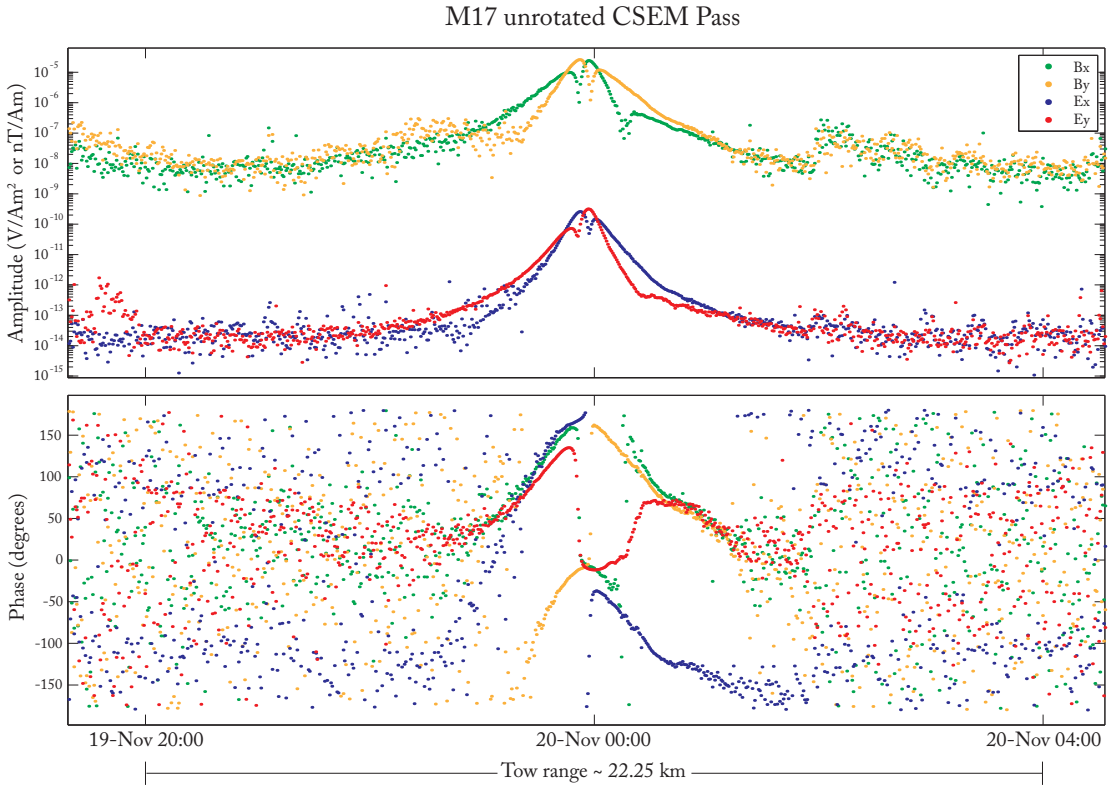

Figure 2.4: An example of 0.25 Hz CSEM data collected during this experiment. The abscissa in both plots is time, but by taking into account the 1.5 kt average speed of the tow, it is seen that coherent CSEM signal continues out to about 5 km in source-receiver offset.

In Chapter 3 we analyze the marine MT data quality at length; here, we provide a brief description of the usable frequencies of marine MT data and usable source-receiver offsets of CSEM data acquired during the survey. Figure 2.4 provides an example of processed CSEM data. In a later section, Figure 3.8 provides an example of processed MT data. The instruments were on the seafloor for a total of 6 weeks, recording on all four channels, B_x, B_y, E_x, and E_y, at a sampling rate of 25 Hz. A continuous section of 31 days in the middle of the data record was used for MT impedance estimation, a process described in Chapter 3. Figure 3.8 depicts the raw estimates of MT apparent resistivity and phase for a shallow water site, M01, and a deep water site, M40. The longest period for which MT apparent resistivity and phase estimates were made is just over 30,000 s; this was made possible by the long data record. Since highly conductive seawater attenuates the higher frequencies of MT signal preferentially, MT signal was greatly attenuated through the thick water column above site M40. This resulted in incoherent MT apparent resistivity and phase estimates at periods below 30 s. The shallow-water site, M01, having less water above it to attenuate the MT signal, achieves much more coherent estimates of MT apparent resistivity and phase at periods below 20 s. Nonetheless, the results at these lower periods are still noisy due to competing energy from wave action. In Chapter 3, we analyze wave spectra from data buoy station 46011 as well as tidal height as measured at Port San Luis (see Figure 2.1), and their relation to the electromagnetic data. The data buoy is maintained by the National Data Buoy Center, and its data are available over the internet (`http://www.ndbc.noaa.gov/`). The tidal data is provided by the National Oceanic and Atmospheric Administration (NOAA), and was available over the internet (`http://www.tidesandcurrents.noaa.gov/`).

Figure 2.4 contains a plot of the amplitudes of electric and magnetic fields at the transmitter fundamental frequency, 0.25 Hz, as measured by site M17 while the CSEM transmitter was being towed past it. Using the average tow speed of 1.5 kt, it is seen that the CSEM data show coherent signal out to transmitter-receiver offsets of about 5 km. This dissertation will neither address the processing nor the interpretation of the CSEM data.

Chapter 3

MT Data Processing

The chapter begins with a presentation of the range of methodologies that have been used for MT data processing over the past few decades; the description culminates with the most modern approach, called robust multi-station processing, which is the method used for the 19 sites of marine MT data addressed in this dissertation. Each method begins with time series of voltages output from electric and magnetic field sensors and results in transfer functions between each sensor, provided in the physical units of electric and magnetic fields. The most commonly analyzed transfer function, the impedance tensor, relates measurements from the horizontal electric and horizontal magnetic sensors at a single site of observation.

The account of data processing will initiate with the theoretical underpinnings of transfer function estimation taking place in the frequency domain. It will then return to the actual method used to make the frequency domain estimates from the Estero MT time series data, and make a qualitative assessment of those transformed data. Finally, the impedance-tensor estimates for the 19 sites of MT measurements will be presented, assessed, and conditioned for use in a 2D inversion process.

3.1 The Basics of Impedance Tensor Estimation

Here we provide the theoretical motivation for multi-station transfer-function estimation drawing from personal communication with R. L. Parker. The 2×2 magnetotelluric impedance tensor, Z, is defined as,

$$\mathbf{E}(\omega) = \frac{1}{\mu}\mathsf{Z}(\omega) \cdot \mathbf{B}(\omega), \tag{3.1}$$

where the $\mathbf{B}$ is the 2-vector of a horizontal magnetic field, and $\mathbf{E}$ the 2-vector of a horizontal electric field, both vectors collocated and contemporaneous; μ is the local magnetic permeability (the free-space value is appropriate for the majority of the earth's surface). We will drop the frequency argument, ω, in the ensuing development, but it should be kept in mind that transfer function estimation takes place in the frequency domain and the estimation processes for each desired frequency are handled independently. Estimation of transfer functions such as Z, given a set of noisy measurements of the electric and magnetic fields is the primary goal of MT data processing.

The impedance tensor measured over an earth consisting purely of horizontally stacked layers of homogeneous conductivity has zeros along the diagonal and its off-diagonal elements differ only in sign. For illustration purposes, we first will focus on this simple case. We then take E and B to be measurements of orthogonal components of the electric and magnetic field, respectively, both complex, zero-mean, normally-distributed, random variables. Note that if the time-domain measurements of $\mathbf{E}(t)$ and $\mathbf{B}(t)$ are determined by zero-mean stochastic processes, their frequency-domain equivalents will also be zero mean. However, this is not true if $\mathbf{E}(t)$ and $\mathbf{B}(t)$ contain deterministic signals that are periodic in nature (e.g., controlled-source electromagnetics (CSEM) or power-line noise); perfect sinusoidal signals are zero-mean in the time domain but have non-zero-mean Fourier components. Signals like CSEM must be handled in a different way than what is presented here.

If we allow there to be noise only in the measurement of E, we may assert the

model,

$$E = \zeta B + \eta, \tag{3.2}$$

where η is zero mean noise, uncorrelated with E. Note that E and B are single measurements, or components, of electric and magnetic field, respectively, and not the full vector fields, as are **E** and **B**. The quantity ζ is an element of the complex impedance tensor which we wish to estimate, the objective of MT processing. With this model we can say that E and B are jointly distributed normal variables with zero mean and the covariance matrix,

$$C_{EB} = \begin{bmatrix} |\zeta|^2\sigma_B^2 + \sigma_\eta^2 & \zeta\sigma_B^2 \\ \zeta^*\sigma_B^2 & \sigma_B^2 \end{bmatrix}, \tag{3.3}$$

where the asterisk denotes the complex conjugate. The covariance matrix (3.3) is assembled by recalling that the covariance of two random variables, X and Y, defined in terms of the expected value, $\mathcal{E}[.]$, is,

$$\mathrm{cov}(X,Y) = \mathcal{E}\left[(X - \mathcal{E}\left[X\right])\left(Y - \mathcal{E}\left[Y\right]\right)\right], \tag{3.4}$$

which, if X and Y are zero mean, simplifies to

$$\mathrm{cov}(X,Y) = \mathcal{E}\left[XY\right]; \tag{3.5}$$

also, we have defined σ_X^2 as the variance of variable X:

$$\sigma_X^2 = \mathrm{var}(X) \equiv \mathrm{cov}(X,X). \tag{3.6}$$

The covariance matrix may be estimated from any set of observations of multiple random variables (an estimate of a given quantity based on observed data is denoted by a '^' over the quantity's symbol, and often made by replacing the expectation operator by an average over the measured data). Furthermore, the covariance matrix contains the entirety of information that may be gleaned from a set of observations of zero-mean, normally-distributed, random

variables.

The classic approach to MT processing is to solve for ζ by least-squares estimation. The choice of least-squares estimation stems from the fact that it yields the maximum-likelihood estimator for a model when η is the only source of error in our experiment, and η is normally distributed. The least-squares estimation problem is posed as,

$$\min_{\zeta} ||E_i - \zeta B_i||_2, \tag{3.7}$$

where i is the sample index for a collection of observations of E and B. This yields the conventional estimator,

$$\hat{\zeta} = \frac{\sum_i E_i B_i}{\sum_i B_i^2}. \tag{3.8}$$

Looking back at (3.3), we see, with little surprise, that (3.8) is simply,

$$\hat{\zeta} = \frac{\hat{C}_{12}}{\hat{C}_{22}}. \tag{3.9}$$

In this case, all estimable quantities in the model can be found with algebraic rearrangements of the covariance matrix. By noting that an $n \times n$ complex covariance matrix is Hermitian, consisting of n^2 real numbers, we see that C_{EB} provides 4 constraints for 4 unknowns: Imζ, Reζ, σ_B^2, and σ_η^2.

What happens when we allow for uncorrelated noise in the measurement of the magnetic field? We then have a new model:

$$B = b + \beta, \tag{3.10}$$

$$E = \zeta b + \eta, \tag{3.11}$$

where b, β, and η are all zero mean, uncorrelated Gaussian random variables. Attempting

to solve for ζ as we did before, we find,

$$\frac{C_{12}}{C_{22}} = \frac{\mathrm{cov}(E,B)}{\mathrm{var}(B)} = \frac{\zeta}{1+\sigma_\beta^2/\sigma_b^2}. \tag{3.12}$$

Thus, estimator (3.8) is biased downward by an unknown amount because we have no measurements of b with which to estimate σ_b^2. Another way to think about this unrecoverable estimation bias, is that the covariance matrix, C_{EB}, still provides 4 independent constraints, yet the model now has 5 unknowns. The well-known solution to this problem of downward bias is called the remote-reference method [Gamble et al., 1979]. It utilizes auxiliary measurements of the magnetic field at a "remote" site. The remote site must be carefully chosen to be distant enough so that its magnetic noise, ρ, is uncorrelated with that at the site of impedance estimation, β, yet close enough so that the source field, b, is uniform between sites. With these provisos, we again update our model, now with the remote magnetic field measurement, R:

$$B = b + \beta \tag{3.13}$$

$$R = b + \rho \tag{3.14}$$

$$E = \zeta b + \eta. \tag{3.15}$$

The quantities b, β, ρ, and η are uncorrelated, normal, random variables, and samples are taken of B, R, and E. We look now at the full covariance matrix for our system of three jointly distributed random variables:

$$C_{EBR} = \begin{bmatrix} |\zeta|^2\sigma_b^2 + \sigma_\eta^2 & \zeta\sigma_b^2 & \zeta\sigma_b^2 \\ \zeta^*\sigma_b^2 & \sigma_b^2 + \sigma_\beta^2 & \sigma_b^2 \\ \zeta^*\sigma_b^2 & \sigma_b^2 & \sigma_b^2 + \sigma_\rho^2 \end{bmatrix}. \tag{3.16}$$

The augmented covariance matrix provides 9 real constraints for a model that now has 7

real unknowns. As always, when faced with uncertainty, the introduction of an independent measurement provides some relief; in this case, it has provided more than enough. We now have two ways to recover the impedance tensor element, $\zeta = C_{12}/C_{23}$ and $\zeta = C_{13}/C_{23}$.

To make use of these excess constraints, one could add flexibility to the model. The local and remote magnetic field measurements, by definition, are separated in space, and therefore sense different earth structure, unless of course both source and earth are perfectly 1D. Barring that, we have no reason to believe that they are sensing the same magnetic field. To account for this we update our model for the remote magnetic field measurement:

$$R = \xi b + \rho, \tag{3.17}$$

with the other two fields unchanged. The resulting covariance matrix is found to be consistent, with 9 constraints on 9 unknowns:

$$C_{EBR} = \begin{bmatrix} |\zeta|^2\sigma_b^2 + \sigma_\eta^2 & \zeta\sigma_b^2 & \xi\zeta\sigma_b^2 \\ \zeta^*\sigma_b^2 & \sigma_b^2 + \sigma_\beta^2 & \xi\sigma_b^2 \\ \xi^*\zeta^*\sigma_b^2 & \xi^*\sigma_b^2 & |\xi|^2\sigma_b^2 + \sigma_\rho^2 \end{bmatrix}. \tag{3.18}$$

A pattern emerges which prefigures multi-station analysis: adding additional uncorrelated fields in the preceding models increases the number of available constraints faster that it increases the number of unknowns. The generic model building upon the progression to this point can be written as a set of random variables,

$$X_k = \zeta_k b + \eta_k,\ k = 1, 2 \ldots, n. \tag{3.19}$$

We have seen that this system affords an $n \times n$ Hermitian covariance matrix containing n^2 real numbers, while the real unknowns grow as $3n + 1$: $\mathrm{Re}\zeta_k$, $\mathrm{Im}\zeta_k$, σ_{η_k}, and σ_b. The minimum number of fields needed to solve for the unknowns of such a system is 4.

Nevertheless, the generic model (3.19) is an optimistic notion for MT. It allows for only one coherent energy source driving the other field variables, b, the presumed MT

plane wave. It does not allow for coherent noise between measurements of E and B at a single station, nor does it allow for noise to be coherent among multiple stations. It is easy to imagine cases where such coherent noise could exist at a single station (e.g., motional noise). Furthermore, the MT plane wave is hardly ever the sole source of EM driving fields coherent across an array of instruments; mankind has filled its environment with EM energy that may be far-reaching and does not originate from the ionosphere.

A solution to this problem of coherent noise, the ultimate method discussed in this chapter, is called the multivariate errors-in-variables (MEV) model [see Gleser, 1981]. The MEV model was introduced into the realm of MT processing by a series of papers [Egbert and Booker, 1989, Egbert, 1997, 2002]; these papers describe the multi-station MT data processing applied to the data used in this thesis. Two other elements of the data processing to be discussed in subsequent sections of this chapter are: (1) robust estimation procedures (Section 3.2); and (2) the transformation of the time series data into Fourier coefficients (FCs), the form of data fed into transfer function estimation (Section 3.3).

First, we must discuss the prologue to the MEV model. Now is a convenient time to leave the framework of a 1D earth and its associated impedance tensor with non-zero values only in the off-diagonal elements. The full impedance tensor presents us with 4 complex unknowns. To solve for these, we must have two independent realizations of a pair of electric and magnetic field measurements, say vectors $[B_x\ B_y\ E_x\ E_y]^T$ and $[B_x^\bullet\ B_y^\bullet\ E_x^\bullet\ E_y^\bullet]^T$, where the subscripts denote instrument coordinate axes, and the bulleted fields are from a source-field of different geometry, such that $\mathbf{B} \times \mathbf{B}^\bullet \neq 0$. Assuming for a moment, the field vectors are free of noise, and recalling (3.1), the impedance tensor Z is found by,

$$\mathsf{Z} = \mu \begin{bmatrix} z_{xx} & z_{xy} \\ z_{yx} & z_{yy} \end{bmatrix} = \mu \begin{bmatrix} E_x & E_x^\bullet \\ E_y & E_y^\bullet \end{bmatrix} \begin{bmatrix} B_x & B_x^\bullet \\ B_y & B_y^\bullet \end{bmatrix}^{-1} . \tag{3.20}$$

Now with incoherent noise in both the electric and magnetic fields, the model for a single

site of MT observation becomes,

$$\begin{bmatrix} B_x \\ B_y \\ E_x \\ E_y \end{bmatrix} = \begin{bmatrix} b_{x1} & b_{x2} \\ b_{1y} & b_{2y} \\ z_{xx}b_{x1} + z_{xy}b_{y1} & z_{xx}b_{x2} + z_{xy}b_{y2} \\ z_{yx}b_{x1} + z_{yy}b_{y1} & z_{yx}b_{x2} + z_{yy}b_{y2} \end{bmatrix} \begin{bmatrix} \alpha_1 \\ \alpha_2 \end{bmatrix} + \begin{bmatrix} \varepsilon_{B_x} \\ \varepsilon_{B_y} \\ \varepsilon_{E_x} \\ \varepsilon_{E_y} \end{bmatrix}. \tag{3.21}$$

The complex vectors $[b_{x1}\ b_{y1}]^T$ and $[b_{x2}\ b_{y2}]^T$ are the magnetic fields that would be measured at the given site for idealized, quasi-uniform, magnetic sources, linearly-polarized in two directions, hence the subscripts 1 & 2; these two principal axes of the MT source field are commonly assumed to be orthogonal, oriented N-S and E-W. The source indices are kept separate from the observation indices, x and y, because the source directions don't necessarily align with the instrument coordinate system. The vector $[\alpha_1\ \alpha_2]^T$ contains real, uncorrelated, zero-mean, normal, random variables, which together define the linear superpositions of the source fields in a given sample. The final vector on the right of (3.21), containing the ε's, represents the noise that is incoherent among the individual measurement channels. Re-applying our previous analysis, we see that there are 22 real-number unknowns in this system. If the assumption that each MT magnetic source vector is linearly polarized holds true (i.e. the $x-$ and $y-$coordinates oscillate in-phase with each other), we see that we can represent the system with real magnetic field vectors, and a complex random vector, $\boldsymbol{\alpha}$. In that case, the number of real unknowns is reduced to 18. Yet the covariance matrix, $\mathrm{cov}([B_x\ B_y\ E_x\ E_y], [B_x\ B_y\ E_x\ E_y])$, would provide only 16 real-number constraints; the system is under-determined. Again, we find the utility in a remote reference. Gamble et al. [1979] provide the equations for the elements of the impedance tensor, which make use of elements of the covariance matrix $\mathrm{cov}([B_x\ B_y\ E_x\ E_y\ B_x^R\ B_y^R], [B_x\ B_y\ E_x\ E_y\ B_x^R\ B_y^R])$, where the superscript R denotes fields from the remote site. Alternatively, MT instruments are often outfitted with a vertical magnetic field measurement, which we can add to the

model:

$$\begin{bmatrix} B_x \\ B_y \\ B_z \\ E_x \\ E_y \end{bmatrix} = \begin{bmatrix} b_{x1} & b_{x2} \\ b_{1y} & b_{2y} \\ v_{zx}b_{x1} + v_{zy}b_{y1} & v_{zx}b_{x2} + v_{zy}b_{y2} \\ z_{xx}b_{x1} + z_{xy}b_{y1} & z_{xx}b_{x2} + z_{xy}b_{y2} \\ z_{yx}b_{x1} + z_{yy}b_{y1} & z_{yx}b_{x2} + z_{yy}b_{y2} \end{bmatrix} \begin{bmatrix} \alpha_1 \\ \alpha_2 \end{bmatrix} + \begin{bmatrix} \varepsilon_{B_x} \\ \varepsilon_{B_y} \\ \varepsilon_{B_z} \\ \varepsilon_{E_x} \\ \varepsilon_{E_y} \end{bmatrix}. \tag{3.22}$$

With the vertical magnetic field, we've added only 4 more unknowns—the real and imaginary parts of the vertical magnetic transfer function, $\mathsf{V} = [v_{zx}\ v_{zy}]$, while bringing the total number of real constraints to 25. Assuming this idealized model, with only incoherent noise between instrument channels and linearly polarized magnetic source vectors, we see that a single 5-channel instrument should contain the requisite information to uniquely identify the signal and noise parameters as well as the impedance tensor and vertical magnetic transfer function. However, these unknowns are deeply buried within the algebra of the covariance matrix, which is far more complicated here than it was with the simplified models we used earlier. Thus, we abandon the search for a solution for the unknowns by algebraic manipulation of covariance matrix elements. Instead, we will follow an iterative approach to solve for the unknowns in (3.22), which we describe next.

Rewriting (3.22) as,

$$\boldsymbol{x} = U\boldsymbol{\alpha} + \boldsymbol{\varepsilon}, \tag{3.23}$$

we can show, with a fair amount of algebra, that,

$$\begin{bmatrix} \mathsf{V} \\ \mathsf{Z}/\mu \end{bmatrix} = \begin{bmatrix} u_{31} & u_{32} \\ u_{41} & u_{42} \\ u_{51} & u_{52} \end{bmatrix} \begin{bmatrix} u_{11} & u_{12} \\ u_{21} & u_{22} \end{bmatrix}^{-1}. \tag{3.24}$$

But we have no measurement of U; we must derive it somehow. We return to the ever-useful

covariance matrix, which we find to be,

$$C_{\boldsymbol{x}} = \mathcal{E}\left[U\boldsymbol{\alpha}\boldsymbol{\alpha}^{\dagger}U^{\dagger}\right] + \mathcal{E}\left[\boldsymbol{\varepsilon}\boldsymbol{\varepsilon}^{\dagger}\right]. \tag{3.25}$$

Note that we can pass the expectation operator through the matrix U because it contains non-random variables. Then, since the random variables within $\boldsymbol{\alpha}$ and $\boldsymbol{\varepsilon}$ are all uncorrelated, we have,

$$C_{\boldsymbol{x}} = U\Sigma_{\boldsymbol{\alpha}}U^{\dagger} + \Sigma_{\boldsymbol{\varepsilon}}, \tag{3.26}$$

where $\Sigma_{\boldsymbol{\alpha}}$ and $\Sigma_{\boldsymbol{\varepsilon}}$ are diagonal matrices with the variances of the elements of $\boldsymbol{\alpha}$ and $\boldsymbol{\varepsilon}$, respectively, along the diagonal. Now, imagine that we knew *a priori* $\Sigma_{\boldsymbol{\varepsilon}}$. We could then rescale our covariance matrix in the following way,

$$C'_{\boldsymbol{x}} = \Sigma_{\boldsymbol{\varepsilon}}^{-\frac{1}{2}}\left[C_{\boldsymbol{x}} - \Sigma_{\boldsymbol{\varepsilon}}\right]\Sigma_{\boldsymbol{\varepsilon}}^{-\frac{1}{2}}. \tag{3.27}$$

Applying an eigenvalue decomposition to the Hermitian matrix $C'_{\boldsymbol{x}}$ would provide,

$$C'_{\boldsymbol{x}} = W\Lambda W^{\dagger}, \tag{3.28}$$

where W is a unitary matrix, and Λ is a diagonal matrix with the eigenvalues of $C'_{\boldsymbol{x}}$ along the diagonal, all of which are real. Then by (3.26), (3.27), and (3.28) we see that if $\Sigma_{\boldsymbol{\varepsilon}}$ was known perfectly *a priori*, Λ should contain only two non-zero eigenvalues, and the columns of W that correspond to those non-zero eigenvalues provide scaled versions of unknown linear combinations of the two columns of U. In fact,

$$W = \Sigma_{\boldsymbol{\varepsilon}}^{-1/2}UA, \tag{3.29}$$

where the matrix A is an arbitrary, invertible, 2×2 matrix which represents the indeterminacy of our model; it is a result of the inability to uniquely determine external source polarizations from observations of total (internal plus external) fields [Egbert and Booker, 1989, Egbert, 1997]. The existence of an unknown A in our estimation of W is no hinder-

ance to our goal of estimating the transfer functions between our channels of data, i.e., we are not actually interested in U but transfer functions between its rows, as (3.24) suggests. We may re-scale the rows of the matrix W to find,

$$\Sigma_{\varepsilon}^{1/2} W = \begin{bmatrix} \mathrm{b}A \\ \mathbf{v}A \\ \mathrm{e}A \end{bmatrix}, \tag{3.30}$$

where b is a 2×2 matrix of the magnetic sources, $\mathbf{v}$ is 2-vector of the resulting vertical magnetic fields, such that $\mathbf{v} = \mathsf{V}\mathrm{b}$, and e is a 2×2 matrix of the resulting electric fields, such that $\mathrm{e} = \mathsf{Z}\mathrm{b}$. Then, the estimation of the impedance transfer function, for example, proceeds as follows

$$\mathsf{Z} = \mu \mathrm{e}A(\mathrm{b}A)^{-1} = \mu \mathrm{e}AA^{-1}\mathrm{b}^{-1} = \mu \mathrm{e}\mathrm{b}^{-1}, \tag{3.31}$$

thus removing the effect of A.

We can say that in the scaled space of $C'_{\boldsymbol{x}}$, only the principal components (columns of W) corresponding to coherent parts of the data should have an eigenvalue greater than 1; this essentially means that the only components with greater variance than the incoherent noise must be coherent signal (the validity of this will depend on the strength of the *a priori* estimate of $\Sigma_{\boldsymbol{\varepsilon}}$). Egbert [1997] expanded the model represented in (3.23) by allowing there to be more than 2 columns in U, and allowing the source fields to be arbitrarily polarized (i.e. no linear polarization assumption). The number of columns of U is left as a free parameter, to be established during the estimation process. The extra columns embody coherent signals in the data, but those which are independent of the ideal MT source field; these may include non-planar natural sources, as well as man-made sources.

The iterative approach to solving the MEV model, described in Egbert [1997], seeks to define all coherent source terms in a vector of random data. It starts with a crude estimate of $\Sigma_{\boldsymbol{\varepsilon}}$, and a robust estimate of $C_{\boldsymbol{x}}$; what we have called the covariance matrix, $C_{\boldsymbol{x}}$, is also known as the spectral density matrix because it is the covariance matrix of Fourier coefficients. Then by (3.28), an estimate of W is made. All of the columns of $\hat{W}$

corresponding to eigenvalues greater than 1 are taken to be coherent signal; then, they are re-scaled by their incoherent noise estimates and gathered into a sub-matrix which we call $\tilde{U}$. Due to the orthogonality of $\tilde{U}$, an estimate of $\boldsymbol{\alpha}$ is then made with,

$$\hat{\boldsymbol{\alpha}} = \tilde{U}^{\dagger}\boldsymbol{x}. \tag{3.32}$$

Now, with $\hat{\boldsymbol{\alpha}}$ and $\tilde{U}$, the residuals, robust weights, and "cleaned" data vector, $\tilde{\boldsymbol{x}}$, are calculated. We will discuss how this is done in Section 3.2 regarding robust estimation. The residuals provide an updated estimate of $\Sigma_{\boldsymbol{\varepsilon}}$. Then, with the updated incoherent noise estimate, the next iteration repeats the foregoing steps after substituting $\tilde{\boldsymbol{x}}$ for the data vector $\boldsymbol{x}$. This procedure is iterated until convergence. The resulting products are estimates of U, $\boldsymbol{\alpha}$, and $\Sigma_{\boldsymbol{\varepsilon}}$, from which transfer-functions between all channels may be derived, using manipulations like (3.24), along with errors in the estimates of those transfer functions. Note that a choice must be made as to which columns of $\tilde{U}$ pertain to the MT sources. The common assumption is that the MT signal is the strongest, so the columns of $\tilde{U}$ corresponding to the two largest eigenvalues in $\hat{\Lambda}$ are used (again, the values in $\hat{\Lambda}$ are estimates of signal-to-noise power ratios for each principle component in W). The details of this entire process are much more intricate than what has been presented here; for a more thorough treatment consult Egbert [1997, 2002].

Even with the robust estimator for the MEV model, it is clear that the maximum number of resolvable coherent source components in a given vector of data is equal to the length of that vector. Thus, with the 5 measurements in (3.22), the 2 components of the MT sources and 3 other coherent noise components may be resolved. This is where the argument for multi-station processing is made. With the multi-station approach, the linear systems for N channels from multiple stations, each described by (3.23), but with the number of columns of U unknown, are vertically integrated, such that the amalgamated

system becomes,

$$\begin{bmatrix} \boldsymbol{x}_1 \\ \boldsymbol{x}_2 \\ \vdots \\ \boldsymbol{x}_N \end{bmatrix} = \begin{bmatrix} U_1 \\ U_2 \\ \vdots \\ U_N \end{bmatrix} \begin{bmatrix} \boldsymbol{\alpha}_1 \\ \boldsymbol{\alpha}_2 \\ \vdots \\ \boldsymbol{\alpha}_N \end{bmatrix} + \begin{bmatrix} \boldsymbol{\varepsilon}_1 \\ \boldsymbol{\varepsilon}_2 \\ \vdots \\ \boldsymbol{\varepsilon}_N \end{bmatrix}. \tag{3.33}$$

With this large simultaneous system, $N-2$ independent coherent noise sources may be resolved by multi-station MT processing (i.e. the maximum possible number of columns of $\tilde{U}$ is N). If the number of significant coherent noise sources is much less than $N-2$, then the system is better-constrained, and as a result, the unknowns U, $\boldsymbol{\alpha}$, and $\Sigma_{\boldsymbol{\varepsilon}}$ are better resolved. If the number of significant noise sources is larger than $N-2$, the system is again under-determined, and the estimates of U, $\boldsymbol{\alpha}$, and $\Sigma_{\boldsymbol{\varepsilon}}$ will have aliased into them the hidden degrees of freedom.

3.2 Robust Estimation

In Section 3.1, for the purposes of MT transfer-function estimation, we found a linear system to be solved, given by (3.23), where U, $\boldsymbol{\alpha}$, and var($\boldsymbol{\varepsilon}$) are all unknowns. An iterative process is used to converge upon estimates of U, $\boldsymbol{\alpha}$, and var($\boldsymbol{\varepsilon}$), which relies upon a robust method for down-weighting outliers in the data vector, $\boldsymbol{x}$. We introduce that process here, following the example of Egbert and Booker [1986].

For a standard linear system of n data, x_i, with random zero-mean noise, e_i, we have

$$x_i = \sum_{j=1}^{p} a_{ij} b_j + e_i, \tag{3.34}$$

or, in matrix notation,

$$\boldsymbol{x} = A\boldsymbol{b} + \boldsymbol{e}, \tag{3.35}$$

where the $[a_{i1}\ a_{i2} \cdots a_{ip}]$, the columns of A, are known basis functions, and the b_j constitute p unknowns. If the data errors, e_i, are uncorrelated and of unequal variances, $\text{var}(e_i) = \sigma_i^2$, then the best linear unbiased estimator (BLUE) of $\boldsymbol{b}$ is achieved through the minimization of the weighted sum of squared residuals,

$$\sum_{i=1}^{n} w_i (x_i - \sum_{j=1}^{p} a_{ij} b_j)^2, \tag{3.36}$$

where the weights are determined by the variances of e, such that $w_i = 1/\sigma_i^2$. Minimization of (3.36) with respect to $\boldsymbol{b}$ requires the solution of a linear system of equations,

$$\sum_{i=1}^{n} 2a_{ji} w_i (x_i - \sum_{j=1}^{p} a_{ij} b_j) = 0. \tag{3.37}$$

This is a well-known process called weighted least squares (WLS) estimation, and the estimator for $\boldsymbol{b}$ in matrix form is,

$$\hat{\boldsymbol{b}} = (A^T \Sigma_e^{-1} A)^{-1} A^T \Sigma_e^{-1} \boldsymbol{x}. \tag{3.38}$$

where, mirroring Section 3.1, Σ_e is a diagonal matrix with the variances of $\boldsymbol{e}$ along its diagonal.

The WLS estimate can be shown to be best among linear estimates, and in the case of normally-distributed e_i, it is the best of *all* estimates; it is the maximum-likelihood estimator for Gaussian-distributed random variables. However, if the actual error distribution deviates from Gaussian, the WLS process can produce unreliable results. In the case of a small number of "bad" data points, which we call outliers, the WLS procedure can be seriously biased; due to this property we say that the WLS estimator is not robust. Outliers are a result of an error distribution that is longer-tailed (meaning larger errors are more probable) than the assumed Gaussian distribution. When outliers exist in an LS estimation process, they wield excessive influence on the resulting model. We must therefore make use of an estimator that accounts for a broader distribution of data errors by down-weighting outliers.

We make use of a new maximum likelihood estimator for a contrived non-Gaussian error distribution. Following Egbert and Booker [1986], we seek estimates of $\boldsymbol{b}$ which minimize what is called a loss function, $\rho(r)$, of the form,

$$\sum_{i=1}^{n} \rho\left(\frac{x_i - \sum_{j=1}^{p} a_{ij} b_j}{\sigma_i}\right), \tag{3.39}$$

where we have chosen r to be the standard-error normalized residual between data and model prediction. The standard LS (L_2-minimization) process derives from the loss function,

$$\rho(r) = r^2/2, \tag{3.40}$$

and alternatively L_1 minimization derives from $\rho(r) = |r|$. For our robust scheme, which will minimize the influence of outliers, we use a hybrid of the two aforementioned loss functions, together called Huber's t-function,

$$\rho(r) = \begin{cases} r^2/2, & |r| < r_0 \\ r_0|r| - r_0^2/2, & |r| \geq r_0, \end{cases} \tag{3.41}$$

where r_0 chosen to be 1.5 gives better than 95% efficiency if r turns out to be normally distributed [Chave et al., 1987]. Note that due to the scaling of (3.39), the transition between L_2 and L_1 minimization occurs at $\sigma_i r_0$, so that the scale parameter σ_i and r_0 decide what is considered to be an outlier. Thus, a robust estimation of the σ_i is an important part of the current process.

The minimization of the loss function with respect to $\boldsymbol{b}$ requires the solution of the linear system of equations,

$$\sum_{i=1}^{n} \frac{\partial r_i}{\partial b_j} \rho'(r_i) = 0, \tag{3.42}$$

Given the loss function (3.41), (3.42) becomes

$$\sum_{i=1}^{n} a_{ji} \frac{\psi(r_i)}{\sigma_i} = 0, \tag{3.43}$$

where,

$$\psi(r) = \begin{cases} r, & |r| < r_0 \\ r_0 r/|r|, & |r| \geq r_0, \end{cases} \tag{3.44}$$

and $\psi(r)$ is called the influence function. Now we define a new function

$$w(r) = \psi/r. \tag{3.45}$$

Then with (3.45) and our definition of r we rewrite (3.43) as

$$\sum_{i=1}^{n} a_{ji} \frac{w(r_i)}{\sigma_i^2} (x_i - \sum_{j=1}^{p} a_{ij} b_j) = 0, \tag{3.46}$$

where, by (3.44), we see that (3.45) is simply,

$$w(r) = \begin{cases} 1, & |r| < r_0 \\ r_0/|r|, & |r| \geq r_0. \end{cases} \tag{3.47}$$

Clearly (3.46) is just another WLS problem like (3.37), but with an iterative solution for $\boldsymbol{b}$ given by,

$$\hat{\boldsymbol{b}}^{(k+1)} = (A^T \Sigma_e^{-1} W^{(k)} A)^{-1} A^T \Sigma_e^{-1} W^{(k)} \boldsymbol{x}, \; k = 0, 1, 2, \ldots \; . \tag{3.48}$$

With (3.48) we now have two diagonal weighting matrices: Σ_e, as before, contains the variances of the error in each datum; whereas $W^{(k)}$ contains the weight applied to each datum, determined by (3.47), given the standardized residuals between the data and the k^{th} model prediction. At first we do not know what these residuals are, as we have yet to estimate a model. This is why our robust estimation must be an iterative process (a

non-linear estimator). We must first make an estimate of the residuals to determine our robust weights. We do this by simply setting all of the weights in W to 1 for the initial ($k = 0$) iteration. We then calculate $\hat{\boldsymbol{b}}^{(1)}$, $r_i^{(1)}$, and finally, $w_i^{(1)}$.

Now we address the likely case where the σ_i are unknown. With such a case it is necessary to assume that all data are affected by an equal error variance, σ, which we may then estimate along the way. Note that with equal variances, Σ_e in (3.48) becomes a scalar matrix and thus is immaterial. However, we still need a measure of σ to scale the residuals, a crucial piece of the iterative weighting scheme. So, assuming equal variances in all data, an estimate of σ is made at each iteration with,

$$\hat{\sigma}^{(k)} = \sqrt{\frac{1}{\beta(n-p)} \sum_{i=1}^{n} (w_i^{(k-1)} r_i^{(k)})^2}, \tag{3.49}$$

where the factor β corrects for the bias produced by using the weights to estimate σ (see Appendix A of Egbert and Booker [1986]). With $\hat{\sigma}^{(k)}$ a new weighting matrix, $W^{(k)}$, is produced and a new iteration of (3.48) follows. Like so, the iterations proceed with updated weights until some norm of the change in $\hat{\boldsymbol{b}}$ from iteration to iteration gets sufficiently close to zero.

It can be shown that the choice of the loss function (3.41) ensures convergence to a unique solution because it is convex, i.e. ψ is non-decreasing. However, while (3.41) diminishes the effect of outliers, their influence is never entirely removed. On the other hand, more stringent loss functions which effectively nullify outliers are not convex, and therefore are not guaranteed to converge to a unique solution. In practice, it is best to use a mix of these two types of loss functions. Begin with the convex loss function until convergence is reached; it can then be assumed that the model estimate is close to the true solution. Then, continue with a fixed number of iterations using a non-convex loss function; it will do better at removing the influence of outliers, but cannot be trusted unless it starts close to the true solution. Egbert and Booker [1986] use the influence function

$$\psi(r) = r \exp\left\{-\exp\left[r_0\left(|r| - r_0\right)\right]\right\}, \tag{3.50}$$

with $r_0 = 2.8$ for the final two iterations of their robust estimation scheme.

An alternative way to robustly estimate $\boldsymbol{b}$ in (3.35) is to introduce the device of a "cleaned" data vector,

$$\tilde{\boldsymbol{x}}^{(k)} = A\hat{\boldsymbol{b}}^{(k)} + W^{(k)}\boldsymbol{r},\ k = 1, 2 \ldots, \tag{3.51}$$

where $\tilde{\boldsymbol{x}}^{(0)} = \boldsymbol{x}$. Then the iterative estimation of $\boldsymbol{b}$ is given by

$$\hat{\boldsymbol{b}}^{(k+1)} = (A^T A)^{-1} A^T \tilde{\boldsymbol{x}}^{(k)},\ k = 0, 1, 2 \ldots\ . \tag{3.52}$$

Note that by (3.47), the cleaned data vector is identical to the observed data vector for small residuals ($r_i \leq r_0\hat{\sigma}$), whereas large residuals are pulled back toward more normal values. The cleaned data vector, $\tilde{\boldsymbol{x}}$ is used in the method described in Section 3.1 for robust estimation of the covariance matrix, or the spectral density matrix.

3.3 Fourier Coefficients

The preceding sections describe methods for transfer function estimation, a central component of MT data processing. The data vectors used in transfer function estimation are Fourier coefficients (FCs) at a range of frequencies. The data are delivered from the instrument in the form of time series of voltages from each measurement channel. Therefore, to continue onto transfer function estimation, the raw data must first be transformed into the Fourier domain and converted to physical units of electric and magnetic field.

Many noise sources in an MT record are intermittent and often come in the form of spikes or discontinuities, which have a broad power spectrum; thus these brief episodes of noise can pollute a broad frequency range of FC estimates. It is therefore optimal to break a full time series into sections and derive multiple estimates of FCs at any given frequency from multiple data sub-records. This approach then relies upon the robust estimation procedure described in Section 3.2 to effectively cull the FCs which derive from sub-records that contain intermittent, abnormal noise. The segmentation of the data record into smaller windows comes at the cost of reducing the longest-period FC estimable from the data.

Luckily, most MT data records are dozens of times longer than the longest period at which the assumption of an MT plane wave source is realistic; so breaking up the full record does not result in a loss of FC data that we would want to use. Note that there is no cost in terms of variance incurred by breaking the longer time record into smaller segments. The variance of an estimate of an FC at a given frequency is unchanged by the number of time samples that went into the discrete Fourier transform (DFT) required to estimate it; as the number of constraints fed into the DFT increases, so do the number of unknowns, and at the same rate. Thus, the uncertainties in the unknowns (the FCs) are unchanged with increasing length of time window.

The full data record is decomposed into smaller windows, the number of which varies by frequency band with a technique called cascade decimation. The goal of cascade decimation is to maximize the number of FCs possible for a given frequency band. The higher frequencies do not need as long of records to make a decent estimate of their FC as do the lower frequencies. So the data record is broken into many more segments of shorter length for the higher frequencies and fewer, longer segments for the lower frequencies. When using longer segments for the lower frequency estimates, if the full data sampling rate were to be used, we would also receive estimates for the higher frequencies. However, these estimates would be correlated to those already gained for the same time window, but broken into smaller segments; they are redundant and amount to a waste of computational effort. Thus, as we "cascade" into estimates for lower frequency bands, a decimation is performed on the full data record to reduce the number of time samples used in the longer segments. Before performing decimation by a simple down-sampling, a low-pass filter must be applied to the data segment. If filtering were not performed before down-sampling, we would risk aliasing high-frequency energy into the decimated record, which would then bias the low frequency estimates.

Once the full data record is decomposed into multiple time windows, each window is multiplied by a Hamming window function before applying the DFT; this is a single-taper method. Multiplying a time series by a "tapered" window function, whose values smoothly approach zero at the edges of the window, reduces bias in the FCs. A DFT of a raw time series of finite length can be seen as the Fourier transform of the product of an infinitely long

signal with a boxcar function. In the frequency domain this amounts to a convolution of the infinite-length signal's Fourier transform by a sinc function. The convolution performs a weighted average over all frequency bins for each FC estimate, hence the bias. Applying a Hamming window function, for example, as opposed to the boxcar, reduces bias because the smoothing kernel has much smaller side-lobes, concentrating the weighted average around the central frequency of each convolution.

The FCs up to this point are given in units of voltage (technically they are first given in terms of digitization counts, for which a nominal digitization calibration converts to voltage). In order to transform the FCs into physical units, we must account for each instrument's response function. When an instrument channel's sensor (input) is exposed to a time-varying environmental field $X(t)$, a voltage $V(t)$ is produced on the channel's output, which is related to the channel's impulse response function, $G(t)$, in the following way,

$$V(t) = G(t) * X(t), \tag{3.53}$$

where the symbol $*$ is the convolution operator. The Convolution Theorem allows us to restate (3.53) in the frequency domain as,

$$\hat{V}(\omega) = \hat{G}(\omega)\hat{X}(\omega). \tag{3.54}$$

Then, to convert FCs of voltage into their respective field units, we have simply,

$$\hat{X}(\omega) = \frac{\hat{V}(\omega)}{\hat{G}(\omega)}. \tag{3.55}$$

The instrument frequency response $\hat{G}(\omega)$ can be derived in the lab by subjecting each instrument channel to a known sinusoidally-varying field at a range of frequencies and measuring the resulting voltages. Least-squares fitting of the known input field to the output voltages produces a frequency response function sampled at the exact frequencies produced in the lab. The fitting of a physical model for the instrument components can then interpolate between the sampled frequencies in order to create a continuous frequency

response function.

Once these steps are completed, we generate a time series of FCs in physical units, a spectrogram, for each channel of data to be analyzed. Spectrograms for three MT stations, M01, M17, and M40, each with 4 channels of data, B_x, B_y, E_x, E_y, are plotted in Figures 3.1 through 3.6. The time-resolution of the FCs decreases with decreasing frequency, because, as was stated before, longer time windows are needed to estimate the lower frequencies. The two stations are at opposite ends of the survey line (see Figure 2.1); M01 is closest to the coast ($\approx$ 15 km), in the shallowest water depth of 320 m; M17 is a moderate distance from the coast ($\approx$ 75 km), in 880 m deep water; M40 is furthest from the coast ($\approx$ 200 km), in much deeper water depth of 3,870 m. The white horizontal lines across all of the spectrograms indicate the levels of cascade decimation used to create the FCs.

We now make a qualitative assessment of a few features in the spectrograms. First, in the magnetic channels of M01 there is an obvious broadband source of energy that seems to turn on and off again, twice a day; there are approximately 8 hour periods of vertical bright streaks in the spectrogram followed by approximately 4 hour periods of lower energy across the spectra. These periodic spectral-energy variations are likely explained by tidal forces. The coastal tide height relative to the mean lower low water (MLLW) as measured at the nearby site of Port San Luis, is plotted with a black line in the upper plot of Figure 3.1. The largest tidal constituent in most locations around the world is known as the principal lunar semi-diurnal (M_2 in Darwin notation), which has a period of approximately 12.5 hours. The time between peaks and troughs of this tidal constituent can be expected to involve increased strength in ocean currents and wave action at the coast, as water is displaced by a large gradient in the earth's gravitational potential; on the other hand, the gravitational potential close to the peaks and troughs of the M_2 is relatively stable, so tidal water movement is minimal. It is difficult without more quantitative analysis to discern how these tidal movements in the ocean translate into magnetic field signals. A few possible means should be considered: water currents may actually rock the instrument, changing the vector magnetic field being measured; micro-tremors induced by waves crashing on the beach may travel to the instrument through the

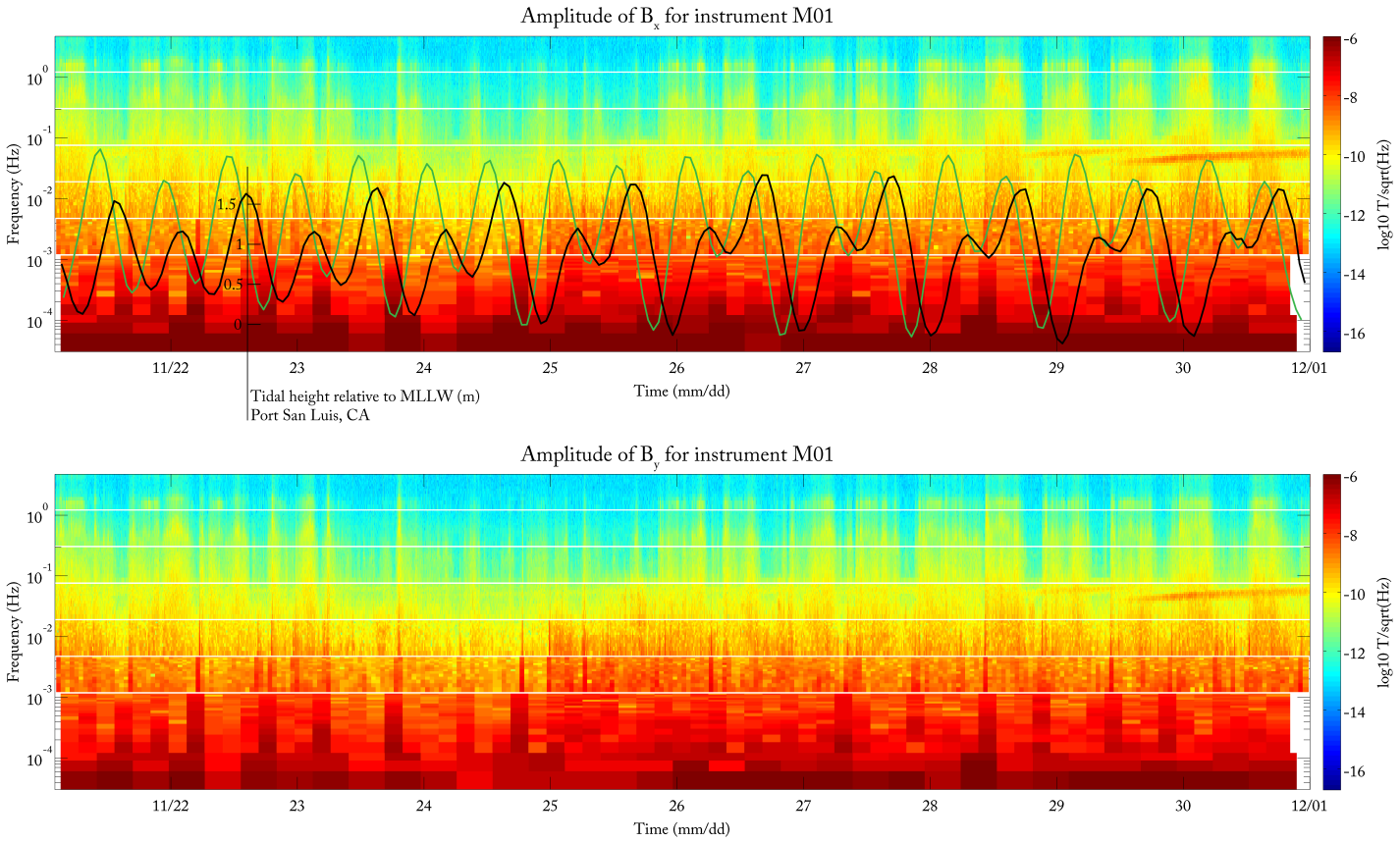

Figure 3.1: Amplitude spectrograms of the first 10 days of horizontal magnetic field measurements (B_x & B_y) at the shallow water site M01 (water depth = 320 m). The time axis is in Coordinated Universal Time (UTC) which is 8 hours ahead of Pacific Time (PT). Tidal height relative to the mean lower low water (MLLW) at an observation station in Port San Luis is plotted with the black line. The green line plots the arbitrarily-scaled first time derivative of tidal height.

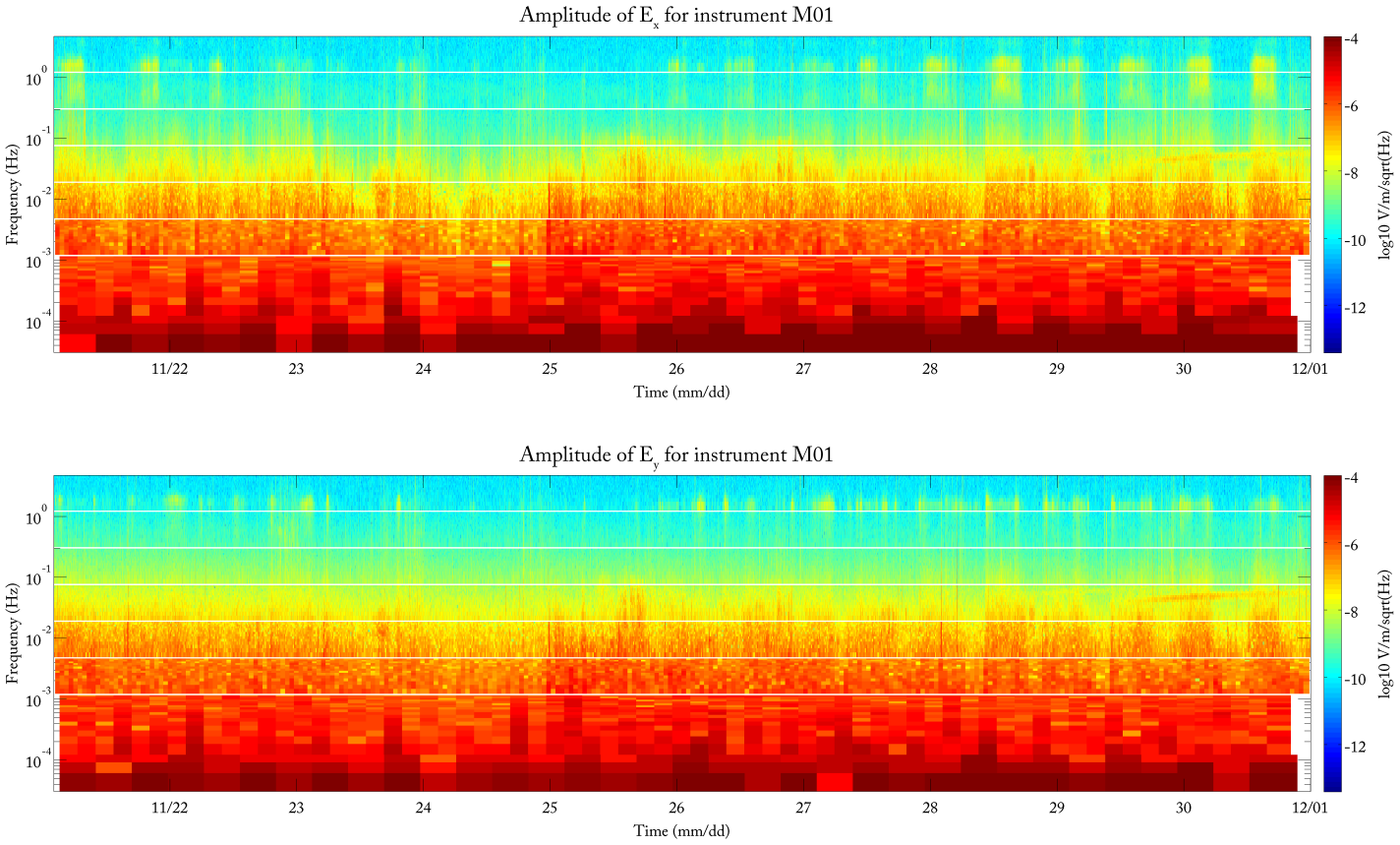

Figure 3.2: Amplitude spectrograms of the first 10 days of horizontal electric field measurements (E_x & E_y) at the shallow water site M01 (water depth = 320 m). The time axis is in Coordinated Universal Time (UTC) which is 8 hours ahead of Pacific Time (PT).

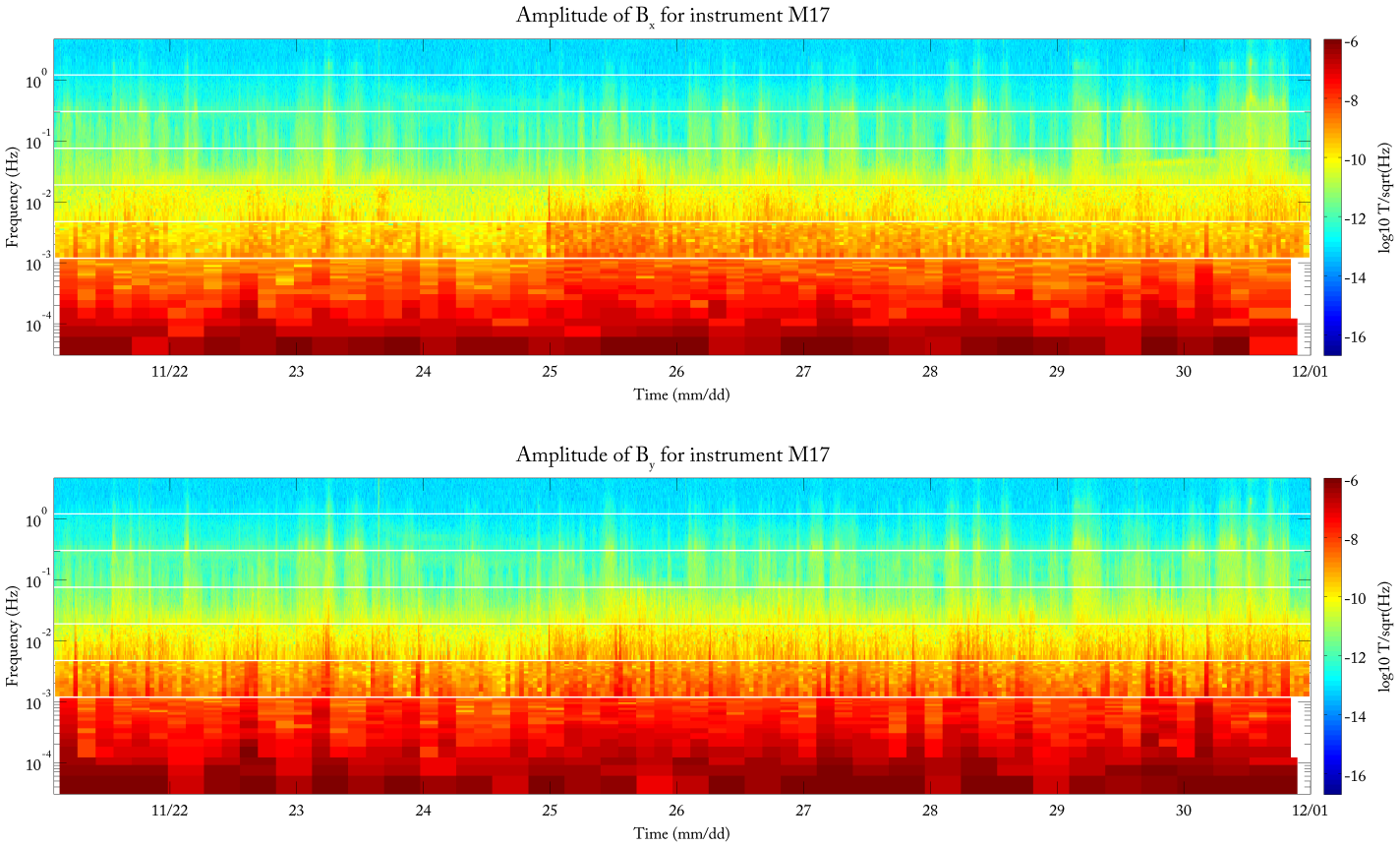

Figure 3.3: Amplitude spectrograms of the first 10 days of horizontal magnetic field measurements (B_x & B_y) at the moderate water depth site M17 (water depth = 880 m). The time axis is in Coordinated Universal Time (UTC) which is 8 hours ahead of Pacific Time (PT).

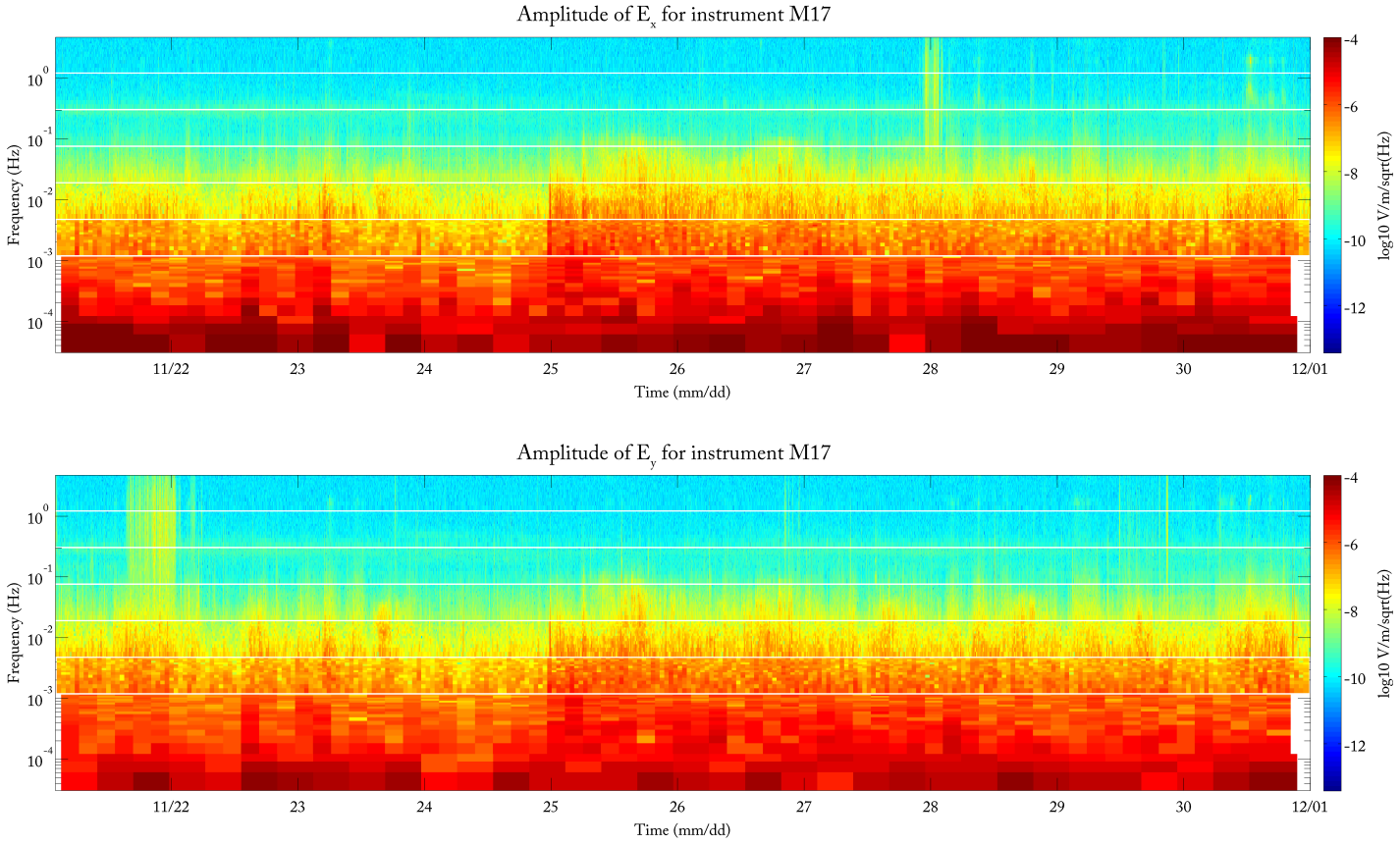

Figure 3.4: Amplitude spectrograms of the first 10 days of horizontal electric field measurements (E_x & E_y) at the moderate water depth site M17 (water depth = 880 m). The time axis is in Coordinated Universal Time (UTC) which is 8 hours ahead of Pacific Time (PT).

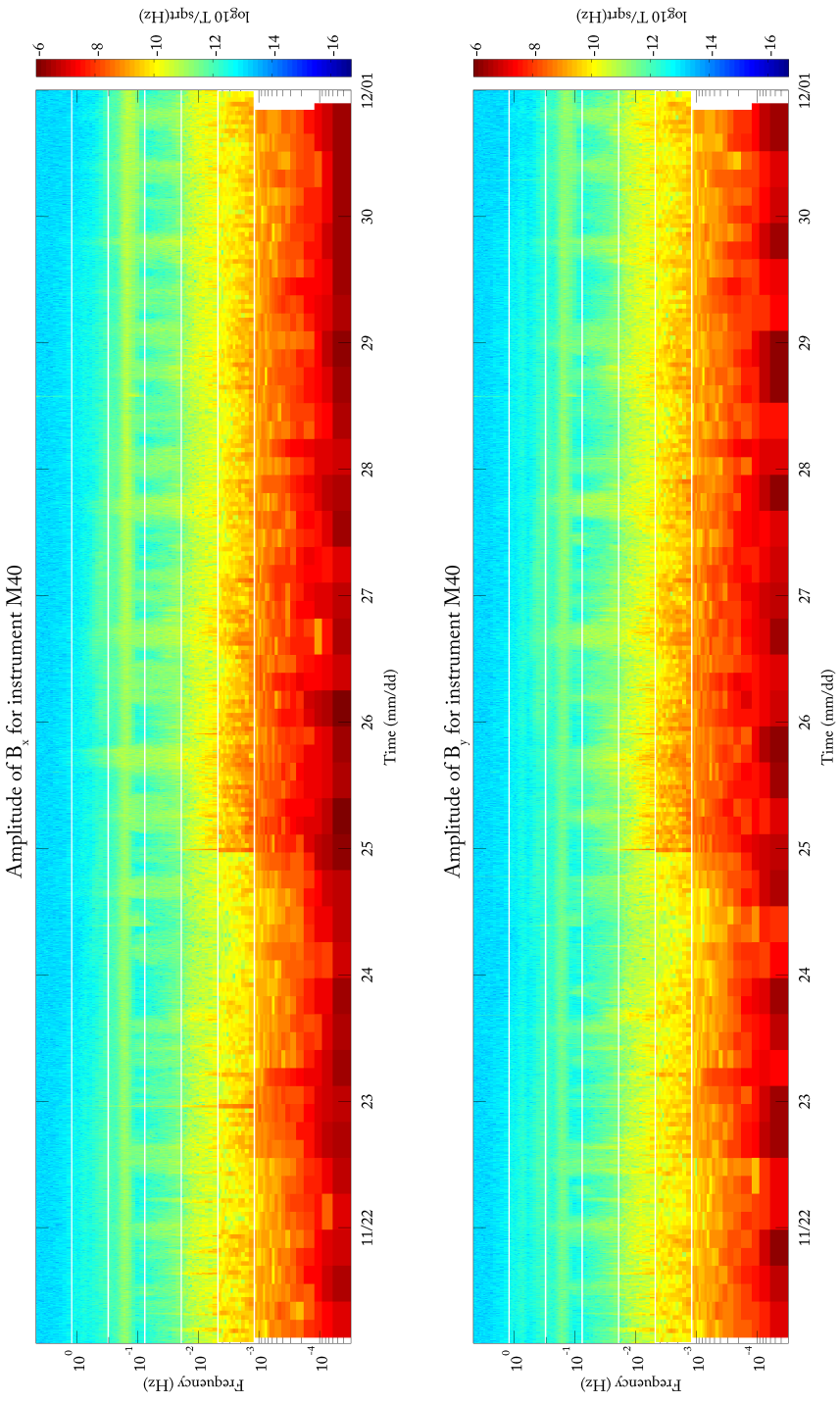

Figure 3.5: Amplitude spectrograms of the first 10 days of horizontal magnetic field measurements (B_x & B_y) at the deep water site M40 (water depth = 3,870 m). The time axis is in Coordinated Universal Time (UTC) which is 8 hours ahead of Pacific Time (PT).

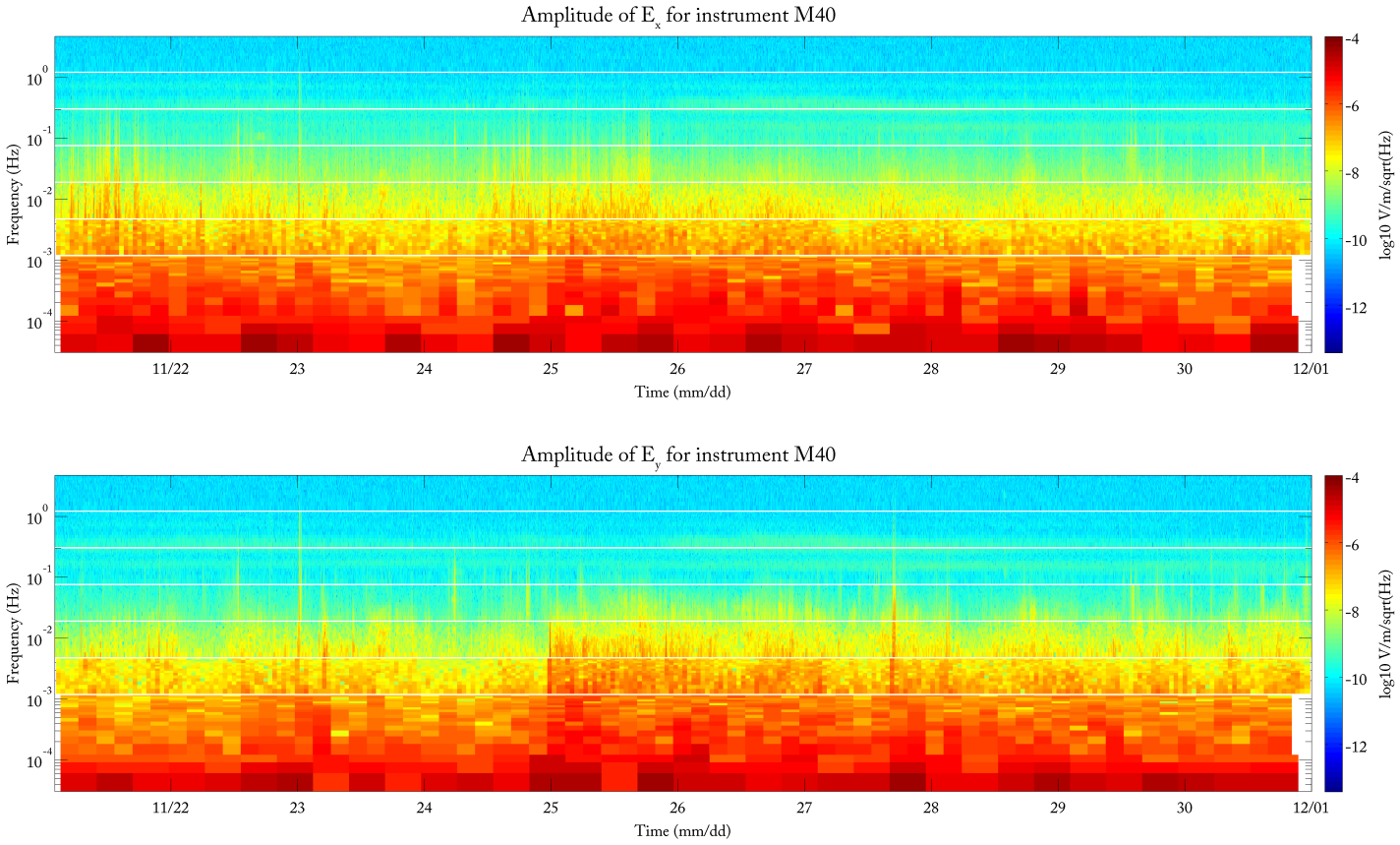

Figure 3.6: Amplitude spectrograms of the first 10 days of horizontal electric field measurements (E_x & E_y) at the deep water site M40 (water depth = 3,870 m). The time axis is in Coordinated Universal Time (UTC) which is 8 hours ahead of Pacific Time (PT).

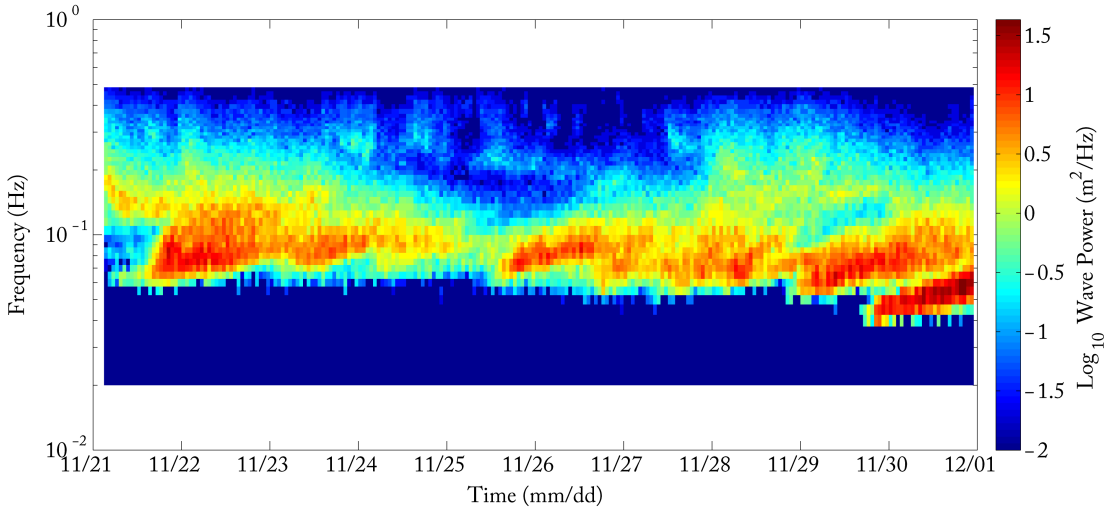

Figure 3.7: Spectrogram of wave power density contemporaneous with the first 10 days of MT data. The time axis is in Coordinated Universal Time (UTC) which is 8 hours ahead of Pacific Time (PT). The wave energy data was collected by the National Data Buoy Station 46011.

seafloor, also rocking the instrument; increased surface wave amplitudes or turbulence in the water column may induce electromagnetic fields through dynamo action [Larsen, 1968, Chave et al., 1989]. There are a few more observations to be made about this semi-diurnal tidal energy variation in the spectrograms: the tidal energy is observed to be much weaker in the electric field records of M01, at least in the band above 10 s period; there is a relative peak in the spectra of site M01 at about 2 s period when the tidal energy is high; the tidal energy is not equally partitioned between the two orthogonal channels of measurement; the tidal energy is less apparent in the spectrograms from site M17, and even less so from site M40; the window of elevated energy aligns with periods of incoming tide (increasing water height), and the integrated energy within the window increases with increasing trough-to-peak differences in tide height. We don't intend to deduce the physics of how the tidal energy is transferred to the electromagnetic sensors at this time. We simply note that these observations of tidal energy indicate there is a large portion of signal in the spectra of measurements, at least at the shallow-water/near-shore sites, that is not sourced from the

MT ionospheric plane wave.

Another example of non-MT energy can be seen in the spectrograms of M01, and to a lesser degree, those of M17. There are two discrete disturbances that occur in the days between November 29th and December 1st. They appear as slightly sub-horizontal bright streaks of energy in the period band between 10 s - 50 s. They are the characteristic sign of a meteorological storm occurring some distance away from the instrument location. The storm produces elevated water wave action that in turn induces elevated electromagnetic fields as charged ions move in the earth's static magnetic field. As the water waves propagate away from their source location, dispersion occurs. The longer period energy travels faster than its higher frequency counterpart. Thus, the energy streaks in the spectrograms are slightly inclined with respect to time; the prominent frequency components of the passing wave-train increase with time as the higher-frequency energy is the slower to arrive. An estimate of the slope of the progression in frequency content in time, along with knowledge about the group velocity of waves in the ocean should provide an estimate of the distance between the original storm and the point of measurement as well as the storm's time of onset [Munk et al., 1963]. Figure 3.7 provides an independent and more direct measurement of the propagating storm energy; it plots the spectrogram of water wave power as measured by a buoy near our seafloor instrument array. While there are many upward-tilting flares of energy apparent in the buoy record, the two final ones between the days of November 29th and December 1st exhibit slightly higher power and lower period content at onset. These two properties may be why signatures of these two storms are the only two that show up in the electromagnetic field record; another possibility is directional variation in storm origin.

Both of the preceding observations about the FC records represent energy sources that do not obey our MT assumptions. They must therefore be removed from the data to be interpreted. Prior to the process of transfer function estimation, the FC records containing the obvious storm-driven energy may be manually removed from subsequent data processing. The manual removal of the tidal signature, due to its pervasiveness in time is much more difficult; visual inspection of data from site M01 would indicate that there is little left unaffected by the tides. We must therefore rely upon robust multi-station processing to deal with the tidal energy in an automated way.

3.4 Apparent Resistivity and Phase Data

Although estimation of impedance tensors and other complex transfer functions, such as vertical magnetic transfer functions, are the central product of MT data processing, their unadulterated units have little intuitive meaning. That is why the data used in MT interpretation quite often take the form of apparent resistivity and phase. Apparent resistivity is derived from the impedance tensor and comes in units of Ωm, as the name implies. Measured over a hypothetical halfspace of uniform resistivity, an MT datum in the form of apparent resistivity would provide the exact resistivity of that halfspace; we supply the proof of this in Section 5.9. The transformation from an element of the impedance tensor, Z_{ij}, to the corresponding apparent resistivity, ρ_{ij}, is as follows,

$$\rho_{ij} = \frac{1}{\mu\omega}|\mathsf{Z}_{ij}|^2, \;\; i = \{1,2\}, \text{ and } j = \{1,2\}. \tag{3.56}$$

Phase, Φ, comes in units of degrees, and is derived from the same impedance tensor elements as follows,

$$\Phi_{ij} = \arg(\mathsf{Z}_{ij}) = \arctan\left(\frac{\operatorname{Im}\mathsf{Z}_{ij}}{\operatorname{Re}\mathsf{Z}_{ij}}\right). \tag{3.57}$$

We may analyze the relationship between the impedance tensor phase, and the complex-valued electric and magnetic fields themselves for the simplified cases of 1D, or 2D conductivity structure with the field components oriented parallel and perpendicular to the axis of 2D strike. For these two cases we may say

$$Z_{ij} = \mu\frac{E_i}{B_j}, \; i = \{1,2\}, \; j = \{1,2\}, \tag{3.58}$$

where the $Z_{ii} = 0$. Applying Euler's formula for complex quantities, (3.58) becomes

$$Z_{ij} = |Z_{ij}|\mathrm{e}^{i\Phi_{ij}} = \mu\frac{|E_i|}{|B_j|}\exp\left[i(\phi_{E_i} - \phi_{B_j})\right], \tag{3.59}$$

where we have introduced two new phase angles:

$$\tan(\phi_B) = \frac{\operatorname{Im} B}{\operatorname{Re} B}, \tag{3.60}$$

and

$$\tan(\phi_E) = \frac{\operatorname{Im} E}{\operatorname{Re} E}. \tag{3.61}$$

From (3.59) we see that for these two simplified cases, the impedance tensor phase is equal to the phase difference between a pair of electric and magnetic field channels.

The plots of apparent resistivity and phase for the three example sites, M01, M17, and M40 are shown in Figure 3.8. We expect some level of smoothness in these apparent resistivity and phase curves. The scatter of the data and the large size of the error bars suggest that below periods of approximately 30 s, the data at site M40 are unreliable. Equivalent statements can be made for the data below periods of approximately 10 s at sites M17 and M01. We turn to a few more plots of to assess these issues of MT data quality.

Figure 3.9 plots the eigenvalues of the spectral density matrices, the diagonal elements of Λ from (3.28), used in the multi-station processing for sites M01, M17, and M40. The two red curves in the plots of Figure 3.8 correspond to the two eigenvectors, u_{i1} and u_{i2} (see equation (3.24)), that are used in impedance tensor estimation at each frequency. We see that for site M40, the top two eigenvalues are not much larger than the other coherent noise eigenvalues (plotted in blue) until about 30 s period. The poor quality of data at periods below 30 s at site M40 are a result of the MT source vectors (corresponding to the top two eigenvalues) being poorly resolved above the noise at those periods. Therefore we must not interpret these data. The same conclusion is drawn by analyzing the spread in eigenvalues for the data below 10 s period and above 10,000 s at site M17. Again the same conclusion holds at site M01, except for two period bins between 1 and 2 s periods. At those two periods there are two eigenvalues (in the red curves) that stand out above the others. Recall that the spectrograms of Figure 3.2 exhibited strong peaks around 2 s concurrent with time periods of elevated tidal action. For further analysis

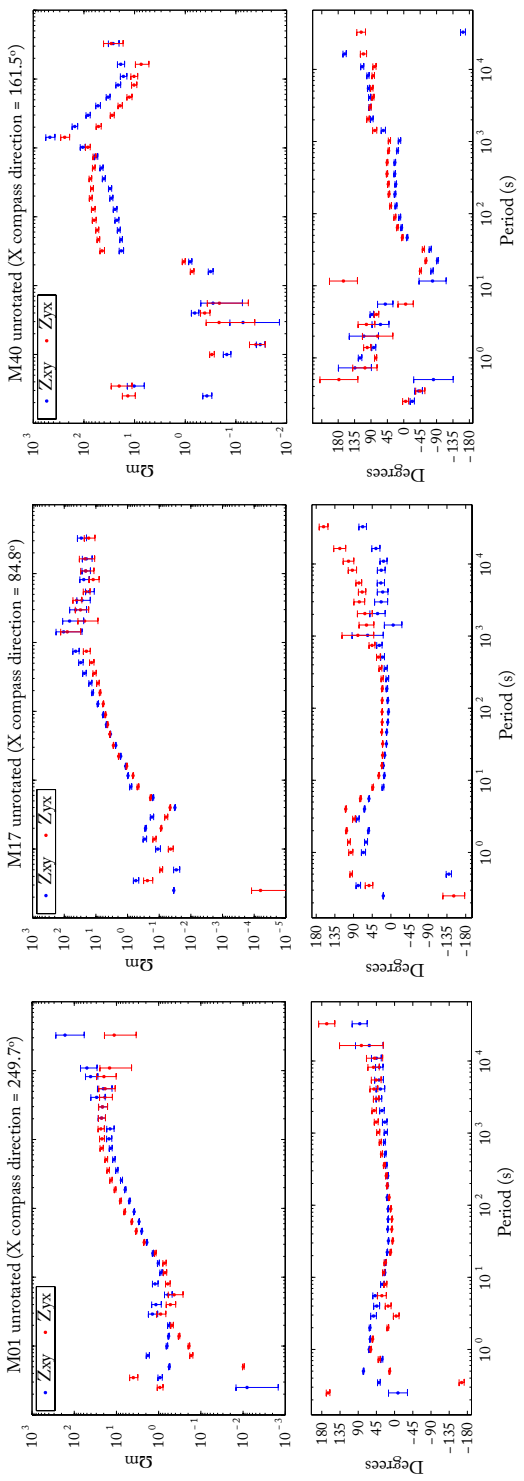

Figure 3.8: Plots of apparent resistivity and phase from sites M01, M17, and M40. Only the values derived from the off-diagonal elements of the impedance tensor are plotted. All estimated values are plotted; not all estimated values were used in later stages of analysis. The values are in the reference frame of the orientation of the instrument as it was on the seafloor. Compass angles for the instrument x-direction are given in degrees East of North.

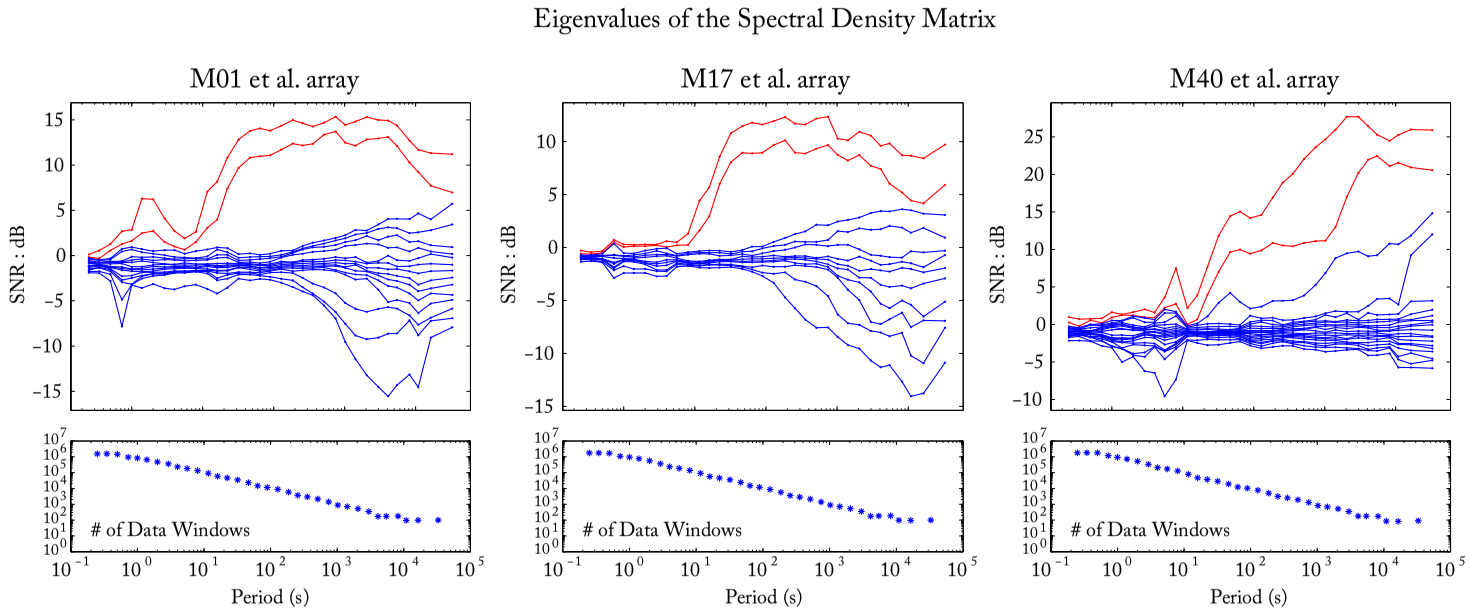

Figure 3.9: The upper row of plots are of the eigenvalues of the spectral density matrices at each frequency for sites M01, M17, and M40. The eigenvalues give an estimate of signal-to-noise ratio (SNR) for each principal component in the multi-station array containing either M01, M17, or M40. The top two eigenvalues at each frequency are highlighted in red as these correspond to the two eigenvectors selected for MT impedance tensor estimation. The lower plots display the number if separate time-window FCs used for the spectral density matrix estimation at each frequency; the number of data windows decreases with increasing period due to the cascade decimation scheme. Site M01 was grouped with other stations, M02, M03, and M12, in the multi-station process. Site M17 was grouped with other stations, M18 and M23, in the multi-station process. Site M40 was grouped with other stations, M36, M35, M34, and M33, in the multi-station process.

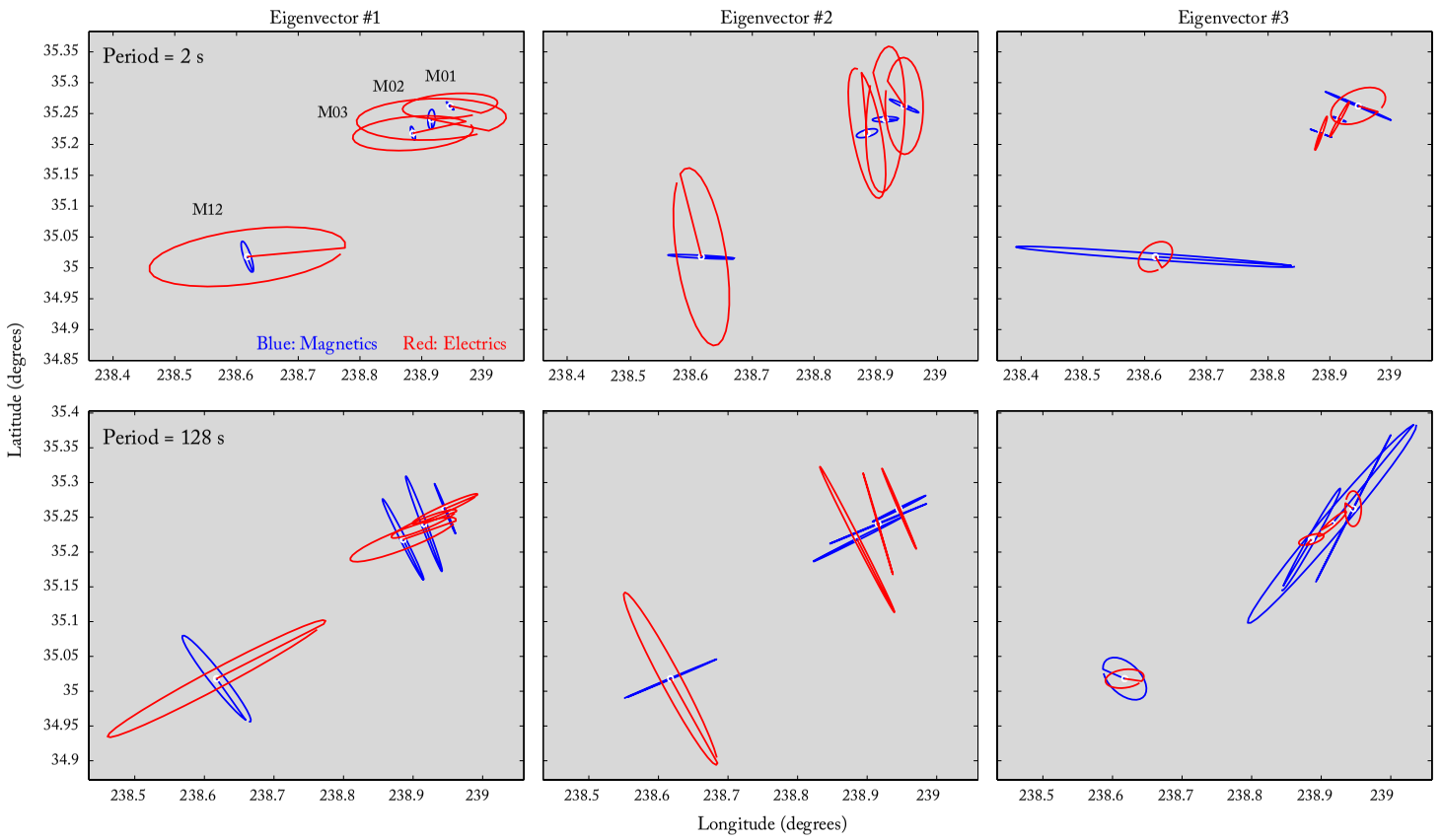

Figure 3.10: Map-view plots of the polar ellipses traced by the first three complex eigenvectors estimated for the M01-M02-M03-M12 array. In each plot, the ellipses are plotted in SNR units relative to each other. The top row plots the top three eigenvectors (sorted by their respective eigenvalue) for the period of estimation of 2 s, whereas the bottom row plots the same for the period of estimation of 128 s.

we look into the corresponding eigenvectors.

Figure 3.10 is a map view plot of the top three eigenvectors, corresponding to the three largest eigenvalues in Λ, at two separate frequencies, 2 s and 128 s, for the multi-station array comprised of M01, M02, M03, and M12. The three eigenvectors have been scaled by their corresponding incoherent noise estimates such that they comprise the first three columns of $\hat{W}$. The first three columns of $\hat{W}$ represent the top three orthogonal coherent signals in the data, in terms of SNR; as stated before, the first two are assumed to be MT signal. The elements of the first 3 columns of $\hat{W}$ are disassembled and regrouped according to their respective stations. For each eigenvector, a station has its own set of complex 2-vectors, $\boldsymbol{\nu}^E$ and $\boldsymbol{\nu}^B$, one for the horizontal electric field and one for the horizontal magnetic field, respectively. In map view, polarization ellipses represent these 2-vectors by tracing the following parametric equations with respect to compass angle, θ,

$$p_x(\theta) = c\left[\mathrm{Re}(\nu_1)\cos(\theta) - \mathrm{Im}(\nu_1)\sin(\theta)\right] + x_0, \tag{3.62}$$

and

$$p_y(\theta) = c\left[\mathrm{Re}(\nu_2)\cos(\theta) - \mathrm{Im}(\nu_2)\sin(\theta)\right] + y_0, \tag{3.63}$$

where p_x and p_y are the longitude the latitude, respectively, of the ellipse line; c is some arbitrary scaling held constant for all ellipses in a single plot; and x_0 and y_0 are the station coordinates. The ellipse represents the path of the tip of the field vector as it progresses with time through one full period of oscillation. When one of these ellipses collapses to a line, we say that the corresponding field is "linearly-polarized", which means that the x-coordinate and the y-coordinate of the field, ν_1 and ν_2, vary in phase with each other, i.e. $\mathrm{Im}(\nu_1)/\mathrm{Re}(\nu_1) = \mathrm{Im}(\nu_2)/\mathrm{Re}(\nu_2)$. Another way to interpret the meaning of a linear-polarized field is that the field vector does not change direction with time; it changes only in magnitude and sign. The MT source field, as mentioned earlier, is assumed to be linearly polarized, and uniform in the horizontal plane, hence the title plane wave. Such an ideal MT plane wave driving a horizontally-layered (1D) earth would result in electric and magnetic field polarization ellipses within a single eigenvector that are linear and uniform

in polarization direction (i.e. the direction of the major axis of the ellipse) from site to site. The linear ellipses of the electric and magnetic field would be orthogonal to each other as well. For the ideal MT plane wave driving 2D earth structure, the ellipses would only be linearly polarized if the source magnetic field was oriented either exactly perpendicular or exactly parallel to the direction of 2D conductivity variation [Kaufman and Keller, 1981]. Polarization ellipses which are not linear are either a result from non-linearly polarized source fields, or conductivity structure of dimensionality greater than 1D. Non-uniformities in polarization direction from site to site can be a result of either 3D conductivity structure, a non-uniform source field, or an inaccurate compass orientation of the instrument.

In Figure 3.10, the top two eigenvectors for 2 s period oscillation show very low SNR in the magnetic fields, relative to the electric fields. Also, the orientation of the major axes of the magnetic polarization ellipses vary dramatically from station to station. We compare these to the polarization ellipses for the top two eigenvectors for 128 s period oscillation. At the larger period, the magnetic field SNR is closer to that of the electric field, also the nearly linear polarization ellipses do not vary in their polarization direction from station to station as much as they did at 2 s period. Taking the top two eigenvectors of the 128 s period oscillation as exemplars of MT signal, we conclude that the top eigenvectors of the 2 s period oscillation are manifestations of coherent noise, likely driven by tidal motion. With repetition of the preceding analysis on all the data, a qualitative separation between good MT impedance tensor estimates, and those polluted by incoherent and coherent noise, may be made. Such analysis was applied as a means of data reduction for the Estero MT dataset, with the exception of the land data, which was delivered to us by our collaborators in a state ready for interpretation.

3.5 Impedance Tensor Rotation

In the Chapter 4, we present an inversion of the MT data with a 2D conductivity model. This means the forward modeling code assumes that the conductivity structure of the earth is uniform along one horizontal direction. Therefore, we must prepare the impedance tensor data so that it conforms as much as possible to this assumption. The

preparation requires a coordinate transformation such that the x- and y-directions of the impedance tensor align perpendicular and parallel, respectively, to the horizontal direction of assumed 2D conductivity variation in the earth. Once transformed, the Z_{xy} component of the impedance tensor will relate to a driving magnetic field aligned with the y-axis (the horizontal direction of constant conductivity), and the Z_{yx} component of the impedance tensor will relate to a driving magnetic field aligned with the x-axis (the horizontal direction of conductivity variation). In a 2D model, the component Z_{xy} encapsulates the transverse-magnetic (TM) mode of induction, so-called because it can be shown that the total magnetic field is everywhere perpendicular (transverse) to the z-axis; it is also usually assumed that the TM mode magnetic fields are perpendicular to the orientation of a survey line, when the survey line is oriented in the direction of horizontal conductivity variation. Conversely, in a 2D model the component Z_{yx} encapsulates the transverse-electric (TE) mode of induction. Here the total electric field is everywhere perpendicular to the z-axis, and assumed to be perpendicular to the orientation of the survey line. As stated earlier, if data were acquired over a perfectly 2D earth, the components Z_{xx} and Z_{yy} would be zero everywhere at all periods of oscillation, when the x- and y-axes are oriented to be either 2D strike perpendicular or 2D strike parallel.

An estimate of the strike direction for the assumed 2D subsurface conductivity variation can be made in a variety of ways [e.g. Groom and Bailey, 1989, McNeice and Jones, 2001, Caldwell and Bibby, 2004, Becken and Burkhardt, 2004]. We elected to use the method described in Becken and Burkhardt [2004] because it employs a physical parameterization of the impedance tensor that does no rely on any *a priori* model assumptions, as do the methods of classical distortion analysis [see e.g. Groom and Bailey, 1989]. First the impedance tensor is decomposed into its two columns, which are called the telluric vectors. Again, these are complex vectors which can be represented by a polarization ellipse in the horizontal plane. As was stated in Section 3.4, if the source magnetic field was linearly polarized and also aligned parallel or perpendicular to the strike of a 2D conductivity distribution, the resulting electric field would also be linearly polarized. Now imagine the telluric vectors to be the electric fields induced by hypothetical, mutually orthogonal, and linearly polarized magnetic fields. Then, Becken and Burkhardt [2004] sought to find the

most appropriate 2D strike from impedance data by minimizing a measure of telluric vector ellipticity (which they defined as the ratio of the minor to major axes of the ellipse) as a function of coordinate system rotation angle. This can be done simultaneously over multiple frequencies and multiple stations by choosing the sum of the squares of ellipticities as the quantity to be minimized. The angle of impedance tensor rotation which minimizes the ellipticity norm is chosen as the most likely 2D strike of the data. Of course, there is a 90° ambiguity in the strike angle, but this is easily sorted out by external information (i.e. geological information, vertical magnetic field induction vectors). Figure 3.11 presents two polar histograms of the estimates of 2D strike, one for the marine stations, and one for the land stations. A single estimate was made for each individual site over the range of frequencies of usable data. These estimates were then grouped according to whether came from a marine or land site. The two groups of estimates served as populations for the histograms in Figure 3.11. The polar histograms exhibit the expected 90° ambiguity, but it is known that the majority of geologic variation occurs along the axis perpendicular to the San Andreas fault, as highlighted by the surface geology map in the background of Figure 3.11. The median rotation angle was chosen for each of the two groups of stations, marine and land, and subsequently the impedance tensor at each site was rotated into the optimally-2D reference frame of its respective group. In geographic coordinates, the marine sites were rotated so that their x-axis aligned with N 46.9°E, and the land sites were rotated so that their x-axis aligned with N 42.2°E. Conversion from geomagnetic rotations to geographic rotations must take into account the average magnetic declination in central California along the marine profile, N 13.6°E. The rotation of the impedance tensor amounts to a change of reference frame for both the electric and magnetic field vectors. For a clockwise rotation of a vector $\mathbf{v}$ by an angle θ in a right-handed coordinate system, we have

$$\mathbf{v}^{\theta} = R\mathbf{v}, \tag{3.64}$$

where the rotation matrix, R is given by,

$$R = \begin{bmatrix} \cos\theta & \sin\theta \\ -\sin\theta & \cos\theta \end{bmatrix}. \tag{3.65}$$

Applying rotations to the vectors related by the impedance tensor we have

$$R^{-1}\mathbf{E}^{\theta} = \frac{1}{\mu}\mathsf{Z}R^{-1}\mathbf{B}^{\theta}, \tag{3.66}$$

from which we can show

$$\mathsf{Z}^{\theta} = R\mathsf{Z}R^{-1}. \tag{3.67}$$

Figure 3.12 presents plots of impedance polar diagrams for all of the acquired marine MT data and the provided land MT data. Impedance polar diagrams offer a dimensionality diagnostic that derives from tensor rotation. A single polar diagram consists of two closed curves, one relating to an on-diagonal element, z^{θ}_{xx}, and one relating to an off-diagonal element, z^{θ}_{xy}, of the impedance tensor as it is rotated incrementally through 360°. At each increment of rotation, the absolute value of each of these elements is used as the radius in a polar plot. The two curves in our plots have been normalized by a common quantity as it is only the relative size between the two curves that is of interest. More specifically, in Figure 3.12, the red lines plot the quantity,

$$P_{xy}(\theta) = |z^{\theta}_{xy}|/a, \tag{3.68}$$

while the blue lines plot the quantity,

$$P_{xx}(\theta) = |z^{\theta}_{xx}|/a, \tag{3.69}$$

as θ, the angle of tensor rotation, varies from [0°,360°). The normalization constant, a, is defined as $\max_{\theta}|z^{\theta}_{xy}|$. We reiterate that the impedance tensor over a 1D earth has the properties $z_{xy} = -z_{yx}$ and $z_{xx} = z_{yy} = 0$, regardless of rotation. In this case, $P_{xy}(\theta)$ traces

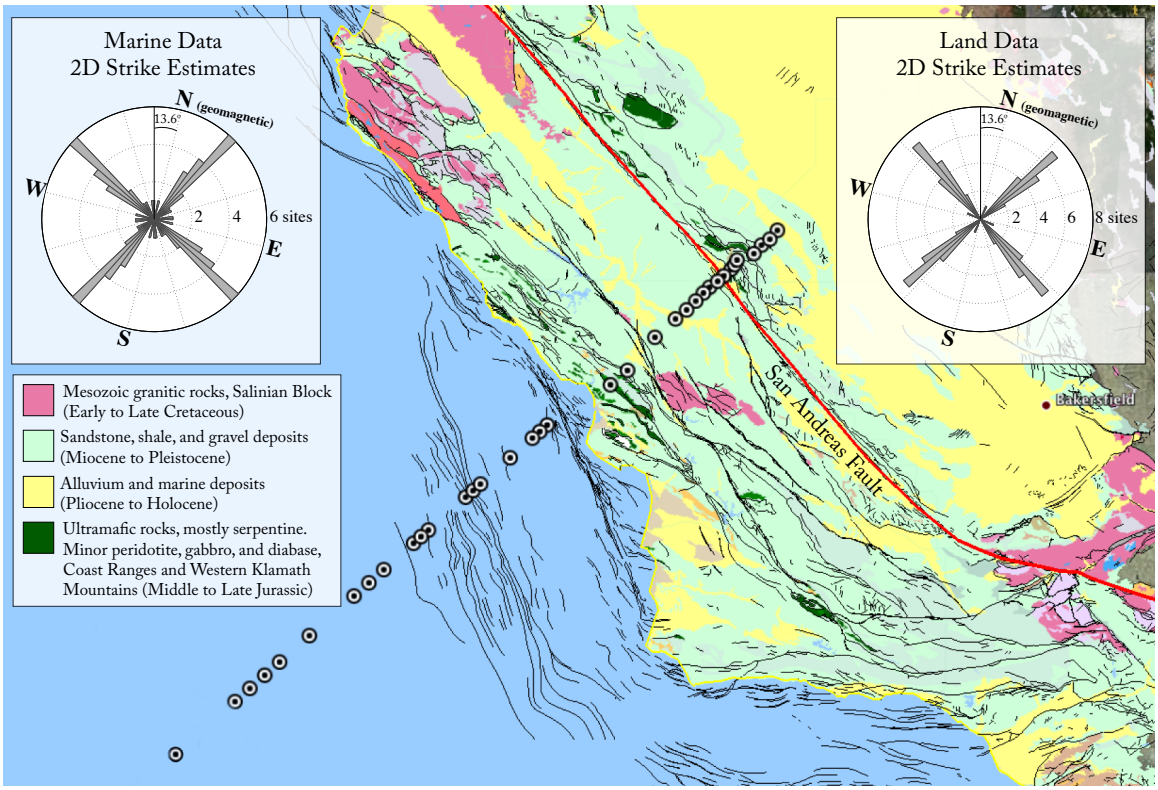

Figure 3.11: Polar histograms of the 2D strike estimates from marine MT sites and land MT sites, respectively. The local magnetic declination is shown as N 13.6°E. The map in the background displays the surface geologic units of central California from Jennings et al. [1977]. The bold red line plots the surface trace of the San Andreas fault, and thinner black lines plot surface traces of other Quaternary faults. The black and white, bulls-eye markers denote the locations of the MT stations used in the 2D strike estimation.

a perfect circle, and $P_{xx}(\theta)$ consists of one point at the origin. The impedance over a 2D earth has the properties $z_{xy} \neq z_{yx}$ and $z_{xx} = z_{yy} = 0$ when rotated to be either 2D strike parallel or perpendicular. For the 2D case, Kaufman and Keller [1981] show that the polar diagrams take the form,

$$P_{xy}(\theta) = \left[|z_{xy}|^2 \cos^4\theta + |z_{yx}|^2 \sin^4\theta - 2|z_{xy}||z_{yx}| \sin^2\theta \cos^2\theta \cdot \cos(\Phi_{xy} - \Phi_{yx})\right]^{1/2}, \quad (3.70)$$

and,

$$P_{xx}(\theta) = \frac{|z_{xy} + z_{yx}|}{2} \sin 2\theta, \quad (3.71)$$

where z_{xy}, z_{yx}, z_{xx}, and z_{yy} are the impedance tensor elements from a reference frame either parallel or perpendicular to the 2D strike, one of which corresponds to the direction of $\theta = 0$. The shape of P_{xy} may take many forms, ranging from an oval to a peanut shape. The maximum radius of P_{xy} occurs with 180° ambiguity in either the direction parallel or perpendicular to the 2D strike, if there is one. Most notably, we see that for 2D earth structure, the shape of P_{xx} will always be the same. It will take the shape of a four-leaf clover, all leaves of equal size and oriented to either ±45° or ±135° of the 2D strike. Also, from (3.70) and (3.71), we see that $\max_\theta P_{xx}(\theta) \leq \max_\theta P_{xy}(\theta)$. When the clover leaves of P_{xx} exhibit asymmetry or become much larger than the lobes of P_{xy}, 3D conductivity structure must exist. The grayscale shading in the background of the plot in Figure 3.12 indicates the value of Swift skew, a measure of 3D structure. The skew is a specific quantity derived from a rank-2 tensor that has the favorable property of being invariant under rotation the tensor. The "Swift skew", coined after Swift [1967], relates to the impedance tensor, and is given by

$$s = \frac{|z_{xx} + z_{yy}|}{|z_{xy} - z_{yx}|}. \quad (3.72)$$

Over 1D and 2D conductivity distributions, z_{xx}^θ and z_{yy}^θ are either both zero, or of equal magnitude but opposite sign so that s is always exactly zero, regardless of orientation of the coordinate axes; thus, large skews can only arise from extreme 3D conductivity structures.

It is traditional practice to accept all data with Swift skews less than 0.2 as reproducible with a 2D model. However, as we show in Section 5.8, a zero value of the Swift skew does not guarantee the absence of 3D conductivity structure.

As an illustration of both 2D and 3D polar diagrams, in Figure 3.13 we plot the impedance polar diagrams for modeled data to compare with the diagrams of the Estero MT data in Figure 3.12. The modeled data come from a calculation made for a simplified coast model with a 90 Ωm seafloor depicted in Figure 4.2, which we will return to in Chapter 4. The coast model is used here to loosely predict the shape of polar diagrams that we would expect for the Estero MT data, if the earth conductivity distribution in central California was perfectly 2D. Plot **A** in Figure 3.13 plots the diagrams derived from the perfectly 2D coast model. Next, we want to explore how 3D-affected tensors might distort the polar diagrams from their 2D forms. So without modeling 3D structures, we simply add non-zero components to the diagonals of the 2D coast tensors to mimic 3D tensors. Three different strategies for creating diagonal components were used, depicted in plots **B**, **C**, and **D**, with the formulae for the sizes of z_{xx} and z_{yy} defined above each plot.

In Figure 3.12 the cross-hatched regions contain data that have been excluded from later analysis based on evidence of noise contamination; a description of such evaluation was given in Section 3.4. Most of these excluded data, especially in the higher frequency range, exhibit high skew values and exotic polar diagrams that are inconsistent with a 2D conductivity distribution. Outside of the cross-hatched regions, there is only one site, 630, for which we can say with some confidence that there is no evidence of effects from 3D conductivity structure. All other sites exhibit 3D effects in varying degrees. These effects become stronger on, and at the base of the continental shelf (sites M25 and M27). They also become stronger near the edge of the San Joaquin Valley (sites 639 and 640). The symptoms of 3D structure are so pervasive that a strategy of rejecting outright all data with skews larger that 0.2, or 3D-looking polar diagrams, would leave less than 40% of an already decimated dataset left for the 2D inversion. Thus, in Section 3.6, we employ the strategy of including the majority of the data, but systematically dampening the influence of some data by assigning weights that are a function of the degree to which the data are 3D-affected.

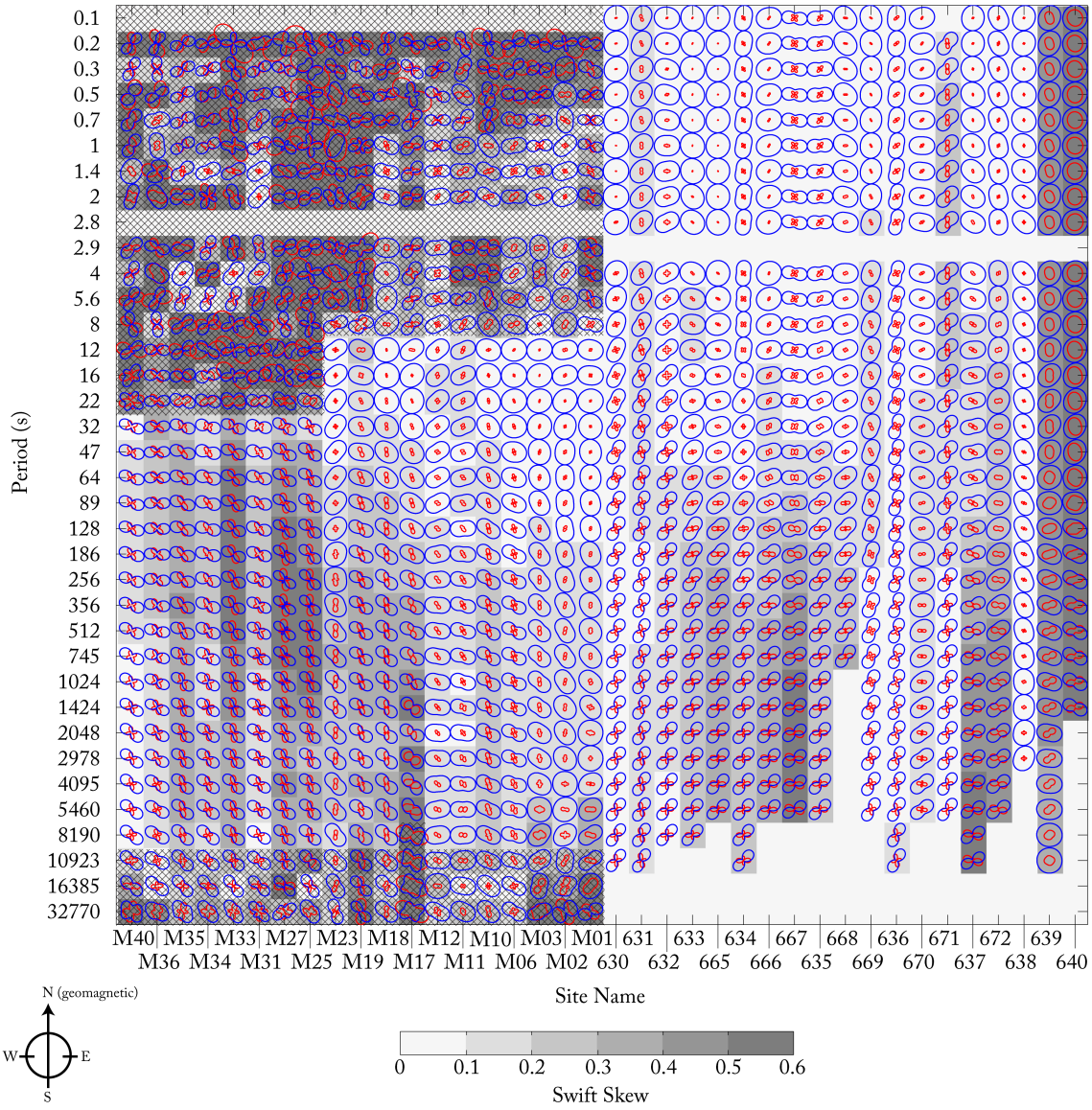

Figure 3.12: Plot of MT impedance polar diagrams for all sites and all frequencies of data. The blue lines plot the impedance tensor element $|z_{xy}^{\theta}|$, while the red lines plot the impedance tensor element $|z_{xx}^{\theta}|$ as a function of tensor rotation angle θ, which ranges from 0 to 2π. The grayscale shading indicates the Swift skew values, which are capped at 0.6, though many data exceed this value. Regions of cross-hatching denote data that were removed from inversion due to noise contamination.

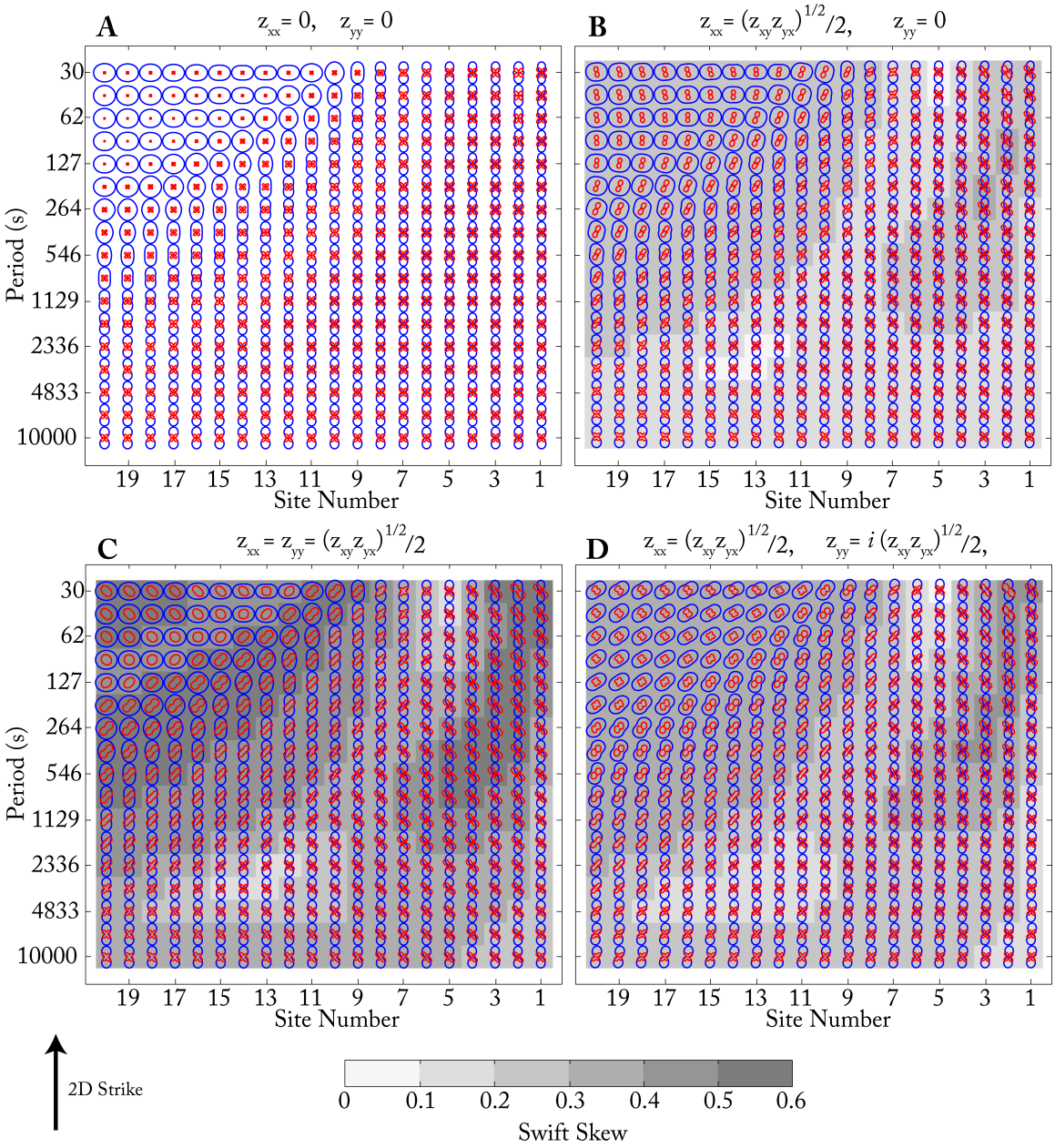

Figure 3.13: (**A**), a plot of MT impedance polar diagrams for all sites and all frequencies of the forward calculation for the 2D model in Figure 4.2. (**B**), (**C**), and (**D**), impedance polar diagrams for three different models for synthetic 3D data, whose off diagonal data (z_{xy} and z_{yx}) are equal to that of the 2D model used for **A**. The blue lines plot the impedance tensor element $|z^{\theta}_{xy}|$, while the red lines plot the impedance tensor element $|z^{\theta}_{xx}|$ as a function of tensor rotation angle θ. The grayscale shading denotes the Swift Skew value, with 0.6 being the approximate maximum value of all the plots of modeled data.

3.6 Data Weighting

In most inverse problems, linear and non-linear alike, weights are applied to data which, as in the robust estimation process, affect the degree of influence any single data point may wield in the solution process. From the perspective of the linear inversion process, or the early stages of a non-linear inverse process, the value of a given weight matters only in its size relative to the other weights; the process of minimizing the L_2-norm of the differences between the data and a model prediction (the residuals) is invariant with respect to left multiplication of the residual vector by an arbitrary scalar matrix. However, the absolute size of the weights does matter for a posterior assessment of an inverse solution, or, in the non-linear case, the transition from seeking the best-fitting model to the smoothest-fitting model. For these purposes, weights are often chosen on some statistical grounds so that an inverse solution may be tied to probabilities; standard errors of data are a natural choice for weights, such that the inverse problem is posed as a minimization of standardized residuals between the data and a model prediction. This strategy works well when the standard errors are well-estimated, the main source of error is stochastic Gaussian noise, and the physics of the real system are completely captured by the model. The final two provisos are not the case with the Estero MT dataset.

While the data redundancy (the number of FC estimates) for the Estero MT dataset is such that the standard errors in the ultimate apparent resistivity and phase data are extremely well resolved, there remain systematic biases in the data and an aspect of the physics that is not captured by the model. The systematic biases may include errors in a seafloor instrument's location, orientation, tilt, and roll, and errors in the instrument frequency response calibration. As was stated before, the conductivity model used in the forward functional of our non-linear inverse solution is 2D. While the predominant geologic variation is assumed to be 2D over the length-scale of our survey, the earth is obviously 3D. Our 2D model is unable to replicate the physics of conductivity variations in one of the horizontal directions, producing another source of systematic error.

One relatively well-known source of conductivity variation in the earth is the land/seawater interface described by bathymetry. This interface constitutes one of the

largest conductivity contrasts in nature, and thus has a significant effect on the impedance data. Bathymetry, of course, varies in both directions of the horizontal plane. However, in some locations around the earth, there is one dominant direction of bathymetric variation; this is the argument we make for central California, the location of the Estero MT survey. Even if the local bathymetry could be adequately represented by a 2D conductivity model, there are errors in the bathymetry measurements as well, particularly away from the coasts where satellite data is solely relied upon. Therefore, uncertainty in bathymetry estimates contributes another source of systematic error in the physics of our model.

We describe the data weights used on the Estero MT dataset in terms of errors even though they are often not derived from the traditional standard error estimation procedure. The data weights are inversely related to the errors; data with large errors are afforded less influence on the inversion process than data with smaller errors. First, to account for systematic biases in the data we set a relative-error floor for the TM mode data at 12.5% of the apparent resistivity amplitude. We set the corresponding error floor in phase of 3.6°. These error floors account for systematic errors in the data and usually supersede the estimated standard error, except at the longer periods where much fewer data records are used in the estimation procedure (see Figure 3.9). Next we sought to down-weight elements of the data which could not be replicated by our 2D model. Multiple MT modeling studies have shown that the TE mode, involving electric current flowing transverse to the vertical plane containing a single profile of data, is more susceptible to distortion from off-axis (3D) structure than the TM mode of those same data [Wannamaker et al., 1984, Becken et al., 2008a]. This is because the 2D TE calculation does not account for the build-up of boundary charges, since the current flow in that mode is always perpendicular to the modeled variations in conductivity; however, the 2D TM mode calculation does account for boundary charges. Becken et al. [2008a] noted that the greater deviation from a 2D response existed in the TE mode apparent resistivity data when calculated over a 3D conductivity distribution, and decided to weight the data intended for a 2D inversion accordingly. They achieved more accurate results from 2D inversion of synthetically created 3D data by down-weighting the TE apparent resistivity data relative to the TM apparent resistivity data. We adopt the same approach and enforced a 25% error floor (twice the TM error floor) on

the TE apparent resistivity data, while leaving the TE phase with an error floor of 3.6°; the TE phase error floor is left as low as that of the TM phase because galvanic boundary charges have a small effect on phase.

Again, the relative size between errors of different data matters more than the absolute size of all errors. The error floors could be made uniformly 10 times bigger or smaller with no effect on the direction of the inversion search. The only effect would be in the determination of convergence in the inversion process, a condition controlled by a quantity we call the tolerance, which must be chosen by the user anyway. A uniform increase in errors along with an appropriately chosen decrease in tolerance will cancel each other's effect on the inversion process. As will be described in Chapter 4, the inversion algorithm we use searches for a model that produces a misfit equal to a chosen tolerance level. If zero mean, Gaussian distributed, random variables were the only things contributing to the misfit, the tolerance level could be rigorously derived on statistical grounds [Parker, 1994]. However, in our case where misfit is almost entirely a result of systematic error and not random error, a tolerance rigorously based on the data's estimated standard errors will never be reached. Instead we took a different approach to setting our data errors. We used our inversion algorithm to find a minimum misfit model by relaxing the smoothness constraints and setting the tolerance to zero (see Section 4.1 for details about the inversion algorithm). With these settings, the inversion algorithm continues to take steps to reduce the misfit until successive iterations produce no detectable progress, at which point we've reached a practical minimum in misfit. Then, we take the minimum misfit model and adjust the data error estimates accordingly so that the model's calculated misfit value is close to our statistically defensible tolerance. In this way, we determine an absolute size for the numbers provided in the preceding paragraph for estimates of the systematic errors.

A further effort was made to down-weight segments of the apparent resistivity and phase data exhibiting distortions from 3D conductivity structure that could not be accounted for by our 2D model. This entailed a change in the relative size of errors different frequencies and different sites. We made use of data metrics known as the Swift skew and phase tensor skew, derivatives of the impedance tensor which are invariant under rotations. Similar to the Swift skew, Bibby and Caldwell [2005] show that for 1D or 2D conductiv-

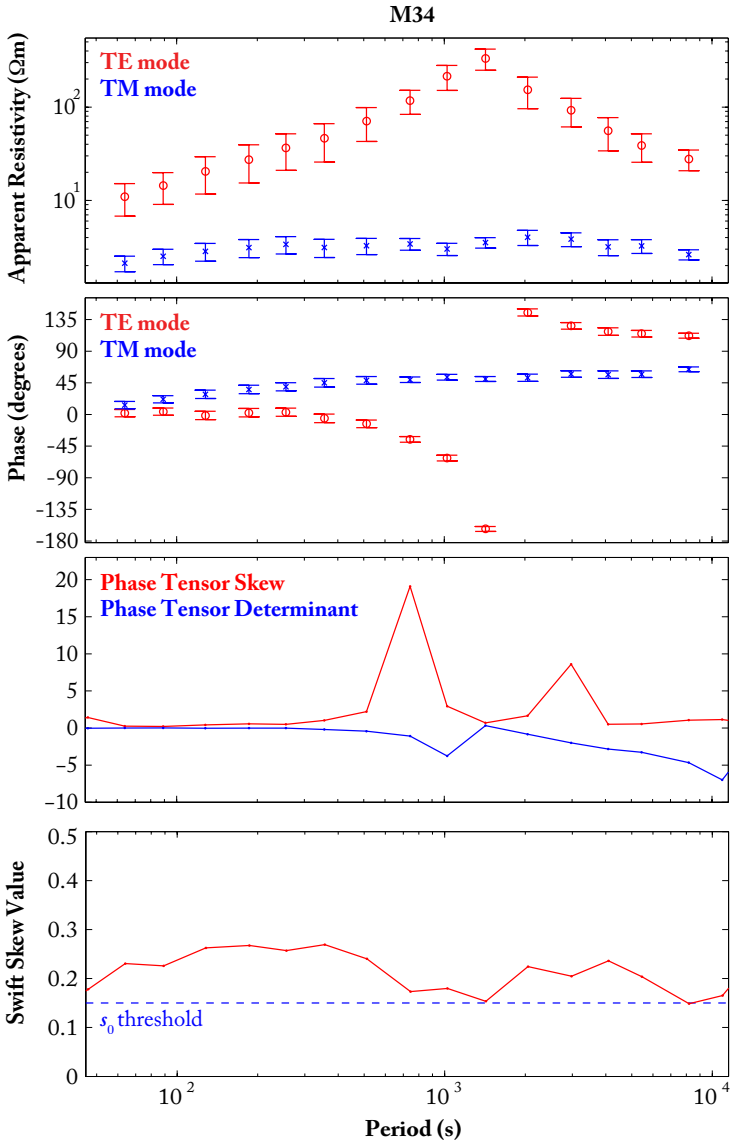

Figure 3.14: The top two plots are of apparent resistivity and phase data for the marine site M34. The phase data span nearly the full range of $-180°$ to $180°$. The bottom two plots are of phase tensor skew, phase tensor determinant, and Swift skew for the data from site M34. The chosen Swift skew threshold, s_0, is also plotted with a blue dashed line.

ity distributions, the phase tensor skew is exactly zero. In addition, Bibby and Caldwell [2005] explain that the phase tensor skew is insensitive to galvanic shifts in electric field measurements. These can be associated with very small-scale, 3D resistive anomalies close to a single electrode, and often occur with land MT stations; such galvanic shifts in marine MT data are rarely a result of a small localized resistive anomaly, since the near-surface material is uniformly saturated in seawater. Nonetheless, galvanic shifts in marine TM data are common and a well-known result of the regional coast effect (see Chapters 5 & 4), which may arise in a perfectly 2D conductivity distribution. The same 2D coast effect in the marine environment produces TE phases that are outside of the 0° to 90° range, a phenomenon considered very rare in land MT responses [e.g. Key and Constable, 2010]. The phase tensor skew at these "anomalous" phases in our marine data was found to vary wildly among adjacent periods, whereas the Swift skew varied more smoothly (see Figure 3.14); both the Swift skew and phase tensor skew varied smoothly with respect to period for the land data. Therefore, we use the Swift skew to identify 3D distortion in the marine data and the phase tensor skew to identify non-galvanic 3D distortion in the land data. A skew threshold, s_0, of 0.15 was chosen and the existing errors, σ_i, were rescaled accordingly,

$$\sigma_i^\star = \frac{s_i}{s_0}\sigma, \text{ for } s_i > s_0, \tag{3.73}$$

where the star denotes the rescaled error, and s_i is either the Swift skew or the phase tensor skew depending upon whether the data were derived from a marine or land station, respectively.

The land stations acquired vertical magnetic field measurements which yielded estimates of vertical magnetic transfer functions; for need of a shorter title, data of this type are often called tippers (see Section 5.11). Recycling notation in (3.22), we define the tipper vector, $\mathsf{V} = [v_{zx}\ v_{zy}]$, as,

$$B_z = \mathsf{V}\mathbf{B}. \tag{3.74}$$

We set an error floor for the dimensionless tipper data at 0.02. In a 2D conductivity distribution, it can be shown that the TE mode of induction, where the driving magnetic

field is aligned in the x-direction, along the axis of horizontal conductivity variation, gives rise only to E_y, B_x, and B_z field components. Conversely, the TM mode of induction, where the driving magnetic field is aligned in the y-direction, perpendicular to the axis of horizontal conductivity variation, gives rise only to B_y, E_x, and E_z field components. Therefore, with a 2D model we see that the TM tipper, v_{zx}, is always zero. We use this property to detect where 3D distortion occurs in the tipper data; any period of estimation that produces a sizeable TM tipper must be affected by 3D structure. We look at the ratio of the two estimated tipper components, which we define as $\gamma = v_{zx}/v_{zy}$, and again choose a threshold for that ratio, $\gamma_0 = 0.8$. Then we use the γ ratio to rescale the errors of the TE tipper component (the only component applicable to a 2D inversion model) in the same way that we used β to rescale the errors in the apparent resistivity and phase data.

All of the data, after applying the aforementioned processes of data reduction and data weighting are plotted in the Figures 3.15 through 3.18. These comprise the final set of data with associated errors (inverse weights) used in the remainder of the thesis.

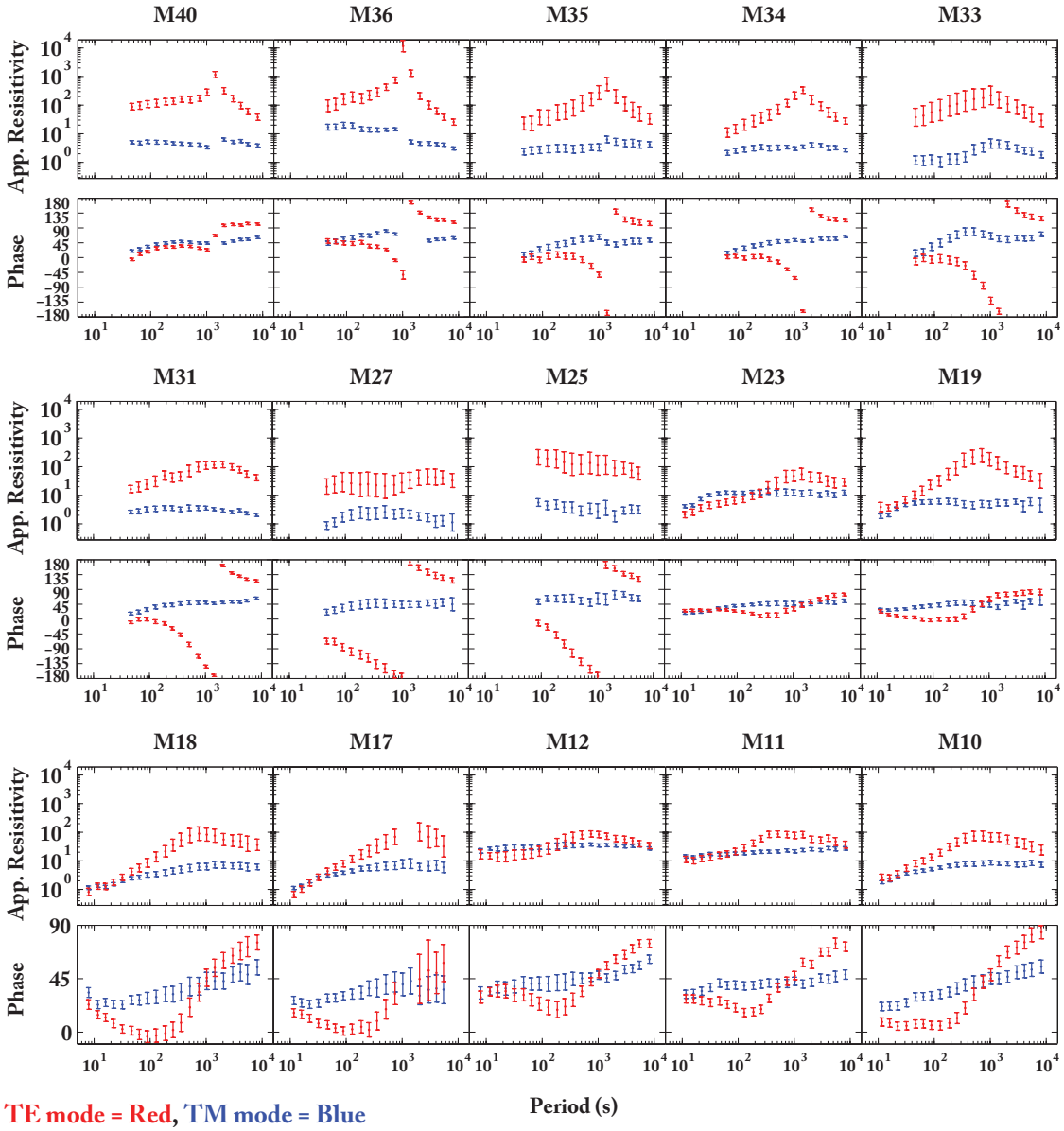

Figure 3.15: Plots of apparent resistivity and phase for the western-most marine sites. The marine sites are named according to their order from the coast, with M01 being the closest and M40 being the farthest. The data error bars are $\pm 1\sigma$.

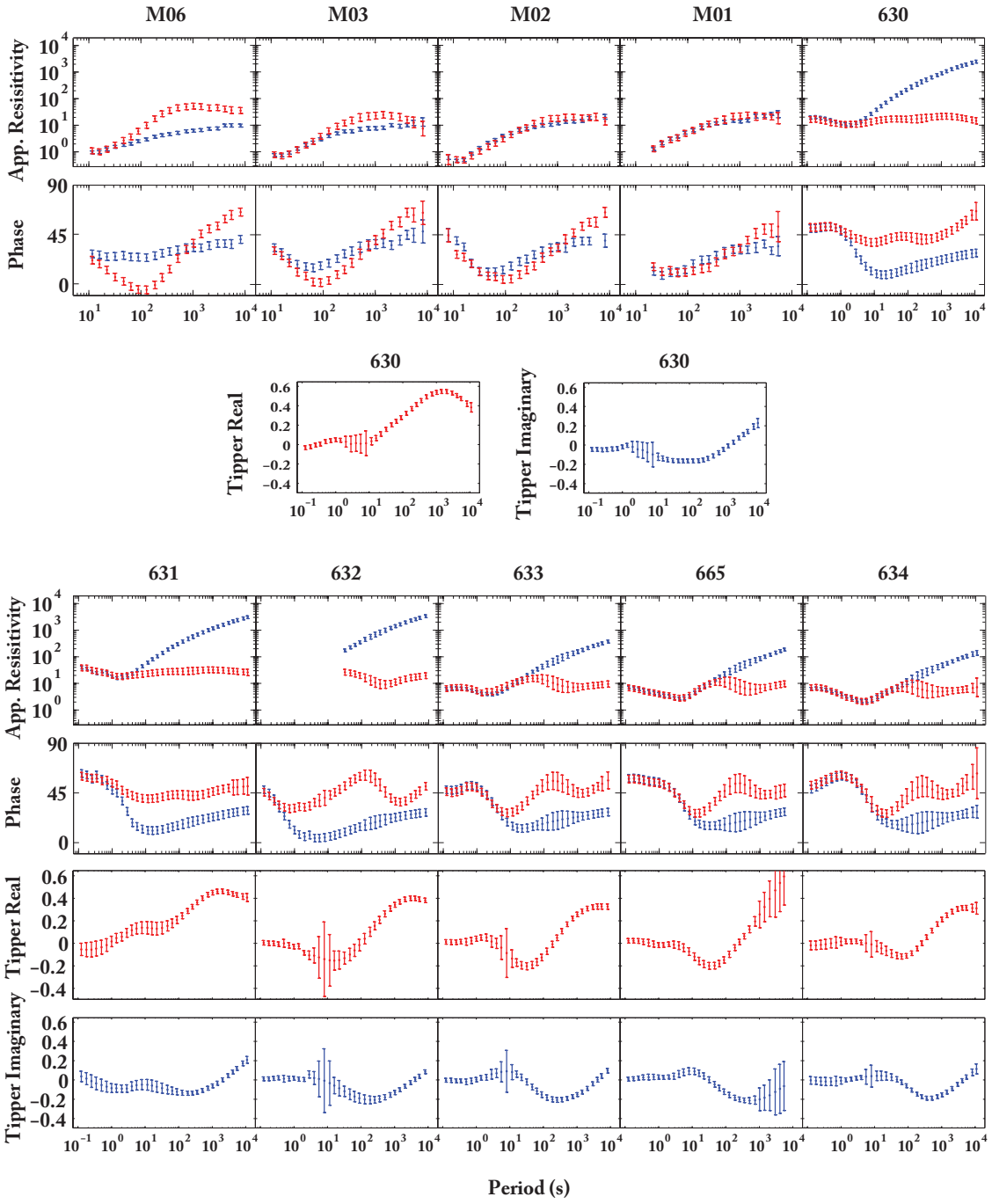

Figure 3.16: Plots of apparent resistivity and phase for the marine sites of data, and apparent resistivity, phase, and real and imaginary tippers for the land sites. Marine sites have titles that begin with the letter M. Sites are plotted in order from west to east, with M06 being the western most site of this group, and 634 being the eastern most site of this group. The data error bars are $\pm 1\sigma$.

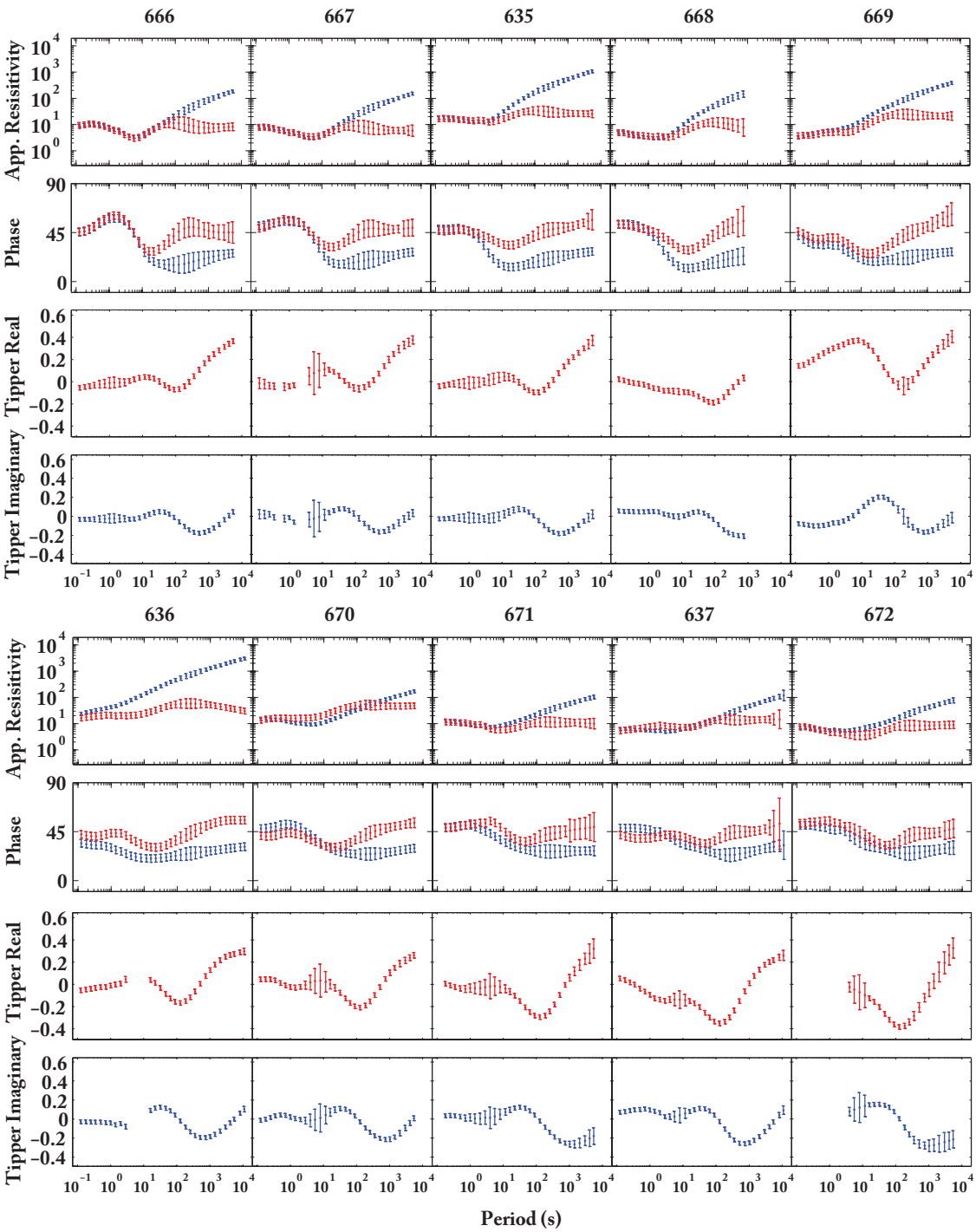

Figure 3.17: Plots of apparent resistivity, phase, and real and imaginary tippers for the land sites. Sites are plotted in order from west to east, with 666 being the western most site of this group, and 672 being the eastern most site of this group. The data error bars are $\pm 1\sigma$.

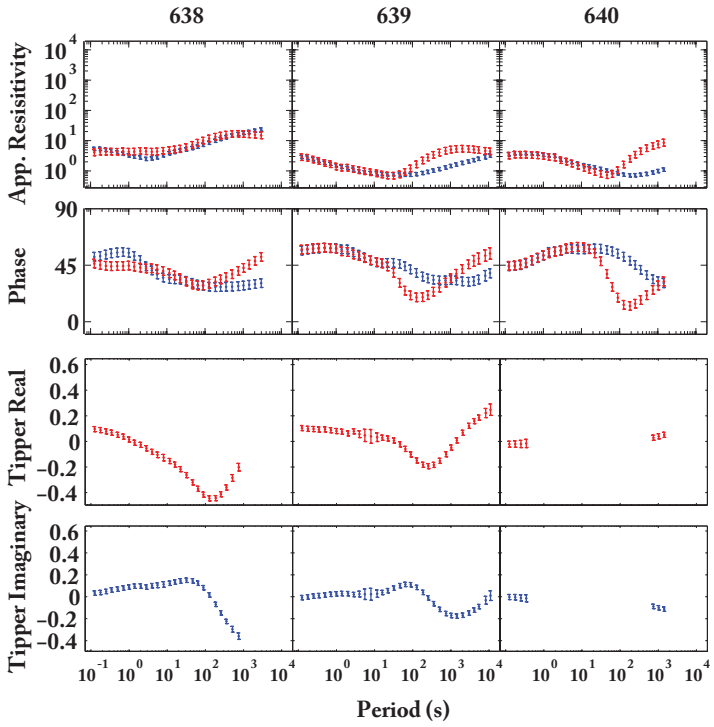

Figure 3.18: Plots of apparent resistivity, phase, and real and imaginary tippers for the most inland sites. Sites are plotted in order from west to east, with 638 being the western most site of this group, and 640 being the eastern most site of this group, as well as the eastern most of the entire dataset. The data error bars are $\pm 1\sigma$.

Chapter 4

2D Inversion

In this chapter we describe the non-linear inversion process used to convert estimates of apparent resistivity and phase from our profile of instruments into a 2D cross-sectional model of earth resistivity. It will start with a brief introduction to the theory of regularized non-linear inversion, particularly the algorithm known as Occam's method. Then, we will discuss an effort to optimize inversion performance based upon transforming the data space. A range of models was produced using different subsets of data and incorporating various forms of external information. Finally, we will analyze the data sensitivity that can be determined from these disparate models.

4.1 Regularized Non-linear Inversion

MT data are non-linearly related to the conductivity structure of all earth models other than a uniform halfspace. Thus, in order to transform the collected MT data into an estimate of conductivity throughout a 2D earth model, we must use a non-linear inversion algorithm. The non-linear inversion algorithm we employ is known as Occam's inversion, first described with 1D model examples in Constable et al. [1987]. More specifically, our 2D inversions of MT data follow DeGroot Hedlin and Constable [1990], which makes use of the 2D finite-element code of Wannamaker et al. [1987].

First, we should point out the two reasons why we employ a 2D inversion rather

than a 3D inversion. The first is that MT modeling and inversion within domains where conductivity is allowed to vary in all three dimensions continues to present a considerable numerical challenge. Algorithms and computer codes which can handle *simple* 3D conductivity structures in the earth have existed for more than three decades [e.g. Hohmann, 1975, Ting and Hohmann, 1981, Wannamaker and Hohmann, 1982]. Since then, both computing power and modeling sophistication have advanced to the point where 3D inversion of real MT data has become feasible [e.g. Mackie and Madden, 1993, Newman and Alumbaugh, 1997, Zhdanov et al., 2000, Sasaki, 2001, Siripunvaraporn et al., 2005, Commer and Newman, 2009, Egbert and Kelbert, 2012]. Despite these developments, the 3D MT inverse problem still presents a large computational burden, invariably necessitating the use of parallel computing. Furthermore, some aspects of full 3D MT modeling remain inaccessible, even with the modern tools. The prime example of this, which certainly applies to the Estero MT dataset, is the modeling of MT on the seafloor. Modeling in the marine environment involves the incorporation 3D bathymetry in both the near- and far-field, requiring small model cells over a very large area. Thus, the problem of adequately replicating the effect of 3D bathymetry becomes prohibitively costly in a computational sense. Instead, we focus on the bathymetric variation directly along the line of the Estero MT survey, encapsulating it into a high-resolution 2D model, and hope that the effects of 3D bathymetric variations off the profile are negligible. The second reason is that the inversion of a single profile of data (i.e., with only 2D coverage) using a model which is free to vary in all three dimensions presents a mathematical problem much more ill-posed and underdetermined than that of the 2D model, a predicament we would like to avoid by restricting the inversion to a 2D model. There are geological reasons to believe that the subsurface varies much less along the strike of the SAF than it does perpendicular to it. So, one might expect that a parameterization of conductivity only in the horizontal direction perpendicular to the SAF is adequate. If that expectation does not hold, more profiles of marine data, parallel to the one presented in this dissertation would need to be acquired. Even if full 3D software and infinite computing resources were available, the need for more data acknowledges the fact that though a 2D profile of data is affected by off-axis structure, it does very little to constrain it.

Here, we briefly describe Occam's Inversion drawing from the seminal work of Constable et al. [1987]. Our goal in an inverse process is to minimize our model prediction's misfit to the data. First, we choose to define a misfit, conforming with the least-squares objective, as,

$$X^2 = \sum_{i=1}^{M} (d_i - F_i[\mathbf{m}])^2 / \sigma_i^2; \tag{4.1}$$

d_i are the data; F is a forward functional dependent upon the model vector, $\mathbf{m}$, which is filled with conductivities for each model element; and σ_i are either standard errors or inverse weights, as described in Section 3.6, of the M data. Note that $F_i[\mathbf{m}]$ is what we will refer to as the model prediction for the i^{th} datum. The class of models we utilize are highly parameterized, such that N, the number of elements in $\mathbf{m}$, is greater—and often much greater—than the number of data, M. This gives our models great flexibility, and ensures that we do not restrict our solution to a certain class of models, such as a four-layered earth, etc. The inverse problem for models where $N > M$ presents an under-determined system; there are more free parameters than there are constraints. Under-determined systems have no unique solution. To deal with nonuniqueness, i.e., an infinitude of models that fit the data to an equal level of misfit, we add a philosophical form of model discrimination. To this end, we follow Tikhonov who introduced the idea of penalizing complexity in the model, which he coined "regularization" [Tikhonov and Arsenin, 1977]. The philosophical aim of not accepting a complicated model when a simpler model will suffice, i.e., fit the data to an equivalent level, harkens back to Occam's razor, the algorithm's namesake. Complexity of a model may be assessed by defining a measure of roughness, which is usually given by the integrated square of the first- or second-order spatial derivatives of the model domain. With this measure, the updated problem is to minimize both misfit to the data as well as model roughness. A minimization of a simple sum of these two quantities would be highly sensitive to the relative sizes of misfit and roughness, which may be an arbitrary accident of the scale of the problem. If roughness varies on a much larger scale than misfit, minimization in this manner would simply select a featureless model (maximally smooth), and ignore the data almost entirely; if misfit is the larger variant, an extremely rough model which fits the data

exactly will be sought. Additionally, finding a model with the smallest misfit to real data with errors would produce spurious features, a result of adhering to random fluctuations in the data; these have no basis in the physics we intend to analyze, but instead are expressions of noise. Thus, we must not seek the model that produces $X^2 = 0$. Instead we choose some finite tolerance, T^2, as a lower bound on misfit. The tolerance value can sometimes be chosen on statistical grounds. The statistical theory for the linear inverse problem is well established. For the standard least-squares problem, assuming independent, Gaussian-distributed d_i, with means given by a linear functional $F_i[\mathbf{m}]$, and standard deviations σ_i^2, X^2 follows a χ^2 distribution with $M-N$ degrees of freedom, assuming $M \geq N$; the expected value of X^2 is then $M - N$, which makes a defensible choice for T^2. Note that for the linear problem, if $M = N$ we have added enough free parameters to be able to fit the data exactly, so our expected tolerance goes to zero. For non-linear $F_i[\mathbf{m}]$, there is no theory to provide the expected value of X^2. Moreover, non-linear problems are often solved with $M < N$, as we have chosen to do here. If the computational cost of the inverse process is not a burden, an expected value for X^2 may be estimated with a Monte Carlo simulation [Parker and Song, 2005]. Currently, such an approach is not feasible for 2D MT inversion where a single inversion may last multiple days. If the discrepancy between the data and our model prediction is the result of random variation alone, we may at least put a bound on misfit, $X^2 \leq M$. This follows from the logic that the addition of free parameters should never push the misfit value above the expected value for the sum of squares of standardized Gaussian errors. If deficiency in our model, rather than random noise, is the major contributor to misfit, as we argued for the Estero MT data in Section 3.6, the tolerance must be chosen heuristically with the forfeit of statistical grounding.

Once an appropriate tolerance is chosen, we have a new problem statement: minimize the roughness while meeting the equality constraint that the misfit be equal to the chosen tolerance. We solve this constrained minimization problem in the usual way, with the introduction of a Lagrange parameter, λ, integrated into the following unconstrained functional expressed in discrete form,

$$U(\mathbf{m}, \lambda) = ||\boldsymbol{\partial}\mathbf{m}||^2 + \lambda^{-1} \left\{ ||W\mathbf{d} - WF[\mathbf{m}]||^2 - T^2 \right\}; \tag{4.2}$$

$||\cdot||$ is the Euclidean norm; $\boldsymbol{\partial}$, our measure of roughness, is the discrete first difference operator, which for the example of a 1D model, may be represented by a bi-diagonal matrix; W is a diagonal weighting matrix with $1/\sigma_i$ along its diagonal. The theory behind Lagrange multipliers states that if $||\boldsymbol{\partial}\mathbf{m}_0||^2$ is a minimum in the roughness as a function of the model vector, then there also exists a λ_0 such that $U(\mathbf{m}_0, \lambda_0)$ is a stationary point, i.e., the first derivatives with respect to parameters $\mathbf{m}$ and λ vanish at that point. The stationary point furnishes two equality constraints which solve our problem. Differentiating U with respect to λ, and setting the derivative to zero provides the first constraint,

$$T^2 = ||W\mathbf{d} - WF[\mathbf{m}_0]||^2, \tag{4.3}$$

which restates what we have already imposed. The other constraint comes from the derivative with repsect to $\mathbf{m}$. Before we take the functional derivative $\partial U/\partial\mathbf{m}$, we see that, in order to do so, we will need the first derivative of our non-linear functional, $\partial F[\mathbf{m}]/\partial\mathbf{m}$. For this we will assume that F is differentiable about some starting model $\mathbf{m}_1$, and since (4.2) uses the Euclidean norm, we may make use of the first-order Taylor expansion,

$$F[\mathbf{m}_1 + \boldsymbol{\Delta}] = F[\mathbf{m}_1] + J_1\boldsymbol{\Delta} + \boldsymbol{\varepsilon}; \tag{4.4}$$

$\boldsymbol{\Delta}$ is some small vector perturbation, which we will define in terms of the nearby model, $\mathbf{m}_2$, such that,

$$\boldsymbol{\Delta} = \mathbf{m}_2 - \mathbf{m}_1; \tag{4.5}$$

J_1 is the Jacobian matrix, evaluated at $\mathbf{m}_1$, and whose elements are given by,

$$j_{kl} = \frac{\partial F_k[\mathbf{m}_1]}{\partial m_l}; \tag{4.6}$$

$\boldsymbol{\varepsilon}$ is the error vector of a local, linear approximation of F, and whose magnitude is $O||\boldsymbol{\Delta}||$. Since this is an algorithm designed for arbitrary non-linearity, it must be iterative. We start with an initial guess of a model vector, which we call $\mathbf{m}_1$, about which, we compute

J_1; if the functional derivative cannot be derived analytically, the Jacobian matrix may be computed either with numerical differencing or the adjoint method [e.g. McGillivray et al., 1994]. Then, we seek to find the next "best" guess at a model, which we call $\mathbf{m}_2$, that will satisfy the problem statement, embodied by the minimization of U. Inserting (4.4), dropping the error vector from now on, and (4.5) into (4.2) we find an approximation of the unconstrained functional,

$$U(\mathbf{m}_2, \lambda) = ||\boldsymbol{\partial}\mathbf{m}_2||^2 + \lambda^{-1}\left\{||W(\mathbf{d} - F[\mathbf{m}_1] + J_1\mathbf{m}_1) - WJ_1\mathbf{m}_2||^2 - T^2\right\}. \tag{4.7}$$

Setting the derivative of (4.7) with repsect to $\mathbf{m}_2$ to zero, we arrive at the following linear system to be solved for the unknown $\mathbf{m}_2$ in terms of knowns, λ, $\mathbf{m}_1$, $F[\mathbf{m}_1]$, and J_1:

$$\mathbf{m}_2 = \left[\lambda\boldsymbol{\partial}^T\boldsymbol{\partial} + (WJ_1)^T(WJ_1)\right]^{-1}(WJ_1)^TW(\mathbf{d} - F[\mathbf{m}_1] + J_1\mathbf{m}_1). \tag{4.8}$$

There are two important matters left to address: one, we must choose λ; and two, due to the non-linearity of the forward functional, we have no guarantee that $F[\mathbf{m}_2]$ will produce a misfit less than or equal to our chosen tolerance, either due to the limitations of the local linear approximation (4.4), or because the original problem statement has no solution at all. The two remaining matters are related, and the Occam algorithm provides a heuristic way of tackling both. The initial stages of the Occam algorithm are aimed at lowering the misfit of sequential model guesses until they reach the tolerance level. The value of λ varies from one iteration to the next. At each iteration we choose the value which produces the greatest reduction in misfit to the data. There is no analytical way of predicting which value of λ will achieve this, so a numerical search is performed over a range of λ's. The equation (4.8) is solved for multiple λ, holding $\mathbf{m}_1$ and J_1 constant, and the misfits of the resulting $F[\mathbf{m}_2]$'s are analyzed with respect to λ. A larger λ directs (4.8) toward smoother models, and a smaller λ toward rougher models. The smoothest model is unlikely to have the required complexity to fit the data and thus will produce a large misfit. One might assume the roughest model to have the smallest misfit. However, that is not normally the case since the roughest model guesses usually require a large step in model space, $\boldsymbol{\Delta}$, which reduces the accuracy of the linear approximation (4.4) upon which

(4.8) is based; these inaccurately-projected models will usually have a larger misfit than a more conservative step associated with a smoother model. This misfit behavior at the extremes in λ-space means that, along the curve of misfit with respect to λ, there is typically a definite minimum. We must search through enough values of λ to find that minimum in misfit; there are many efficient algorithms for performing such a line search [e.g., Press et al., 2007]. In the initial iterations, the minimum misfit is usually found to lie above the chosen tolerance (see Figure 4.1). In that case a new iteration begins, starting from the model corresponding to the λ which produced the minimum misfit. New F and J are calculated for this model and the search over λ is repeated. This process continues until λ's are found that produce misfits which are below the tolerance; achieving a misfit below the tolerance is not guaranteed to happen, and may never happen. The inability of an inversion to reach the chosen tolerance level usually indicates that the magnitude of errors in the data, whether systematic or random, are underestimated. One could increase the error amplitudes or increase the tolerance level, two similar solutions to the same problem. Once a model with a misfit less than or equal to the tolerance level is reached, the second and final stage of the Occam algorithm begins. In subsequent iterations, it is likely that multiple λ's will produce misfits that are below the tolerance. The largest of these is chosen as the correct λ because it produces the smoothest model that satisfies the tolerance in misfit, our prescribed objective. The iterations of the second stage proceed by repeatedly choosing the largest λ which meets the tolerance in misfit until convergence is reached, i.e., successive iterations produce negligibly different models. The second stage can be called the smoothing stage because it methodically removes excess structure that is not required to keep the misfit equal to the tolerance level. The final model can be said to be the smoothest model, *within the search path*, that meets the data constraints to the chosen level of tolerance. As has already been stated, infinitely many more models may fit the constraints to the same level of tolerance as our smooth model. While the second stage of the Occam algorithm is aimed at removing any excess model roughness that is not required by the data, there is no proof which allows us to state that the final Occam model is the smoothest of *all* models producing the tolerated amount of misfit. However, an apt starting model may increase the chances of this being true. The logic for the choice of starting model

procedes as follows: if one uses a starting model that is maximally smooth, i.e., all model parameters are equal, from there the Occam process slowly adds only enough complexity so as to meet the requirements of the data. One would expect the final model from such a starting point to be the smoothest possible. As a check on this expectation, different values for a uniform initial model vector may be tested. In practice it has been found that different starting models of uniform resistivity result in the same final model, providing some evidence that the final model may be uniquely the smoothest.

In Figure 4.1 we plot an example of the Occam inversion algorithm. The example is of DC resistivity data produced over a layered earth; the layer resistivities are plotted with a blue dashed line in plot **B**. The DC resistivity array is of Schlumberger type, with current electrode spacing denoted as AB. The resulting apparent resistivity calculations had 10% noise added to create synthetic data, plotted as blue asterisks in plot **C**. In plot **A**, the gray lines depict the line search over λ for the first two iterations of stage 1 of the Occam process, which reduce the misfit toward the chosen tolerance level; the curves corresponding to these two iterations are numbered chronologically. The Lagrange parameter search of the third iteration reaches misfits below the tolerance level, thus beginning stage 2 of the Occam process. The largest-λ intersection between the black curves in plot **A** and the tolerance level is chosen in each of the iterations of stage 2. This finds increasingly smooth models that fit the data to the same level of misfit. Finally, successive iterations yield little difference in the chosen model, so the process is terminated with a final model. The final model and its prediction are plotted with black in plots **B** and **C**, respectively; in those plots, models and predictions from the intermediate iterations are plotted in gray.

4.2 The Effect of Data Forms in MT Inversion

With any inverse problem, a data vector, derived from the same set of observations, may take multiple forms. In the case of MT measurements, the common options are: real and imaginary impedance; apparent resistivity and phase; or the logarithm of apparent resistivity and phase. All these forms are related by simple analytic transformation formulae, yet they have a discernible effect on the inversion process. In this section, we compare

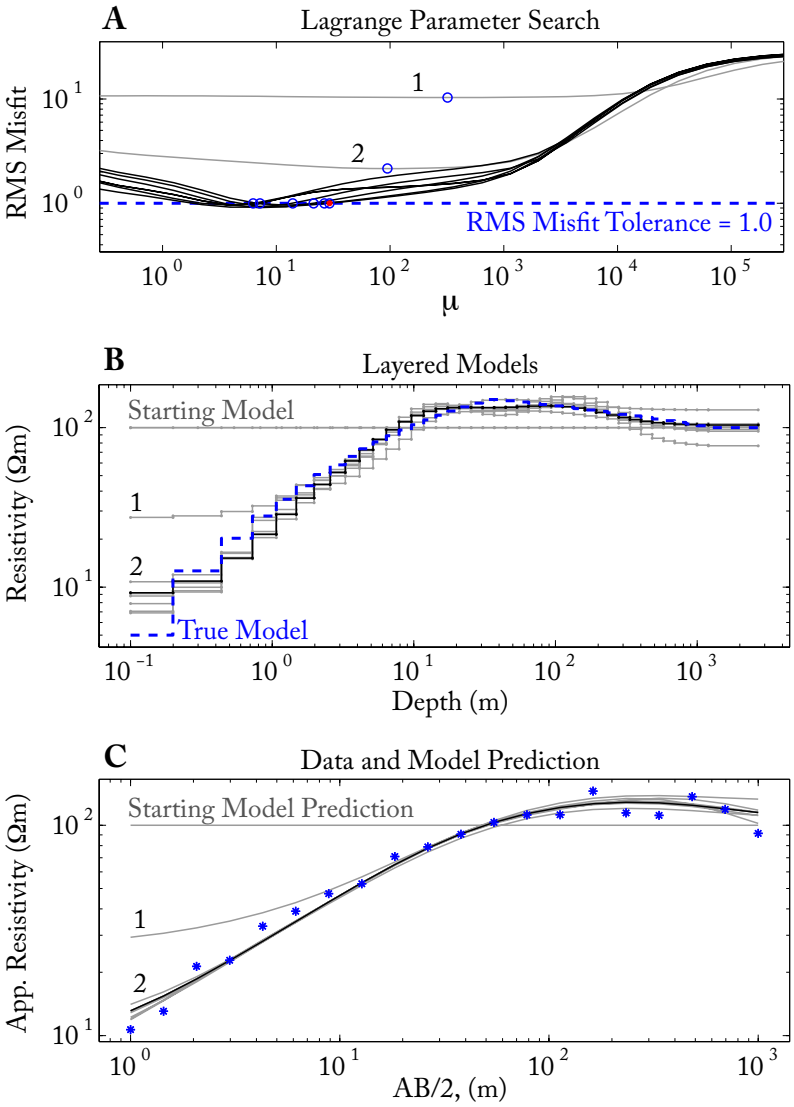

Figure 4.1: An example of an Occam inversion of synthetic 1D DC resistivity data. **A**.) A plot of the Lagrange-parameter line search at each iteration. Iterations from stage 1 are plotted in gray and numbered chronologically, while iterations from stage 2 are plotted in black. The λ parameter chosen at each iteration is plotted with a small circle; the final λ is plotted in red. **B**.) A plot of the model guesses, in terms of layer resistivities at depth, corresponding to each iteration of the Occam process. The final model is plotted in black, while the true model is plotted in blue. **C**.) The 1D DC synthetic data (apparent resistivity as a function of half the current-electrode spacing of a Schlumberger array, AB/2) is plotted with blue asterisks, along with each iteration's model prediction in gray lines; the final model's prediction is plotted in black.

the behaviors of MT inversion under these different data forms and judge which form is optimal.

We will use synthetic measurements from an example model which is roughly akin to a model for central California in that it produces a strong coast effect. The coast effect is a phenomenon observed particularly in marine MT data, in the vicinity of the coastline of a resistive continent [e.g. Constable et al., 2009, Key and Constable, 2010]. The following are signatures of the 2D coast effect in MT data: negative TE-mode phases that wrap from -180° to 180° at some characteristic period of field oscillation, where a concomitant cusp in the TE-mode apparent resistivity is found; and a depression of the TM-mode apparent resistivity relative to the value for a similar model without a nearby coast (see Figures 4.3 and 4.4). Key and Constable [2010] provided an explanation for these phenomena with 2D modeling of the Poynting vector near a coastline. We provide a 3D exploration of the coast effect in Section 6.1.

Figure 4.2 depicts the simple 2D coast model we use in this study of data forms. It has a gradual continental slope which levels out to a 4 km deep ocean. The model has a uniform sub-seafloor resistivity which we will vary over multiple forward calculations. At each of the 20 seafloor sites we will calculate the MT quantities of impedance tensor (Z) and vertical magnetic transfer function, or tipper (V).

Figures 4.3 and 4.4 contain plots of two separate calculations of our simple coast model using two different seafloor resistivities, 90 Ωm and 115 Ωm. These figures also show the 1D values which would correspond to models with the same seafloor resistivities but with no coast. Without dwelling on the physics of the coast effect, the point we make here is that coastlines create extreme effects in the apparent resistivity, phase, and tipper data which vary in a complicated way with respect to the conductivity of the earth; this provides a challenge for non-linear inversion which must make a linear approximation to predict how a change in model parameter will effect a fit to the data. In contrast, the change in the data over the same change in model parameter for the model without a coast is much more banal; it would appear that a coast-free inversion presents far less of a challenge.

The Occam inversion algorithm, along with other gradient-based algorithms, finds an optimal model by traversing the misfit space in a consistently downhill fashion (i.e.,

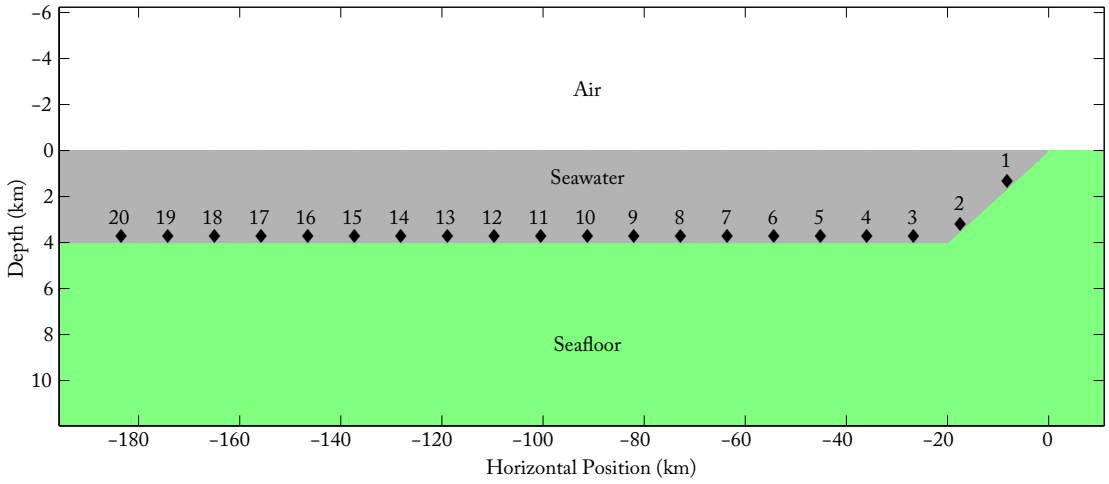

Figure 4.2: Model with a simple coast and uniform seafloor used in synthetic misfit study. The black diamonds indicate locations of hypothetical MT receivers.

in the direction of decreasing misfit). Due to this behavior, there are a few properties of misfit spaces that ensure success with such non-linear inversion schemes. First, the Occam inversion has the best chance of finding the "true" model if the misfit space, given by the data and the forward functional, is convex (i.e., has a single minimum). This is because the Occam inversion algorithm has no explicit mechanism for escaping local minima, as would, for example, a stochastic inversion method by accepting models that constitute an uphill step in misfit. Gradient-based non-linear inversion methods simply march downhill in the misfit space until the only choice left is to move uphill (i.e., the conditions of a local minimum), at which point it accepts the current position in model-space as the final solution. The only possibility for an Occam inversion to escape a local minimum comes during the Lagrange parameter search. The Lagrange parameter search will sample models of varying roughness, some of which may lie outside the local minimum at a lower level of misfit. However, the Lagrange parameter search does not sample models of varying absolute size (unless a model norm is employed instead of a roughness norm), which may be what is required to get out of a local minimum and back on the way toward the absolute minimum. Second, the parameter values of the final model of an inversion are better constrained if the misfit surface around the true model, has steep walls. This means that a small change in

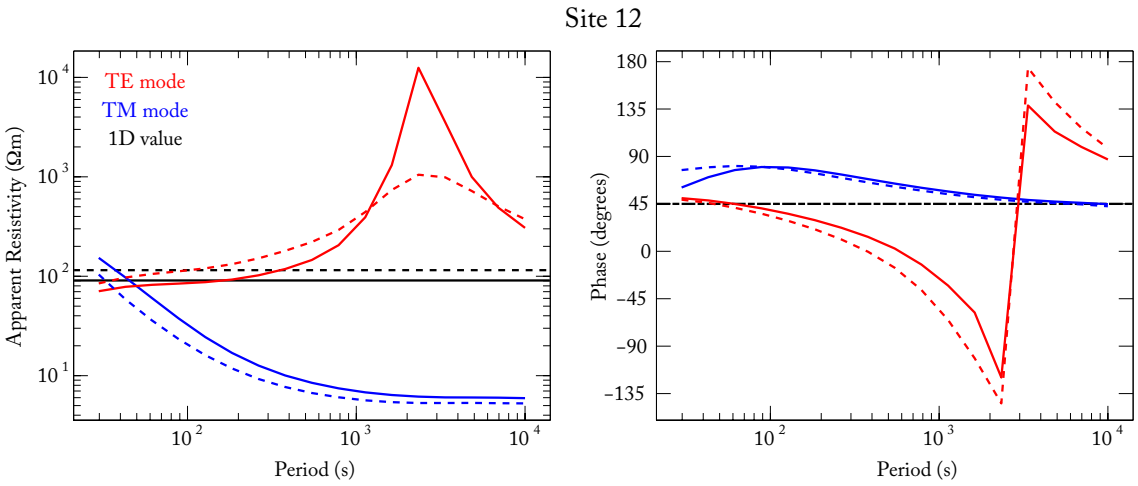

Figure 4.3: MT apparent resistivity and phase alculations for the model pictured in 4.2. Two uniform seafloor resistivities were used: 90 Ωm (solid lines) and 115 Ωm (dashed lines). The black lines plot the respective values for models with equivalent seafloor resistivities but no coast (i.e., purely 1D), in which case TE and TM modes are equivalent, and the phase is always 45°.

model parameters away from the true value will create a greater increase in misfit, bestowing greater statistical significance to the final model parameters. Finally, the misfit value of the true model must meet the statistically expected value so that the user is aware when a probable model is reached. We will now examine plots of the misfit spaces for our simple coast model with data packaged in the different possible forms, and appraise the misfit spaces of these different data forms in terms of the aforementioned properties that facilitate success for the Occam algorithm.

The proposed misfit spaces are 1D, i.e., they vary with only one model parameter ($N = 1$). Low-dimensionality, while not representative of regularized inversion, where $N \gg M$, makes the misfit spaces amenable to plotting and analysis. We expect the differences observed between data types to carry over to higher-dimension problems, as we will show with some highly-parameterized synthetic studies at the end of this section.

The misfit spaces are computed in the following way. We choose one seafloor resistivity to be the true model. A MT calculation is made for the true model and independent

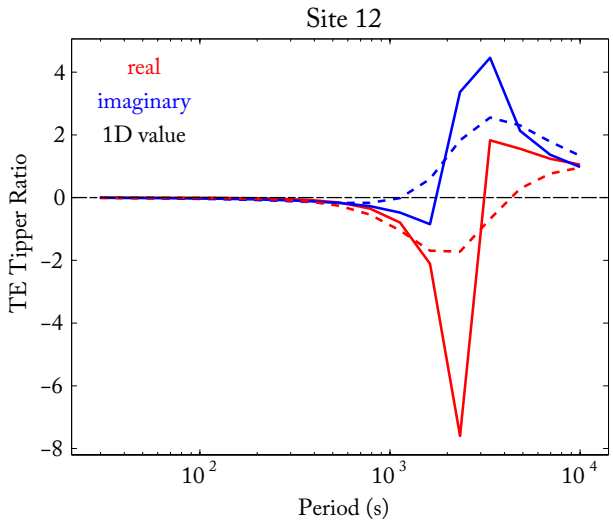

Figure 4.4: MT tipper calculations for the model pictured in Figure 4.2. Two uniform seafloor resistivities were used: 90 Ωm (solid lines) and 115 Ωm (dashed lines). The black lines plot the respective values for models with equivalent seafloor resistivities but no coast (i.e., purely 1D), in which case all tipper ratios are exactly zero.

Gaussian errors are added to the real and imaginary components of the impedance tensor and the tipper vector to create synthetic data. The standard deviation of the pseudo-random, Gaussian errors are chosen to be a defined percentage of $|\mathsf{Z}|$ and $|\mathsf{V}|$, for Z and V, respectively; this ensures that the real and imaginary parts of each synthetic datum are jointly distributed with a probability distribution that is circularly symmetric in the complex plane, an assumed characteristic of actually measured data. Then, MT calculations are made over many models that span a range of seafloor resistivities. These serve as the model predictions made by the forward functional. For each of these predictions, a root-mean-square (RMS) misfit is computed relative to our synthetic data. Building from (4.1), the RMS misfit is defined as,

$$X_{\mathrm{RMS}} = \sqrt{X^2/M}. \tag{4.9}$$

Based on the previous discussion in Section 4.1, we predict,

$$\mathrm{E}[X_{\mathrm{RMS}}] \leq 1 - \frac{1}{4M} + \frac{1}{32M^2} + O(M^{-3}), \tag{4.10}$$

making use of the formula for $\mathrm{E}[||\mathbf{X}||]$, derived for the random vector $\mathbf{X}$ in Parker [1994]. For each of the data forms we compare the misfit spaces for inversions with and without tipper information. The data vectors which include tippers have an $M = 2040$, whereas with the tipper information excluded $M = 1360$. In either case, M is large enough that we expect the RMS misfit to be very close to 1.0 at the true model.

Figures 4.5 through 4.7 depict the results of the misfit space calculations. The initial observation, common to all plots, is that the solid and long-dashed green lines are much more jagged with multiple local minima than the other curves. The green lines relate to impedance data in the form of apparent resistivity and phase. Data in this form seem to present the worst option for MT inversion near a coast. The blue solid and long-dashed lines, which represent the misfit spaces for the real and imaginary components of the impedance tensor and tipper vector, also have multiple local minima, but theirs are less pathological than those of apparent resistivity and phase. For this simple model, we conclude that the real and imaginary components of the impedance tensor and tipper vector are the second worst choice for the form of coast-affected data. It is the apparent resistivity and not the phase that causes the multiplicity of local minima. Once apparent resistivity is put into the logarithmic form, the jaggedness of the misfit space is reduced despite the continued use of phase. Likewise, once the tipper vector is put into the form of the logarithm of amplitude and phase, the jaggedness of the misfit space is further reduced.

Next, we note that all of the dotted curves, deriving from the different data forms over a 1D halfspace (HS), are perfectly smooth and convex. These represent data for the same range of model parameters but without a coast. As expected, the coast-free inverse problem is much simpler. In fact, the uni-parameter, coast-free inverse problem is guaranteed to converge to within some expected uncertainty of the true solution, regardless of the form that the data takes, and regardless of what the initial model guess is (i.e., where along the misfit curve the inversion search begins); this is not guaranteed when a coast

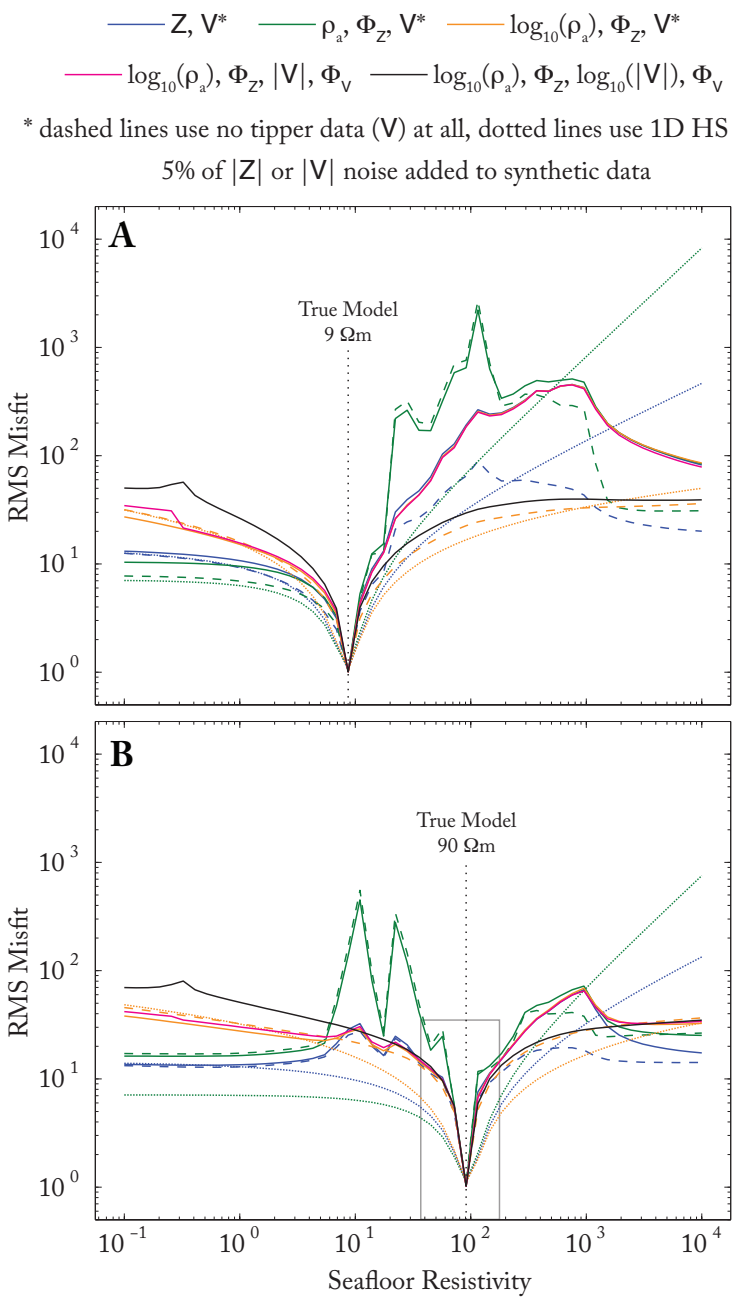

Figure 4.5: Misfit spaces around two different seafloor models (**A** & **B**). The solid lines plot the misfit spaces for five different data forms derived from the same synthetic data vector. The data symbols include: real and imaginary components of the impedance tensor, Z, the real and imaginary components of the tipper vector, V, apparent resistivity, ρ_a, impedance phase, Φ_{Z}, and tipper phase, Φ_{V}. The long-dashed lines plot the misfit spaces for the same data collections but without any tipper data. The dotted lines plot the misfit spaces for data collections calculated over a 1D halfspace, i.e., a coast-free model, and thus also do not include tipper data.

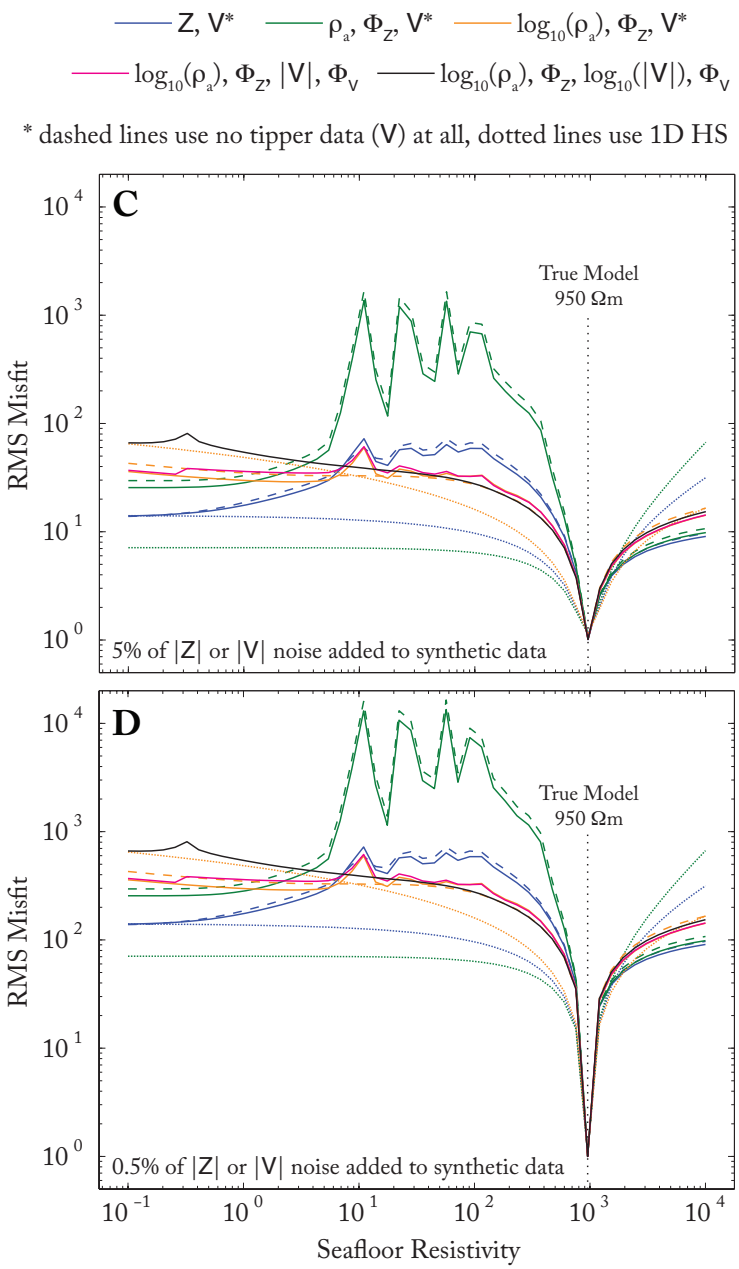

Figure 4.6: Misfit spaces around the same seafloor model, but with two different magnitudes of Gaussian errors added (**C** & **D**). Lines and symbols follow the same conventions as in Figure 4.5.

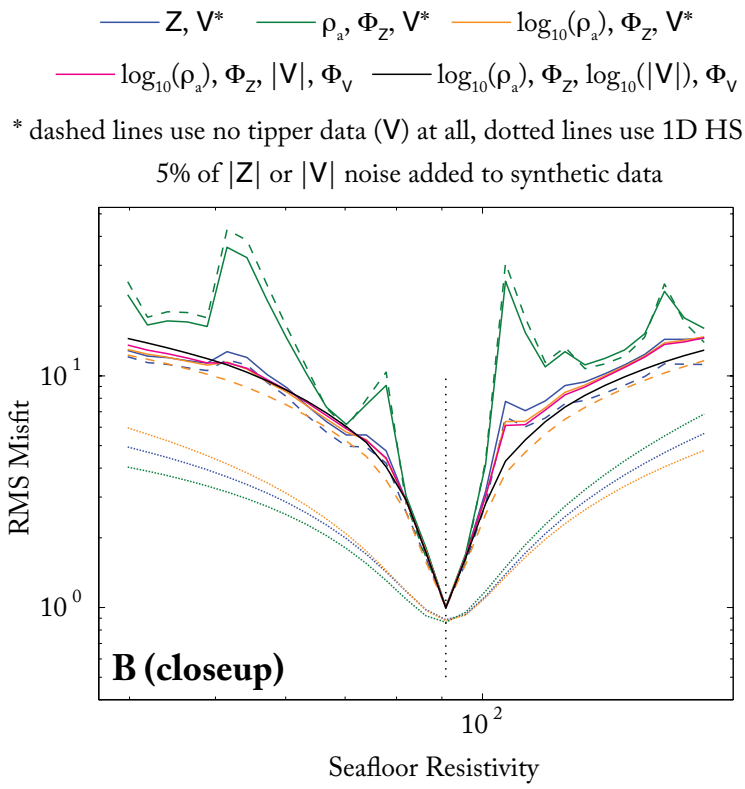

Figure 4.7: A close-up of the portion of Plot **B** in Figure 4.5 delineated by the gray box. Lines and symbols follow the same conventions as in Figure 4.5. We should note that different realizations of a random vector were added to the 1D halfspace and coast-affected data. This produces the slight mismatch in RMS misfit between these two groups of data at the true model.

is added. However, we also note that the walls of the valleys in the misfit curves around the true models are steeper for the coast-affected data than they are for the coast-free data (see Figure 4.7). The coast-effect acts to better constrain the seafloor resistivity, a consequence of the increase in wavenumber-richness in the electromagnetic fields that have been distorted by the coast (see Section 5.9). For the more conductive model (Plots **A** & **B**), the same misfit valleys are even steeper when including tipper data than without. The only difference between plots **C** and **D** is the magnitude of the Gaussian errors introduced into the synthetic data; **C** was made with errors 10 times greater than that of **D**. The valleys

in the misfit surfaces around the true model for plot **D** are much steeper than that of plot **C**. As we would expect, the lower the magnitude of data errors the better constrained the final parameter value.

The curves for all of the linearly-scaled data forms flatten as the model prediction moves toward more conductive seafloors; this does not happen with the log-scaled data forms. To explain this flattening, we look first at the 1D HS curves where we can ignore impedance phase, which is always 45° regardless seafloor resistivity, and the tippers which are always zero. We note that for the linearly-scaled data forms over a 1D HS, $F_i[\mathbf{m}] \to 0$ as $||\mathbf{m}|| \to 0$, and analyze how this limit affects our different misfit measures. For the linearly-scaled misfit we write,

$$\lim_{F_i \to 0} X^2 = \lim_{F_i \to 0} \sum_{i=1}^{M} \left(\frac{d_i - F_i[\mathbf{m}]}{\sigma_i} \right)^2 = \sum_{i=1}^{M} \left(\frac{d_i}{\sigma_i} \right)^2 = \text{const.} \,. \tag{4.11}$$

This explains the flattening in the misfit curves when the seafloor resistivity is much lower than that of the true model. The same flattening is seen in the models with a coast because the coast effect vanishes as the seafloor resistivity approaches that of seawater. Next, we write the definitions of the log-scaled data, model predictions, and error estimates in terms of their linearly-scaled counterparts. With the log-scaled values denoted by the $\breve{\cdot}$, we have,

$$\breve{d}_i = \log_{10} d_i, \tag{4.12}$$

$$\breve{F}_i[\mathbf{m}] = \log_{10} F_i[\mathbf{m}], \tag{4.13}$$

and

$$\breve{\sigma}_i = \frac{\sigma_i}{d_i \ln 10}, \tag{4.14}$$

where (4.14) is found through linear propagation of error, which we derive in Appendix A.

Then, the log-scaled misfit measure is,

$$\begin{aligned}\breve{X}^2 &= \sum_{i=1}^{M}\left(\frac{\breve{d}_i - \breve{F}_i[\mathbf{m}]}{\breve{\sigma}_i}\right)^2 \\ &= \sum_{i=1}^{M}\left[\frac{(\log_{10} d_i - \log_{10} F_i[\mathbf{m}])(d_i \ln 10)}{\sigma_i}\right]^2 \\ &= \sum_{i=1}^{M}\left[\ln\left(\frac{d_i}{F_i[\mathbf{m}]}^{\left(\frac{d_i}{\sigma_i}\right)}\right)\right]^2 . \end{aligned} \tag{4.15}$$

Taking the limit again, we find,

$$\lim_{F_i\to 0} \breve{X}^2 = \infty. \tag{4.16}$$

With the log-scaled inverse problem, there is no flattening in the misfit curve on the conductive end of the parameter space. Conversely, we analyze the different misfit behaviors as the seafloor becomes more resistive. By noting that for the 1D HS, $F_i[\mathbf{m}] \to \infty$ as $||\mathbf{m}|| \to \infty$, we find,

$$\lim_{F_i\to\infty} X^2 = \infty, \tag{4.17}$$

and

$$\lim_{F_i\to\infty} \breve{X}^2 = \infty. \tag{4.18}$$

In summary, the log-scaled misfit measure never leads to a flat curve in parameter space, whereas the linearly-scaled measure leads to a flat curve on the low end of parameter space (assuming the parameter is defined as resistivity). Flat misfit curves can lead to divergence in the Occam inversion process as it is very difficult to detect, within the limits of numerical precision, which direction in parameter space leads downhill in misfit. This behavior at the limits of parameter space provides another argument for the superiority of the logarithm of apparent resistivity and the logarithm of tipper magnitude as the form of data to be

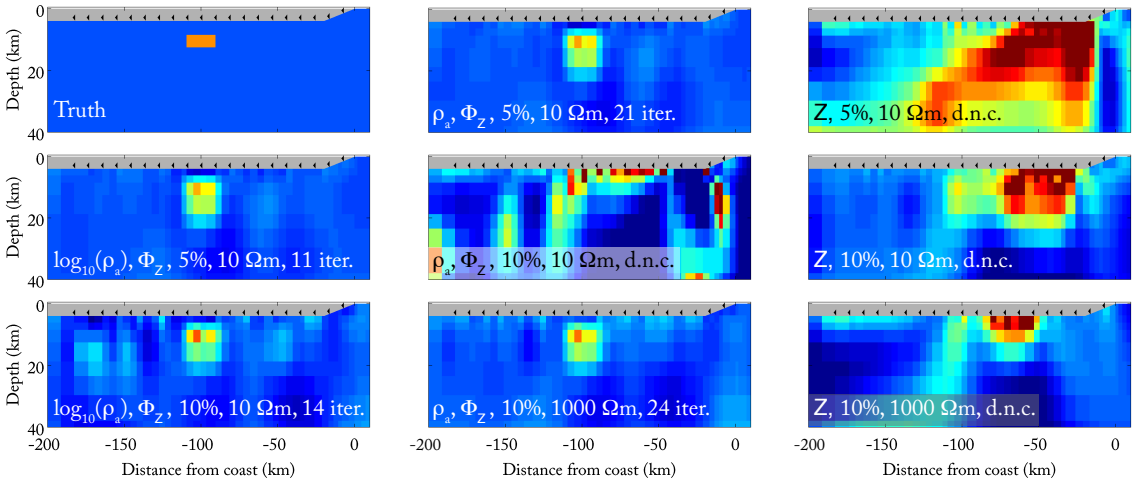

Figure 4.8: The true model and final models produced by synthetic inversion experiments with different data types. The labels in each plot describe the setup for the that inversion. The data types used are: logarithmic apparent resistivity ($\log_1 0(\rho_a)$), linear apparent resistivity (ρ_a), impedance phase (Φ_Z), and the real and imaginary components of the raw impedance (Z). The standard deviation of synthetic Gaussian noise added to the data for each inversion are in terms of percentage amplitude of the raw impedances, either 5% or 10%. Finally, the number of iteration that it took for each inversion to converge is reported, except for the cases where the inversion did not converge (d.n.c.).

inverted. Looking back to (4.15), the only way the logarithmic form of data would lead to a flat misfit curve is when none of the $F_i[\mathbf{m}]$ change with a change in $\mathbf{m}$. In this case, the inverse problem is inescapably ill-posed.

Finally, we note that all forms of data reach the expected value of RMS misfit, 1.0, only at the true model. Thus, assuming data errors are well estimated, one should have little trouble identifying when the most probable model has been reached, regardless of data form.

We close this section with a more practical illustration of how data forms affect the inverse problem. We perform synthetic, regularized inversions on each different data type generated from a highly-parameterized model, as opposed to the single parameter model addressed before. The "true" model shown in the upper left corner of Figure 4.8 is parameterized with 799 blocks below the same simple seafloor used previously. The

background resistivity is 100 Ωm, with an anomalously conductive block of 5 Ωm. The other plots in Figure 4.8 show a synopsis of the final models resulting from some of the inversions using different data forms, different quantities of synthetic noise, and different uniform starting models. Reported in each of these plots is the number of iterations required for the inversion to converge upon the smoothest model to fit the data to an RMS misfit of 1.00, or "d.n.c." (did not converge) when an inescapable local minimum was encountered at an RMS misfit greater than 1.00. Much of the behavior encountered in these highly-parameterized synthetic models confirm what was inferred from the uni-dimensional model space, but there are slight differences that are presumably enabled by the increase in degrees of freedom. The logarithm of apparent resistivity with phase is still the top performer for data distorted by 2D bathymetry, as was found with the uni-dimensional misfit space. It consistently converges to the expected RMS misfit, recovering, in a smoothed form, a model consistent with the true model, regardless of the amount of noise added and the starting model used. Another important observation is that inversion of data in this form converges with the fewest iterations, about a factor of two fewer than the next best form of data. The next best form of data, contrary to what the uni-dimensional misfit spaces predicted, is linear apparent resistivity and phase. However, with this data form, larger components of random error led to divergence, when given a starting model more conductive than the true background. When given a starting model on the more resistive side of the true background, convergence is reached even with the greater component of random error added. Nonetheless, the linear apparent-resistivity inversions that did converge, did so in twice as many iterations as their logarithmic counterpart. Also, note that in Appendix A we show that use of data in the linear apparent resistivity form introduces a minute bias when it is assumed that errors are Gaussian in the real and imaginary components of an impedance element; alternatively, there is no bias in the logarithmic form of apparent resistivity. Lastly, the raw impedance (real and imaginary components) inversions diverged at every attempt: all combinations of low noise, high noise, conductive starting model, and resistive starting model.

The conclusions drawn from these synthetic studies have little immediate effect on the practice of 2D inversion of marine data because the logarithm of apparent resistivity has

been the default data form for some time, albeit, prior to this study, the author has never encountered an argument as to why. Also, as stated earlier, the smoothness of impedance curves with respect to period from areas that do not suffer from the coast effect make it unlikely that a 2D inversion of MT data collected far inland would be noticeably affected by data form. Nonetheless, as 3D inversion becomes more widespread, where the use of all four elements of the impedance tensor is required, the results presented here may be of use. The diagonal elements of the impedance tensor do not inherit the intuitive interpretation that the form of apparent resistivity provides for the off-diagonal elements. This has left room for debate over which form these data should take. Consequently, the author has seen a return to interpreting and inverting data in the form of real and imaginary impedance components in the growing number of 3D MT studies. The preceding conclusions argue for the continued use of all four 3D impedance elements in the form of logarithmic apparent resistivity and phase, especially when the extreme effects of the coast are confronted. Conclusions similar to those of this study have been confirmed with another electromagnetic method, CSEM. It was found in the inversion of actual CSEM data that an inversion of the logarithm of amplitude (and phase) was able to converge to an acceptable model when the linear amplitude inversion did not (personal communication with Kerry Key).

4.3 Inversion of Estero MT Data

In this section we present a collection of models that result from Occam inversions of the Estero MT dataset. The entire usable dataset, presented in Figures 3.15-3.18, results in an M =4,896. As mentioned in Section 4.1, the Occam approach is to over-parameterize the model and compensate with regularization. So, we use a model of a 2D earth with 16,810 rectangular blocks, each filled with a constant resistivity that is left as a free parameter in the inversions (see Figure 4.9); thus, N =16,810. In spite of the vertical exaggeration in Figure 4.9, one can see that, in the area of our model discretization that is plotted, there are more vertical boundaries than horizontal boundaries over an equivalent distance. The majority of MT inversion schemes (including that used in Becken et al. [2011]) use this sort of model discretization in which the height of model blocks grow with depth, usually

exponentially. Such spacing is a means of meeting the computational limit on the number of model parameters which may be inverted, by exploiting the fact that the resolution of diffusive electromagnetic methods diminish with depth within the earth. Thus, more model blocks are placed near the surface of the model and increasingly fewer toward the base. The necessary growth in model block size is disproportionally accommodated in the vertical dimension as it is difficult to do otherwise when using a rectangular model discretization, as we do here. While the inversion software used here *does* allow model blocks to grow in width with depth, the creation of a model grid with well-behaved aspect-ratios is not automatic and cumbersome. The new trend toward the use of an automated, unstructured, triangular discretization of a model more easily accommodates growth in cell size evenly in the horizontal and vertical directions. We return to this aspect of our rectangular discretization in Chapter 6. From this point on, all models are plotted with zero vertical exaggeration, unless otherwise stated. Bathymetry along the line connecting the instruments sites was acquired from the National Geophysical Data Center (`http://www.ngdc.noaa.gov/`). The bathymetry is used to delineate the region of the model that is held fixed at the conductivity of seawater, 3.3 S/m (denoted by a gray fill color in subsequent model plots).

An inner region of the final inversion model is plotted in Figure 4.10; we will refer back it often as Model 1. The final level of tolerated misfit was chosen to be $X_{\mathrm{RMS}} = 1.30$. Initially, after adjusting the data errors as described in Section 3.6, an inversion of the data was attempted with the tolerated misfit set at $X_{\mathrm{RMS}} = 1.00$. The inversion algorithm reached a point where it could no longer find a reduction in misfit at $X_{\mathrm{RMS}} = 1.28$. We viewed this to be the minimum achievable misfit given our data, data errors, model parameterization, and model regularization. In order to allow for the smoothing iterations (stage 2) of the Occam algorithm to relax to some level of convergence we chose our final target misfit to be slightly higher than 1.28.

The overall RMS misfit value, while pivotal in the Occam algorithm, carries no information about which individual model predictions do worse relative to others at meeting the data constraints. One would need only to look at a plot of the model predictions alongside the data to make this assessment, but we find these plots overwhelmingly busy

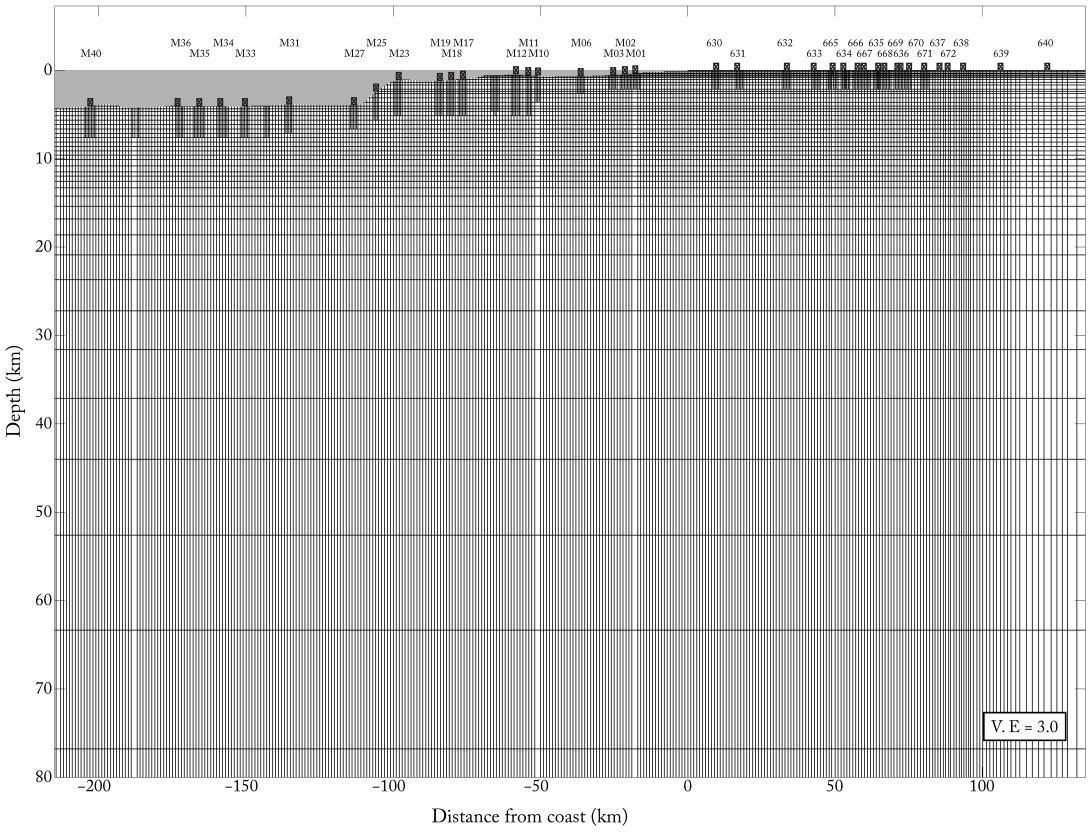

Figure 4.9: Partial grid of model parameter blocks used in the inversions. The full grid extends to ±4,500 km on either side of the coast, to a depth below sea-level of 3,200 km and a height above sea-level of 4,500 km. There are a total of 16,810 free parameter blocks in the full grid. The parameter blocks increase in height with increasing model depth. They also increase in width with increasing horizontal distance from the region containing the receivers, the region pictured. The rectangles with inscribed X's and accompanying site-name labels denote the location of the MT receivers within the model setup. The gray region denotes the portion of the model with a fixed resistivity of 0.3 Ωm, that of seawater. The vertical exaggeration (V.E.) in the image is 3.

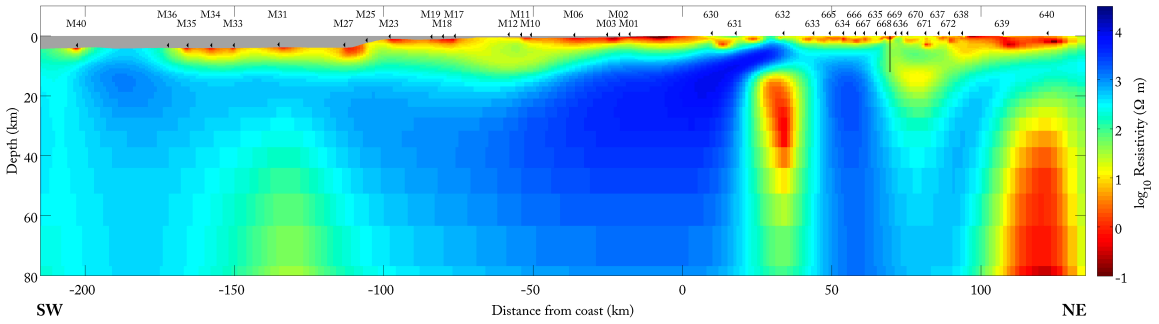

Figure 4.10: (Model 1) The final model result of a smooth 2D inversion of the Estero MT dataset, as presented in Figures 3.15 - 3.18. Model block resistivity is plotted in color with warmer colors indicating conductive features and cooler colors indicating resistive features. The vertical black line plotted at 70 km from the coast is the approximate location and depth extent of the San Andreas fault.

and difficult to digest. Instead, we have condensed the model prediction information into local measures of RMS misfit. The word "local" conveys that it is a measure calculated over a specific subset of the data and model predictions. We choose these subsets in three different ways: by data period, by data type (e.g., apparent resistivity or phase), and by instrument site. In this way, we may categorize where the model predictions are succeeding or failing. Such a distillation of misfit by data subset is plotted for our final model in Figure 4.11. Immediately, we identify a few trends. As the data period increases, so does the final model's misfit to the data. The inversion process did the worst at fitting TE-mode data, both apparent resistivity and phase, relative to the other data types. The inversion process found it especially difficult to fit the sites of marine data in the deepest water (M40 and M36).

We now appraise the Estero MT data's sensitivity to the final model parameters given in Figure 4.10. As a rough measure of any single parameter block's relative importance in terms of affecting misfit, we look to the weighted Jacobian matrix. The inversion process uses as model parameters the logarithm of block resistivity, such that,

$$m_i = \log_{10} \rho_i, \; i = 1, 2, \ldots N. \tag{4.19}$$

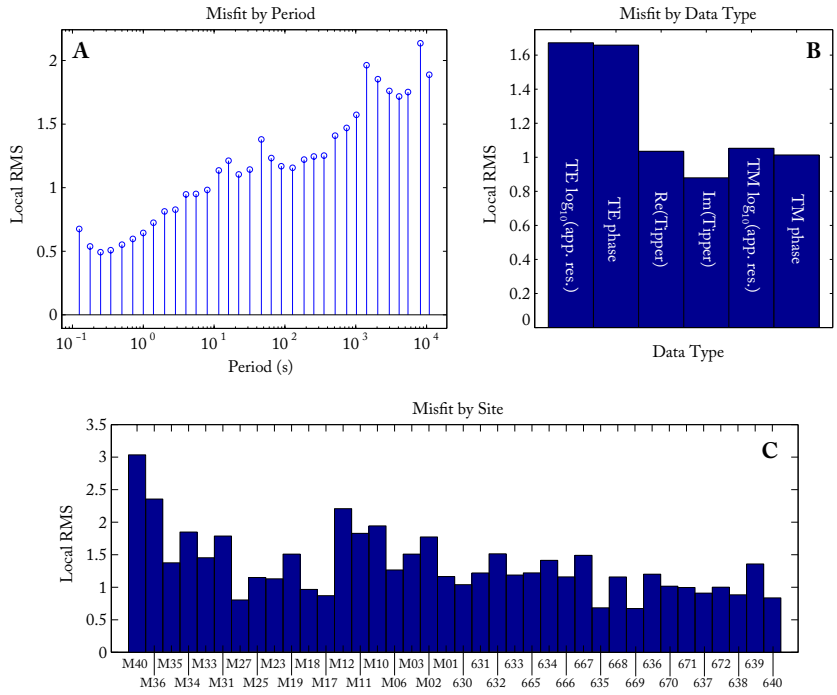

Figure 4.11: A breakdown of the misfit resulting from the model in Figure 4.10 by period (**A**), data type (**B**), and site (**C**). The overall RMS misfit is 1.30.

This choice of model parameter has the advantageous effect of forcing the resistivity throughout the model to be positive, thus confining all models within the realm of what is physically possible. (Note that the log-domain, for all practical purposes, prohibits both infinite conductivities and infinite resistivities. Models containing such extreme properties have been shown to to achieve the minimum possible misfit for data derived from 1D models [Parker, 1980, 1981]. However, such models have no geological relevance, so we intentionally prohibit them.) Also, the roughness measure is affected. Instead of penalizing absolute changes in resistivity from block-to-block, we penalize *relative* changes in resistivity from block-to-block. Applying the chain rule to the continuous representation of the roughness measure, we find

$$\boldsymbol{\partial}\mathbf{m} = \partial \log_{10} \rho_i = \frac{1}{\ln(10)\rho_i} \partial \rho_i. \tag{4.20}$$

In the actual discrete roughness measure, the change in resistivity from block-to-block is implicitly normalized by the local resistivity value. This normalization carries over to our Jacobian. Substituting $\tilde{d}_k$ for the k^{th} model prediction, $F_k[\mathbf{m}]$, in (4.6), we have,

$$j_{kl} = \frac{\partial \tilde{d}_k}{\partial \log_{10} \rho_l} = \ln(10)\rho_l \frac{\partial \tilde{d}_k}{\partial \rho_l}. \tag{4.21}$$

Thus, the weighted Jacobian matrix,

$$(WJ)_{kl} = \ln(10)\frac{\rho_l}{\sigma_k}\frac{\partial \tilde{d}_k}{\partial \rho_l}, \tag{4.22}$$

is dimensionless, given in units of standard deviations per proportional change in resistivity. Similar to MacGregor et al. [2001], we use the Jacobian matrix to develop a measure of sensitivity as the cumulative absolute change in model prediction per proportional change in resistivity per unit area:

$$\text{Sensitivity} = \ln(10)\sum_{k=1}^{N}\frac{\rho_l}{A_l\sigma_k}\left|\frac{\partial \tilde{d}_k}{\partial \rho_l}\right|, \tag{4.23}$$

where A_l is the area of the l^{th} model block. A plot of the data's sensitivity to a broad portion of the model is presented in Figure 4.12. It should be kept in mind that the Jacobian matrix is a linearization of a non-linear phenomenon. It is only useful for small perturbations about the current model. A significant change in the model would likely produce a significant change in the data's sensitivity. Nonetheless, it provides a rough idea of which model blocks are better constrained by the data, given the current model. We choose to narrow down the interpretable area of Model 1 to the region within the gray line of Figure 4.12 based on the sensitivity values. Within that sub-region the majority of the parameter blocks have a data sensitivity that is within three orders of magnitude of the greatest sensitivity found in our model.

As one would expect, the greatest data sensitivity is found closest to the instrument sites. A broader comparison of Figures 4.10 and 4.12 evokes the traditional maxim that MT is sensitive to conductors; the areas with high data sensitivity predominantly correspond

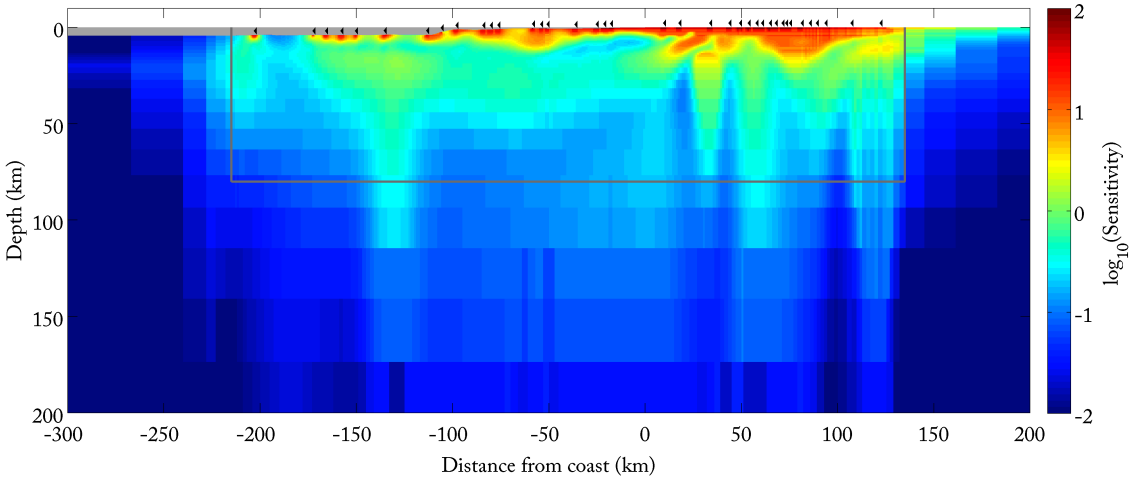

Figure 4.12: A Plot of the data's sensitivity to the model parameters of Model 1. The sensitivity is given in units of standard deviations of data per proportional change in model parameter value. Warm colors indicate that a small perturbation of a given model parameter from its final value has a large effect on the modeled data, whereas cooler colors indicate that the same perturbation has a small effect on the modeled data. The thick gray lines circumscribe the region of Model 1 chosen for interpretation and plotted in Figure 4.10. The majority of model blocks in the chosen region have a sensitivity within three orders of magnitude of the highest sensitivity found in the entire model.

to areas of high conductivity. However, Figure 4.13 provides an example of where this maxim does not hold. The region of the data sensitivity outlined with the dashed black line corresponds to model blocks with relatively high resistivity (7,500 Ωm).

As a means of discerning which model predictions produce the high sensitivity in the region of high resistivity, we create a test model and analyze how its model predictions compare with those of our final model. The test model depicted in plot **A** of Figure 4.14 is equivalent to Model 1 of Figure 4.10 except for a 30 Ωm connection between the near-surface conductive region below site 631 and the deeper conductor below site 632; this test conductor breaches the high-resistivity, high-sensitivity region which forms a cap on the southwestern side of the comet-shaped deeper conductor. Solely as a matter of convenience, we will call the lower crustal conductor below site 632 the Rinconada conductor, as it is centered almost directly below the surface trace of the Rinconada fault. At its most conductive point, the

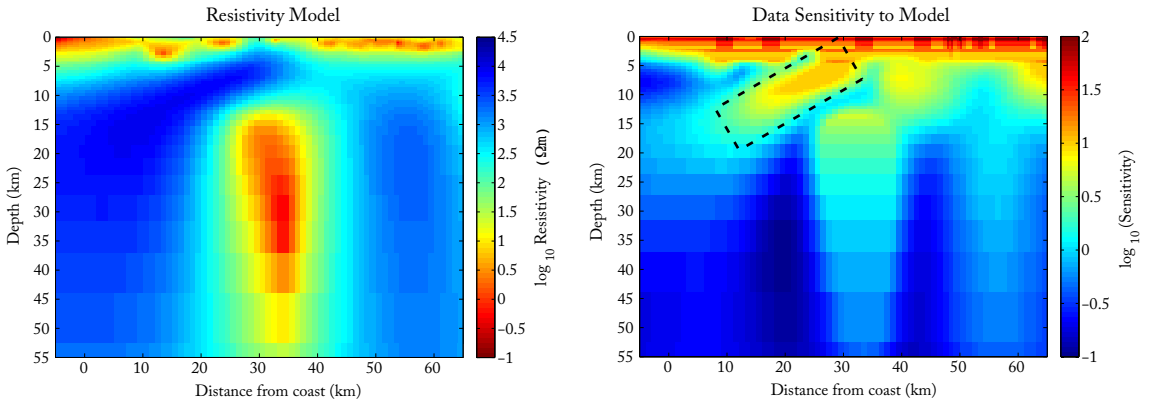

Figure 4.13: A close-up comparison of the final model-parameter values (left) and their corresponding data sensitivity (right). The majority of parameter blocks with high sensitivity correspond to low resistivity values, whereas, the dashed black line outlines a region of high sensitivity that corresponds to very high resistivity values.

Rinconada conductor has a resistivity of 0.5 Ωm, nearly as conductive as seawater. The overall misfit for the test model is 1.79, a significant increase over our final model. Plots **B** and **C** in Figure 4.14 display the difference in local RMS misfit between the test model and the final model. Positive values of local RMS indicate that the test model produces a worse match to the given subset of data than does the final model, while negative values indicate that the test model produces a better match. The relatively small change in resistivity structure presented by the test model produces significant and adverse changes in the local misfits. While one would expect the nearby sites 630, 631, and 632 to experience large increases in misfit under the test model, one would not expect site M40 to experience an appreciable change in misfit; yet, it does. Site M40 is over 200 km away from the test model's change in resistivity structure. In contrast, site 634 is less than 30 km away from the change in resistivity structure, but experiences no change in misfit. In fact, outside of the direct vicinity of the test conductor, the land sites show negligible changes in misfit while all of the marine sites show an increase in misfit. Therefore, we can say that, given the final model, the high-resistivity region below sites 631 and 632 is heavily required by the marine data; on the contrary, the land data are mostly indifferent toward its existence. Furthermore, the high-resistivity cap is heavily required by the TM-mode apparent resistivity, and to a

lesser extent TM-mode phase data. The test model has almost no effect on the misfit to all TE-mode data or tipper data. The levels of relative misfit between the test model and Model 1 show an increase with increasing period of oscillation.

Figures 4.15 and 4.16 illustrate the physics behind the marine data's strict requirement for the resistive barrier between the surface conductors near the coast and the Rinconada conductor. It is a manifestation of what is known as the TM-mode coast effect [e.g. Cox, 1980, Heinson and Constable, 1992], to which we alluded in Section 4.2. The TM-mode coast effect is recognized as a depression of the apparent resistivity curve relative to the 1D response of a similar earth with no coast. At longer periods, it is nearly independent of the period of energy; accordingly, it is described as a galvanic effect rather than an inductive effect. The traditional explanation for the TM-mode coast effect is that charge accumulates at the coastline where horizontal electric current, induced in the conductive seawater of the deep ocean, has its landward progress thwarted by the relatively resistive continent. The charge accumulation produces an electric field which counteracts the primary electric field on the marine side of the coast. The net effect is a reduction in the amplitude of the total electric field on the marine side of the coast. On the land side of the coast, the effect is the opposite; the charge accumulation bolsters the total field. In terms of apparent resistivity, the TM-mode coast effect translates into a downward shift on the marine side and an upward shift on the land side, relative to a similar 1D response. In Figure 4.15, we see that the addition of the test conductor that connects the Rinconada conductor to the surface conductors near the coast opens a conduit for currents induced in the ocean to escape into the upper mantle, reducing the charge accumulation at the coast. This short-circuit through the resistive continental crust dramatically changes the current distribution in the ocean and seafloor, a consequence detectable by all of the Estero MT seafloor receivers. Figure 4.16 provides plots of the change in electric and magnetic field amplitude and phase due to the addition of the test conductor. The test conductor partially neutralizes the TM-mode coast effect. The lack of charge accumulation increases the total electric field in the ocean and decreases it on land. Also, by producing a near-vertical sheet current from the ocean into the mantle, the test conductor produces a dipolar change in the total magnetic field. The broader observation is that the changes to both the amplitude

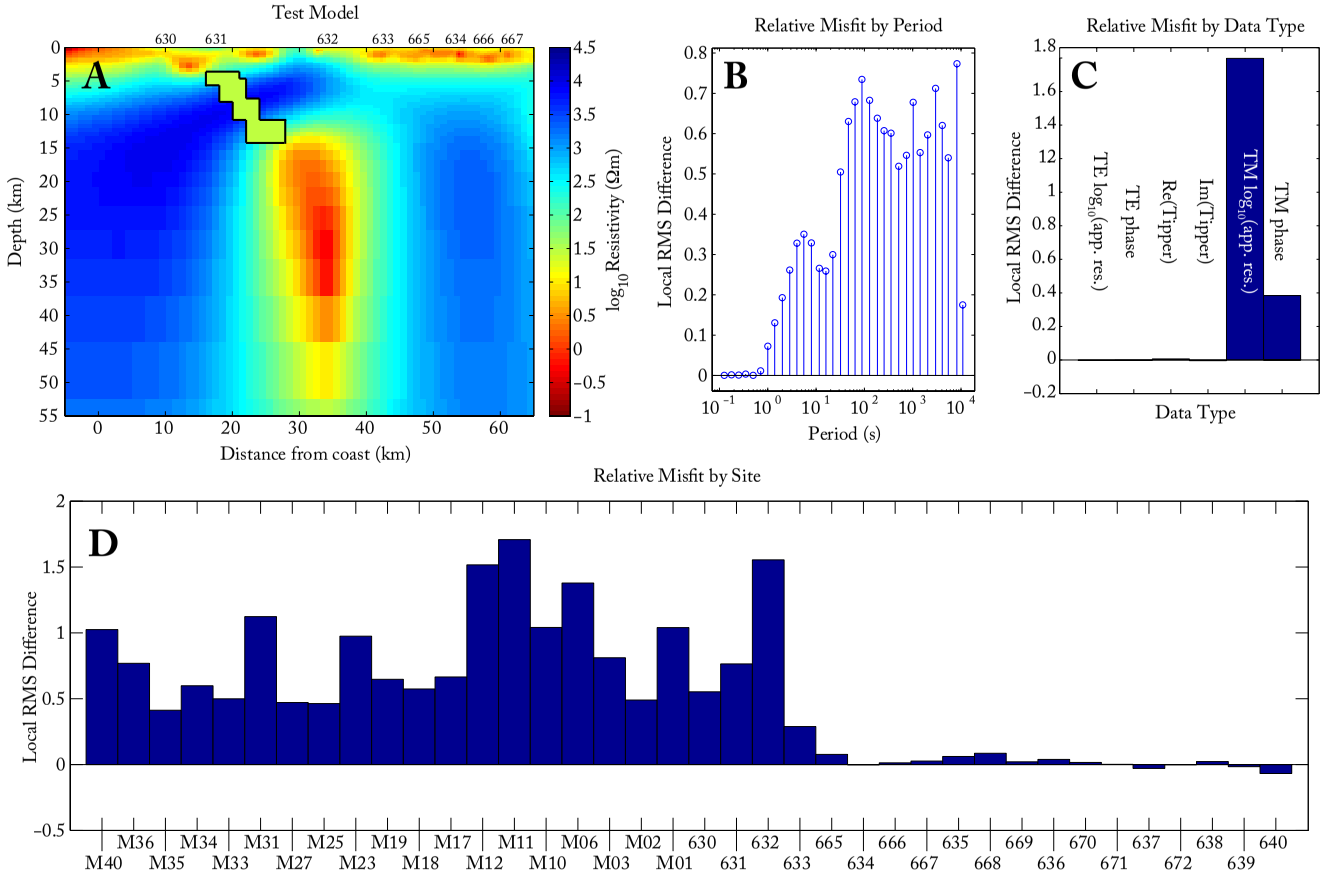

Figure 4.14: Misfit results for the test model pictured in **A**. The test model is exactly the same as Model 1 pictured in Figure 4.10 everywhere except in the region of 30 Ωm material outlined in black in **A**. The test model explores the data's sensitivity to a possible connection between the deeper conductor below site 632 and the shallow conductors below sites 630 and 631. The change in misfit due to the outlined region in the test model relative to the misfit of Model 1 is plotted in **B**, binned by period, **C**, binned by data type, and in **D**, binned by site. The overall RMS misfit of the test model is 1.79.

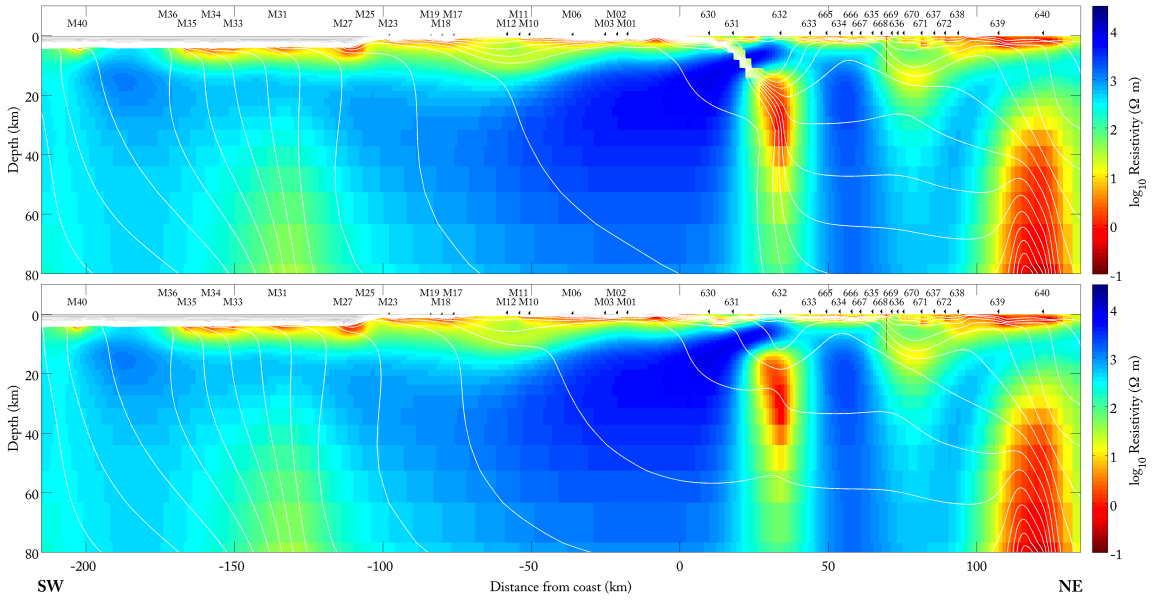

Figure 4.15: A comparison of the electric current density in the test model (above) and Model 1 (below) at an oscillation period of 128 s. The model-block resistivities are indicated in color, as in Figure 4.10. The white lines are streamlines of electric current density. Therefore, the closer the spacing of the white lines, the higher current density, and the lines point in the direction of current flow.

and phase of the fields are farther-reaching on the marine side of the coast than on the land side. This explains why the resistive boundary at the coast is mostly required by the marine data. In essence, the TM-mode coast effect gives the seafloor data enhanced sensitivity to the resistivity structure beneath the coast, even at sites over 200 km away. If the inversion of the land data demands the Rinconada conductor, then it is the marine data that require this conductor to be electrically isolated from the dense current distribution induced in the ocean. Such electrical isolation is achieved with the high resistivity material above and seaward of the Rinconada conductor.

Is electrical isolation required deeper below the continental margin? If the Rinconada conductor is to be a fluid reservoir, as suggested by Becken et al. [2011], one hypothetical origin of such fluids is the subducted oceanic crust, believed to underplate the continental margin and the continent west of the SAF [Trehu and Wheeler, 1987, Tréhu,

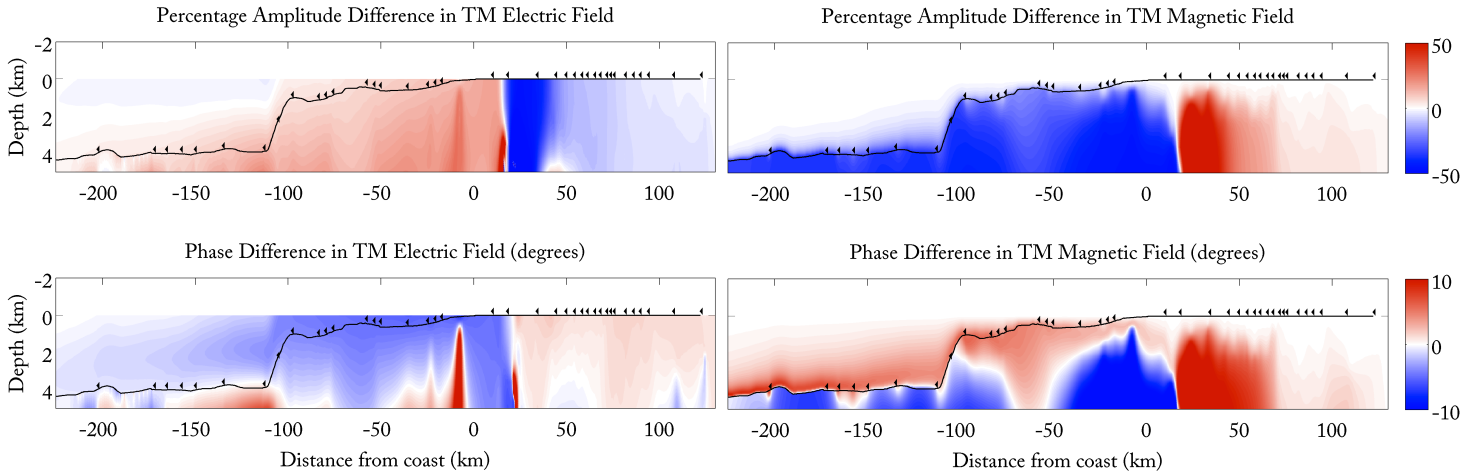

Figure 4.16: Plots of the changes in amplitude and phase of the TM-mode electromagnetic fields in Model 1 as a result of the test conductor (see Figure 4.14). The left column of plots shows the difference in electric fields, while the right column of plots shows the difference in magnetic fields. The upper row shows the percentage difference in amplitude between the fields of the two models, while the bottom row shows the phase difference between the fields of the two models.

1991, Meltzer and Levander, 1991, Miller et al., 1992, Howie et al., 1993, Henrys et al., 1993]. We use results from seismic imaging studies to place a conductive test region at the imaged boundary between the continental crust and the subducted oceanic plate, providing an electrical connection between the Rinconada conductor and the material below the continental margin (see Figure 4.17). The test model is a relatively conservative deviation from the final model, yet it has a significant effect on the misfits to all of the marine sites of data as well as the data from the land sites closest to the coast. Again, the change in misfit occurs almost entirely in the TM-mode data, reflecting that the mechanism for the marine data's sensitivity to this deeper electrical connection is very similar to that of the shallower connection in Figure 4.14. There is a defined peak at about 100 s in the periods affected by the test model, likely a function of the depth of burial and the thickness of the test conductor.

Next, we check whether the inversion process would allow a conductive connection below the coast, between the oceanic crust and the Rinconada conductor, if no regularization was applied to the sub-horizontal boundary between the continental crust below the margin and the oceanic crust just below it. One area where a sharp contrast in conductivity is expected is the boundary between the continental crust and the underplated oceanic crust. This boundary is characterized by a sharp increase in seismic velocity with depth as well as a sharp increase in density with depth [Howie et al., 1993]. The hypothesis we test here is that the smoothness constraint, when applied to a region where the conductivity of the actual earth is far from smooth, causes the inversion to compensate with unnatural structures like the Rinconada conductor and the highly resistive region above and to the southwest of it. Therefore, we remove, or "cut", the roughness penalty at the parameter block boundaries that lie along the plate interface as imaged by Howie et al. [1993]; the boundaries which have no roughness penalty are highlighted with white in Figure 4.18. The inversion with the penalty cut changes the shape of the shallow conductive section beneath the continental shelf; material of less than 100 Ωm fills the space between the seafloor and the penalty cut until about 10 km inland where is comes to an abrupt stop. The oceanic plate, below the penalty cut is very resistive (>5,000 Ωm) until about 20 km inland. A new conductor appears just below the coast, sitting atop the penalty cut, but is kept electrically

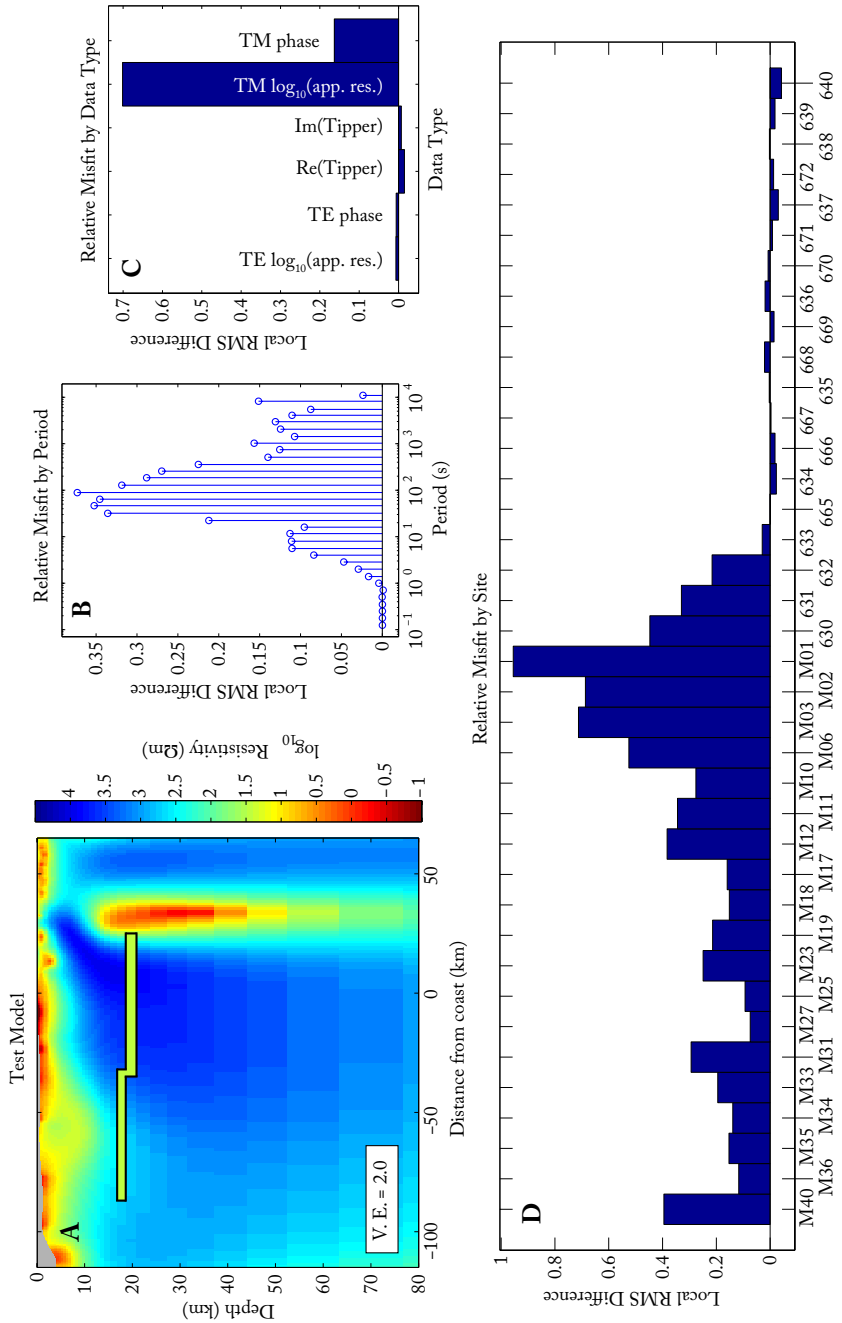

Figure 4.17: Misfit results for the test model pictured in **A**. The test model is exactly the same as Model 1 pictured in Figure 4.10 everywhere except in the region of 30 Ωm material outlined in black in **A**. The test model explores the data's sensitivity to a possible electrical connection between the lower-crustal conductor below site 632 and the conductivity structure below the continental margin. The change in misfit due to the outlined region in the test model relative to the misfit of Model 1 is plotted in **B**, binned by data type, and in **C**, binned by site. The overall RMS misfit of the test model is 1.46

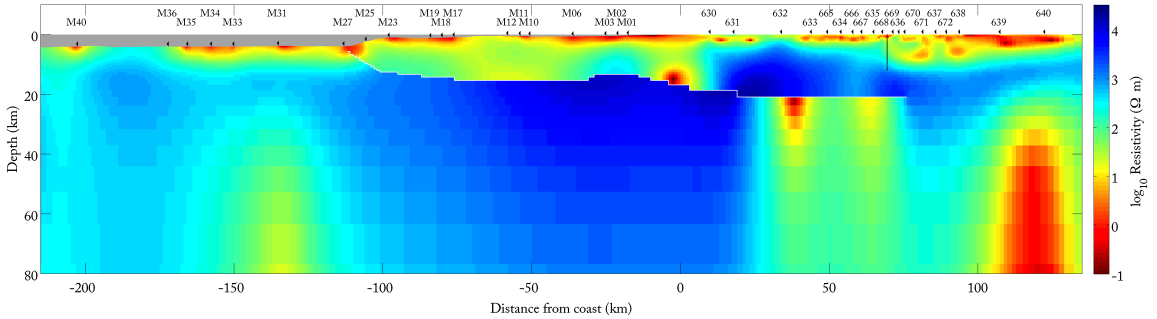

Figure 4.18: The final model result of a smooth 2D inversion where there is no roughness penalty applied across the cell boundaries highlighted in white. These boundaries lie along the top of the subducted oceanic plate as imaged by Howie et al. [1993]. The vertical black line plotted at 70 km from the coast is the approximate location and depth extent of the San Andreas fault.

isolated from the material to the northeast by the now familiar resistivity wall. A lower crustal conductor remains below site 632, but has has been pushed below the penalty cut into the proposed underplated crust, at a depth of about 22 km. The material just above the lower crustal conductor is now very resistive, as is the material below the 12 km under the SAF. The main conclusion derived from this test inversion is that, even with the added flexibility, the penalty cut inversion must place a resistive wall between the conductive material beneath the continental shelf and a landward conductor similar to the Rinconada conductor; the data adamantly demand that no electric current induced in the ocean be allowed to escape into the lower crust and mantle of the continent.

Now that we have made the case for electrical isolation between the continent and the electric current induced in the ocean, a question which naturally follows is whether the Rinconada conductor is required to be electrically connected to the shallow conductive material on the *inland* side of it. Model 1 has high resistivities to the southwest (seaward) of the Rinconada conductor, but to the northeast (inland), the connection between the Rinconada conductor and the shallow section is about 20 times more conductive (300 Ωm). We test the necessity for this lower resistivity and plot the results in Figure 4.19. The test model places a 3,000 Ωm lid atop and to the northeast of the Rinconada conductor. The effect of this test model on the misfit is much less dramatic than the previous test

conductor on the southwestern side. The overall misfit is practically unchanged by the test resistor, 1.301 relative to 1.30 for the final model. For some sites, frequencies, and data types, the local misfit is actually improved. Where the misfit is adversely affected by the test resistor, the magnitude of the local misfit difference is 50 times smaller than the same local misfit difference for the previous test conductor to the southwest (see Figure 4.14). Thus, we conclude that the somewhat conductive (100s of Ωm) connection between the Rinconada conductor and the shallow conductive structure in Model 1 is not significantly required by the data. Since the data lack significant sensitivity to this region, the inversion process elected to fill it with more conductive material to appease the demand for roughness minimization. The Rinconada conductor could possibly be electrically isolated from the conductive shallow crust on the northeastern side of it, just as it seems to be on the southwestern side.

Having established that the TM-mode coast effect in the marine data is the predominant constraint requiring high resistivity below the coast, we wish to know what independent inversions of just the land data, and just the marine data would produce. Figure 4.20 displays the inversion solution to just the land data (**A**), the final solution to all the data (**B**), and the inversion solution to just the marine data (**C**) for comparison. The inversion of the land data was able to reach a much lower level of overall misfit (0.90 RMS) than the inversion of all the data. This could be predicted with Figure 4.11, which shows that that the majority of the misfit produced by Model 1 derives from the marine sites. To compensate for this, we elected to have the inversion of the land data meet an RMS misfit tolerance of 1.00 so that the local misfits of the land sites approximately matched the local misfits of the lands sites from the inversion of all the data. The inversion of the marine data was kept at the prior RMS misfit tolerance of 1.30.

Figure 4.21 displays the difference in misfits achieved between the land-only inversion and the full data inversion. Even though the land-only inversion fits the land data better than the inversion of the full dataset, the land-only inversion seems to poorly resolve the size of the more prominent conductors on the land side of the two models. In the land-only model, the Rinconada conductor is much wider and its base extends deep into the mantle. The resolution of the Rinconada conductor achieved by our land-only

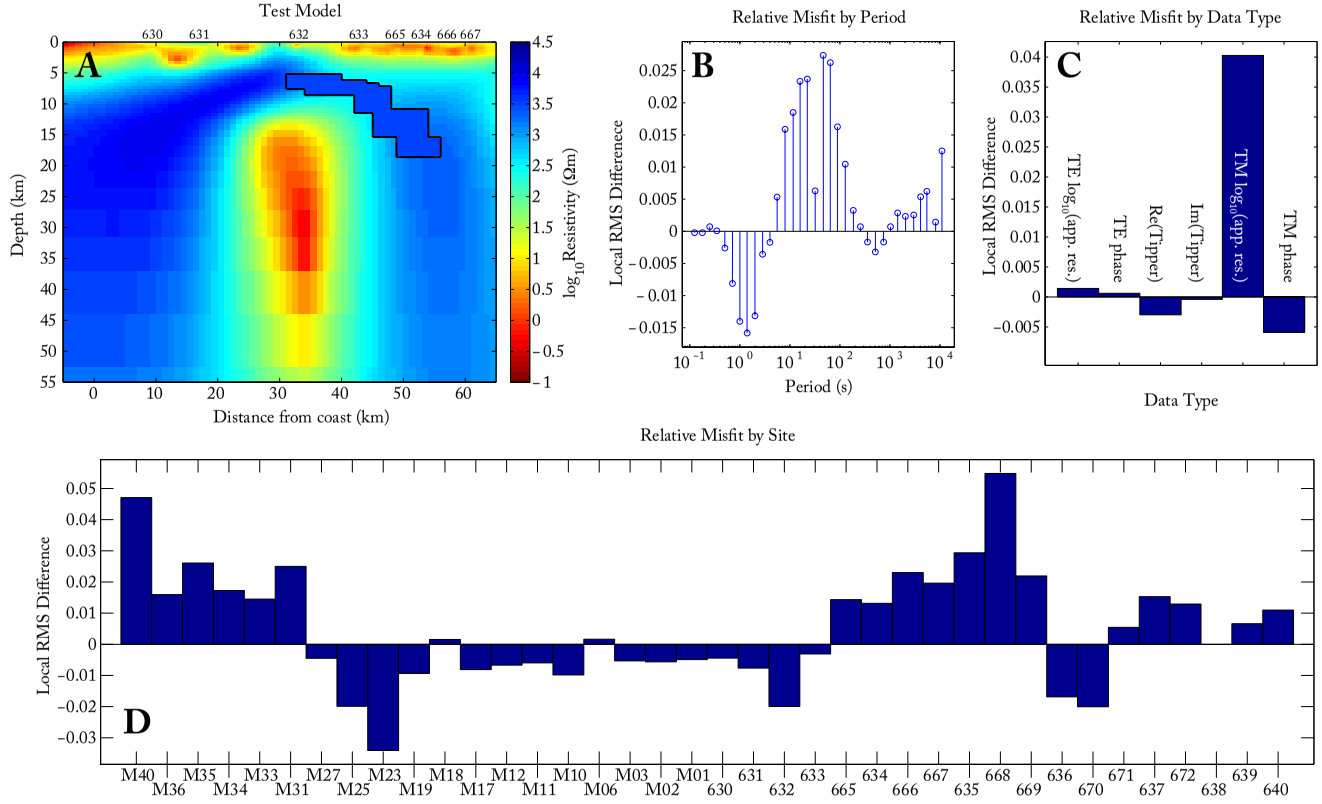

Figure 4.19: Misfit results for the test model pictured in **A**. The test model is exactly the same as Model 1 pictured in Figure 4.10 everywhere except in the region of 3,000 Ωm material outlined in black in **A**. The test model explores the data's sensitivity to an apparent connection, of ≈ 300 Ωm material, between the deeper conductor below site 632 and the shallow conductors below sites 633 and 665. The change in misfit due to the outlined region in the test model relative to the misfit of Model 1 is plotted in **B**, binned by period, in **C**, binned by data type, and in **D**, binned by site.

inversion qualitatively matches that presented in Becken et al. [2011], which uses the same data. Similar to the Rinconada conductor, the base of the conductor coincident with, and extending about 90 km to the northeast of the SAF is smeared downward into the deep mantle. This reinforces the popular idea that MT data lack sensitivity to the base of strong conductors. However, it is clear from the inversion of the full dataset, that the addition of marine data provides more rigorous constraints on the borders of some these landward conductors. Note that the inversion of solely land data allows for there to be extremely conductive material throughout the continental margin, seaward of the land data's aerial coverage. A comparison with the inversion of all the data, reveals that the emplacement of an overly conductive seafloor trades-off with the conductor on the NE end of the data profile, below the Great Valley of California (GV).

On a site-by-site basis, the inversion of marine data alone does significantly better at fitting the marine data, except for two sites close to the coast. In the marine-only inversion, an extremely resistive, vertical structure appears below these coastal sites. Such a resistor is needed to appease the more seaward marine sites whose TM-mode data, harkening back to Figure 4.14, require electrical isolation between the ocean and the continent. Since there are no constraints on land, the inversion has been able to place a near homogeneous wash of more conductive material (60-130 Ωm) there. It has been found in practice that 2D MT inversions have a tendency to place conductors on the edges of the extent of data coverage in a model; all of the models found in this dissertation are examples of that. We conjecture that this is a 2D inversion's way of fitting data that have distortions from 3D structures, such as curvature in the coastline. So, while the 2D inversion is inclined toward a conductive quarter-space on land, outside the aerial coverage of the marine data, the majority of marine data counter by requiring an insulating resistive wall at the coast. The data from two of the sites close to the coast object to the extreme structure built up below them, but they are outnumbered by the more seaward sites. Below the continental slope, at about 40 km depth in the model resulting from marine data alone, arises a spire-shaped region of higher conductivity material. The inversion of the full dataset also results in a conductor near the slope but it is much more diffuse and resides more toward the deep ocean. Again, there seems to be a trade-off with this sub-slope conductor and the conductor on the

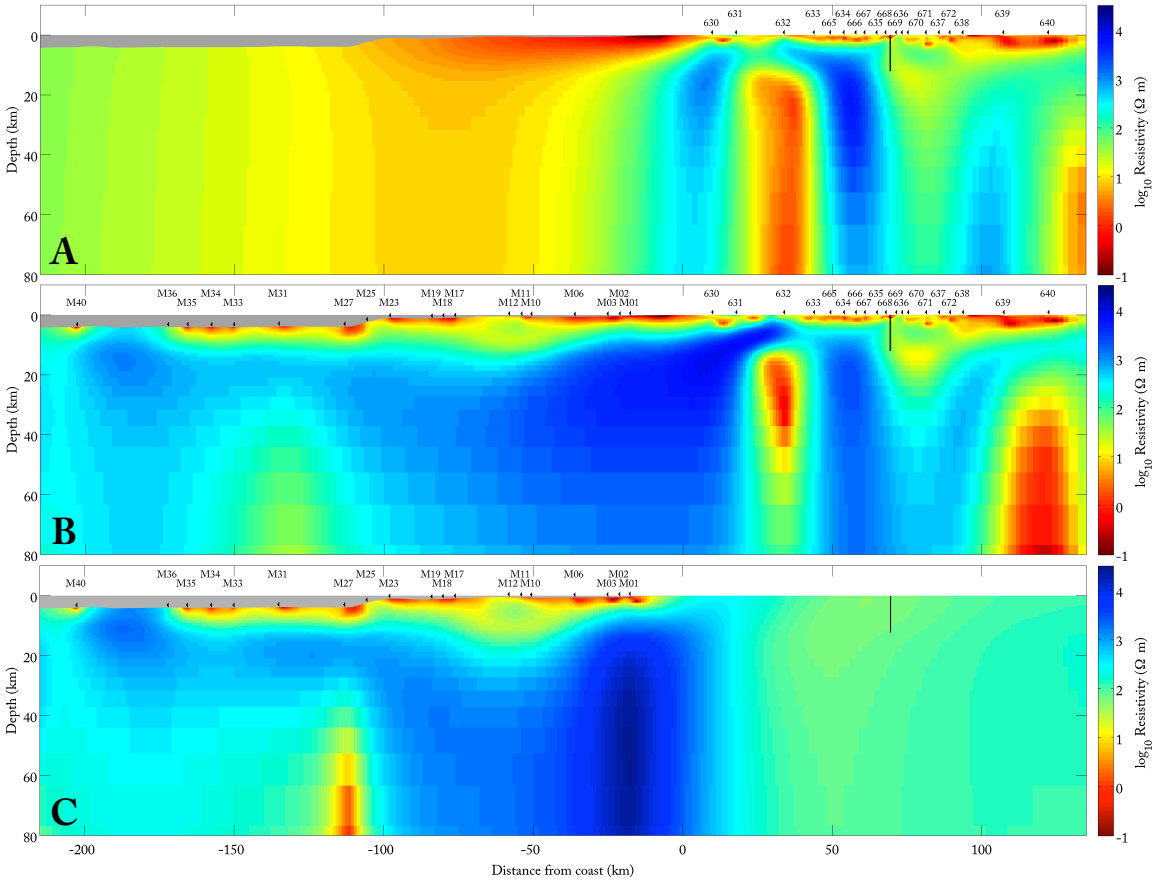

Figure 4.20: (**A**) the final model result of an inversion of only the land sites in the Estero MT dataset. (**B**) for comparison, Model 1, the result from inversion of both land and marine data. (**C**) the final model result for an inversion of only the marine sites in the Estero MT dataset

NE end of the data profile. In Section 6.2 we put forth the argument that these conductors are both artifacts resulting from the inversion's struggle to fit both the coast-effect and other 3D distortions in the data.

To gain insight into which data require the anomalous conductors found in Model 1, we again employ misfit analyses with test models. Within each of the four test models we replace one the four large anomalous conductors with the local background resistivity, so as to erase the effect of that conductor from the model prediction. The misfit to the

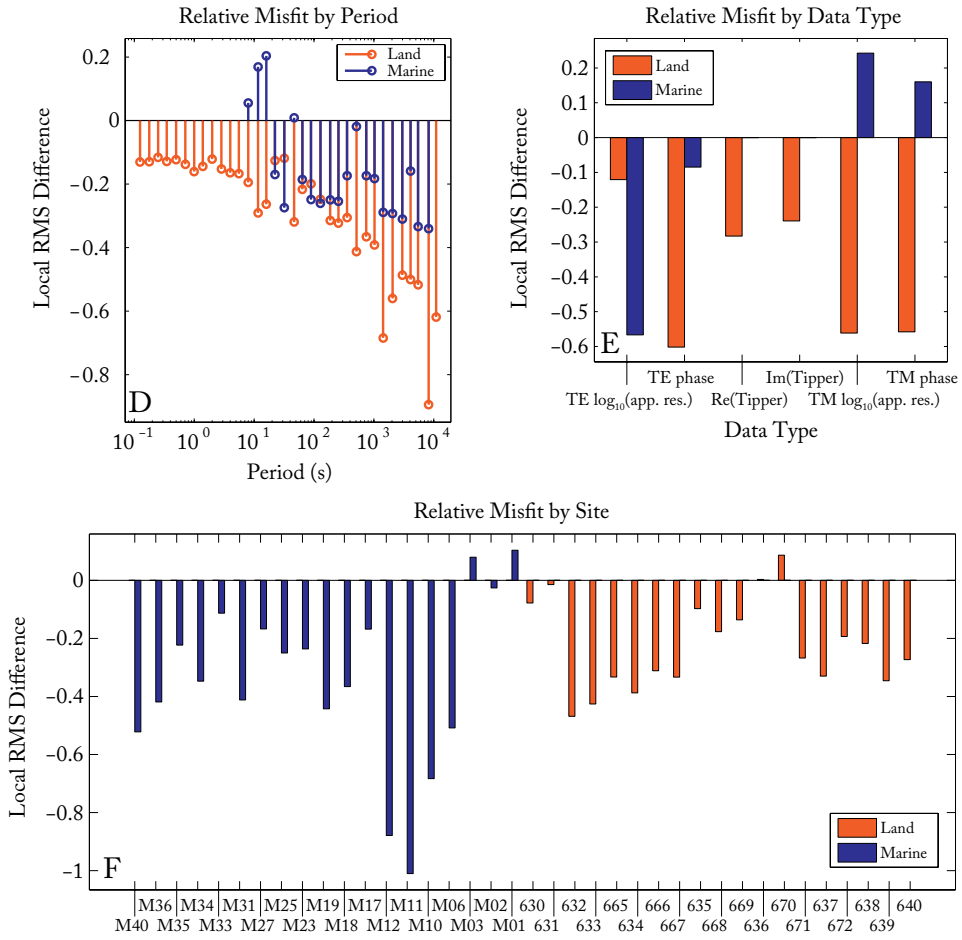

Figure 4.21: A breakdown of the differences in misfit resulting from the models in (**A**) and (**C**) of Figure 4.20, from inversions using only land data, and only marine data, respectively, relative to the misfit resulting from the model in (**B**) of Figure 4.20, from an inversion using both land and marine data. The misfit has been binned in three different ways: by period (**D**), data type (**E**), and site (**F**). The overall RMS misfit of the land-only inversion result is 1.00.

data is calculated for the "cleansed" model prediction, which is then compared to the misfit of Model 1. Figure 4.22 presents each of the four test models with the erased conductors labeled **A**-**B**. Note that the plots of the test models show a larger region of the model domain than what has been selected for interpretation (see Figure 4.10). With this wider view, we see that two very large and very conductive regions appear at each end of the

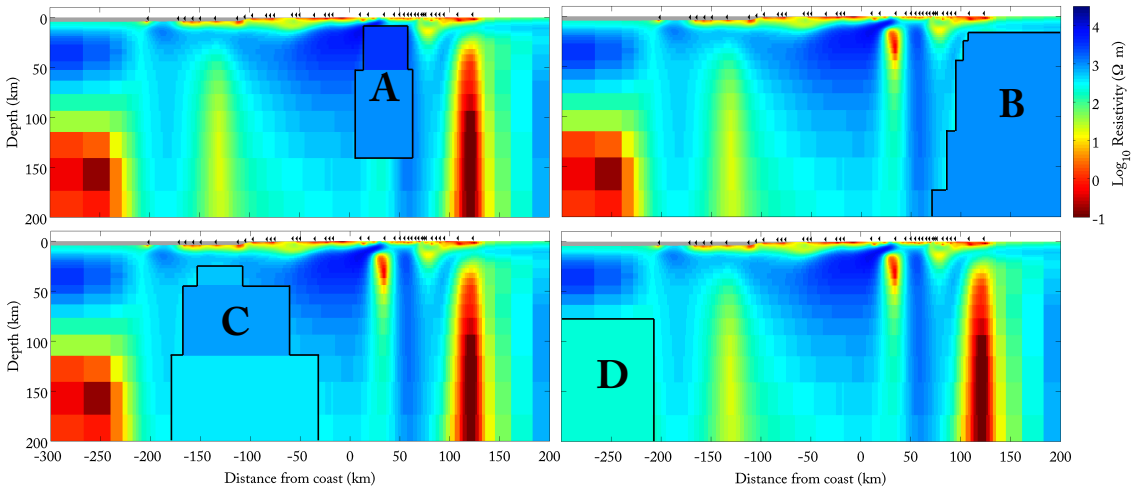

Figure 4.22: Four separate test models for testing data sensitivity to four highly conductive regions in the final inversion of Figure 4.10. The letters **A**-**D** label each of the tested regions, outlined with a black line. These letters correspond to the plots in Figure 4.25, which present the change in misfit caused by each of the test regions.

line of sites. These extreme conductors are not expected geologically and occur suspiciously at the edge of the resolvable portions of our model. We wish to know which data have demanded these implausible structures.

First, we analyze the requirement for the Rinconada conductor, labeled **A**. Figure 4.25 shows that the removal of conductor **A** causes a great increase in misfit to the tipper data, largely in the real and to a lesser extent in the imaginary component. The removal of conductor **A** also causes an increase in misfit to the TE mode apparent resistivity and phase, but this effect is at least 4 times smaller than the effect on the tippers. The TM mode data is practically unaffected. In general, it is the misfit to the land sites that is most affected by the removal of conductor **A**; all land sites, except the two furthest inland, experience an increase in misfit. Strangely, site 632, closest to conductor **A**, is no more affected than the sites further inland of it. This may be because it is missing its short period apparent resistivity data, a complication we revisit later. The greatest increase in misfit occurs at the two sites closest to the coast, 630 and 631. It is important to note that the misfit at many of the marine sites is improved, most appreciably at sites M06, M10, M11, and M12, when

conductor **A** is removed. Figures 4.23 & 4.24 show the model predictions for Model 1 and the model with conductor **A** removed along with the data from sites 630 and M11. Site 630 is the land site with the greatest increase in misfit resulting from the removal of conductor **A**, while site M11 is the marine site with the greatest decrease in misfit resulting from the removal of conductor **A**. Figure 4.23 shows that the fluctuations in the TE-mode apparent resistivity and phase of site 630 are actually poorly fit, even with conductor **A**, but this goes largely unnoticed in the misfit measure because of the inflated error bars. There is a bounded period range, between 10 and 6,000 s, over which the existence of conductor **A** is discernible, with peak sensitivity to conductor **A** at 400 s. In the Sections 6.1 we address the possibility that conductor **A** is caused by 3D land-side coast-effects, but the lowest period within our 3D modeling capabilities is 745 s.

Next, we test the need for the large upper-mantle conductor beneath the north-eastern edge of the line of sites, labeled **B**. In Figure 4.25, we see that the removal of this conductor adversely affects the misfit to nearly every site of data, especially 630 which is right at the coast, and M40 which is almost 350 km away. On average, this conductor is required more by the land sites, but the marine sites factor in as well. Conductor **B** is required by all data types to a noticeable degree, but the largest driver is again the tipper data. As expected given its depth of burial and deep extent, conductor **B** is a long period feature, affecting periods greater 100 s in an amount that increases with period. The fact that it occurs on the northeastern edge of the profile indicates that it might be related to the Great Valley (GV). The GV is filled with a thick layer of sediments, presumed to be conductive; the upper 3 km of Model 1 below sites 639 and 640 support the existence of 3 Ωm material. It is nearly a 2D basin, relative to the strike of our line of sites, except that it is truncated on its southwestern end by the Tehachapi mountains, only 140 km from site 640. This closure of the basin may produce 3D effects that occur predominantly at long periods and in the tipper data; we explore this possibility with 3D modeling in the Section 6.1.

Though large in size, conductor **C** is not terribly conductive; the lowest resistivity found in the region of **C** is 18 Ωm. It may then be expected that this subtler of the four anomalies is the one most tenuously required by the data. Its removal produces negligible

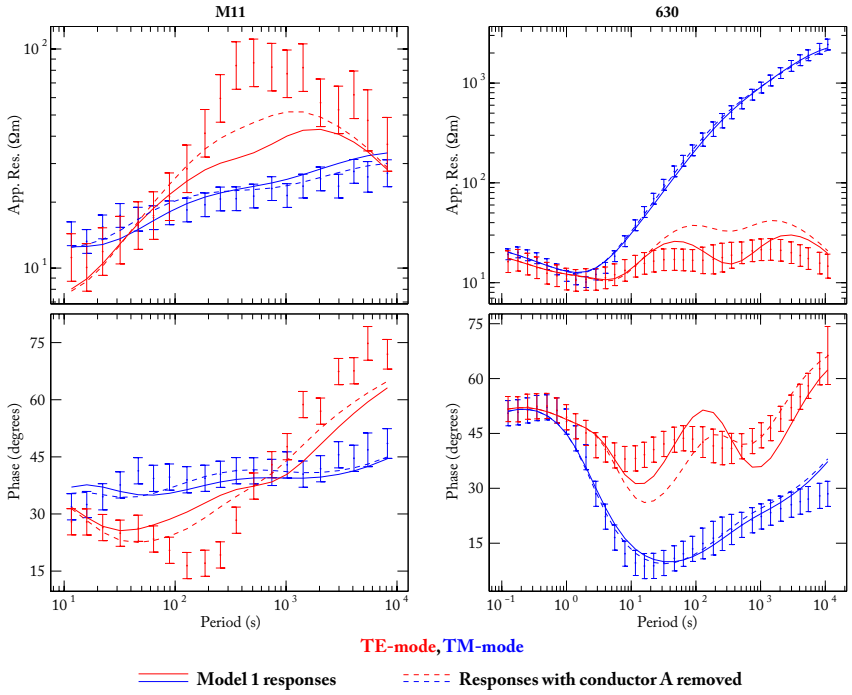

Figure 4.23: Plots of MT apparent resistivity and phase data along with the respective model predictions for two models: solid lines are from Model 1 of Figure 4.10, and dashed lines are from the model with conductor **A** removed (see Figure 4.22). Two sites of data are plotted: M11, the site with the greatest decrease in misfit due to the removal of conductor **A** and 630, the site with the greatest increase in misfit due to the removal of conductor **A**. The TE-mode data are plotted in red and the TM-mode data are plotted in blue.

effects in misfit for all but a few of the marine sites; namely M36, M34, M12, M11, and M10, in order of decreasing change in misfit. Site M40's misfit is noticeably improved. The increase in misfit peaks at a period of 745 s, and, somewhat non-intuitively, shows up only in the TE phase and TM apparent resistivity data. Altogether, conductor **C** is not firmly supported by the data, and may be a result of the inversion's struggle to fit sites M36, M34 and M12, which, with respect to the final inversion model, are among the top 5 sites in terms of misfit (see Figure 4.11).

Finally, we analyze the requirement for the southwestern-most conductor, labeled **D**. It is the largest in our model, albeit it lies entirely outside the horizontal range of the

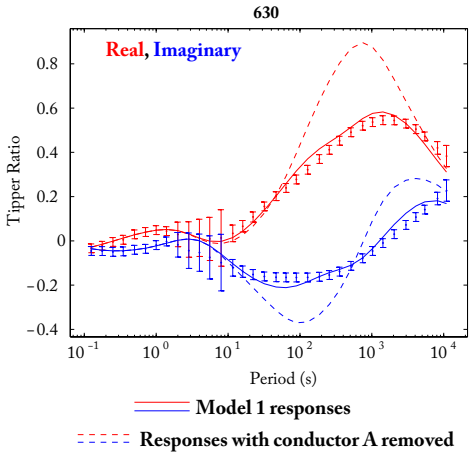

Figure 4.24: Same as Figure 4.23 except that the real (red) and imaginary (blue) tipper ratios are plotted.

measurement sites. Such qualities makes this conductor uninterpretable and highly suspect. However, we must ensure that it is not affecting the fit to the data in a significant way, else it might be compensating for other portions of the model which we *do* intend to interpret. Figure 4.25 shows that the absence of conductor **D** produces a greater effect in the overall misfit to the data than does the absence of conductor **C**. The removal of conductor **D** adversely affects the misfit of all of the marine sites, but mainly those farthest from the coast, particularly M40, M36, M35, and M34. Again, these are the sites of data that the inversion struggled most to fit. The difference in misfit grows with distance seaward from the coast. Also, the removal of conductor **D** has the greatest effect on TE phase, and, to lesser degrees, TE apparent resistivity, and TM apparent resistivity.

Since the tippers supply the majority of the weight behind the existence of conductors **A** and **B**, we test whether an inversion that does not use tipper information would reproduce similar extreme conductors. The final model of a the tipper-free inversion is presented in Figure 4.26. Note, that since tipper data only existed on land, their exclusion implicitly shifts more weight toward fitting the marine data than do the previous inversions of all data. Without the tipper data, the Rinconada conductor has vanished. The deeper conductor below the GV has been moved off the northeastern edge of the data profile, barely

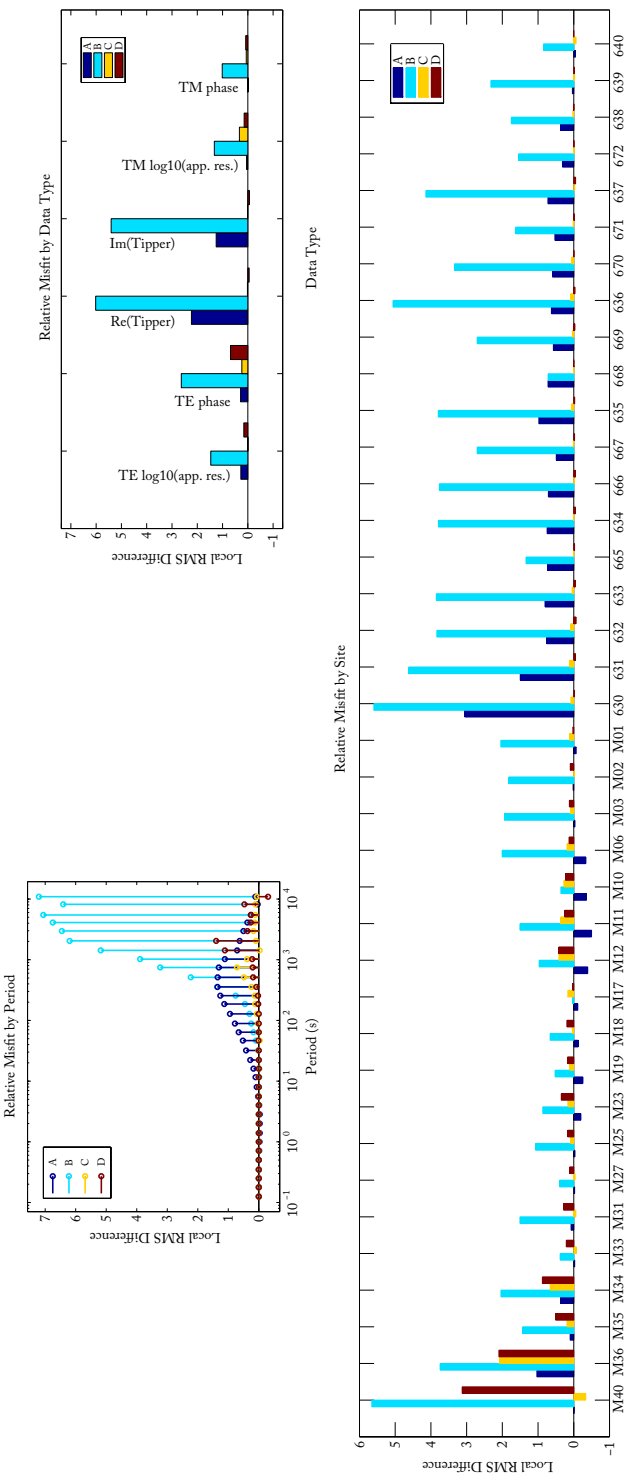

Figure 4.25: Misfit results for the four test models pictured in 4.25. The changes in misfit due to the outlined regions in the four test models relative to the misfit of Model 1 are plotted binned by period (upper left), binned by data type (upper right), and binned by site (below). The overall RMS misfits for the test models are: 1.91 (**A**), 4.20 (**B**), 1.43 (**C**), and 1.55 (**D**).

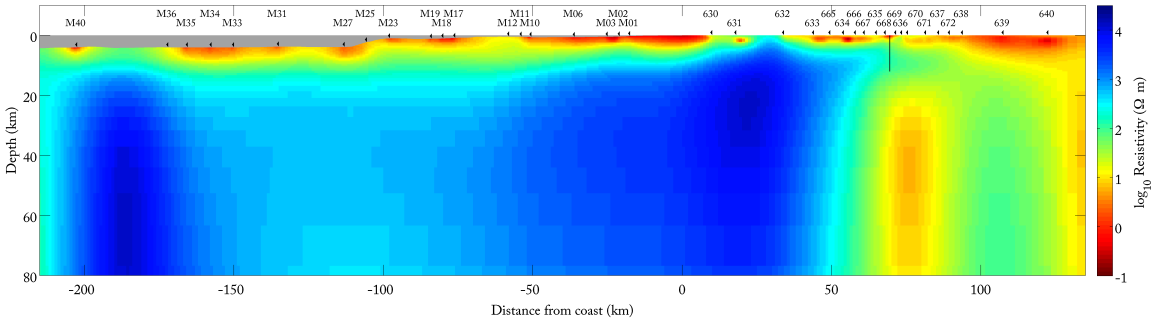

Figure 4.26: (**A**) the final model result of a smooth 2D inversion where none of the tipper data was used. (**B**) Model 1, the result of a smooth 2D inversion of all of the data. The vertical black lines plotted at 70 km from the coast is the approximate location and depth extent of the San Andreas fault.

visible in Figure 4.26. A new prominent conductor has appeared just to the northeast of the SAF at a depth below 20 km. This conductor is only about 7 Ωm, more than an order of magnitude more resistive than the Rinconada conductor. The tipper-free inversion, after many iterations of no progress, reached a minimum in RMS misfit at 1.55. The RMS misfit for Model 1, if excluding tipper data from the misfit calculation, would be 1.39, lower than was achieved by the tipper-free inversion. Figure 4.27 shows that the tipper-free inversion does worse at fitting the deep marine sites, with the degree of misfit growing with distance from the coast. The land site that is fit worse by the tipper-free inversion is 632, the one directly above the Rinconada conductor in our final model. Figure 4.28 presents the model predictions for Model 1 and the model produced by excluding tipper data from inversion, along with the data from sites 632 and 633. As an aside, we must point out that the data in the gray region of site 632 in Figure 4.28 were not used in any of the inversions due to the discontinuous shift at about 20 s period. The data were delivered with this glitch from our colleagues who conducted the land MT data collection. The glitch splits only the apparent resistivity data into two continuous sections, short-period and long-period. We chose to use only the long-period section because they are comparable to the same data at neighboring sites, whereas the short-period section is not. In Section 6.2 we restore the omitted section of data in our synthetic studies to ensure that this gap in data coverage isn't the root cause for the Rinconada conductor. Nonetheless, that is not too great of a worry

as we have shown that the Rinconada conductor improves the misfit at many other sites in the Estero MT dataset. Furthermore, Becken et al. [2011] showed that a similar conductor is required by the other profiles of land data which lie parallel to the one we analyze in this dissertation. Continuing, there is little difference between the two model predictions in the TM-modes of Figure 4.28. Yet, the TE-modes show large deviations between the two models at periods above 30 s, with the no-tipper model making a poorer match to the data. Note, however, ignoring the large error bars for a moment, that neither model does well at fitting the long-period TE-mode data at either of the two sites. In contrast, site 630 and a few of the marine sites on the continental shelf are better fit when tippers are not used. Figures 4.29 & 4.30 present the same model predictions for data from sites 630, M11, M06, and M18. The TE-mode data from sites M06, M11, and M18 benefit significantly from the preference of the tipper-free inversion for resistive material below 15 km and within $\pm$50 km horizontally of the coast. An assessment of the fits in Figures 4.23, 4.29, and 4.30, implies that the data from the continental shelf sites are not consistent with the Rinconada conductor. Note that the period range exhibiting the greatest misfit in TE-mode apparent resistivity in Figures 4.29 & 4.30 corresponds to the period range of the relative misfit increase due to the removal of conductor **A** in 4.25.

On average, the marine sites of data closest to the coastline are better fit by the no-tipper inversion, while the marine sites furthest from the coast experience a degradation in fit (see Figure 4.27). The story is the opposite on land; the sites of data closest to the coast are fit worse by the no-tipper inversion, while the sites furthest inland fare better without tippers. Such odd symmetry in misfit about the coastline suggests that there is some form of data distortion related to the coast, which a smooth 2D model is unable to fit. The distortion seems to be satisfied with opposing measures on either side of the coast by the 2D inversion of all the data. On the land side the Rinconada conductor is produced, whereas, on the marine side, great lengths are taken to neutralize the effect of the that conductor. An obvious candidate for a distortion that has opposing effects on the land and marine sides of the coast is 3D bathymetry and coastlines. Therefore, we investigate the possible effects of 3D bathymetry in Chapter 6.

As a final illustration of the obstacle posed by coast effects in the Estero MT

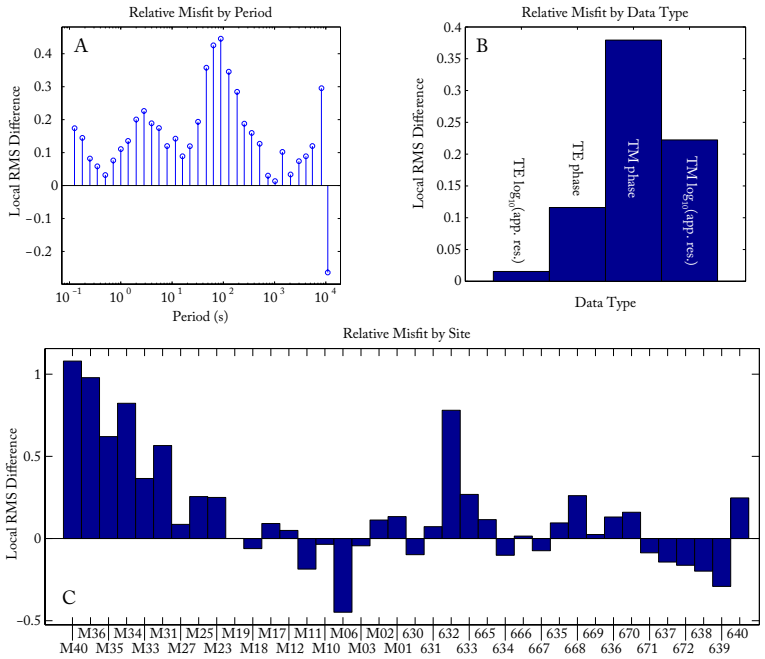

Figure 4.27: A breakdown of the differences in misfit resulting from the model achieved without using tipper data (see Figure 4.26) relative to the misfit resulting from an inversion using all data. The misfit has been binned in three different ways: by period (**A**), data type (**B**), and site (**C**). The overall RMS misfit of the inversion which excludes tipper data is 1.55.

dataset, we perform an inversion of only the TM-mode apparent resistivity and phase data. There is a conventional belief that the TM-mode is less susceptible to the distortions caused by 3D conductive structures [e.g. Berdichevsky et al., 1998]. The TE-mode suffers more from 3D distortion because, unlike the TM-mode, a 2D TE-mode calculation has no means of replicating the galvanic effects which only bleeds into the TE-mode with 3D anomalous bodies. For this reason, when 3D resistivity structures are suspected, yet only a 2D inversion process exists, or only a 2D model is desired, the TM-mode data are often preferred as the more robust choice for inversion. While the TM-mode has little sensitivity to small conductive bodies, it is generally found through synthetic studies that a TM-mode-only inversion recovers the average background resistivity (see Figure 4.31). It is well-acknowledged that the TM-mode in a 2D sense is greatly affected by large horizontal discontinuities in re-

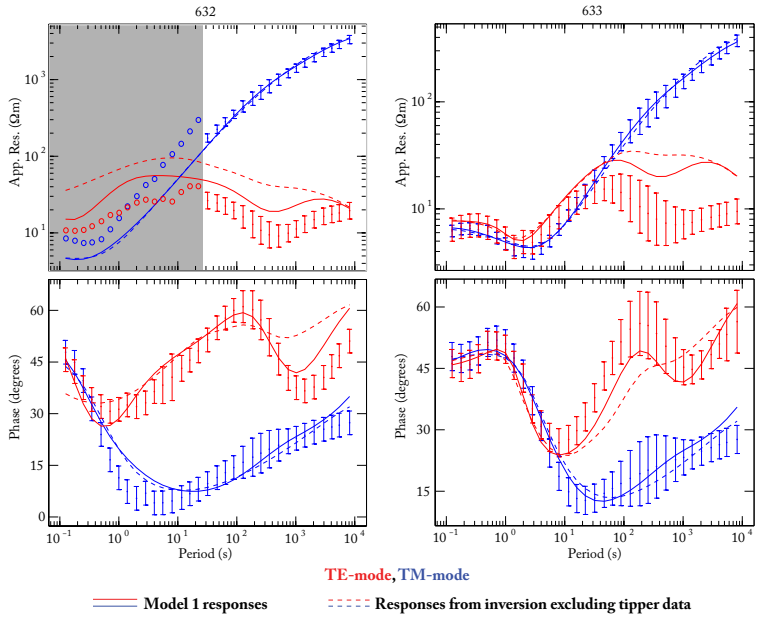

Figure 4.28: Plots of MT apparent resistivity and phase data along with the respective model predictions for two models: solid lines are from Model 1 of Figure 4.10, and dashed lines are from the model resulting when no tipper data is used (see Figure 4.26). The TE-mode data are plotted in red and the TM-mode data are plotted in blue. The gray region encloses apparent resistivity data (circles) which were excluded from inversions due to the discontinuous shift in the data.

sistivity, such as a linear coastline; we have provided ample illustrations of such behavior in this section. Thus, the coast and seafloor boundaries must be well represented in the fixed structure of a 2D inversion. However, it is assumed that the more subtle variations from the 2D representation of a coast, such as slight curvature in it, have a small relative effect on the TM-mode. The final model from a TM-mode-only inversion of the Estero MT data implies that this is not the case (see Figure 4.32); either that, or the 2D inversion algorithm is simply unable to reproduce an actual 2D structure within the earth, presumably because it has become stuck in a local minimum. The TM-mode inversion creates an oceanic lithosphere of less than 100 Ωm, over two orders of magnitude more conductive than predicted by laboratory data and CSEM measurements [Heinson and Constable, 1992]. Despite the overly conductive oceanic lithosphere, notice the ever-persistent high-resistivity

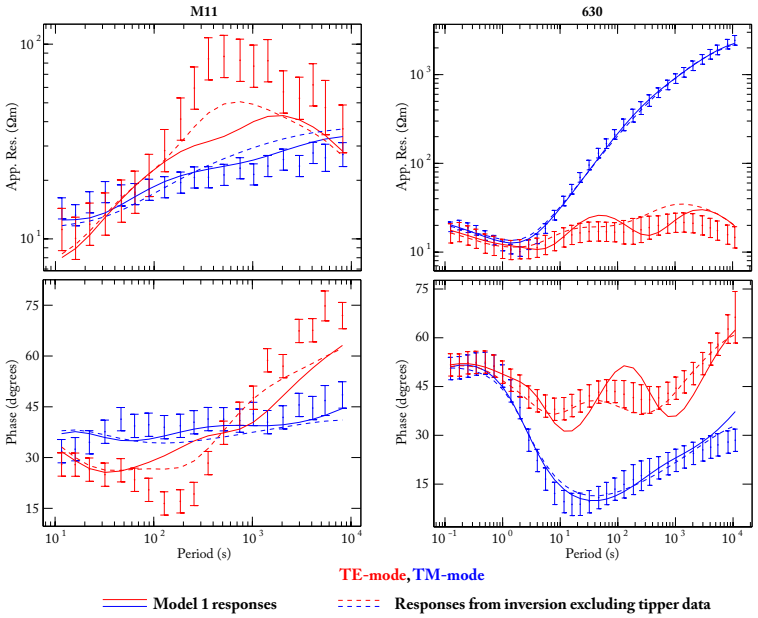

Figure 4.29: Plots of MT apparent resistivity and phase data along with the respective model predictions for two models: solid lines are from Model 1 of Figure 4.10, and dashed lines are from the model resulting when no tipper data is used (see Figure 4.26). The two sites of data, M11 and 630, are plotted here for comparison with Figure 4.23. The TE-mode data are plotted in red and the TM-mode data are plotted in blue.

deep structure beneath the coast. In addition, the TM-mode inversion places very resistive (10,000 Ωm) shallow material below sites M03, M02, M01, contrary to the expectation of conductive sediments just below the seafloor near the coast. The Rinconada conductor is absent, as would be expected; we have already shown that removal of the Rinconada conductor affects almost exclusively the fit to the TE-mode data (impedance and tipper). In all, the TM-mode inversion creates a model that is highly unlikely given other geophysical and geological knowledge. We conjecture that a TM-mode-only inversion cannot be relied upon to deliver meaningful results when coast effects are prominent. Yet a synthetic study shown in Figure 4.31 indicates that such an erroneous model would not result if the real world were characterized by a relatively simple 2D model; either our real-world example derives from a more complicated 2D model (i.e., rougher than the algorithm would prefer), or it does not derive from a 2D model at all. In Sections 6.1 & 6.2 we perform synthetic

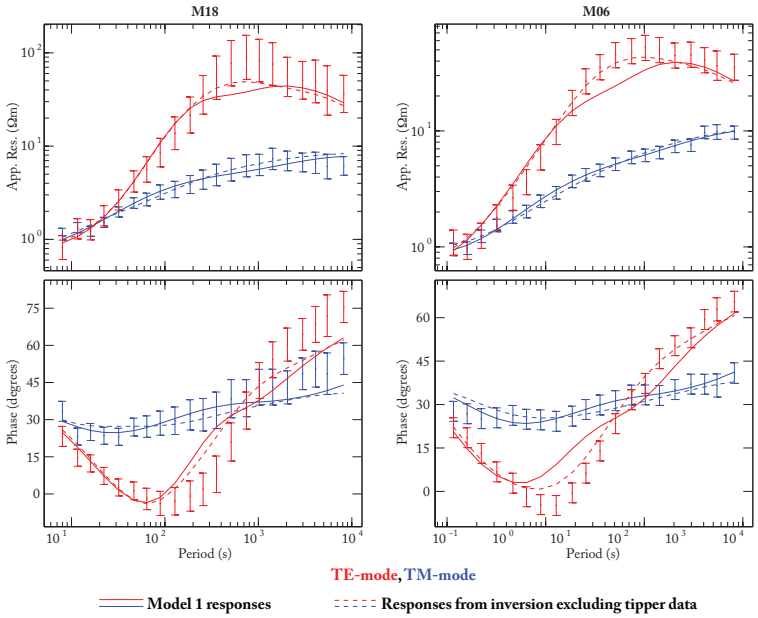

Figure 4.30: Plots of MT apparent resistivity and phase data along with the respective model predictions for two models: solid lines are from Model 1 of Figure 4.10, and dashed lines are from the model resulting when no tipper data is used (see Figure 4.26). The two sites of data from the continental shelf, M06 and M18, are plotted here. The TE-mode data are plotted in red and the TM-mode data are plotted in blue.

studies that are more in line with what is known about the oceanic lithosphere to discern whether the exotic structures in TM-mode model and in Model 1 are a result of our 2D inversion algorithm, 3D bathymetry, or both.

In summary, we have found that the marine TM-mode data impose a strong demand for electrical isolation between the shallow conductors on the continental shelf and the deeper Rinconada conductor (conductor **A**). The oceanic plate beneath the continental shelf appears to be highly resistive, but overlaid by more conductive material. If the deep crust is truly conductive on the land side of the coast, our inversions establish that it must be electrically isolated from the lower crust seaward from it. The Rinconada conductor is required predominantly by the tipper data, and almost exclusively by the land sites. A separate inversion that excluded the tipper data did not reproduce the Rinconada conductor, but instead placed a slightly less conductive plum-like structure below and to the *northeast*

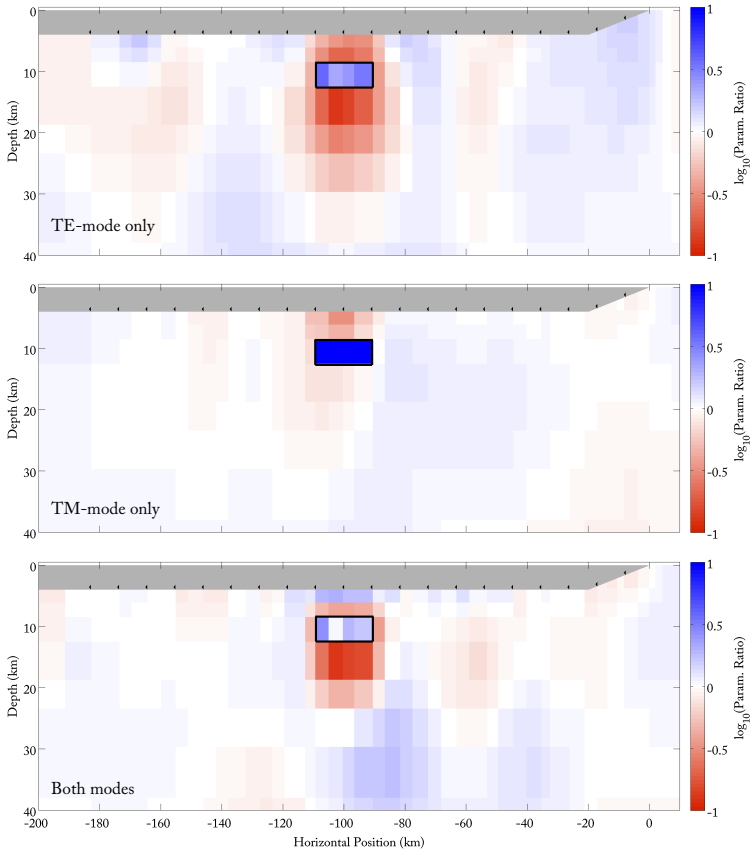

Figure 4.31: Synthetic 2D inversion studies analyzing the use of the separate modes of MT data (10% errors added to create synthetic data). The synthetic model is equivalent to that in Figure 4.8, but has embedding within a 100 Ωm background a conductive block (outlined in a thick black line) of resistivity 5 Ωm. The TE-mode only does well at recovering the anomalous block's resistivity, but worse at recovering the uniform background resistivity. The TM-mode only does well at recovering the uniform background resistivity, but worse at recovering the anomalous block resistivity (it makes the anomalous block 65 Ωm). The use of both modes recovers the anomalous block resistivity the best, and does quite well with the background resistivity, except that it smears the conductive block downward.

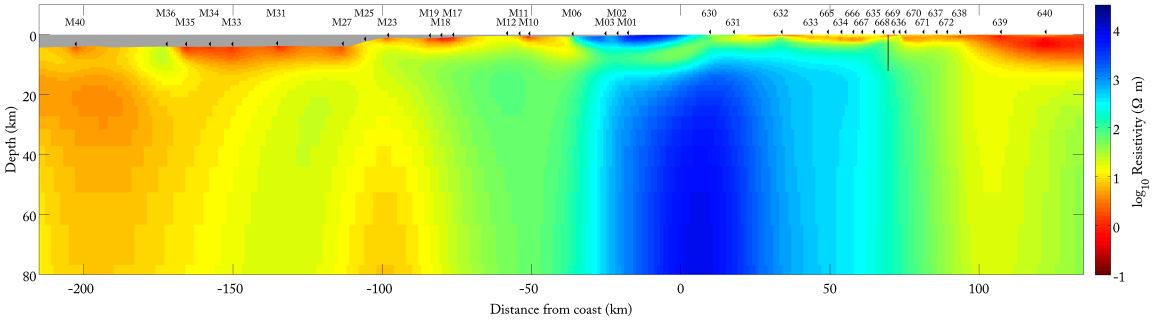

Figure 4.32: The final model result from the inversion of only the TM-mode data from the Estero MT dataset. The inversion reached an RMS misfit of 1.00.

of the SAF. A number of the marine sites on the continental shelf improve in misfit when the Rinconada conductor is removed. An inversion of marine data only does not require a localized conductor on the land side of the model. In Section 6.2, we analyze how sensitive the marine data on their own are to a conductor like the the Rinconada conductor. The deep conductor below the GV (conductor **B**) affects nearly all the sites, but more so the land sites, as would be expected given its location. Conductor **B** is also heavily driven by the tipper data, but by longer periods than the Rinconada conductor. The conductors below the marine side of the model (conductors **C** & **D**) both affect only a few of the marine sites to any significant degree, and affect mostly the sites furthest from the coast.

Chapter 5

Electromagnetic Modeling Using a Thin Sheet

This chapter develops the theory for the incorporation of a thin sheet of variable conductance in electromagnetic modeling. The thin-sheet construct is useful for modeling earth conductivity structures which are predominantly one-dimensional (1D) along the vertical direction, but have a single confined depth range within which three-dimensional (3D) conductivity structures occur. If that confined depth range is deemed small based on relative length-scale arguments, a representation of these 3D structures by an infinitesimally-thin sheet at a single depth produces a close approximation to the electric and magnetic fields of the true model. The zero-thickness sheet is placed at a single depth but has a conductance equal to the vertically integrated conductivity of the depth range it represents, effectively mapping 3D conductivities into a 2D conductance in a horizontal plane (see Figure 5.1).

The thin-sheet method applied to modeling geo-electromagnetic induction was developed in a series of papers written a few decades ago [Vasseur and Weidelt, 1977, Dawson and Weaver, 1979, McKirdy et al., 1985]. More recently, a new method of solution for a thin sheet model, which takes place in the Fourier domain, was introduced by Parker and Wheelock [2012]. The new method confers faster computations and better convergence properties for the thin sheet problem than the previous treatments. The following theoretical develop-

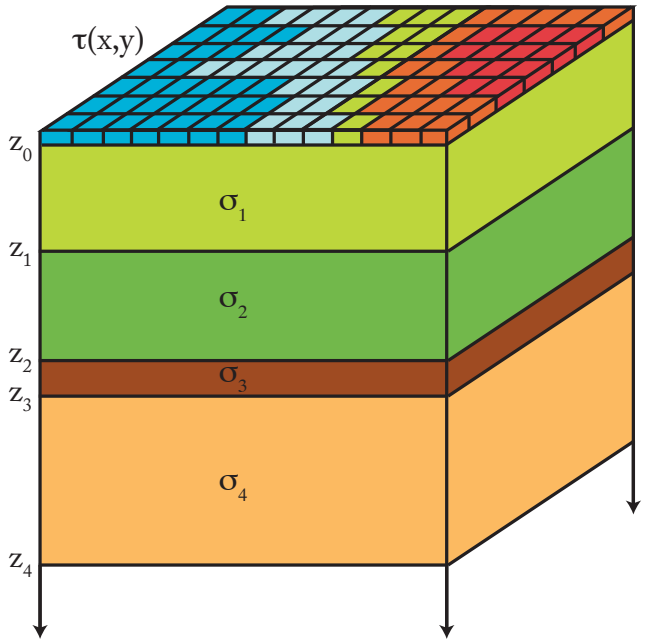

Figure 5.1: An illustration of the model with layers of uniform conductivity, σ_n, below a thin sheet of 2D varying conductance, $\tau(x, y)$.

ments will borrow from these prior works, but also will expand the theory into new territory which includes anisotropic conductivity, layers above the thin sheet, and non-planar sources (e.g. electric and magnetic dipole currents). Finally, this chapter will introduce some intriguing, measurable quantities that precipitate from a spatial Fourier domain analysis of the electric and magnetic fields, and discuss their implications and potential use.

A central goal of the theoretical development in the current chapter is to derive equations for the horizontal magnetic fields above and below the thin sheet that depend only on the horizontal electric field. The motivation behind this quest is the boundary condition for the horizontal magnetic fields across a surface current. The current in a thin horizontal surface is only dependent upon two things, the electric field within the thin sheet, and the conductance of the thin sheet. By using the boundary condition for the horizontal magnetic

fields and the sought-after equations relating the horizontal magnetic fields to the horizontal electric fields, an integral equation dependent only on the electric field in the thin sheet can be assembled. After solving this integral equation for the horizontal electric field in the thin sheet, all other electric and magnetic field components above and below the thin sheet can be found. The remainder of the chapter chapter will follow the logical progression of first deriving the equation relating the horizontal magnetic field to the horizontal electric field below the thin sheet, at the top of a stack of conducting layers, then do the same for the space above the thin sheet, at the base of a stack of conducting layers, and finally modify these derivations to add electric and magnetic source currents within the stack of layers.

5.1 A Thin Sheet atop a Stack of Anisotropic Layers

The model of the earth we will use starts with a stack of N layers underlain by a halfspace. Each of these regions has a uniform, tri-axially anisotropic conductivity, with one of the principal axes of the conductivity tensor aligned with the vertical direction. This sort of conductivity tensor is given by,

$$\underline{\sigma} = \begin{bmatrix} \sigma_{xx} & \sigma_{xy} & 0 \\ \sigma_{xy} & \sigma_{yy} & 0 \\ 0 & 0 & \sigma_{zz} \end{bmatrix}. \tag{5.1}$$

The underline on Greek characters denotes a tensor quantity. Other tensor quantities will be designated by upper-case, sans-serif English characters. Notice the conductivity tensor is symmetric and therefore there also exist principal axes in the horizontal plane such that, when rotated into the reference frame of the these principal axes, the conductivity tensor is made diagonal. We define ϑ as the angle between the horizontal principal axes and the horizontal coordinate axes, and the rotated conductivity tensor takes the form,

$$\underline{\sigma}^{\vartheta} = \mathbf{R}(\vartheta)\underline{\sigma}\mathbf{R}(\vartheta)^T = \sigma \begin{bmatrix} 1 & 0 & 0 \\ 0 & \lambda & 0 \\ 0 & 0 & \nu \end{bmatrix}. \tag{5.2}$$

In the previous equation, we have introduced the horizontal rotation matrix, $\mathbf{R}$, and the ϑ superscript to denote a quantity rotated into the reference frame of the horizontal principal axes. Later, we will use another definition, the sub-tensor of anisotropic conductivity in only the horizontal directions, which we write as,

$$\underline{\check{\sigma}} = \begin{bmatrix} \sigma_{xx} & \sigma_{xy} \\ \sigma_{xy} & \sigma_{yy} \end{bmatrix}. \tag{5.3}$$

The stack of layers is overlain, at $z_0 = 0$, by an infinitesimally thin sheet of anisotropic conductance,

$$\underline{\tau}(\mathbf{r}) = \begin{bmatrix} \tau_{xx}(\mathbf{r}) & 0 \\ 0 & \tau_{yy}(\mathbf{r}) \end{bmatrix}. \tag{5.4}$$

Note that $\underline{\tau}$ is defined here as diagonal. The conductance tensor of an anisotropic thin sheet is also symmetric, so we pose this entire problem pre-rotated into the reference frame of the principal axes of the conductance tensor, $\underline{\tau}$. The parameters σ, λ, ν, and ϑ are constant within their respective layers, but τ_{xx} and τ_{yy} may vary in the horizontal plane.

The derivation of the magnetotelluric (MT) response over this model starts with dimensionless quasi-static Maxwell's equations for the electric and magnetic field, $\mathcal{E}$ and $\mathcal{B}$, respectively, which can be found in (3.1) of McKirdy et al. [1985] (henceforth MWD). These equations hold within the n^{th} conductive layer. Also note that these equations have been Fourier-transformed along the time axis, and thus already lie in the frequency domain. To make these equations dimensionless we make the following adjustments: conductivity is scaled by some characteristic conductivity σ_*, which is normally chosen to be the conductivity of the first layer below the thin sheet; length scales are normalized by the characteristic skin depth, d_*, given by $\sqrt{2/\mu_0\omega\sigma_*}$, where μ_0 is the magnetic permeability of free space, and ω is the angular frequency of the inciting energy, oscillating in time as $\mathrm{e}^{i\omega t}$; conductance is scaled by $\sigma_*\mathrm{d}_*$; $\mathcal{B}$ occurs in units of B_*, the magnitude of the driving magnetic field; and $\mathcal{E}$ occurs in units of $\omega\mathrm{d}_*B_*$. We restate equations (3.1) of MWD here with the exception of

(5.6) and (5.7), which have now been modified for the anisotropic conductivity model:

$$\nabla\times\mathcal{E} = -i\mathcal{B}, \tag{5.5}$$

$$\nabla\times\mathcal{B} = 2\underline{\sigma}_n \cdot \mathcal{E}, \tag{5.6}$$

$$\nabla\cdot(\underline{\sigma}_n \cdot \mathcal{E}) = 0, \tag{5.7}$$

$$\nabla\cdot\mathcal{B} = 0. \tag{5.8}$$

Note that (5.7) is found by taking the divergence of (5.6). There is an important consequence of (5.7) that comes with an anisotropic conductivity model. We see that with a non-uniform conductivity tensor, we can non longer state that the divergence of the electric field is zero. This means that in an anisotropic earth, the electric field is not guaranteed to be solenoidal and therefore precludes the use of the toroidal and poloidal scalar potentials that MWD employed. This derivation will have to work with the vector fields themselves.

To decouple the electric and magnetic fields, we take the curl of (5.5), combine it with (5.6), and use the vector identity,

$$\nabla\times\nabla\times\mathsf{A} = \nabla(\nabla\cdot\mathsf{A}) - \nabla^2\mathsf{A}, \tag{5.9}$$

to get,

$$\nabla^2\mathcal{E} - \nabla(\nabla\cdot\mathcal{E}) - 2i\underline{\sigma}_n \cdot \mathcal{E} = 0. \tag{5.10}$$

To ease further derivation and align ourselves with Parker and Wheelock [2012] (henceforth, PW), we immediately move the horizontal coordinates of (5.6), (5.7), and (5.10) into the Fourier domain. As preparation, we define the 2-dimensional Fourier transform

(FT) operation by

$$\mathcal{F}[f](\mathbf{k}) = \int_{\mathsf{R}^2} f(\mathbf{r}) \mathrm{e}^{-2\pi i \mathbf{r}\cdot\mathbf{k}} d^2\mathbf{r} = \hat{f}(\mathbf{k}), \tag{5.11}$$

and keep the following property of the FT in the horizontal plane in mind as it will soon become useful,

$$\mathcal{F}\left[\nabla f\right](\mathbf{k}, z) = 2\pi i \mathbf{k} \hat{f}(\mathbf{k}, z) + \bar{\mathbf{z}} \frac{\partial}{\partial z} \hat{f}(\mathbf{k}, z), \tag{5.12}$$

where $\bar{\mathbf{z}}$ denotes the vertical unit vector. Also, we should reiterate a few definitions of notation found in PW. We define $\mathbf{E}(\mathbf{r}, z)$ and $\mathbf{B}(\mathbf{r}, z)$ as the horizontal, dimensionless electric and magnetic fields, respectively, where $\mathbf{r}$ is the component of the position vector normal to the vertical axis. The quantities $E_3(\mathbf{r}, z)$ and $B_3(\mathbf{r}, z)$ are defined as the vertical, dimensionless electric and magnetic fields, respectively. The superscripts of '$-$' and '$+$' denote fields above and below a layer interface, respectively. The prime notation denotes differentiation with respect to z.

In the Fourier domain we find that (5.10), separated into horizontal and vertical projections, becomes,

$$-4\pi^2 k^2 \hat{\mathbf{E}} + \hat{\mathbf{E}}'' - 2\pi i \mathbf{k}(2\pi i \mathbf{k} \cdot \hat{\mathbf{E}} + \hat{E}_3') - 2i \underline{\check{\sigma}}_n \cdot \hat{\mathbf{E}} = 0, \tag{5.13}$$

and,

$$-4\pi^2 k^2 \hat{E}_3 - 2\pi i \mathbf{k} \cdot \hat{\mathbf{E}}' - 2i\sigma_n \nu_n \hat{E}_3 = 0, \tag{5.14}$$

where, in (5.14), all instances of $\hat{E}_3''$ cancel. Equation (5.5), rearranged to match the left-hand side of equation (3.24) from MWD, again separated into horizontal and vertical projections, becomes,

$$-i\bar{\mathbf{z}} \times \hat{\mathbf{B}} = 2\pi i \mathbf{k} \hat{E}_3 - \hat{\mathbf{E}}', \tag{5.15}$$

and

$$-i\hat{B}_3 = 2\pi i\bar{\mathbf{z}} \cdot (\mathbf{k} \times \hat{\mathbf{E}}) \tag{5.16}$$

where $\bar{\mathbf{z}}$ denotes the unit vector in the z-direction.

Our goal is to find a form of (5.15) where the right-hand side is reduced to a dot product between some field-independent kernel and the horizontal electric field, $\hat{\mathbf{E}}$. Therefore we must find substitutions for $\hat{\mathbf{E}}'$ and $\hat{E}_3$. To do this for $\hat{\mathbf{E}}'$ we will have to construct a recurrence relation for an admittance transfer function between $\hat{\mathbf{E}}$ and $\hat{\mathbf{E}}'$; we will get to that later. First, we deal with the vertical electric field, $\hat{E}_3$. From equation (5.7), we find that,

$$\hat{E}_3' = -\frac{2\pi i}{\sigma_n \nu_n}\mathbf{k} \cdot (\underline{\breve{\sigma}}_n \cdot \hat{\mathbf{E}}), \tag{5.17}$$

and by rearrangement of (5.14),

$$\hat{E}_3 = -\frac{2\pi i}{2i\sigma_n\nu_n + 4\pi^2 k^2}(\mathbf{k} \cdot \hat{\mathbf{E}}'). \tag{5.18}$$

Rearranging (5.13) and inserting expression (5.17) for the derivative of the vertical electric field, we get the following vector differential equation governing the horizontal electric field within the n^{th} layer,

$$\hat{\mathbf{E}}'' - \left[4\pi^2 k^2 \mathsf{I} + 2i\underline{\breve{\sigma}}_n - 4\pi^2 \mathbf{k}\mathbf{k} \cdot \left(\mathsf{I} - \frac{1}{\sigma_n\nu_n}\underline{\breve{\sigma}}_n\right)\right] \cdot \hat{\mathbf{E}} = 0. \tag{5.19}$$

In the preceding equation, we have introduced the dyadic notation, $\mathbf{kk}$, and the 2×2 identity tensor, I. It is convenient to rewrite (5.19) in the simpler form,

$$\hat{\mathbf{E}}'' - \underline{\boldsymbol{\Gamma}}_n \cdot \hat{\mathbf{E}} = 0, \tag{5.20}$$

where $\underline{\mathbf{\Gamma}}_n$ is the 2×2 tensor given by,

$$\underline{\mathbf{\Gamma}}_n = 4\pi^2 k^2 \mathsf{I} + 2i\underline{\check{\sigma}}_n - 4\pi^2 \mathbf{k}\mathbf{k} \cdot \left(\mathsf{I} - \frac{1}{\sigma_n \nu_n} \underline{\check{\sigma}}_n \right). \tag{5.21}$$

Now we take advantage of the process of matrix diagonalization. For most matrices, $\underline{\mathbf{\Gamma}} \in \mathcal{C}^{K \times K}$, there exists a decomposition,

$$\underline{\mathbf{\Gamma}} = P \Lambda P^{-1}, \tag{5.22}$$

such that $\Lambda = \text{diag}(\lambda_1, \ldots, \lambda_K)$, where λ_i, for $i = 1, \ldots, K$, are the eigenvalues of $\underline{\mathbf{\Gamma}}$, and P is a matrix of column vectors, $P = (\mathbf{u}_1 \ \cdots \ \mathbf{u}_K)$, where $\mathbf{u}_i$ are the corresponding eigenvectors.

We define a new vector, $\mathbf{F}$, defined by the following change of basis of $\hat{\mathbf{E}}$,

$$\mathbf{F} = P^{-1} \hat{\mathbf{E}}. \tag{5.23}$$

Then using (5.22), we can rewrite (5.20) as,

$$\mathbf{F}'' = \Lambda \mathbf{F}, \tag{5.24}$$

which, due to the diagonal nature of Λ, decouples into two equations, one for each component of $\mathbf{F}$. Within the n^{th} layer of homogenous conductivity, $\underline{\sigma}_n$, the general solution to (5.24) in component form is,

$$F_i(z) = \alpha_i \exp\left[\sqrt{\lambda_i}(z - z_n)\right] + \beta_i \exp\left[-\sqrt{\lambda_i}(z - z_n)\right], \\ z_{n-1} \leq z \leq z_n, \text{ and } i = \{1, 2\}. \tag{5.25}$$

In all instances of $\sqrt{\lambda_i}$, we choose the root with the positive real part. Let us analyze the case where the values of F_i and F_i' are known at the bottom of the n^{th} layer, where $z = z_n$, which we will write as F_i^- and $F_i'^-$, respectively. Conversely, we will write the values of F_i and F_i' at the the top of the n^{th} layer, where $z = z_{n-1}$, as F_i^+ and $F_i'^+$. This superscript

convention is analogous to the thin-sheet notation of PW where a '+' denotes quantities measured below a conductivity interface, and a '−' denotes quantities measured above a conductivity interface. We find the general coefficients of (5.25) to be,

$$\alpha_i = \frac{1}{2}\left(F_i^- + \frac{F_i'^-}{\sqrt{\lambda_i}}\right), \tag{5.26}$$

and

$$\beta_i = \frac{1}{2}\left(F_i^- - \frac{F_i'^-}{\sqrt{\lambda_i}}\right). \tag{5.27}$$

Plugging this into (5.25) we can relate F_i^- to F_i^+ and $F_i'^-$ to $F_i'^+$ in the n^{th} layer as follows:

$$F_i^+ = F_i^- \cosh\left(\sqrt{\lambda_i}h_n\right) - \frac{F_i'^-}{\sqrt{\lambda_i}} \sinh\left(\sqrt{\lambda_i}h_n\right), \tag{5.28}$$

and

$$F_i'^+ = \sqrt{\lambda_i}F_i^- \sinh\left(\sqrt{\lambda_i}h_n\right) - F_i'^- \cosh\left(\sqrt{\lambda_i}h_n\right), \tag{5.29}$$

where, h_n, the thickness if the n^{th} layer, is defined as $h_n = z_n - z_{n-1}$.

Conditions are different at the base of our stack of layers. Within the halfspace which we place at the bottom of the stack of layers, at $z = z_N$, α_i must be zero; otherwise, this would imply energy originating from the center of the earth, which is not the subject of the magnetotelluric problem at hand. From this imposition we deduce that within the basal halfspace,

$$F_i(z) = -\frac{1}{\sqrt{\lambda_i}}F_i'(z), \quad z > z_N. \tag{5.30}$$

Now, we must address the boundary conditions across the layer interfaces. In the absence of free charges and free currents at the interface, and assuming a homogeneous magnetic permeability throughout the domain, Maxwell's equations dictate that both the tangential electric and tangential magnetic fields are continuous across the interface. Also,

the current density normal to an interface is conserved. In our notation, these boundary conditions are written as:

$$\hat{\mathbf{E}}^{+}_{n+1} = \hat{\mathbf{E}}^{-}_{n}, \tag{5.31}$$

$$\hat{\mathbf{B}}^{+}_{n+1} = \hat{\mathbf{B}}^{-}_{n}, \tag{5.32}$$

and

$$\nu_{n+1}\sigma_{n+1}\hat{E}^{+}_{3(n+1)} = \nu_{n}\sigma_{n}\hat{E}^{-}_{3(n)}. \tag{5.33}$$

Note that continuity of the tangential magnetic field, (5.32), and of the normal electric field, (5.33), does not hold across a thin sheet of finite conductance because it contains free current; yet, (5.31) does hold across a thin sheet of finite conductance. We will need to know how to propagate $\mathbf{F}$ and $\mathbf{F}'$ across the interfaces. Inserting (5.23) into (5.31), we readily find that

$$\mathbf{F}^{-}_{n} = P^{-1}_{n} P_{n+1} \mathbf{F}^{+}_{n+1}. \tag{5.34}$$

The propagation of $\mathbf{F}'$ at a boundary takes a little more work. We revisit (5.15), which by (5.32) affords us,

$$2\pi i \mathbf{k}\hat{E}^{+}_{3(n+1)} - \hat{\mathbf{E}}'^{+}_{n+1} = 2\pi i \mathbf{k}\hat{E}^{-}_{3(n)} - \hat{\mathbf{E}}'^{-}_{n}. \tag{5.35}$$

Next we subsitute (5.18) and (5.33) into (5.35), and after some rearrangement find,

$$\hat{\mathbf{E}}'^{-}_{n} = \left[\frac{4\pi^2}{2i\sigma_{n+1}\nu_{n+1} + 4\pi^2 k^2} \left(\frac{\nu_{n+1}\sigma_{n+1}}{\nu_{n}\sigma_{n}} - 1 \right) \mathbf{kk} + \mathsf{I} \right] \cdot \hat{\mathbf{E}}'^{+}_{n+1}. \tag{5.36}$$

By employing (5.23) in (5.36) we have,

$$\mathbf{F}_n'^{-} = P_n^{-1}\left[\frac{4\pi^2}{2i\sigma_{n+1}\nu_{n+1}+4\pi^2k^2}\left(\frac{\nu_{n+1}\sigma_{n+1}}{\nu_n\sigma_n}-1\right)\mathbf{kk}+\mathsf{I}\right]P_{n+1}\cdot\mathbf{F}_{n+1}'^{+}. \tag{5.37}$$

Getting back to the substitution for $\hat{\mathbf{E}}'$ in (5.15), we introduce a transfer function we call the admittance tensor, C_1, which defined at the top of the first layer as,

$$\hat{\mathbf{E}}_1^{+} = -\mathsf{C}_1\cdot\hat{\mathbf{E}}_1'^{+}. \tag{5.38}$$

We now have all the tools necessary to find $\hat{\mathbf{E}}_1^{+}$ and $\hat{\mathbf{E}}_1'^{+}$ at the top of our stack of layers, given base conditions for $\hat{\mathbf{E}}_{N+1}^{+}$. However, we are only interested in computing C_1. The 2×2 tensor, C_1 presents us with four unknowns. In order to solve for these we need four independent constraints, which we find by using two, independent initial conditions for $\hat{\mathbf{E}}_{N+1}^{+}$ at the base of our stack. Since we are neither interested in the absolute magnitude of $\hat{\mathbf{E}}_1^{+}$ nor $\hat{\mathbf{E}}_1'^{+}$, but the transfer function between them, C_1, we can impose whatever value for $\hat{\mathbf{F}}_{N+1}^{+}$ we like. Thus, we arbitrarily choose to start with the two, independent initial conditions

$$\mathbf{F}_{N+1}^{+}\in\left\{\begin{bmatrix}1\\0\end{bmatrix},\begin{bmatrix}0\\1\end{bmatrix}\right\}. \tag{5.39}$$

Starting from (5.39) we use (5.30), (5.28), (5.29), (5.34), (5.37) and (5.23) to compute two independent realizations of $\hat{\mathbf{E}}_1^{+}$ and $\hat{\mathbf{E}}_1'^{+}$, by which we solve for C_1.

Finally, by combining (5.15) with (5.18) and (5.38), we can write the horizontal magnetic field just below the thin sheet in terms of the horizontal electric field as,

$$i\hat{\mathbf{z}}\times\hat{\mathbf{B}}^{+}(\mathbf{k}) = \left[\left(\frac{4\pi^2}{2i\sigma_1\nu_1+4\pi^2k^2}\mathbf{kk}-\mathsf{I}\right)\cdot\mathsf{C}_1^{-1}\right]\cdot\hat{\mathbf{E}}^{+}(\mathbf{k}) = \hat{\mathsf{L}}_l(\mathbf{k})\cdot\hat{\mathbf{E}}^{+}(\mathbf{k}), \tag{5.40}$$

where the subscript denotes a tensor quantity related to a layered halfspace. By analyzing

(5.21) and (5.30) for the case of an isotropic halfspace of conductivity, σ_0, we find

$$\mathsf{C}_1 = \frac{1}{\sqrt{2i\sigma_0 + 4\pi^2 k^2}}\,\mathsf{I}. \tag{5.41}$$

Plugging (5.41) into (5.40) we find the reassuring result that $\hat{\mathsf{L}}_l(\mathbf{k})$ matches the half-space kernel in (3.26) of MWD after compensating for their different definition of the FT.

Equation (5.40) is the second ingredient needed for the right-hand side of (2.1) of MWD, which relates the current density in the thin sheet to a discontinuity in the horizontal magnetic field. For the first ingredient of (2.1) we look to (2.2) in MWD, which describes the relationship between the electric and magnetic fields in the halfspace of perfectly insulating air above the earth's surface. The Fourier domain equivalent of (2.2) in MWD is,

$$-i\hat{\mathbf{z}} \times \hat{\mathbf{B}}^-(\mathbf{k}) = i\delta(\mathbf{k})\bar{\mathbf{x}} + [\hat{\mathsf{M}}(\mathbf{k}) - \hat{\mathsf{M}}(0)] \cdot \hat{\mathbf{E}}^-(\mathbf{k}) \tag{5.42}$$

where we have folded the $1/2\pi$ in (2.1) into M. By noting $\bar{\mathbf{z}} \times \bar{\mathbf{y}} = -\bar{\mathbf{x}}$, the delta function in (5.42) accounts for a $\bar{\mathbf{y}}$-directed plane wave ($k = 0$) magnetic field of magnitude 1, the driving field for induction. The tensor product in (5.42) accounts for the magnetic field produced by scattering due to conductance of the thin sheet. Before taking the FT, the tensor M from MWD is simplified to,

$$\mathsf{M}(\mathbf{r}) = \frac{1}{4\pi r^3}\begin{bmatrix} 1 - 3\cos 2\theta & -3\sin 2\theta \\ -3\sin 2\theta & 1 + 3\cos 2\theta \end{bmatrix}, \tag{5.43}$$

with $\mathbf{r} = \bar{\mathbf{x}} r\cos\theta + \bar{\mathbf{y}} r \sin\theta$. To find $\hat{\mathsf{M}}$ we need only the three following transforms previously used in PW:

$$\mathcal{F}\left[\frac{1}{r^3}\right] = -4\pi^2 k, \tag{5.44}$$

$$\mathcal{F}\left[\frac{\cos 2\theta}{r^3}\right] = -\frac{4\pi^2 k \cos 2\phi}{3}, \tag{5.45}$$

and

$$\mathcal{F}\left[\frac{\sin 2\theta}{r^3}\right] = -\frac{4\pi^2 k \sin 2\phi}{3}, \tag{5.46}$$

given that $\mathbf{k} = \bar{\mathbf{x}}k\cos\phi + \bar{\mathbf{y}}k\sin\phi$. We then quickly find,

$$\hat{\mathsf{M}}(\mathbf{k}) = -2\pi k \begin{bmatrix} \sin^2\phi & -\sin\phi\cos\phi \\ -\sin\phi\cos\phi & \cos^2\phi \end{bmatrix}. \tag{5.47}$$

Now we can return to reconstructing the Fourier domain version of (2.1) from MWD, which we rewrite here,

$$2i\tau(\mathbf{r})\mathbf{E}(\mathbf{r}) = i\bar{\mathbf{z}} \times \left[\mathbf{B}^+(\mathbf{r}) - \mathbf{B}^-(\mathbf{r})\right]. \tag{5.48}$$

Equation (5.48) is the boundary condition of the horizontal magnetic field across an infinitesimally thin sheet of current, which constitutes the crux of thin sheet modeling. We write (5.48) in the Fourier domain as,

$$\mathcal{F}\left[2i\underline{\tau}(\mathbf{r}) \cdot \mathbf{E}(\mathbf{r})\right] = i\bar{\mathbf{z}} \times \left[\hat{\mathbf{B}}^+(\mathbf{k}) - \hat{\mathbf{B}}^-(\mathbf{k})\right]. \tag{5.49}$$

Finally, we substitute (5.40) and (5.42) into (5.49) to get,

$$\mathcal{F}\left[2i\underline{\tau}(\mathbf{r}) \cdot \mathbf{E}(\mathbf{r})\right] = i\delta(\mathbf{k})\bar{\mathbf{x}} + \left[\hat{\mathsf{M}}(\mathbf{k}) + \hat{\mathsf{L}}_l(\mathbf{k})\right] \cdot \hat{\mathbf{E}}(\mathbf{k}), \tag{5.50}$$

noting that $\hat{\mathsf{M}}(0) = 0$. This is the vector equation which governs the horizontal electric fields within the thin sheet in our model. Like its space-domain counterpart, (5.50) is another Fredholm integral equation because of FT. This is a system analogous to (7) in PW, and we will solve it with methods similar to those they described. We describe the solution method in the Section 5.4.

5.2 Adding Layers above the Thin Sheet

It would be useful to create a model in which the 2D-varying thin sheet is embedded in the stack of layers. One could imagine the necessity for a model in which the thin sheet is still placed at the earth's surface, but in which there are layers of non-zero conductivity in the atmosphere, say to represent the ionosphere. Alternatively, one might want to model the case of a thin layer of 3D conductivity embedded within and otherwise 1D earth and calculate the resulting fields at the earth's surface. For these sorts of situations we extend our mathematical treatment to include layers above a thin sheet.

In order to place layers above the thin sheet, we need to derive a new version of (5.42) that does not assume a halfspace of air directly above the thin sheet. We will derive this in much the same way as we did (5.40) with a slight twist. We will decompose the fields above the thin sheet into plane wave components ($\mathbf{k} = 0$) and scattered components, precisely as is done in (5.42).

To remain consistent with our treatment below the thin sheet, we will again define z_0 as the depth of placement for the thin sheet. Thus, z_n for $n > 0$ still refer to depths below the thin sheet, while z_n for $n < 0$ will refer to depths above the thin sheet, and $n = 0$ will be the index of the first layer above the thin sheet. We will place an initiating halfspace at the top of our new stack, which will be given layer index M, with $M < 0$.

We draw another important distinction between our treatment of the fields above the thin sheet and those below the thin sheet. Whereas in the layers below the thin sheet we solved for the total fields, in the layers above, we will solve for the primary electric and magnetic fields, $\mathcal{E}_p$ and $\mathcal{B}_p$, and the scattered electric and magnetic fields, e and b, separately. The total field is the sum of these two components:

$$\mathcal{E} = \mathcal{E}_p + \mathrm{e}, \tag{5.51}$$

and

$$\mathcal{B} = \mathcal{B}_p + \mathrm{b}. \tag{5.52}$$

The primary field, we define as the fields existent in a 1D earth with no thin sheet due to a linearly-polarized, horizontal, and planar source field; these are the standard MT source-field assumptions. With this definition, $\mathcal{E}_{p3}$ and $\mathcal{B}_{p3}$ are everywhere zero, and $\hat{\mathbf{E}}_p(\mathbf{k})$ and $\hat{\mathbf{B}}_p(\mathbf{k})$ are non-zero only when $k = 0$. The scattered electric and magnetic fields are those resulting only from currents diverted by the anomalous conductance of the thin sheet, thus they both go to zero as z goes to positive or negative infinity.

Due to the linearity of the Maxwell equations with respect to the fields, we quickly see that (5.20), (5.23), (5.24), and (5.15) again hold for the *scattered* electric and magnetic fields in the layers above the thin sheet, with the substitutions of $\hat{\mathbf{e}}$ for $\hat{\mathbf{E}}$, $\hat{\mathbf{b}}$ for $\hat{\mathbf{B}}$, and $\mathbf{f}$ for $\mathbf{F}$. Now we must imagine the scenario where we know the values of f_i^+ and $f_i'^+$ at the top of each layer. So, much as before, within the n^{th} layer of homogenous conductivity, $\underline{\sigma}_n$, the general solution to (5.24) in component form is,

$$f_i(z) = \alpha_i \exp\left[\sqrt{\lambda_i}(z - z_{n-1})\right] + \beta_i \exp\left[-\sqrt{\lambda_i}(z - z_{n-1})\right], \\ z_{n-1} \leq z \leq z_n, \text{ and } i = \{1, 2\}. \tag{5.53}$$

Note the change in indices of the layer depths. Solving for α_i and β_i as we did before, we find,

$$f_i^- = f_i^+ \cosh\left(\sqrt{\lambda_i} h_n\right) + \frac{f_i'^+}{\sqrt{\lambda_i}} \sinh\left(\sqrt{\lambda_i} h_n\right), \tag{5.54}$$

and

$$f_i'^- = \sqrt{\lambda_i} f_i^+ \sinh\left(\sqrt{\lambda_i} h_n\right) + f_i'^+ \cosh\left(\sqrt{\lambda_i} h_n\right), \tag{5.55}$$

where there is a sign difference from our previous formulation, a result of the arguments of the exponents in (5.53) and h_n, the thickness if the n^{th} layer, still defined as $h_n = z_n - z_{n-1}$.

We must define conditions for the initiating halfspace at the top of our stack of layers. Within this halfspace, β_i must be zero, since we are only dealing with the scattered fields here. The coefficient β_i represents energy that grows for decreasing z (increasing altitude), which we have precluded by our definition of the scattered field. With β_i=0, we

find that in the initiating halfspace,

$$f_i(z) = \frac{1}{\sqrt{\lambda_i}} f_i'(z), \quad z < z_M. \tag{5.56}$$

By analogy with the previous case of layers below the thin sheet, the boundary conditions for $\mathbf{f}$ and $\mathbf{f}'$ across the interfaces are,

$$\mathbf{f}_n^+ = P_n^{-1} P_{n-1} \mathbf{f}_{n-1}^- \tag{5.57}$$

and

$$\mathbf{f}_n'^+ = P_n^{-1} \left[\frac{4\pi^2}{2i\sigma_{n-1}\nu_{n-1} + 4\pi^2 k^2} \left(\frac{\nu_{n-1}\sigma_{n-1}}{\nu_n \sigma_n} - 1 \right) \mathbf{kk} + \mathsf{I} \right] P_{n-1} \cdot \mathbf{f}_{n-1}'^-. \tag{5.58}$$

To address the substitution for $\hat{\mathbf{e}}'$ in (5.15), we introduce an admittance tensor, C_0, for the scattered electric field, which we compute at the bottom of the first layer above the thin sheet, defined as,

$$\hat{\mathbf{e}}_0^- = -\mathsf{C}_0 \cdot \hat{\mathbf{e}}_0'^-. \tag{5.59}$$

We solve for C_0 in a similar fashion as we did for C_1. We calculate two independent realizations of $\hat{\mathbf{e}}_0^-$ and $\hat{\mathbf{e}}_0'^-$ using (5.56), (5.54), (5.55), (5.57), and (5.58), after imposing two independent initial conditions for $\mathbf{f}_M^-$. Then we solve the 2×2 system for C_0.

Finally, the horizontal scattered fields above the thin sheet are related by,

$$-i\bar{\mathbf{z}} \times \hat{\mathbf{b}}^-(\mathbf{k}) = \left[\left(\mathsf{I} - \frac{4\pi^2}{2i\sigma_0\nu_0 + 4\pi^2 k^2} \mathbf{kk} \right) \cdot \mathsf{C}_0^{-1} \right] \cdot \hat{\mathbf{e}}(\mathbf{k}) = \hat{\mathsf{M}}_l(\mathbf{k}) \cdot \hat{\mathbf{e}}(\mathbf{k}), \tag{5.60}$$

where we have now defined a new tensor $\hat{\mathsf{M}}_l$ for the scenario of layers above the thin sheet. A relationship for the total fields above the thin sheet is still needed. We set the primary field just above the thin sheet to be,

$$\hat{\mathcal{B}}_p^- = \delta(\mathbf{k})\bar{y}, \tag{5.61}$$

a plane-wave primary field with unity amplitude, as before. It is always true that $\hat{\mathbf{E}}_p^+ = \hat{\mathbf{E}}_p^-$, and since $\hat{\mathbf{E}}_p$ is non-zero only when $k = 0$, by (5.36), $\hat{\mathbf{E}}_p'^+ = \hat{\mathbf{E}}_p'^-$. Also, with no vertical primary fields, (5.15) gives us,

$$\hat{\mathbf{E}}_p'^- = i\bar{\mathbf{z}} \times \hat{\mathbf{B}}_p^- = -i\delta(\mathbf{k})\bar{\mathbf{x}}. \tag{5.62}$$

Then, because of the continuity of the primary horizontal electric field and its vertical derivative at $z = z_0$, we find the primary electric field above the thin sheet,

$$\hat{\mathbf{E}}_p^- = -\mathsf{C}_1\hat{\mathbf{E}}_p'^- = i\delta(\mathbf{k})\mathsf{C}_1 \cdot \bar{\mathbf{x}}. \tag{5.63}$$

Next, we plug (5.51) and (5.52) into (5.60), and use (5.61) and (5.63) to get the following relationship between the total fields above the thin sheet,

$$\begin{aligned} -i\bar{\mathbf{z}} \times \hat{\mathbf{B}}^-(\mathbf{k}) &= i\delta(\mathbf{k})\bar{\mathbf{x}} - i\delta(\mathbf{k})\hat{\mathsf{M}}_l(\mathbf{k}) \cdot \mathsf{C}_1 \cdot \bar{\mathbf{x}} + \hat{\mathsf{M}}_l(\mathbf{k}) \cdot \hat{\mathbf{E}}^-(\mathbf{k}) \\ &= i\delta(\mathbf{k})\bar{\mathbf{x}} - i\delta(\mathbf{k})\mathsf{C}_0^{-1}(0) \cdot \mathsf{C}_1(0) \cdot \bar{\mathbf{x}} + \hat{\mathsf{M}}_l(\mathbf{k}) \cdot \hat{\mathbf{E}}^-(\mathbf{k}). \end{aligned} \tag{5.64}$$

Finally, by inserting (5.64) into (5.49) we find,

$$\mathcal{F}\left[2i\underline{\tau}(\mathbf{r}) \cdot \mathbf{E}(\mathbf{r})\right] = i\delta(\mathbf{k})\bar{\mathbf{x}} - i\delta(\mathbf{k})\mathsf{C}_0^{-1}(0) \cdot \mathsf{C}_1(0) \cdot \bar{\mathbf{x}} + \left[\hat{\mathsf{M}}_l(\mathbf{k}) + \hat{\mathsf{L}}_l(\mathbf{k})\right] \cdot \hat{\mathbf{E}}(\mathbf{k}), \tag{5.65}$$

the governing equation for the electric fields in a thin sheet embedded in a stack of layers with anisotropic conductivities. As a check for consistency we return to the model with a perfectly insulating halfspace above the thin sheet, within which $\sigma_0 = 0$, and therefore,

$$\mathsf{C}_0 = -\frac{1}{2\pi k}\mathsf{I}. \tag{5.66}$$

After plugging (5.66) into (5.60) we again find a reassuring result that the form of M_l within a perfectly insulating halfspace matches (5.47).

5.3 Adding a Dipole Source within the Layers above the Thin Sheet

Now we leave the exclusive realm of driving fields of a single wavenumber, $k = 0$, the traditional model for MT, and enter the realm of driving fields with energy at arbitrary wavenumbers, which includes all types of controlled-source electromagnetic induction. The first task is to derive a new set of primary fields, $\mathcal{E}_0$ and $\mathcal{B}_0$, that result from an electric or magnetic dipole positioned above the thin sheet. These primary fields will be utilized in a very similar way as they were used in Section 5.2. We will solve for the primary fields in the plane containing the sources of arbitrary wavenumber content and propagate those fields down to the depth containing the thin sheet of variable conductance. The propagated fields are then used as the new source vector which drives the induction governed the Fredholm integral equation for the electric field within the thin sheet.

To model the fields resulting from any combination of electric and magnetic dipoles, we must introduce electric and magnetic source currents, $\mathcal{J}$, and $\mathcal{M}$, respectively. Strictly speaking, the introduction of $\mathcal{M}$ requires the existence of magnetic monopoles, a fictitious device which produces an accurate approximation to reality in the macroscopic view we take here. To align with our prior Maxwell's equations, $\mathcal{J}$ and $\mathcal{M}$ will also be dimensionless, in units of $B_*/(\mathrm{d}_*\mu_0)$ and $\omega B_*/\mu_0$, respectively. Our choice for quantities by which we define our dimensionless system is open, yet different source types make specific normalizations more natural. For systems that contain a single electric source current of known dipole moment, it will be more convenient to define dimensionless $\mathcal{J}$ in units of $I_* ds/\mathrm{d}_*^3$, a measure of average current density of the electric dipole, where I_* is the dipole current and ds is the dipole length. In this case, $\mathcal{E}$ is given in units of $2I_* ds/(\mathrm{d}_*^3\sigma_*)$, and $\mathcal{B}$ is given in units of $\mu_0 I_* ds/\mathrm{d}_*^2$. For an alternative system which contains a single known magnetic source current, $\mathcal{M}$ may be given in units of $I_* da/\mathrm{d}_*^3$, the magnetic dipole moment density, where I_* is the current in a loop whose enclosed area is da. In this case, $\mathcal{E}$ is then given in units of $\mu_0\omega I_* da/\mathrm{d}_*^2$, and $\mathcal{B}$ is given in units of $\mu_0 I_* da/\mathrm{d}_*^3$. In addition, we will lift the quasi-static assumption (no displacement currents) and restore the time-derivative of the electric field on the right-hand side of Ampere's Law to allow for the modeling of higher frequencies.

With this augmentation, we will need to introduce a dimensionless electrical permittivity, ε, which is measured in units of σ_*/ω, and a dimensionless admittivity tensor, given by the following

$$\underline{\epsilon} = \underline{\sigma} + i\varepsilon \mathbf{I}, \tag{5.67}$$

where we will assume an isotropic electrical permittivity, and again use the ' $\check{}$ ', to signify the horizontal-component sub-tensor. The modified set of Maxwell's equations we will now use within the n^{th} layer of admittivity, $\underline{\epsilon}_n$, are:

$$\nabla \times \mathcal{E} = -i\mathcal{B} - i\mathcal{M}, \tag{5.68}$$

$$\nabla \times \mathcal{B} = 2\underline{\epsilon}_n \mathcal{E} + \mathcal{J}, \tag{5.69}$$

$$2\nabla \cdot (\underline{\epsilon}_n \mathcal{E}) + \nabla \cdot \mathcal{J} = 0, \tag{5.70}$$

and

$$\nabla \cdot \mathcal{B} + \nabla \cdot \mathcal{M} = 0. \tag{5.71}$$

Versions of these Maxwell's equations with electric and magnetic source currents in physical units can be found in Ward and Hohmann [1988]. Using the same strategy and notation as in Section 5.1, we combine (5.68) and (5.69), to get

$$-4\pi^2 k^2 \hat{\mathbf{E}} + \hat{\mathbf{E}}'' + 4\pi^2 \mathbf{k}\mathbf{k} \cdot \hat{\mathbf{E}} - 2\pi i \mathbf{k} \hat{E}_3' - 2i\check{\underline{\epsilon}} \cdot \hat{\mathbf{E}} - i\hat{\mathbf{J}} - \bar{\mathbf{z}} \times (2\pi \mathbf{k} \hat{M}_3 + i\hat{\mathbf{M}}') = 0, \tag{5.72}$$

for the horizontal projection, and

$$-4\pi^2 k^2 \hat{E}_3 - 2\pi i \mathbf{k} \cdot \hat{\mathbf{E}}' - 2i(\sigma_n \nu_n + i\varepsilon_n)\hat{E}_3 - i\hat{J}_3 + 2\pi \bar{\mathbf{z}} \cdot (\mathbf{k} \times \hat{\mathbf{M}}) = 0, \tag{5.73}$$

for the vertical projection. Then, from the electric field, the components of the magnetic field can be found with,

$$-i\bar{\mathbf{z}} \times \hat{\mathbf{B}} = 2\pi i \mathbf{k} \hat{E}_3 - \hat{\mathbf{E}}' + i\hat{\mathbf{M}}, \tag{5.74}$$

and

$$-i\hat{B}_3 = 2\pi i \bar{\mathbf{z}} \cdot (\mathbf{k} \times \hat{\mathbf{E}}) + i\hat{M}_3. \tag{5.75}$$

From (5.70) we find,

$$\hat{E}_3' = -\frac{1}{2(\sigma_n \nu_n + i\varepsilon_n)} \left[\hat{J}_3' + 2\pi i \mathbf{k} \cdot \left(2\check{\underline{\epsilon}} \cdot \hat{\mathbf{E}} + \hat{\mathbf{J}} \right) \right] \tag{5.76}$$

and by rearrangement of (5.73),

$$\hat{E}_3 = -\frac{1}{2i(\sigma_n \nu_n + i\varepsilon_n) + 4\pi^2 k^2} \left[i\hat{J}_3 - 2\pi \bar{\mathbf{z}} \cdot (\mathbf{k} \times \hat{\mathbf{M}}) + 2\pi i \mathbf{k} \cdot \hat{\mathbf{E}}' \right]. \tag{5.77}$$

Rearranging (5.72) and inserting (5.76) for the derivative of the vertical electric field, we get the following vector differential equation governing the horizontal electric field within the n^{th} layer with some distribution of $\mathcal{J}$ and $\mathcal{M}$,

$$\hat{\mathbf{E}}'' - \underline{\mathbf{\Pi}}_n \cdot \hat{\mathbf{E}} = \hat{\mathbf{S}}, \tag{5.78}$$

where,

$$\underline{\mathbf{\Pi}}_n = 4\pi^2 k^2 \mathsf{I} + 2i\check{\underline{\epsilon}}_n - 4\pi^2 \mathbf{k}\mathbf{k} \cdot \left(\mathsf{I} - \frac{1}{(\sigma_n \nu_n + i\varepsilon_n)} \check{\underline{\epsilon}}_n \right) \tag{5.79}$$

and,

$$\hat{\mathbf{S}} = -\frac{\pi i}{(\sigma_n \nu_n + i\varepsilon_n)} \left[\mathbf{k} \hat{J}_3' + 2\pi i \mathbf{k}\mathbf{k} \cdot \hat{\mathbf{J}} \right] + i\hat{\mathbf{J}} + \bar{\mathbf{z}} \times (2\pi \mathbf{k} \hat{M}_3 + i\hat{\mathbf{M}}'). \tag{5.80}$$

While $\underline{\mathbf{\Pi}}_n$ is nearly identical to $\underline{\mathbf{\Gamma}}_n$, equation (5.78) is made much more complicated than

(5.19) by the source vector, $\hat{\mathbf{S}}$; it is now an inhomogeneous ODE. However, this complication only arises in layers where $\hat{\mathbf{S}}$ is non-zero, which, in most real situations, is limited to a single depth.

Rather than solve the inhomogeneous ODE, let us use the tools already developed for a thin sheet of current, which will require us to solve only homogeneous versions of (5.78). First we examine a simple system. Imagine the scenario where there are no magnetic source currents and only one localized electric source current, with a dipole moment of $I_* ds$, at a single depth above the thin sheet of variable conductance. Considering only the horizontal components of the electric source current for now, we can represent the source as another horizontal thin sheet of current and make use of a modified version of (5.49),

$$\hat{\mathbf{T}}(\mathbf{k}) = \bar{\mathbf{z}} \times \left[\hat{\mathbf{B}}^{+}(\mathbf{k}) - \hat{\mathbf{B}}^{-}(\mathbf{k}) \right], \tag{5.81}$$

where $\hat{\mathbf{T}}(\mathbf{k})$ is the Fourier transform of a dimensionless surface current density, given in units of $I_* ds / \mathrm{d}_*^2$. An advantage here is that $\hat{\mathbf{T}}$ is usually known for controlled source problems, and thus does not need to be solved-for along with the horizontal electric field. Instead, we first solve for the primary fields due to the thin-sheet equivalent of the known source. Recall that the primary fields are defined as those occurring in the layered earth without the heterogeneous thin sheet; this time the primary fields will be driven by a dipole source current as opposed by a plane wave. We incorporate the thin sheet of a known source current into our model for the primary fields by adding a new layer interface at the depth of the electric dipole source and using source-modified boundary conditions. For a purely horizontal electric source current, the equation to be solved for the primary horizontal electric field at the depth of the source is,

$$\begin{aligned} i\hat{\mathbf{T}} &= \left[\left(\frac{4\pi}{g_{n+1}^2} \mathbf{k}\mathbf{k} - \mathsf{I} \right) \cdot {}^{s}\mathsf{C}_1^{-1} - \left(\frac{4\pi}{g_n^2} \mathbf{k}\mathbf{k} - \mathsf{I} \right) \cdot {}^{s}\mathsf{C}_0^{-1} \right] \cdot \hat{\mathbf{E}}_p \\ &= \left[{}^{s}\mathsf{L}_l + {}^{s}\mathsf{M}_l \right] \cdot \hat{\mathbf{E}}_p, \end{aligned} \tag{5.82}$$

where,

$$g_n^2 = 2i(\sigma_n \nu_n + i\varepsilon_n) + 4\pi^2 k^2. \tag{5.83}$$

The prescript s, as in ${}^s\mathsf{C}_0$ and ${}^s\mathsf{C}_1$, indicates the relation to the stacks of layers above and below, respectively, the depth at which the known source resides. These new admittance tensors are calculated in the same way as were the admittance tensors at the depth of the heterogeneous thin sheet, albeit with different sets of layer stacks.

If there is a non-zero vertical component of the electric dipole source, $\hat{J}_3 \neq 0$, things change again. We will derive the fields due to a vertical electric source current separately from those of the horizontal source current, and sum the two independent fields when necessary. Assuming we may make the approximation that all electric source current is vertically oriented and resides in a single horizontal plane, then (5.33) becomes,

$$(\sigma_{n+1}\nu_{n+1} + i\varepsilon_{n+1})\hat{E}^+_{3(n+1)} - (\sigma_n \nu_n + i\varepsilon_n)\hat{E}^-_{3(n)} = \frac{1}{2}\hat{J}_3. \tag{5.84}$$

The foregoing boundary condition is derived from the integral formulation of (5.70). Incorporating (5.84) into the boundary condition for $\hat{\mathbf{E}}'$, we find that with a vertical current component,

$$\hat{\mathbf{E}}'^-_n = \left[\frac{4\pi^2 u_{n+1}}{g^2_{n+1}}\mathbf{k}\mathbf{k} + \mathsf{I}\right] \cdot \hat{\mathbf{E}}'^+_{n+1} - \frac{2\pi i}{\sigma_n \nu_n + i\varepsilon_n}\mathbf{k}\hat{J}_3 \tag{5.85}$$

where,

$$u_{n+1} = \left(\frac{\sigma_{n+1}\nu_{n+1} + i\varepsilon_{n+1}}{\sigma_n \nu_n + i\varepsilon_n} - 1\right). \tag{5.86}$$

If the depth of the source does not coincide with a change in admittivity, (5.85) simplifies to,

$$\hat{\mathbf{E}}'^-_n = \hat{\mathbf{E}}'^+_{n+1} - \frac{2\pi i}{\sigma_n \nu_n + i\varepsilon_n}\mathbf{k}\hat{J}_3. \tag{5.87}$$

We need an equation to solve for the horizontal electric field within the thin sheet containing the vertical source. For this we insert the definitions for the admittance tensors, (5.38) and (5.59) into (5.85), which yields,

$$ {}^{s}\mathsf{C}_0^{-1} \cdot \hat{\mathbf{E}}_n^{-} = \left[\frac{4\pi^2 u_{n+1}}{g_{n+1}^2} \mathbf{k}\mathbf{k} + \mathsf{I} \right] \cdot {}^{s}\mathsf{C}_1^{-1} \cdot \hat{\mathbf{E}}_{n+1}^{+} + \frac{2\pi i}{\sigma_n \nu_n + i\varepsilon_n} \mathbf{k} \hat{J}_3. \tag{5.88} $$

Making use of the continuity of the horizontal electric fields across a thin sheet of electric current, we finally have an equation to be solved for the primary horizontal electric field at the depth of a vertical controlled source:

$$ -\frac{2\pi i}{\sigma_n \nu_n + i\varepsilon_n} \mathbf{k} \hat{J}_3 = \left[\left(\frac{4\pi^2 u_{n+1}}{g_{n+1}^2} \mathbf{k}\mathbf{k} + \mathsf{I} \right) \cdot {}^{s}\mathsf{C}_1^{-1} - {}^{s}\mathsf{C}_0^{-1} \right] \cdot \hat{\mathbf{E}}_p. \tag{5.89} $$

The quantities on the left-hand sides of (5.82) & (5.89) form vectors of known source currents. For each source component, the solution for $\hat{\mathbf{E}}_p$ requires the inverse of the tensorial quantity in square brackets, which in the discrete world amounts to a block diagonal matrix with 2×2 blocks along its diagonal (see Section 5.4). Solutions for the primary electric fields from the horizontal electric source component, (5.82), and the vertical electric source component, (5.89) may be calculated independently and then summed to produce the full primary field of a dipping electric current source. Once $\hat{\mathbf{E}}_p$ at the depth of the controlled source has been found, we use the method presented in Section 5.7 to propagate the primary electric and magnetic fields down to the depth of the thin sheet of variable conductance.

As a brief aside, we document a pair of important identities involving the tensors used in this chapter. Through much algebra we find,

$$ \left[\frac{4\pi^2}{g_n^2} \mathbf{k}\mathbf{k} - \mathsf{I} \right]^{-1} = -\left[\frac{4\pi^2}{2i(\sigma_n \nu_n + i\varepsilon_n)} \mathbf{k}\mathbf{k} + \mathsf{I} \right], \tag{5.90} $$

which we use to find,

$$ -\mathsf{C}_0^{-1} \cdot \mathsf{M}_l^{-1} \cdot \mathsf{L}_l \cdot \mathsf{C}_1 = \left[\frac{4\pi^2}{g_n^2} \mathbf{k}\mathbf{k} - \mathsf{I} \right]^{-1} \left[\frac{4\pi^2}{g_{n+1}^2} \mathbf{k}\mathbf{k} - \mathsf{I} \right] = \frac{4\pi^2 u_{n+1}}{g_{n+1}^2} \mathbf{k}\mathbf{k} + \mathsf{I}. \tag{5.91} $$

Utilizing (5.91), we may then rewrite (5.89) as,

$$\frac{2\pi i}{\sigma_n \nu_n + i\varepsilon_n}\mathbf{k}\hat{J}_3 = \left[{}^s\mathsf{C}_0^{-1} \cdot \left({}^s\mathsf{M}_l^{-1} \cdot {}^s\mathsf{L}_l + \mathsf{I}\right)\right] \cdot \hat{\mathbf{E}}_p. \tag{5.92}$$

Notice that horizontal electric dipoles of finite length are easily handled within $\hat{\mathbf{T}}$. An electric dipole of current I_* and finite length $ds = L$ oriented along the x-axis can be represented in dimensionless form with the following,

$$\mathbf{T}(x, y) = \text{rect}\left(\frac{x}{L}\right)\delta(y)\bar{\mathbf{x}}, \tag{5.93}$$

where we have introduced the rectangular function, rect(x). In the Fourier domain (5.93) is,

$$\hat{\mathbf{T}}(\mathbf{k}) = \frac{\sin(\pi L k \cos\phi)}{\pi k \cos\phi}\bar{\mathbf{x}}. \tag{5.94}$$

Aside from a more accurate rendering of reality, there is another advantage to modeling an electric dipole of finite length with the thin-sheet method described in this chapter. In (5.94), we see that as $k_x \to \infty$, $\hat{\mathbf{T}} \to 0$, whereas, for a point dipole $\hat{\mathbf{T}}$ is constant for all k. It is found in practice that the damping of large-k components of the electric field leads to faster convergence of the iterative solution (see Secton 5.4). Of course, dipoles of finite length dipping out of the horizontal plane must be treated with care. While we've shown that we can model a source with some vertical polarization, if the projection of that source's length in the vertical dimension is large enough to violate our thin-sheet assumptions ($\mathbf{ds}\cdot\bar{\mathbf{z}} \ll \mathrm{d}_*$), the computed fields will not be accurately modeled with this thin-sheet treatment.

How are magnetic dipoles to be incorporated? In practice, magnetic dipoles are created with a closed loop of electric current. A vertical magnetic dipole involves a loop of current essentially confined in the horizontal plane. To account for this we repeat the process used for a horizontal electric dipole where we represent the dipole by a surface current density in a thin sheet; however, we now must change the shape of the current density in the thin sheet, $\mathbf{T}$. In our dimensionless system, the surface current density for a

circular loop of wire with radius, r_0, carrying clockwise current, I_*, is given by,

$$\mathbf{T}(\mathbf{r}) = -\bar{\mathbf{z}} \times \bar{\mathbf{r}}\delta(r - r_0), \tag{5.95}$$

where $\mathbf{T}$ is now given in units of $I_* da/d_*^3$. In component form,

$$T_1(\mathbf{r}) = \delta(r - r_0)\sin\theta, \tag{5.96}$$

and

$$T_2(\mathbf{r}) = -\delta(r - r_0)\cos\theta. \tag{5.97}$$

This is a vertical magnetic dipole centered at the origin, with the dipole moment pointing downward along the z-axis. We then must find the FT of (5.96) and (5.97), which can be inserted into (5.82). To find the FT of our cylindrically symmetric loop of current we will use the Hankel transform. Consider the Fourier transform of multipole functions, g, in the horizontal plane, such that $g(\mathbf{r}) = f(r)\mathrm{e}^{im\theta}$, where $\mathbf{r} = \bar{\mathbf{x}}r\cos\theta + \bar{\mathbf{y}}r\sin\theta$. For such functions we have,

$$\mathcal{F}[g](\mathbf{k}) = 2\pi i^m \mathrm{e}^{im\phi} \int_0^\infty f(r)\, \tilde{J}_m(2\pi kr)\, r\, \mathrm{d}r, \tag{5.98}$$

where $\mathbf{k} = \bar{\mathbf{x}}k\cos\phi + \bar{\mathbf{y}}k\sin\phi$, and $\tilde{J}_m$ is a Bessel function or order m. The integral in (5.98) represents a generalized Hankel transform for multipole functions. Applied to our loop of current and recalling the sifting property of the delta function, we have,

$$\hat{T}_1(\mathbf{k}) = 2\pi i \sin\phi \int_0^\infty \delta(r - r_0)\tilde{J}_1(2\pi kr) r dr \tag{5.99}$$

$$= -2\pi i \tilde{J}_1(2\pi kr_0) r_0 \sin\phi, \tag{5.100}$$

and,

$$\hat{T}_2(\mathbf{k}) = -2\pi i \tilde{J}_1(2\pi kr_0) r_0 \cos\phi. \tag{5.101}$$

The surface current density is different for a rectangular loop of current in the horizontal plane. This geometry is often used in land surveys, as it is much simpler lay out a large rectangular loop than a circular one. Now our surface current density for a rectangle of dimensions $x_0 \times y_0$, centered at the origin, with sides aligned with the horizoal coordinate axes, is given in component form by,

$$T_1(x,y) = [\mathrm{rect}(2x/x_0)\delta(y+y_0/2) - \mathrm{rect}(2x/x_0)\delta(y-y_0/2)] \tag{5.102}$$

and

$$T_2(x,y) = [\mathrm{rect}(2y/y_0)\delta(x-x_0/2) - \mathrm{rect}(2y/y_0)\delta(x+x_0/2)]\,. \tag{5.103}$$

The FTs of these equations are then,

$$\hat{T}_1(\mathbf{k}) = \left[\frac{\sin(\pi(x_0/2)k\cos\phi)}{\pi k\cos\phi}\mathrm{e}^{\pi i y_0 k\sin\phi} - \frac{\sin(\pi(x_0/2)k\cos\phi)}{\pi k\cos\phi}\mathrm{e}^{-\pi i y_0 k\sin\phi}\right], \tag{5.104}$$

$$= \frac{2i\sin(\pi(x_0/2)k\cos\phi)\sin(\pi y_0 k\sin\phi)}{\pi k\cos\phi} \tag{5.105}$$

and analogously,

$$\hat{T}_2(\mathbf{k}) = -\frac{2i\sin(\pi(y_0/2)k\sin\phi)\sin(\pi x_0 k\cos\phi)}{\pi k\sin\phi}. \tag{5.106}$$

Notice that for both the circular and the rectangular current loops, the limit of their equivalent surface current as $k \to 0$ is zero. No energy of wavenumber $k = 0$ is produced by a finite magnetic dipole. On the other hand, $k = 0$ is the wavenumber of dominant energy for an electric dipole of finite length.

If horizontal magnetic dipoles are to be considered, an electric surface current density, $\mathbf{T}$, will not suffice; the current loop of such a dipole is perpendicular to the horizontal plane. Instead we make use of the artifice of a magnetic surface current density, $\mathbf{m}$, given in units of $I_* da/\mathrm{d}_*^2$, and a different boundary condition for magnetic current. The integral

form of (5.68) is

$$\oint_{\mathcal{P}} \mathcal{E} \cdot dl = -i \iint_{\mathcal{S}} (\mathcal{B} + \mathcal{M}) \cdot dS. \tag{5.107}$$

To derive the boundary condition across a thin sheet of magnetic current, we construct a rectangular Amperian loop which straddles the horizontal plane within which the horizontal magnetic dipole is placed. In the limit as the vertical dimension of the Amperian loop vanishes, the magnetic flux through the loop vanishes, but a surface magnetic current does not. We are left with,

$$\mathbf{E}^+ \cdot \mathbf{l} - \mathbf{E}^- \cdot \mathbf{l} = -i\mathbf{m} \cdot (\bar{\mathbf{z}} \times \mathbf{l}) = -i(\mathbf{m} \times \bar{\mathbf{z}}) \cdot \mathbf{l}. \tag{5.108}$$

Hence, in the Fourier domain, we have a new boundary condition for the horizontal electric field across a depth which contains a surface distribution of magnetic current,

$$\hat{\mathbf{E}}^+ - \hat{\mathbf{E}}^- = i\bar{\mathbf{z}} \times \hat{\mathbf{m}}. \tag{5.109}$$

In order to be able to use this boundary condition to incorporate horizontal magnetic dipoles, the point-dipole approximation must hold; that is, the finite diameter of the loop of current must be small enough to be sufficiently represented by a thin sheet of magnetic current at the frequency of interest. Given that the approximation along the vertical dimension holds, a string of magnetic dipoles in the horizontal plane is easily represented by a surface magnetic current. An example of this would be a cylinder wrapped with current-carrying wire, aligned with the x-axis, having negligible diameter but non-negligible length, L. In our dimensionless system, the surface current equivalent of the cylinder is

$$\mathbf{m}(x, y) = \text{rect}\left(\frac{x}{L}\right) \delta(y) \bar{\mathbf{x}}, \tag{5.110}$$

which in the Fourier domain becomes,

$$\hat{\mathbf{m}}(\mathbf{k}) = \frac{\sin(\pi L k \cos\phi)}{\pi k \cos\phi} \bar{\mathbf{x}}. \tag{5.111}$$

We will solve for the horizontal electric fields due to the horizontal magnetic dipole independently as we did for each of the electric source currents before. Combining (5.109) with (5.40) & (5.60), and recalling that the horizontal magnetic field is continuous across a thin sheet containing no electric current, we find the equation for the electric field below a horizontal thin sheet containing magnetic source current,

$$i\bar{\mathbf{z}} \times \hat{\mathbf{m}} = \left[{}^{s}\mathsf{M}_l^{-1} \cdot {}^{s}\mathsf{L}_l + \mathsf{I} \right] \cdot \hat{\mathbf{E}}_p^{+}. \tag{5.112}$$

Note that the solution of (5.112) strictly delivers the primary horizontal electric field below the depth where a magnetic source current exists, unlike (5.82) or (5.89). Thus in the presence of horizontal magnetic dipoles, (5.109) must be used to determine the horizontal electric fields above the source depth.

Instead of (5.50), the equation to be solved at the depth of the heterogeneous thin sheet for a model which has dipole sources driving it from above, rather than a plane wave, is given by,

$$\mathcal{F}\left[2i\underline{\tau}(\mathbf{r}) \cdot \mathbf{E}(\mathbf{r})\right] = -\hat{\mathbf{s}} + \left[\hat{\mathsf{M}}_l(\mathbf{k}) + \hat{\mathsf{L}}_l(\mathbf{k}) \right] \cdot \hat{\mathbf{E}}(\mathbf{k}), \tag{5.113}$$

where the MT primary fields have been removed and replaced by the driving field $\hat{\mathbf{s}}$, due to sources above the thin sheet. For sources above the heterogeneous thin sheet,

$$\hat{\mathbf{s}} = i\bar{\mathbf{z}} \times \hat{\mathbf{B}}_p^{-} + \hat{\mathsf{M}}_l \cdot \hat{\mathbf{E}}_p^{-}, \tag{5.114}$$

where $\hat{\mathbf{B}}_p^{-}$ and $\hat{\mathbf{E}}_p^{-}$ are the primary fields propagated down to the depth of the thin sheet. Note that when source currents reside at multiple depths (i.e., an electric dipole of finite vertical dimension), $\hat{\mathbf{B}}_p^{-}$ and $\hat{\mathbf{E}}_p^{-}$ are simply given by a sum of the primary fields resultant from a sheet of source current at each individual depth.

The theory developed here does not preclude placing the dipole sources below the thin sheet of variable conductance or even within the thin sheet itself. It is easy to see that

for sources placed below the thin sheet,

$$\hat{\mathbf{s}} = -i\bar{\mathbf{z}} \times \hat{\mathbf{B}}_p^+ + \hat{\mathsf{L}}_l \cdot \hat{\mathbf{E}}_p^+, \tag{5.115}$$

with $\hat{\mathbf{B}}_p^+$ and $\hat{\mathbf{E}}_p^+$, the primary fields propagated upward from below the thin sheet. Models with sources above and below the thin sheet are handled with a simple sum of the two independent source vectors, that from above and that from below. As for putting a horizontal electric dipole source or a vertical magnetic dipole within the thin sheet, we do not need to solve for primary fields beforehand; we merely modify equation (5.113) with a source term so that we have,

$$\mathcal{F}\left[2i\underline{\tau}(\mathbf{r}) \cdot \mathbf{E}(\mathbf{r})\right] = -i\hat{\mathbf{T}}(\mathbf{k}) + \left[\hat{\mathsf{M}}_l(\mathbf{k}) + \hat{\mathsf{L}}_l(\mathbf{k})\right] \cdot \hat{\mathbf{E}}(\mathbf{k}). \tag{5.116}$$

Placing a horizontal magnetic dipole in the thin sheet disrupts the condition of continuity of the horizontal electric field across the thin sheet, upon which the method is hinged. Horizontal magnetic dipoles placed in the thin sheet cannot be modeled in the manner presented by this chapter.

As previously implied, there is no limit to the number of current sources that can be modeled simultaneously. The only limiting factor is the size of the discrete $\mathbf{T}$, and thus the number of wavenumbers being modeled. As will be discussed in more detail in Section 5.5, inherent periodicity of the Fourier domain treatment demands that sources be placed away from the edges of the spatially discretized grid. This means that if one were to model multiple current sources simultaneously, the discretized grid would have to be large enough to encompass all of them and still have a spatial buffer of a few skin depths between them and the edge of the grid.

5.4 Method of Solution and Convergence

We turn now to the solution of equations of the type,

$$\mathcal{F}\left[\mathsf{T}(\mathbf{r}) \cdot \mathbf{E}(\mathbf{r})\right] = -\hat{\mathbf{v}}(\mathbf{k}) + \hat{\mathsf{K}}(\mathbf{k}) \cdot \hat{\mathbf{E}}(\mathbf{k}), \tag{5.117}$$

which includes (5.50), (5.65), (5.113), and (5.116). These represent inhomogeneous Fredholm equations of the second kind. With the Fourier-transform, the convolution integral of the typical integral equation method conveniently collapses into a single multiplication; the integral of the Fredholm equation now takes the form of a Fourier integral, whose numerical realization is well-established. A solution to this type of equation and the proof of its convergence were originally presented in PW; this section will elaborate slightly on the original presentation.

First, we define the linear operator,

$$\mathsf{F}_{\mathsf{S}} \cdot \hat{\mathbf{E}} = \mathcal{F}[\mathsf{S} \cdot \mathcal{F}^{-1}[\hat{\mathbf{E}}]], \tag{5.118}$$

so that we can rewrite (5.117) as,

$$\left(\hat{\mathsf{K}} - \mathsf{F}_{\mathsf{T}}\right) \cdot \hat{\mathbf{E}} = \hat{\mathbf{v}}. \tag{5.119}$$

Equation (5.119) represents a linear system whose direct solution is impractically large due to the form of $\mathsf{F}_{\underline{\mathbf{t}}}$. Therefore we appeal to classical iterative methods for solving linear systems. One of the simplest of these methods is known as the Jacobi iteration [Golub and Van Loan, 1983]. For a square system of linear equations,

$$Ax = b, \tag{5.120}$$

the Jacobi iteration uses $A = D + R$ with D containing the diagonal portion of A, and R the non-diagonal components. The advantage to this decomposition is that D has a simple inverse. Then, in a situation where the inverse of A is inaccessible, one could attempt an approximate solution for x, which we will call $x^{(k)}$, with the following Jacobi iteration,

$$x^{(k+1)} = D^{-1}\left(b - Rx^{(k)}\right),\ k = 0, 1, 2, 3 \ldots, \tag{5.121}$$

where $x^{(0)}$ is some initial guess at a solution. The repetition of (5.121) will only converge

to the true $x = A^{-1}b$ given the following property is true,

$$\rho(D^{-1}R) < 1, \tag{5.122}$$

where ρ is the spectral radius. The spectral radius of a matrix B is defined as,

$$\rho(B) \stackrel{\text{def}}{=} \max_i(|\lambda_i|), \tag{5.123}$$

where $\{\lambda_i\}$ is the set of eigenvalues of B. Note that $\rho(B) = \rho(-B)$, which we make use of later. The spectral radius is related to the convergence behavior of the power sequence of a matrix. Furthermore, it can be shown that,

$$\lim_{k\to\infty} B^k = 0 \text{ if and only if } \rho(B) < 1. \tag{5.124}$$

Then, following Golub and Van Loan [1983] by choosing ϵ^k to be the error in the k^{th} iterate, such that,

$$\epsilon^k = x^k - x, \tag{5.125}$$

and restating the Jacobi iteration as,

$$Dx^{(k+1)} = b - Rx^{(k)}, \tag{5.126}$$

we can show that,

$$\epsilon^{(k+1)} = -D^{-1}Re^{(k)} = (-D^{-1}R)^k\epsilon^{(0)}. \tag{5.127}$$

If the condition (5.122) holds, equations (5.124) and (5.127) ensure that,

$$\lim_{k\to\infty} \epsilon^k = 0, \tag{5.128}$$

and thus the Jacobi iterative process is guaranteed to converge. Not only does the spectral

radius provide a diagnostic of asymptotic behavior, it provides a bound on the rate of convergence as well. If we let rewrite (5.127) as

$$\epsilon^{(k+1)} = B^k \epsilon^{(0)}, \tag{5.129}$$

we find that we can also write,

$$\epsilon^{(k+1)} - \epsilon^{(k)} = x^{(k+1)} - x^{(k)} = (B^k - B^{k-1})\epsilon^{(0)}. \tag{5.130}$$

We will soon employ the spectral radius as the matrix norm compatible with the Euclidean vector norm, but first let us discuss another property of the spectral radius. We return the canonical eigenvalue problem:

$$Ax = \lambda x. \tag{5.131}$$

It can be easily shown that,

$$A^k x = \lambda^k x, \tag{5.132}$$

and so for the spectral radius we have,

$$\rho(A^k) = \max(|\lambda_1^k|, |\lambda_2^k|, \ldots) = \max(|\lambda_1|, |\lambda_2|, \ldots)^k = \rho(A)^k. \tag{5.133}$$

Now returning to (5.130), our equation for rate of convergence, we use the spectral norm and the triangle inequality property of a norm to get,

$$||x^{(k+1)} - x^{(k)}||_2 \leq \rho(B)^k \left(1 - \frac{1}{\rho(B)}\right) ||\epsilon^{(0)}||_2 = \alpha\rho(B)^k. \tag{5.134}$$

Thus, the 2-norm of the difference between solution vectors of successive iterations will be bounded by some constant multiplied by the k^{th} power of the spectral radius; the decline of the log-normed difference between solutions with respect to iteration number, will have a slope equal to or less than $\rho(B)$ at later iterations. This allows one to make an approximate

projection for the maximum number of iterations it should take to achieve some desired level of convergence.

Next, we note that the construction of a Jacobi iteration does not require that D be a diagonal matrix and R be a non-diagonal matrix. It only requires that D^{-1} be efficiently computable, and that $A = D + R$, which gives us license to create our own modified-Jacobi iteration to solve (5.119). We nonetheless must ensure $\rho(D^{-1}R) < 1$ in order to have an iteration that will converge.

To continue along this path we break up the diagonal tensor, $\underline{\mathbf{t}}$ into its constant and anomalous parts so that,

$$\mathsf{T}(\mathbf{r}) = \mathsf{T}_0 + \underline{\boldsymbol{\Delta}}(\mathbf{r}). \tag{5.135}$$

Then we can rewrite (5.117) as,

$$\left(\hat{\mathsf{K}} - \mathsf{T}_0\right) \cdot \hat{\mathbf{E}} = \hat{\mathbf{v}} + \mathsf{F}_{\underline{\boldsymbol{\Delta}}} \cdot \hat{\mathbf{E}}, \tag{5.136}$$

where we have extracted the linear operator with the computationally burdensome direct inverse and moved it to the right-hand side. The Jacobi-like iteration in the language of the discrete system, is then

$$\hat{e}^{(k+1)} = B^{-1}\hat{v} + B^{-1}F_{\Delta}\hat{e}^{(k)}, \quad k = 0, 1, 2, 3, \cdots . \tag{5.137}$$

We distinguish between the numerical vectors of the discrete system and the physical vectors of the continuous equations by using italic font for the former and bold font for the latter. The Fourier-domain electric field vector $\hat{e}$ is organized so that its two horizontal components are grouped in pairs for the j^{th} wavenumber such that,

$$\hat{e} = [\hat{e}^1_1 \hat{e}^2_1 \ \cdots \ \hat{e}^1_j \hat{e}^2_j \ \cdots \ \hat{e}^1_{n/2} \hat{e}^2_{n/2}], \tag{5.138}$$

where n is the number of grid cell in the discretized thin sheet. Then the matrix B is given

by,

$$B = \hat{K} - IT_0, \tag{5.139}$$

and is block diagonal with 2×2 matrices along the diagonal. The inverse of such a matrix is trivial to compute. The inverse of B is also a block diagonal matrix composed of the inverses of each 2×2 block along its diagonal.

As stated before, in order for an iteration like (5.137) to converge, $\rho(B^{-1}\mathsf{F}_\Delta)$ must be less than 1. For the anisotropic layered earth, this is difficult to prove analytically. However, once the tensor $\hat{K}$ is constructed from a given earth model, the eigenvalues of $(B^{-1}\mathsf{F}_\Delta)$ can be found numerically to provide a check on the convergence potential of a given model before the iterative procedure is begun.

The eigenvalues of $\hat{K}$ for a simpler earth model of an isotropic but inhomogeneous thin sheet sandwiched between two homogeneous, isotropic halfspaces of arbitrary conductivities *are* accessible analytically; with this, convergence can be assured for all isotropic halfspace conductivities. We turn now to placing bounds on the discrete $\rho(B^{-1}F_\Delta)$ in order to prove that the iteration (5.137) will converge. We will make use of a few properties of the spectral radius, which we state without proof:

$$\rho(AB) \leq \rho(A)\rho(B), \tag{5.140}$$

$$\rho(A - Ic) = \max_i(|\lambda_i - c|), \tag{5.141}$$

and,

$$\rho(A^{-1}) = \max_i \frac{1}{|\lambda_i|}, \tag{5.142}$$

where λ_i are the eigenvalues of A. The property of (5.140) allows us to analyze the eigenvalues of B^{-1} and F_Δ separately. In its discrete form, the Fourier transform can be represented

by a unitary matrix, G. We state the eigenvalue problem of F_Δ with the following,

$$F_\Delta x = G\Delta G^{-1}x = \lambda x, \tag{5.143}$$

where Δ is a diagonal matrix whose diagonal elements are the anomalous conductance values of the gridded thin sheet. We can rearrange (5.143) to make the following,

$$\Delta G^{-1}x = \lambda G^{-1}x. \tag{5.144}$$

We then define a new eigenvector, $u = G^{-1}x$, and a new eigenvalue equation for the same eigenvalues is given by,

$$\Delta u = \lambda u. \tag{5.145}$$

Since Δ is diagonal, it's eigenvalues, λ are simply the elements along its diagonal. Therefore we can write,

$$\rho(F_\Delta) = 2\max_n |\tau_n - \tau_0|, \tag{5.146}$$

remembering $t(\mathbf{r}) = 2i\tau(\mathbf{r})$, and n is the number of cells by which the sheet is discretized. Combining (5.141) and (5.142) we find that,

$$\rho(B^{-1}) = \max_j \frac{1}{|\lambda_j - t_0|}, \tag{5.147}$$

where λ_j are the eigenvalues of $\hat{K}$. Drawing from (5.65), (5.40), (5.60), (5.30), and (5.56), we can show that for a thin sheet sandwiched between two isotropic halfspaces,

$$\hat{\mathsf{K}} = \begin{bmatrix} (\tilde{G}_0 + \tilde{G}_1) + (\tilde{H}_0 + \tilde{H}_1)\cos 2\phi & (\tilde{H}_0 + \tilde{H}_1)\sin 2\phi \\ (\tilde{H}_0 + \tilde{H}_1)\sin 2\phi & (\tilde{G}_0 + \tilde{G}_1) - (\tilde{H}_0 + \tilde{H}_1)\cos 2\phi \end{bmatrix}, \tag{5.148}$$

where,

$$\tilde{G}_n = -\frac{2i\sigma_n + 2\pi^2 k^2}{\sqrt{2i\sigma_n + 4\pi^2 k^2}}, \tag{5.149}$$

$$\tilde{H}_n = \frac{2\pi^2 k^2}{\sqrt{2i\sigma_n + 4\pi^2 k^2}}, \tag{5.150}$$

σ_0 is the conductivity of the halfspace above, and σ_1 is the conductivity of the halfspace below the thin sheet. To find the eigenvalues of $\hat{K}$, we solve its characteristic equation given by,

$$\lambda^2 - (\hat{K}_{11} + \hat{K}_{22})\lambda + \hat{K}_{11}\hat{K}_{22} - \hat{K}_{12}\hat{K}_{21} = 0. \tag{5.151}$$

From (5.148), this becomes,

$$\lambda^2 - 2(\tilde{G}_0 + \tilde{G}_1)\lambda + (\tilde{G}_0 + \tilde{G}_1)^2 - (\tilde{H}_0 + \tilde{H}_1)^2 = 0, \tag{5.152}$$

with solutions,

$$\lambda = (\tilde{G}_0 + \tilde{G}_1) \pm (\tilde{H}_0 + \tilde{H}_1). \tag{5.153}$$

Inserting (5.149) and (5.150), these become,

$$\lambda_+ = -2i\left(\frac{\sigma_0}{\sqrt{2i\sigma_0 + 4\pi^2 k^2}} + \frac{\sigma_1}{\sqrt{2i\sigma_1 + 4\pi^2 k^2}}\right), \tag{5.154}$$

and,

$$\lambda_- = -\sqrt{2i\sigma_0 + 4\pi^2 k^2} - \sqrt{2i\sigma_1 + 4\pi^2 k^2}. \tag{5.155}$$

We now use a Taylor expansion to analyze the large-k behavior of these eigenvalues:

$$\lambda_+ = -\frac{i}{\pi k}(\sigma_0 + \sigma_1) - \frac{1}{4\pi^3 k^3}(\sigma_0^2 + \sigma_1^2) - O(k^{-5}), \tag{5.156}$$

and,

$$\lambda_- = -4\pi k - \frac{i}{2\pi k}(\sigma_0 + \sigma_1) + O(k^{-3}). \tag{5.157}$$

These expansions hold only when $\sigma_0/(2\pi^2 k^2) \leq 1$ and $\sigma_1/(2\pi^2 k^2) \leq 1$. To understand the limits of this approximation, we restore physical units to the variables, which will be denoted by brackets, for example $[\sigma_0] = \sigma_0 \sigma_*$. We quickly find the following requirements,

$$[dx] \leq \sqrt{2}\pi[\mathrm{d}_n],\ n = 0, 1, \tag{5.158}$$

that is, the sample spacing in the thin sheet, $[dx]$, must be no more than about 4.44 times larger than the skin depth in either halfspace. These requirements should be easily satisfied by a decently sampled grid. It is clear from (5.147) that the smallest λ will set the spectral radius of $\hat{B}^{-1}$; this is found on the λ_+ branch as k becomes large. The largest k on the 2D grid of τ occurs on the diagonal of a square where $k = \sqrt{2}k_0 = (\sqrt{2}dx)^{-1}$. Thus, employing the large-k approximation for λ_+, we find,

$$\rho(B^{-1}) = \left(2\tau_0 + \frac{(\sigma_0 + \sigma_1)}{\pi k_{max}}\right)^{-1} = \frac{1}{2\tau_0 + 2^{3/2} dx(\sigma_0 + \sigma_1)}. \tag{5.159}$$

Combining (5.146) and (5.159) we arrive at bound on the spectral radius for the full iteration:

$$\rho(B^{-1}\mathsf{F}_\Delta) \leq \frac{\max_n |\tau_n - \tau_0|}{\tau_0 + \sqrt{2}dx(\sigma_0 + \sigma_1)} = \rho_b. \tag{5.160}$$

This bound on the spectral radius is independent of frequency and weakly dependent on dx since it is usually much smaller than τ. Remember that we are free to choose τ_0 to be that which guarantees the best convergence. The value of τ_0 that makes ρ_b the smallest is $\tau_0 = \frac{1}{2}(\tau_{min} + \tau_{max})$, which gives the bound,

$$\rho_b = \frac{\tau_{max} - \tau_{min}}{\tau_{max} + \tau_{min} + \sqrt{2}dx(\sigma_0 + \sigma_1)}. \tag{5.161}$$

Since dx is normally chosen to be small compared to τ_{max}, ρ_b depends mostly on the ratio of the smallest to greatest value of thin-sheet conductance. Most importantly, with our chosen τ_0, the iterative method of solution presented here is guaranteed to converge as long as $\tau_{max} > 0$, and $\tau_{max} = 0$ is the case where one would not need a thin-sheet at all.

This section has presented a proof of convergence of the modified Jacobi iterative scheme for a model of a thin sheet sandwiched between two halfspaces of arbitrary conductivities. PW proved convergence of the modified Jacobi scheme for one halfspace of arbitrary conductivity below the thin sheet and a vacuum above. PW then extended the proof of convergence to encompass models with layered structure below the thin sheet. Since we have shown that adding a conducting halfspace above the thin sheet does no harm to the convergence property of our solution method, we conjecture that adding conducting layers above the thin sheet will also not harm convergence. A more rigorous proof of this property could be made by extending the arguments made in Appendix D of PW to a model with layers above and below the thin sheet.

5.5 Edge Effects and Multi-Grid Computation

The handling of the electric and magnetic fields in the spatial Fourier domain carries the implicit property of periodicity. This would not pose a constraint were our calculations done on a continuous and infinite area, i.e. over an infinite number of wavenumbers. However, the calculations discussed here take place over a finitely-sampled confined area of a rectangle. It then becomes necessary that we address the boundary conditions at the edge of our region. All the FTs previously discussed involve an integral which extends over the whole plane. The numerical FT (e.g. FFT) computes the exact integral over the whole plane as well by interpolating our given sample points with a series continuous, periodic functions—sines and cosines. A numerical FT assumes these periodic interpolating functions continue indefinitely beyond the region of computation, duplicating the fields within the region endlessly in all directions. Thus, the implicit boundary condition for the fields on one side of our rectangular region is that it must match the fields on the opposing side of the rectangle; this is the topology of a torus. A difference between the conductance of

the thin sheet on one side of the rectangle and its opposing side introduces a discontinuity in electric current which affects the fields over a broad range of wavenumbers, and therefore results in effects that can pervade far into the grid when the characteristic skin depth is comparable to the size of the modeled region.

A simple solution to this problem would be to use an ever larger grid, effectively moving the edge effects further away, and then interpret only the inner region. However, if fine-scale modeling is intended for the interpreted region, the size of the problem could become numerically unfeasible since the sample spacing of the grid must remain constant throughout. The numerical limit to using a grid much larger than the area of interest can be surmounted by using multiple grids of cascading resolution. This solution proceeds by dividing the system into long- and short-wavelength pieces. The conductance of the thin sheet decomposed into $T + S$, consisting of the large-scale, more smoothly varying T, and the residual high-wavenumber component S. The solution vector for the horizontal electric field is also split in two: $e + \epsilon$. Then inserting these into (5.117), we get,

$$\mathcal{F}\left[(T+S)(e+\epsilon)\right] = -\hat{v} + \hat{K}(\hat{e}+\hat{\epsilon}). \tag{5.162}$$

Then we define the long wavelength problem as,

$$\mathcal{F}\left[Te\right] = -\hat{v} + \hat{K}\hat{e}. \tag{5.163}$$

Subtracting (5.163) from (5.162),

$$\mathcal{F}\left[(T+S)\epsilon\right] = -\mathcal{F}[Se] + \hat{K}\hat{\epsilon}, \tag{5.164}$$

the equation governing the short wavelength fields. In (5.164) we see that the source field for the short wavelength problem is the long wavelength field, e, scattered by the short wavelength conductance, S. No new approximations have been introduced, we've only exploited the linearity of the FT. Since T by definition is smooth, we can solve (5.163) on a large, but lower resolution grid (large dx), cutting down the computational cost of moving the edges of our modeled region away from the area of interest. Then (5.164) can

be solved in the smaller area of interest at a much higher resolution after interpolating the long wavelength solution, e onto the finer grid. This example uses two grids (see Figure 5.2), but one could repeat this process on any number of inset grids with cascading resolution; this is a general multi-grid method.

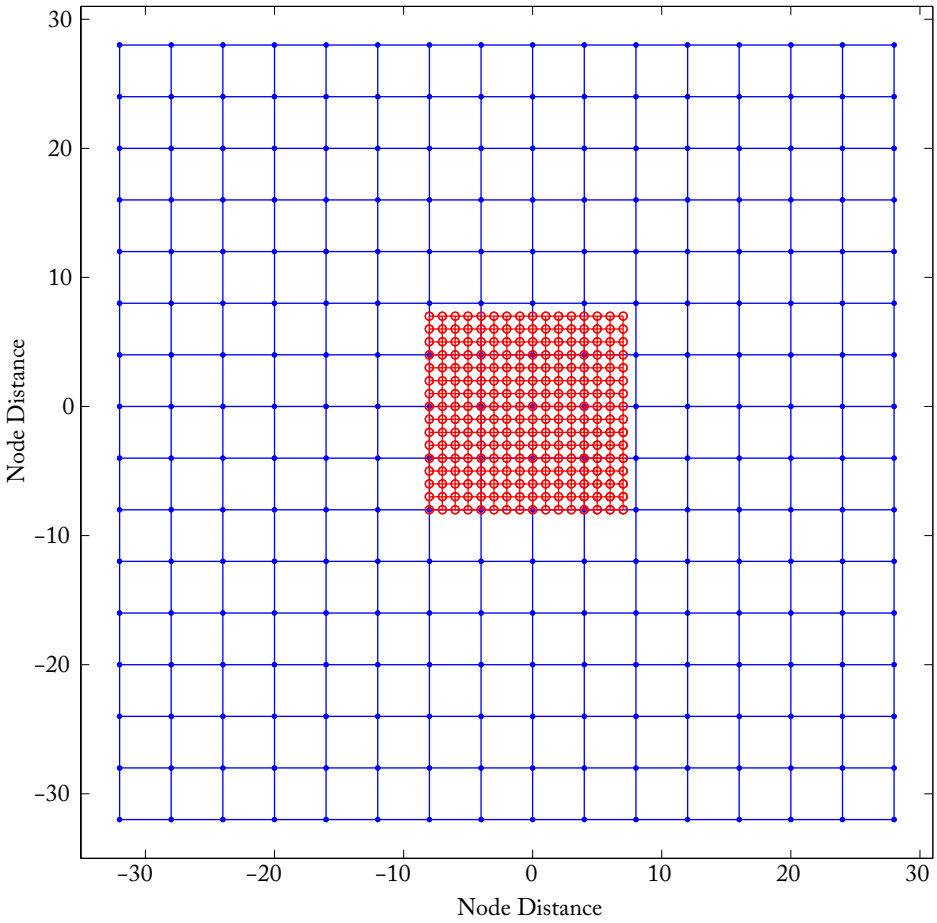

Figure 5.2: Example node spacing for the multi-grid method. Two overlapping 16×16 discretizations of the thin sheet are depicted. The blue dots signify nodes in the larger, low-resolutions grid, and the red circles signify the nodes of the inner, high-resolution grid.

In equation (5.162), $\hat{v}$ represents the MT source vector, which contains a single component at $k = 0$, the longest wavelength. Thus, it does not require a decomposition

into short- and long-wavelength components, as the multi-grid method requires of the conductance and electric field. However, when the vector $\hat{v}$ represents the primary fields from a more geometrically complicated source, say an electric dipole, it too must be decomposed. With the definition, $v = V + \nu$, we may rewrite equations (5.163) & (5.164) as,

$$\mathcal{F}\left[Te\right] = -\hat{V} + \hat{K}\hat{e}, \tag{5.165}$$

and,

$$\mathcal{F}\left[(T+S)\epsilon\right] = -\mathcal{F}[Se] - \hat{\nu} + \hat{K}\hat{\epsilon}, \tag{5.166}$$

respectively.

The key to making this multi-grid method work in practice is to ensure that ϵ, the short wavelength field, goes to zero before the edges of the smaller, high resolution grid; otherwise there again will be wrap-around effects in the smaller grid. Achieving vanishing short wavelength fields at the edges essentially requires that S be zero near the edges of the smaller grid. One way to achieve this is to create two buffer regions around the small grid of total conductance: the outer region consists of just the long wavelength conductance, T, up-sampled onto the finer resolution of the small grid; and the inner region consists of a smooth interpolation between T on its outer border, and $T + S$ on its inner border. The region inside of these two buffer zones is the new area of interest which is safe from edge effects and houses the solution of the full resolution fields. An important point here is that the edge-effects due to the shorter wavelength fields are far less pervasive than those of the longer wavelength fields, so the higher resolution grid even with its buffer zones around the edges is still smaller than the low-resolution grid for the long wavelength fields needs to be. Done properly, the only edge effects will occur around the edges of the large, low-resolution grid, which is not to be interpreted anyway; it serves merely as a means to meet boundary conditions on the edges of the small grid. Taking advantage of the fact that it will not be used for interpretation, smoothing across opposite edges of the large grid of conductance T, can further reduce the pervasiveness of edges effects on the large grid by easing discontinuities at the toroidal seams around the large grid.

5.6 Thin Sheet Validity

The thin-sheet method presented in the current chapter is always an approximation. In nature there are no sheets of electric current with zero thickness. However, one can make an argument that relative to the characteristic wavelength of the energy in a model, the fields resulting from actual currents are, in fact, indistinguishable from those of a thin sheet equivalent. This section introduces this scaling argument, and assesses the limits of a thin sheet's validity in reproducing MT responses for an archetypal model.

The source of error in a thin-sheet approximation arises from the condition of continuity of the horizontal electric field across the thin sheet. Continuity across the thin sheet forces the horizontal electric field to be continuous across the depth range in the model which is to approximated by a thin sheet. An estimate of the error that results from this restriction must be made for each particular model. The error is best expressed in the quantities that are most often analyzed with MT data: apparent resistivity and phase. Here we will only analyze the case of $k = 0$, which provides only a lower bound on error, a consequence of the lowest wavenumber of energy being subject to the weakest attenuation through the model, and therefore adheres best to the condition of continuity across the thin sheet. Nonetheless, current MT interpretation would assume that the source field above the thin sheet has only one wavenumber component, $k = 0$. Such a planar source field does undergo dispersion as it filters through the thin sheet, but for most smooth geologic models, the energy remains predominantly at low wavenumbers. One could make a more thorough error estimate which depends upon k, say for non-plane wave sources or rougher geology, but there would be no way of knowing, *a priori*, the wavenumber spectrum of that energy after it has been filtered by the thin sheet. Such a complete estimate of the error could only take place once a solution for horizontal electric field in a specific thin sheet model is achieved.

It is common practice with MT data to set an error floor of about 10% of the apparent resistivity amplitude, which sets a complementary error floor in phase of 2.86°. Taking these as the threshold of accuracy of common MT data, we wish to determine an upper bound on the frequencies for which the thin sheet model of ocean bathymetry produces

apparent resistivity and phase results that are consistent with realistic data. Attenuation of the electric field through the layers of our model will increase as the frequency of energy increases; the more attenuation there is in the layer represented by a thin sheet, the less valid the thin sheet approximation will be. Therefore, we will find a bound on the highest frequency (or lowest period) at which the thin sheet approximation produces MT responses over a 1D earth that are indistinguishable from MT data with realistic errors.

First, we wish to determine the effect errors in the modeled complex electric field have on MT apparent resistivity and phase of a layered earth. We start with the modeled electric and magnetic fields at the surface of a model. These are complex valued fields such that,

$$E = a + ib,\ H = c + id. \tag{5.167}$$

We define the MT impedance as the ratio of the complex fields,

$$Z = \frac{E}{H} = x + iy = \frac{1}{c^2 + d^2}\left[(ac + bd) + i(bc - ad)\right]. \tag{5.168}$$

Then the MT impedance phase is defined as

$$\phi = \arg Z = \arctan \frac{y}{x}. \tag{5.169}$$

We perform linear propagation of errors, which for the case of impedance phase error requires the formula,

$$\delta\phi = \left(\left|\frac{\partial\phi}{\partial a}\right|^2 \delta a^2 + \left|\frac{\partial\phi}{\partial b}\right|^2 \delta b^2 + \left|\frac{\partial\phi}{\partial c}\right|^2 \delta c^2 + \left|\frac{\partial\phi}{\partial d}\right|^2 \delta d^2 \right)^{1/2}. \tag{5.170}$$

Defining y/x as R we break up the partial differentials in (5.170) using the chain rule,

$$\frac{\partial\phi}{\partial s} = \frac{\partial\phi}{\partial R}\frac{\partial R}{\partial s}, \tag{5.171}$$

for $s \in \{a, b, c, d\}$. The first partial differential on the right hand side of (5.171) is well

known,

$$\frac{\partial \phi}{\partial R} = \frac{1}{1+R^2} = \frac{(ac+bd)^2}{(ac+bd)^2+(bc-ad)^2}. \tag{5.172}$$

For the real part of E, we find that,

$$\frac{\partial R}{\partial a} = \frac{-d(ac+bd)-c(bc-ad)}{(ac+bd)^2} = \frac{-b(c^2+d^2)}{(ac+bd)^2}, \tag{5.173}$$

which when combined with (5.172) gives,

$$\frac{\partial \phi}{\partial a} = -\frac{b}{|E|^2}, \tag{5.174}$$

by noticing that

$$\frac{(ac+bd)^2+(bc-ad)^2}{c^2+d^2} = |H|^2|Z|^2 = |E|^2. \tag{5.175}$$

For the imaginary part of E, we find that,

$$\frac{\partial R}{\partial b} = \frac{c(ac+bd)-d(bc-ad)}{(ac+bd)^2} = \frac{a(c^2+d^2)}{(ac+bd)^2}, \tag{5.176}$$

which we combine with (5.172) to get,

$$\frac{\partial \phi}{\partial b} = \frac{a}{|E|^2}. \tag{5.177}$$

For the real part of H, we find that,

$$\frac{\partial R}{\partial c} = \frac{d(a^2+b^2)}{(ac+bd)^2}, \tag{5.178}$$

which when combined with (5.172), gives,

$$\frac{\partial \phi}{\partial c} = \frac{d}{|H|^2}, \tag{5.179}$$

by noticing that

$$\frac{(ac+bd)^2+(bc-ad)^2}{a^2+b^2} = |E|^2/|Z|^2 = |H|^2. \tag{5.180}$$

For the imaginary part of H, we find that,

$$\frac{\partial R}{\partial d} = \frac{-c(a^2+b^2)}{(ac+bd)^2}, \tag{5.181}$$

which we combine with (5.172) to get,

$$\frac{\partial \phi}{\partial d} = -\frac{c}{|H|^2}. \tag{5.182}$$

Plugging (5.174), (5.177), (5.179), and (5.182) into (5.170) we find

$$\delta\phi = \left[\left(\frac{b}{|E|}\right)^2\left(\frac{\delta a}{|E|}\right)^2 + \left(\frac{a}{|E|}\right)^2\left(\frac{\delta b}{|E|}\right)^2 + \left(\frac{d}{|H|}\right)^2\left(\frac{\delta c}{|H|}\right)^2 + \left(\frac{c}{|H|}\right)^2\left(\frac{\delta d}{|H|}\right)^2\right]^{1/2}. \tag{5.183}$$

Next we shall examine the effect on apparent resistivity. Apparent resistivity is defined as,

$$\rho_a = \frac{1}{\mu\omega}\left|\frac{E}{H}\right|^2 = \frac{1}{\mu\omega}\left(\frac{a^2+b^2}{c^2+d^2}\right). \tag{5.184}$$

Again we use linear propagation of errors. Looking for the fractional error in apparent resistivity, we use,

$$\frac{\delta\rho_a}{\rho_a} = \frac{1}{\rho_a}\left(\left|\frac{\partial\rho_a}{\partial a}\right|^2\delta a^2 + \left|\frac{\partial\rho_a}{\partial b}\right|^2\delta b^2 + \left|\frac{\partial\rho_a}{\partial c}\right|^2\delta c^2 + \left|\frac{\partial\rho_a}{\partial d}\right|^2\delta d^2\right)^{1/2}. \tag{5.185}$$

We quickly find the partial differentials with respect to the electric field components in (5.185) to be,

$$\frac{\partial\rho_a}{\partial s} = \frac{2s}{\mu\omega|H|^2} = \frac{2s\rho_a}{|E|^2}, \tag{5.186}$$

for $s \in \{a, b\}$, and those with respect to the magnetic field components in (5.185) to be,

$$\frac{\partial \rho_a}{\partial q} = \frac{-2q\rho_a}{|H|^2}, \tag{5.187}$$

for for $q \in \{c, d\}$. Plugging (5.184), (5.186), and (5.187) into (5.185) we find,

$$\frac{\delta\rho_a}{\rho_a} = 2\left[\left(\frac{a}{|E|}\right)^2\left(\frac{\delta a}{|E|}\right)^2 + \left(\frac{b}{|E|}\right)^2\left(\frac{\delta b}{|E|}\right)^2 + \left(\frac{c}{|H|}\right)^2\left(\frac{\delta c}{|H|}\right)^2 + \left(\frac{d}{|H|}\right)^2\left(\frac{\delta d}{|H|}\right)^2\right]^{1/2}. \tag{5.188}$$

In the case of the thin sheet modeling where H is not a variable in itself, but a quantity linked to the electric field by an impedance relationship; we must modify the error formulae. We simply note that

$$H = c + id = Z^{-1}E = \left(\frac{x}{|Z|} - i\frac{y}{|Z|}\right)(a + ib) = \frac{1}{|Z|}\left[(ax + by) + i\,(bx - ay)\right]. \tag{5.189}$$

Then we can show that,

$$\left(\frac{\delta c}{|H|}\right)^2 = x^2\left(\frac{\delta a}{|E|}\right)^2 + y^2\left(\frac{\delta b}{|E|}\right)^2, \tag{5.190}$$

$$\left(\frac{\delta d}{|H|}\right)^2 = y^2\left(\frac{\delta a}{|E|}\right)^2 + x^2\left(\frac{\delta b}{|E|}\right)^2, \tag{5.191}$$

$$\left(\frac{c}{|H|}\right)^2 = \left(x\frac{a}{|E|} + y\frac{b}{|E|}\right)^2, \tag{5.192}$$

and

$$\left(\frac{d}{|H|}\right)^2 = \left(x\frac{b}{|E|} - y\frac{a}{|E|}\right)^2. \tag{5.193}$$

Finally, (5.183) and (5.188) slightly rearranged and modified for magnetic fields fixed to a

variable electric field are,

$$\delta\phi^2 = \left(\frac{b}{|E|}\right)^2\left(\frac{\delta a}{|E|}\right)^2 + \left(\frac{a}{|E|}\right)^2\left(\frac{\delta b}{|E|}\right)^2 + \dots \\ \cdots + \left(x\frac{b}{|E|} - y\frac{a}{|E|}\right)^2\left(x^2\left(\frac{\delta a}{|E|}\right)^2 + y^2\left(\frac{\delta b}{|E|}\right)^2\right) + \dots \\ \cdots + \left(x\frac{a}{|E|} + y\frac{b}{|E|}\right)^2\left(y^2\left(\frac{\delta a}{|E|}\right)^2 + x^2\left(\frac{\delta b}{|E|}\right)^2\right), \quad (5.194)$$

and

$$\left(\frac{\delta\rho_a}{2\rho_a}\right)^2 = \left(\frac{a}{|E|}\right)^2\left(\frac{\delta a}{|E|}\right)^2 + \left(\frac{b}{|E|}\right)^2\left(\frac{\delta b}{|E|}\right)^2 + \dots \\ \cdots + \left(x\frac{a}{|E|} + y\frac{b}{|E|}\right)^2\left(x^2\left(\frac{\delta a}{|E|}\right)^2 + y^2\left(\frac{\delta b}{|E|}\right)^2\right) + \dots \\ \cdots + \left(x\frac{b}{|E|} - y\frac{a}{|E|}\right)^2\left(y^2\left(\frac{\delta a}{|E|}\right)^2 + x^2\left(\frac{\delta b}{|E|}\right)^2\right). \quad (5.195)$$

With (5.194) and (5.195) we have formulae for estimating errors in MT data that result from relative errors in an electric field calculation. Now, using these formulae we will estimate a bound in frequency for validity of the thin sheet in representing some archetypal models of an ocean. To do this we will compute the true electric field values for a range of oceanic layered models: first, we will keep the lower crust and mantle structure fixed to the Heinson and Constable [1992] model, but will vary the depth of the ocean, and the conductivity of the uppermost 2 km of the crust; and second, we will place halfspaces of varying conductivity below an ocean whose depth we will again vary. For each of these 1D models we will treat the vertical attenuation of the horizontal electric field through the ocean layer as modeling errors, δa and δb, inherent to the thin sheet method. Using (5.194) and (5.195), for each model we will search for the frequency at which the attenuation in the real and imaginary parts of the electric field results in an error greater than 10% in apparent resistivity or greater than 2.86° in phase. This frequency will be the upper bound at which the thin sheet model is deemed consistent with realistic MT data.

Again, our layered model consists of a layer of seawater conductivity representing

the ocean, underlain by of a set of layers of uniform conductivities representing the earth. We wish to calculate the electric field at the top of the layered model, E_0, as well as at the base of the ocean layer, E_1. As a measure of attenuation to be used in (5.194) and (5.195), we will then calculate the relative difference between the real and imaginary parts of these electric fields:

$$\frac{\delta a}{|E|} = \frac{\Re(E_0 - E_1)}{|E_0|}. \tag{5.196}$$

and

$$\frac{\delta b}{|E|} = \frac{\Im(E_0 - E_1)}{|E_0|}. \tag{5.197}$$

We start by determining the plane-wave impedance of an N-layered isotropic earth. We will be working in full physical units, following a derivation found in Ward and Hohmann [1988]. First, we define the impedance observed at the top of the n-th layer as

$$Z_n = \frac{E_{n-1}}{H_{n-1}} \tag{5.198}$$

where E_n and H_n are the horizontal and mutually orthogonal electric and magnetic field values, respectively, as measured at the base of the n-th layer. Z_n is computed by applying the following recursive formula starting at the base of the stack of layers:

$$Z_n = \zeta_n \frac{Z_{n+1} + \zeta_n \tanh(ik_n h_n)}{\zeta_n + Z_{n+1} \tanh(ik_n h_n)} \tag{5.199}$$

where

$$k_n = -i\mu_0 \omega \sigma_n \tag{5.200}$$

is the complex wavenumber in the material of the n-th layer, h_n is the thickness of that

layer, and

$$\zeta_n = \frac{\omega\mu_0}{k_n} \tag{5.201}$$

is that layer's intrinsic impedance. By setting $h_N = \infty$ we see that $Z_N = \zeta_N$ for the half space at the base of the layered model. From (5.198) we see that the electric field at the top of our layered model is given by

$$E_0 = Z_1 \frac{B_0}{\mu_0}. \tag{5.202}$$

Again borrowing from Ward and Hohmann [1988], we have

$$E_n = E_{n-1} / \left(\cosh(ik_n h_n) + \frac{\zeta_n}{Z_{n+1}} \sinh(ik_n h_n) \right). \tag{5.203}$$

Combining (5.202) and (5.203), the relative attenuation of the horizontal electric field through the ocean layer is

$$\frac{E_0 - E_1}{|E_0|} = \frac{Z_1}{|Z_1|} \left[1 - \frac{Z_2}{Z_2 \cosh(ik_1 h_1) + \zeta_1 \sinh(ik_1 h_1)} \right]. \tag{5.204}$$

In Figures 5.3 and 5.4 we have plotted the lower bound in terms of period at which the thin sheet approximation is valid, under the pre-described conditions, for a range of layered models. It is apparent that the inaccuracy of the thin sheet approximation is far more sensitive to the ocean depth than it is to the seafloor resistivity, except, of course when the seafloor resistivity nears that of seawater. Also, the lower bounds in period for the MT phase are higher than the lower bounds in period for MT apparent resistivity, a consequence of the thin sheet model having greater difficulty reproducing the imaginary component of the electric fields.

Figures 5.5 and 5.6 are similar to 5.3 and 5.4 with the exception that for each of the models, the resistivity below the seafloor is uniform. With this modification, we see that the dependence of the bound on thin sheet validity with seafloor resistivity arrises at higher resistivity values, especially in the thicker-ocean models, compared to the same

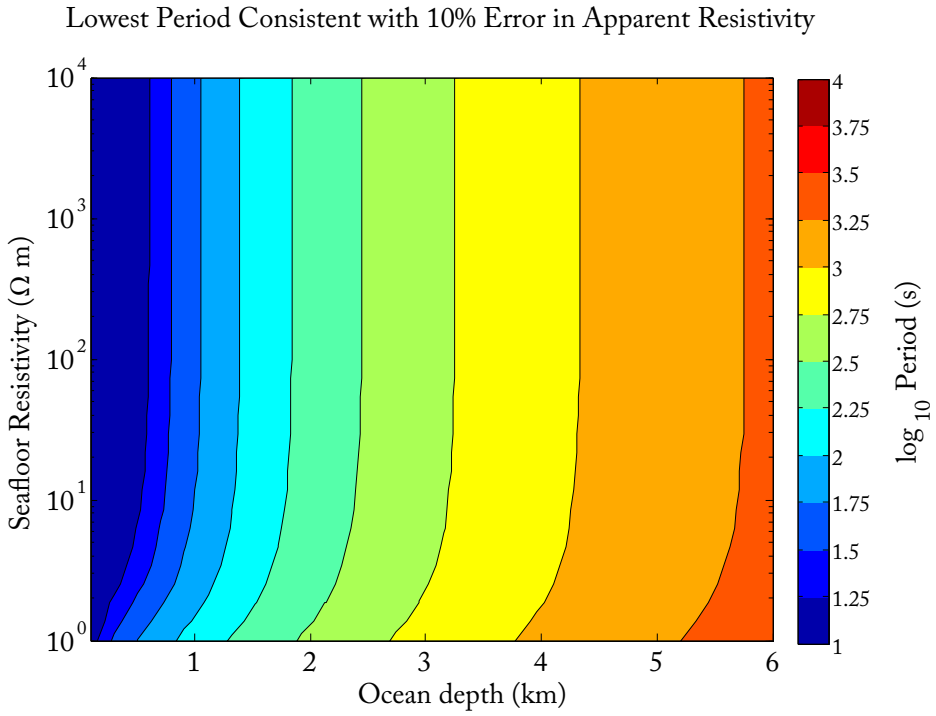

Figure 5.3: Lower bound in period for which a thin sheet calculation of a given model is consistent with a 10% error in MT apparent resistivity. The bounds were calculated over models that range in thickness of an ocean layer, and resistivity of the first 2 km below the seafloor. Beyond 2 km below the seafloor, all models have the layered structure used in Heinson and Constable [1992].

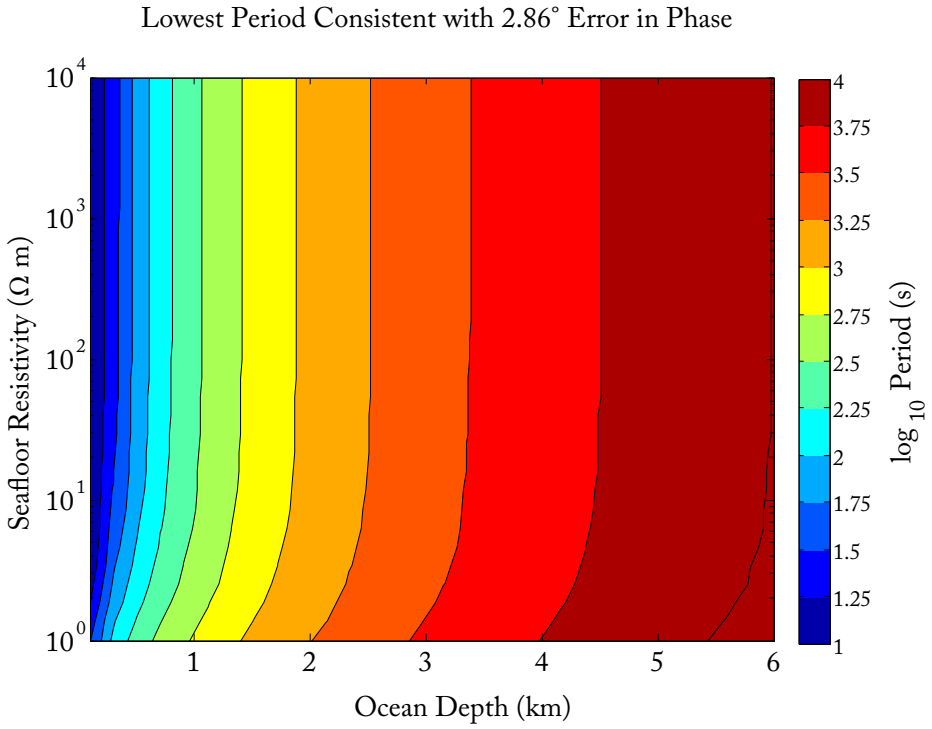

Figure 5.4: Lower bound in period for which a thin sheet calculation of a given model is consistent with a 2.86° error in MT phase. The bounds were calculated over models that range in thickness of an ocean layer, and resistivity of the first 2 km below the seafloor. Beyond 2 km below the seafloor, all models have the layered structure used in Heinson and Constable [1992].

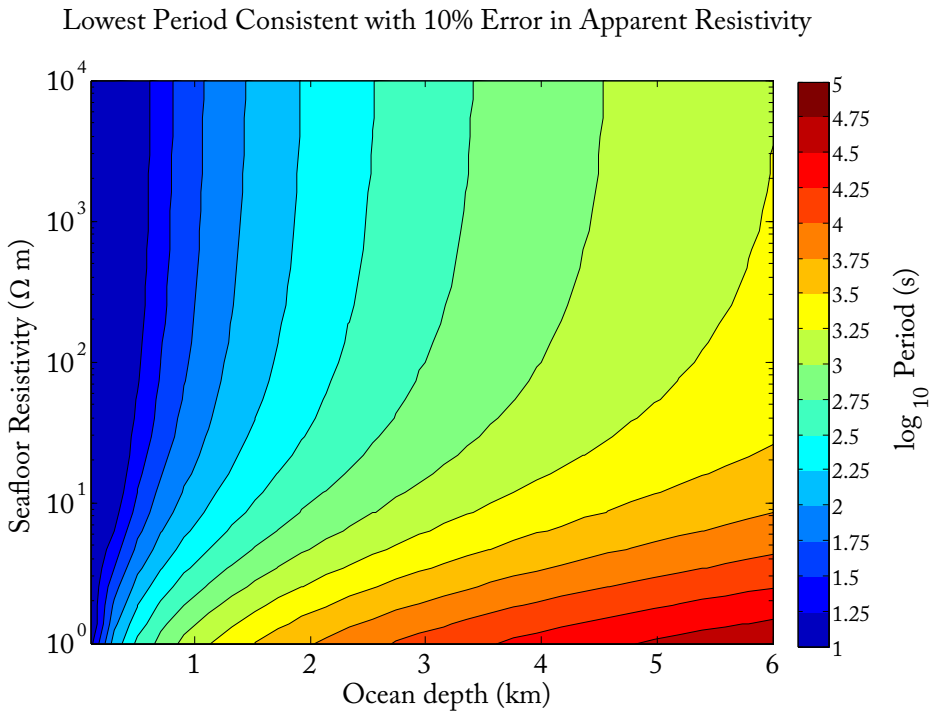

Figure 5.5: Lower bound in period for which a thin sheet calculation of a given model is consistent with a 10% error in MT apparent resistivity. The bounds were calculated over models that range in thickness of an ocean layer, and resistivity of a halfspace below the seafloor.

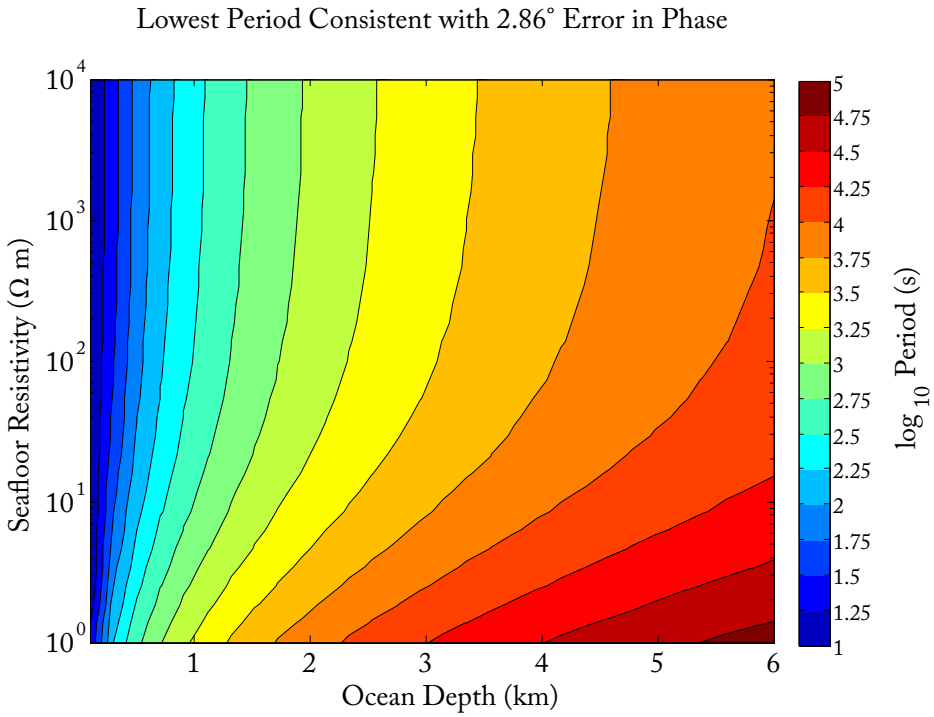

Figure 5.6: Lower bound in period for which a thin sheet calculation of a given model is consistent with a 2.86° error in MT phase. The bounds were calculated over models that range in thickness of an ocean layer, and resistivity of a halfspace below the seafloor.

bound for the Heinson and Constable [1992] layered models. These figures illustrate that the bound on the thin sheet validity will vary both with ocean depth and the resistivity structure below the seafloor in a nonlinear way. Therefore estimates of thin sheet validity must be made for each specific model using the algorithm presented in this section.

5.7 Propagation of Fields

The solution of equations of the type (5.50) yields only the horizontal electric field within the thin sheet. The quantities analyzed in practice are not the fields themselves but transfer functions between them, such as the magnetotelluric impedance tensor. These transfer functions require the knowledge of all the components of the electric and magnetic fields. We now describe how the other components of the fields can be calculated throughout the model domain once a solution for the horizontal electric field within the thin sheet has been achieved.

We start with all the fields at the depth of the thin sheet, where a distinction must be made between the fields above and below the thin sheet, as it constitutes a discontinuity in the horizontal current density. The horizontal electric field, following (5.31), will be the same above and below the thin sheet. Given the horizontal electric field, the horizontal magnetic field below the thin sheet is found with equation (5.40). A rearrangement of (5.48) yields the horizontal magnetic field above the thin sheet:

$$\hat{\mathbf{B}}^{-} = \hat{\mathbf{B}}^{+} + 2\bar{\mathbf{z}} \times \mathcal{F}\left[\underline{\tau}(\mathbf{r}) \cdot \mathbf{E}(\mathbf{r})\right]. \tag{5.205}$$

Using (5.5) and (5.6), the vertical fields, anywhere in the model, can then be derived from their complementary horizontal fields:

$$\hat{B}_3 = -2\pi\bar{\mathbf{z}} \cdot (\mathbf{k} \times \hat{\mathbf{E}}), \tag{5.206}$$

and

$$\hat{E}_3 = \frac{\pi i}{\nu_n \sigma_n}\bar{\mathbf{z}} \cdot (\mathbf{k} \times \hat{\mathbf{B}}). \tag{5.207}$$

However, (5.207) is undefined in regions of the model where the vertical conductivity goes to zero, i.e., a halfspace of air above the thin sheet. We must turn to another method for the derivation of the vertical electric field. Instead we use (5.18) and the definition of the admittance tensor, (5.59), to get the electric field just above the thin sheet,

$$\hat{E}_3^- = \frac{2\pi i}{2i\sigma_n\nu_n + 4\pi^2 k^2}(\mathbf{k}\cdot\mathsf{C}_0^{-1}\cdot\hat{\mathbf{E}}), \tag{5.208}$$

where C_1 could replace C_0 to get the electric field below the thin sheet. Inserting (5.66) into (5.208), we have the formula for the vertical electric field above the thin sheet and within a perfectly insulating halfspace:

$$\hat{E}_3^- = \frac{i}{k}(\mathbf{k}\cdot\hat{\mathbf{E}}), \quad \text{when } \sigma = 0 \text{ for } z < z_0. \tag{5.209}$$

In order to propagate the values of the horizontal fields at the thin sheet into other portions of the model domain, the vertical derivatives of the electric field above and below the thin sheet are needed. Once all of the horizontal and vertical fields above and below the thin sheet are known, equation (5.5) provides,

$$\hat{\mathbf{E}}' = 2\pi i\mathbf{k}\hat{E}_3 + i\bar{\mathbf{z}}\times\hat{\mathbf{B}}. \tag{5.210}$$

Now, armed with the values of the horizontal fields and their vertical derivatives above and below the thin sheet, we can use the machinery developed in Sections 5.1 & 5.2 for propagating the horizontal electric field and its vertical derivative away from the thin sheet, either upward or downward through the layers. With the electric field and its vertical derivative known at any depth, calculation of the magnetic field at any depth is straightforward. A combination of (5.18) and (5.15) relates the horizontal magnetic field to the vertical derivative of the horizontal electric field:

$$\hat{\mathbf{B}} = i\bar{\mathbf{z}}\times\left[\mathsf{I} - \frac{4\pi^2}{2i\sigma_n\nu_n + 4\pi^2 k^2}\mathbf{k}\mathbf{k}\right]\cdot\hat{\mathbf{E}}'. \tag{5.211}$$

It is important to note that this method for the propagation of fields applies only to source-

free depths. The modification of this method to include depths where sources occur requires the source-modified boundary conditions presented in Section 5.3.

5.8 MT Calculation around a Gaussian Seamount

This section provides an illustration of the thin sheet modeling capability using the simple model of a Gaussian-shaped seamount (see Figure 5.7). The seamount will have a maximum height of 3.5 km and resides in a water layer with a maximum thickness of 4 km. The seamount shape is governed by a 2D symmetric Gaussian function whose radius at half-maximum is 5.98 km. The conductivity of the water is 3.3 S m^{-1}, while the layered conductivity structure below the seafloor is made to match that given in Heinson and Constable [1992], depicted in Figure 5.8, and also used in Section 5.6. The period to be modeled is 5000 s. Were there no seamount, the apparent resistivity measured on the seafloor over the given this 1D stack of layers and period, would be 244.99 Ωm and the impedance phase would be 73.59°. The seamount is integrated into conductance of a thin sheet comprising a square grid of dimensions 120×120 km discretized into 512×512 cells. This affords a sample spacing of 470 m. This thin-sheet calculation requires only a few seconds on a modern computer.

Figures 5.9 & 5.10 plot the anomalous apparent resistivity, and phase, respectively, of the xy component of the impedance tensor as measured at the base of the thin sheet representation of the seamount. A single thin sheet method was used for this calculation. Due to the radial symmetry of the seamount, plots of the yx component of the impedance tensor are given simply by a 90° rotation of Figures 5.9 & 5.10. The anomaly is defined relative to the 1D value at the seafloor were there no seamount. The black line outlines a radius of 15 km, three standard deviations of the Gaussian seamount; there is essentially no seamount topography outside of this circle. The error in the thin sheet approximation for this model, propagated for $k = 0$ as described in Section 5.6, is 1.60% in apparent resistivity and 2.55° in phase.

The xy component of the impedance tensor, in a 1D sense, involves current induced along the x-direction by a driving magnetic field along the y-direction; these are the primary

fields. In the 3D world the primary, x-directed currents induced in the water column are impeded as they meet the higher resistivity of the seamount flanks. This causes a charge buildup on the faces of the seamount that are normal to the direction of primary current flow. The charge buildup has the effect of turning the seamount into an electric dipole of sorts, whose orientation opposes the primary current flow. Thus, along the flanks of the seamount that are normal to the primary current flow, the seamount dipole creates an opposing electric field, a negative electric field anomaly, which results in a "conductive" apparent resistivity anomaly; along the flanks of the seamount parallel to the predominant current flow, the seamount dipole creates a supporting electric, a positive electric fields anomaly, which results in a "resistive" apparent resistivity anomaly. This is the description of a galvanic effect, as it involves a build up of charge at the conductivity contrast produced by a seamount. The phase anomaly indicates that there is also an inductive effect, one which requires a more complicated explanation that is beyond the scope of this section.

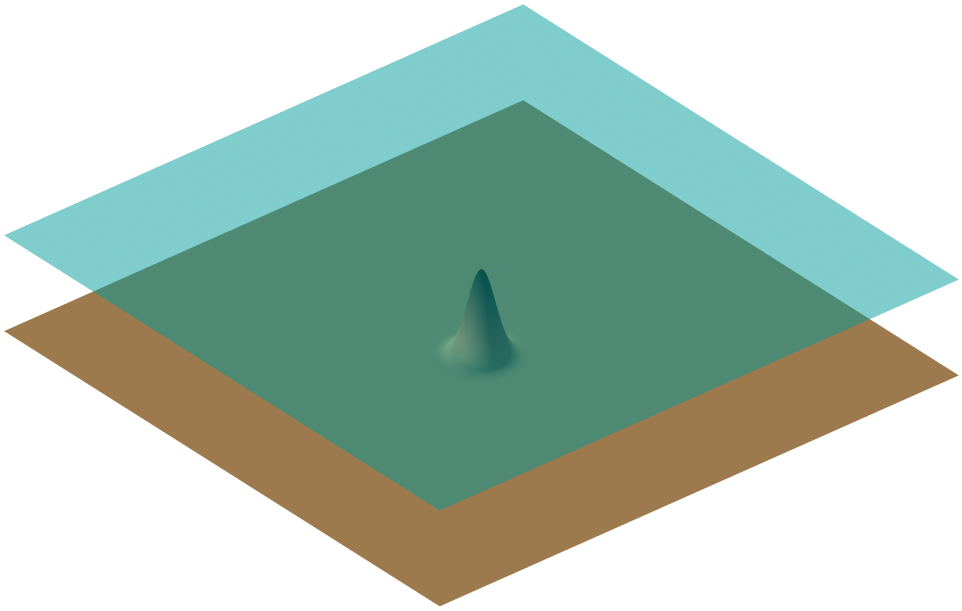

Figure 5.7: Illustation of the Gaussian seamount on the 120 $\times$ 120 km square in a 4 km deep ocean.

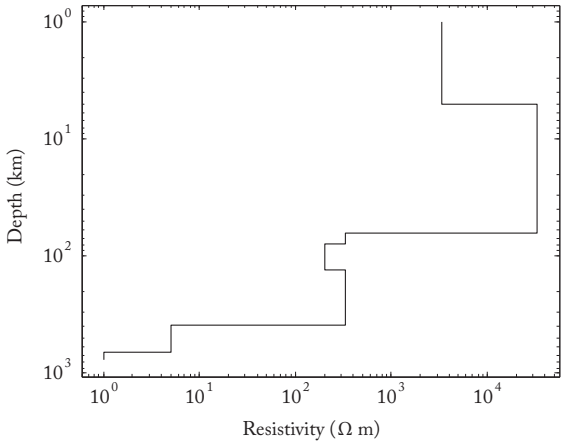

Figure 5.8: Layered resistivity model placed below the seafloor in the Gaussian seamount illustration. Layered model taken from Heinson and Constable [1992].

In 1D- and 2D-conductivity environments, the diagonal components of the impedance tensor, oriented strike perpendicular or parallel in the case of 2D, are zero everywhere; they are not zero, in general, for 3D-conductivity structure like the example of a Gaussian seamount. Figure 5.11 plots the apparent resistivity and phase of the xx component of the impedance tensor. Again, a plot of the yy component can be reproduced by rotating the plots in Fig. 5.11 by a positive 90°. The phase of Z_{xx} and Z_{yy} is divided into four quadrants centered around the peak of the seamount. Neighboring quadrants are are identical with the exception that they are 180° out of phase from each other. This produces an important consequence in this case of the radially symmetric seamount, that

$$Z_{xx} + Z_{yy} = 0 \tag{5.212}$$

everywhere. The tensor invariant, s, known as the "Swift skew", is given by,

$$s = \frac{|Z_{xx} + Z_{yy}|}{|Z_{xy} - Z_{yx}|}. \tag{5.213}$$

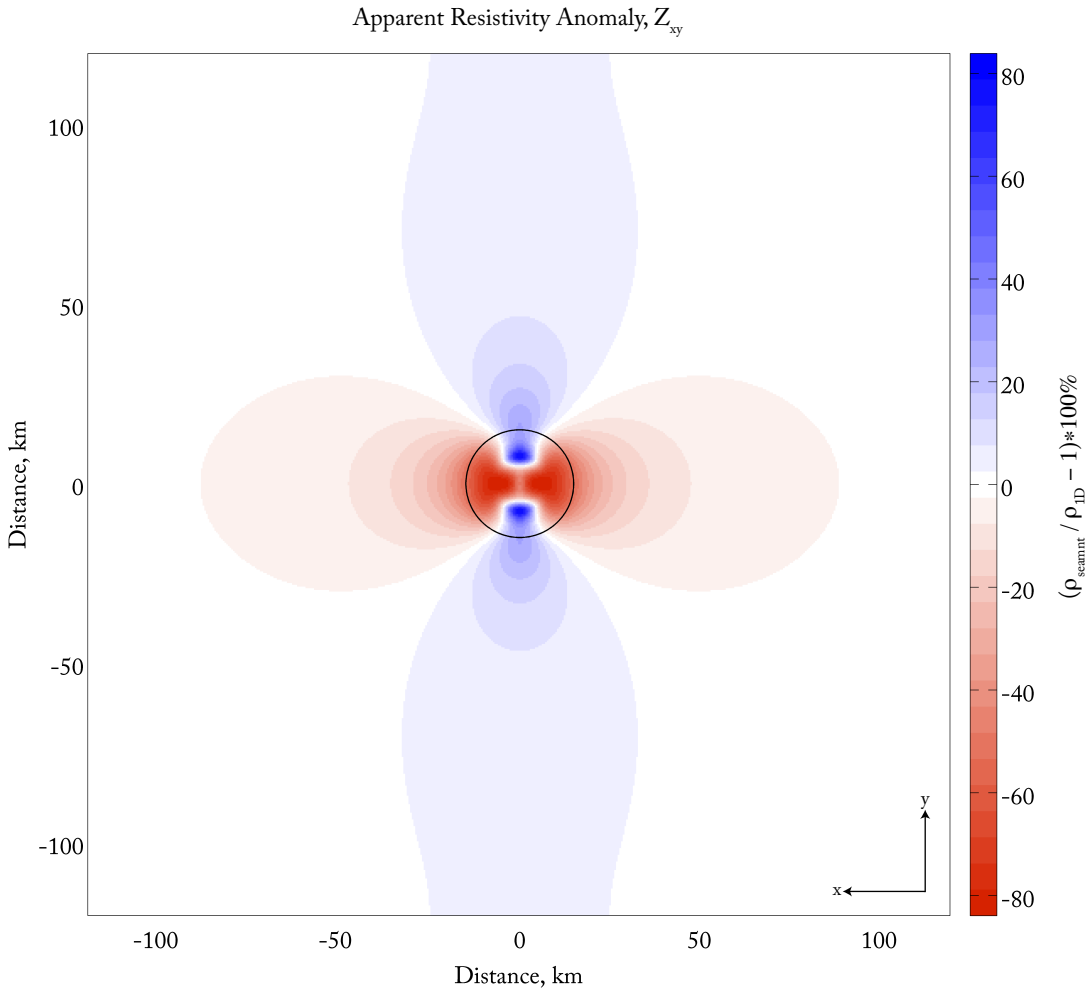

Figure 5.9: Percentage apparent resistivity anomaly in Z_{xy} caused by the Gaussian seamount relative to the 1D background plotted in Fig. 5.8, as would be measured on the seafloor. The black line outlines the radius of three standard deviations of the Gaussian seamount, the putative edge of the seamount. Blue colors represent a positive or "resistive" anomaly, and the red colors represent a negative or "conductive" anomaly produced by the existence of a seamount.

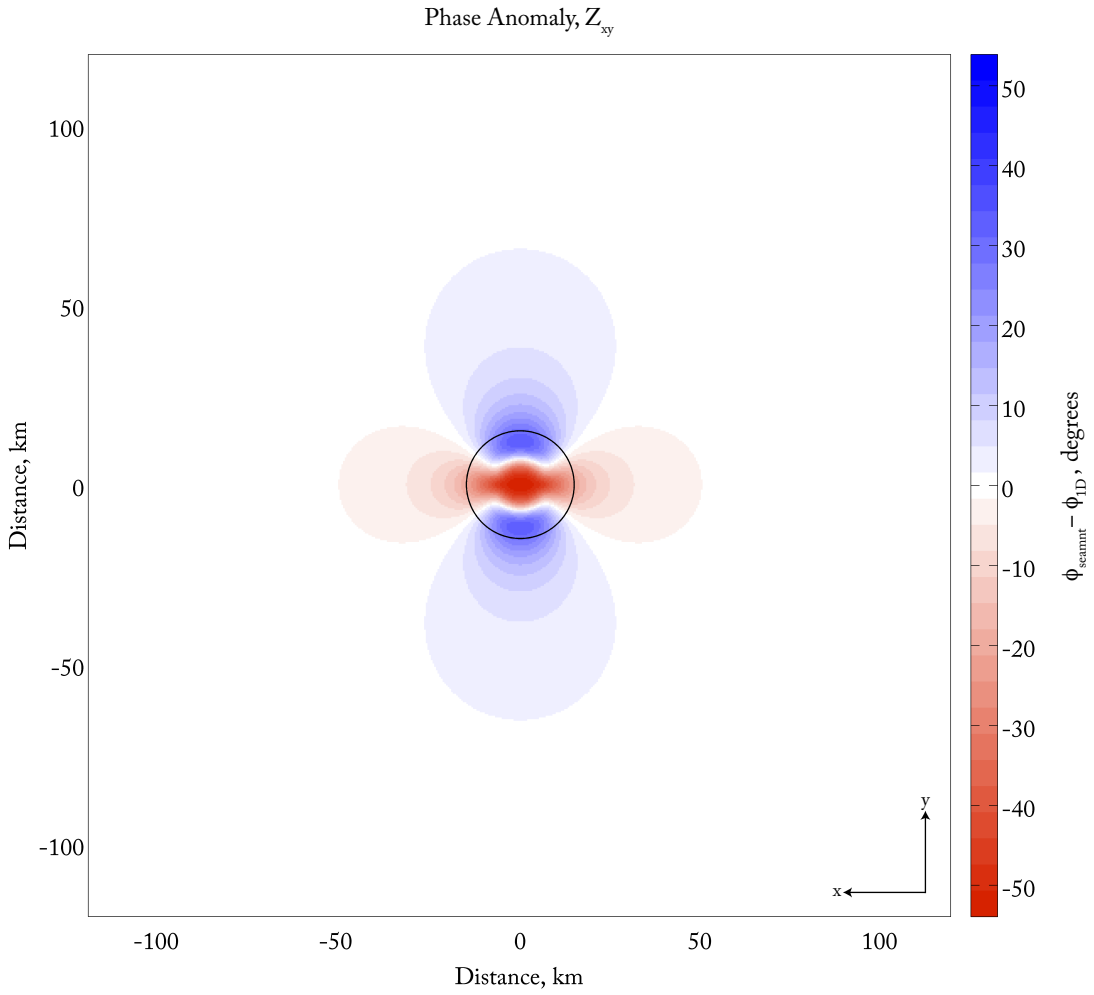

Figure 5.10: Phase anomaly in Z_{xy} caused by the Gaussian seamount relative to the 1D background plotted in Fig. 5.8, as would be measured on the seafloor. The black line outlines the radius of three standard deviations of the Gaussian seamount, the putative edge of the seamount. Blue colors represent a positive anomaly, and the red colors represent a negative anomaly produced by the existence of a seamount.

It is named after C. M. Swift [Swift, 1967], who first suggested its use in identifying 3D structures from impedance tensor data alone (see also Section 3.5). Swift propagated the now widely used rule of thumb that impedances with Swift Skews equal to or greater than 0.2 cannot be interpreted with 2D modeling. It is important to note that this precept does not state that all impedances with Swift Skews less than 0.2 *can* be interpreted with 2D modeling. In fact, by noting (5.212), we see that the Gaussian seamount is a perfect example of an obviously 3D structure that produces a Swift Skew exactly equal to zero everywhere. If one were intent upon 2D modeling and chose to blindly keep all data with a Swift Skew of less than 0.2, they would have no reason to reject data on or around the Gaussian seamount. Based on the anomalies in Figures 5.9 & 5.10, it is assured that the true subsurface resistivities would be unrecoverable from a 2D inversion of such data.

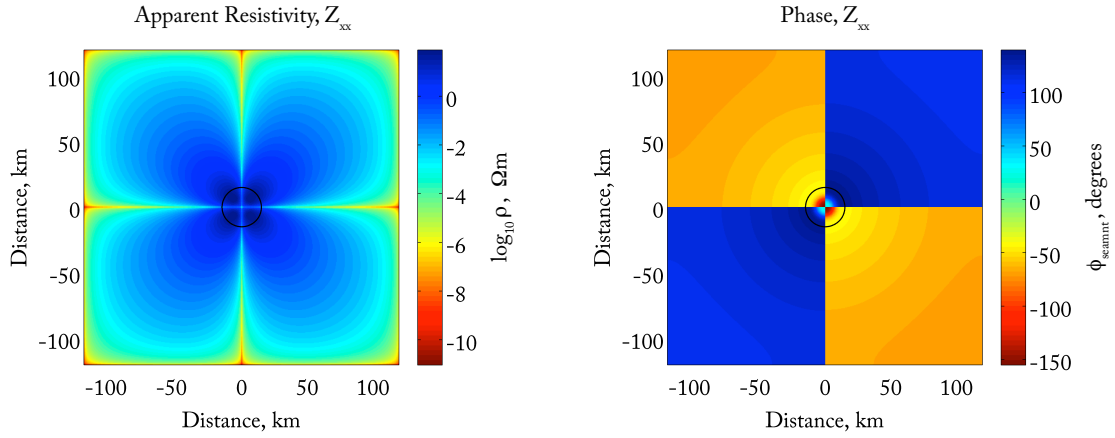

Figure 5.11: Apparent resistivity and phase of Z_{xx} for the Gaussian seamount. The black line again outlines the edge of the seamount.

A better diagnostic of 3D conductivity structure from the impedance tensor is the analysis of polar diagrams. Polar diagrams provide a way of visualizing the relative sizes of diagonal and off-diagonal (3D vs. non-3D) components of the impedance tensor as it is rotated about one full rotation. In Figure 5.12, polar diagrams are plotted for many

locations on the seafloor around the seamount. The red lines plot the radial length,

$$P_{xy}(\vartheta) = |Z^{\vartheta}_{xy}|, \tag{5.214}$$

while the blue lines plot the radial length,

$$P_{xx}(\vartheta) = |Z^{\vartheta}_{xx}|, \tag{5.215}$$

as ϑ, the angle of tensor rotation, varies from 0-360 degrees (see also Section 3.5). The impedance over a 1D earth has $Z_{xy} = -Z_{yx}$ and $Z_{xx} = Z_{yy} = 0$ regardless of rotation. In this case, $P_{xy}(\vartheta)$ traces a perfect circle, and $P_{xx}(\vartheta)$ consists of one point at the origin. The impedance in a 2D earth has $Z_{xy} \neq Z_{yx}$, but still has zeros along the diagonal. In this case $P_{xx}(\vartheta)$ makes a four-leafed clover shape, whose symmetric leaves are oriented either $\pm 45^{\circ}$ or $\pm 135^{\circ}$ to the strike of the 2D conductivity structure. For 2D structure, $P_{xy}(\vartheta)$ can take a variety of shapes, ranging from an oval to a peanut shape, with their major and minor axes oriented either parallel or perpendicular to the 2D strike. For impedances measured around 3D earth structures, $P_{xx}(\vartheta)$ is no longer required to have symmetric leaves (see also Figure 3.13). Yet, there is no such visible evidence of 3D structures in the polar diagrams around the seamount. Furthermore, in Figure 5.12, there is a location that exhibits a perfectly 1D polar diagram, directly below the peak of the seamount. It is reasonable to assume that this property of the polar diagram would hold on top of the peak of the seamount as well. It seems that impedances measured atop a radially symmetric seamount, would have polar diagrams that predict purely 1D structure below. However, the contours of apparent resistivity anomaly in Figure 5.12 make clear that the impedance measured directly below the seamount does not reflect the 1D structure below; it is biased by more than 40%. We find that polar diagrams measured near 3D structures with some level of symmetry are misleading. They offer little evidence of 3D structure, but rather, in locations of symmetry, imply perfectly 1D structure. Another one-sided rule of thumb, like that applied to Swift Skews, then must apply to the polar diagrams: while 3D-looking polar diagrams always indicate 3D conductivity structure, 1D- or 2D-looking polar diagrams do not guarantee 1D or even 2D conductivity structure.

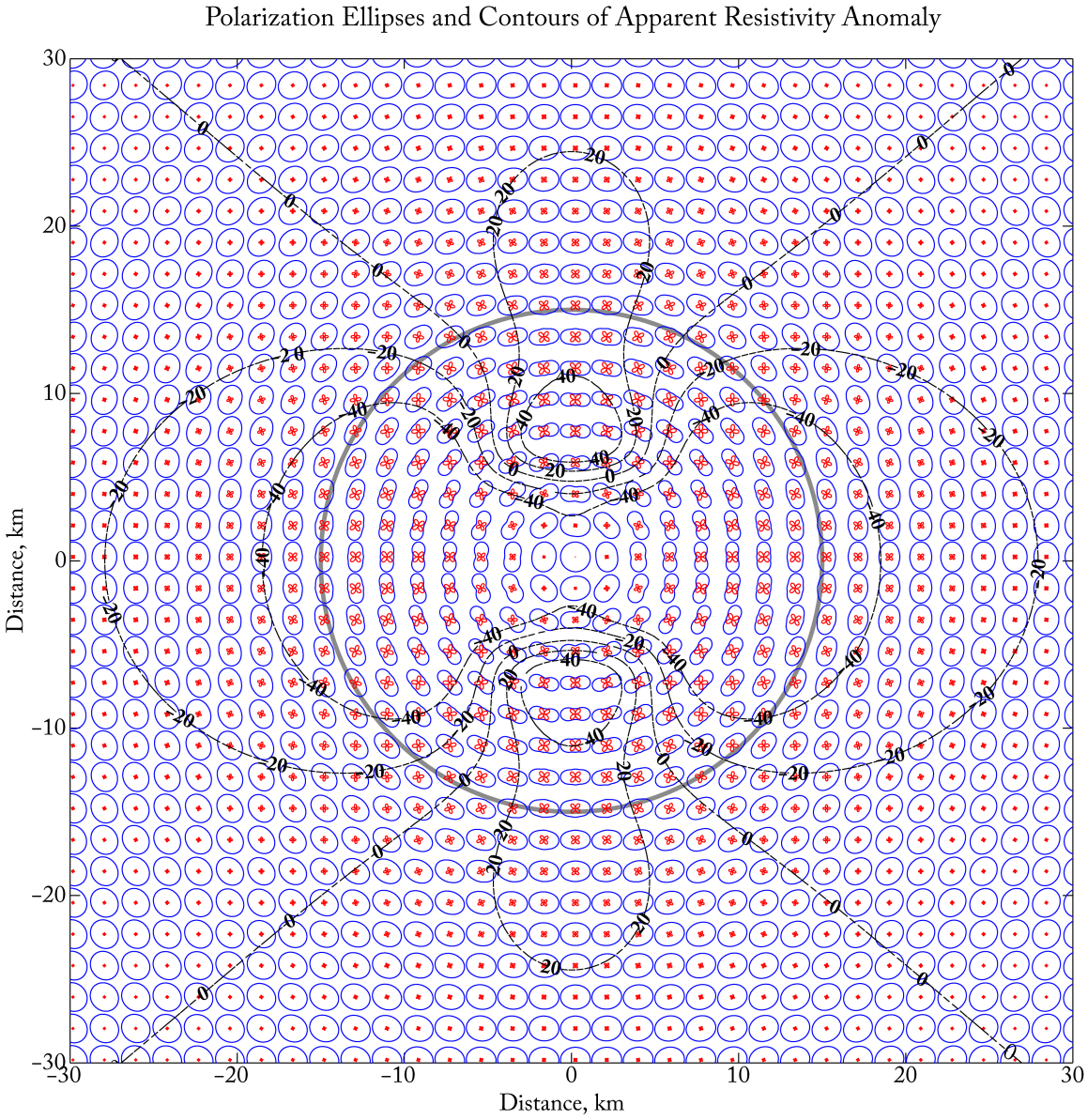

Figure 5.12: Polar diagrams around the Gaussian seamount. The red lines represent the off-diagonal components of the impedance tensor as the tensor moves through one full rotation. The blue lines represent the diagonal components of the impedance tensor over the same rotation. The thick gray line denotes the edge of the seamount. The black dashed lines are the labelled contours of the percentage apparent resistivity anomaly due to the seamount. These contours come from the same data that is portrayed in Figure 5.9.

What happens when there is no longer radial symmetry? Figure 5.13 illustrates a non-radially symmetric model composed of the average of two Gaussian seamounts identical to the one used before, but with their peaks offset by $10\sqrt{2}$ km. The long axis of the dual-seamount is oriented 45° from the y-axis. Figure 5.14 plots the polar diagrams and contours of the apparent resistivity anomaly for this non-radially symmetric model. The impedance tensor was rotated by 45° before calculating the apparent resistivity of Z_{xy}, to align with the most 2D strike. The Swift Skew was less than 0.05 in the entire model domain. Note that due to averaging, the volume of the dual-seamount is equal to the volume of the single seamount in the previous example, but the max height of the dual-seamount is half that of the single seamount. In Figure 5.14, the polar diagrams appear very 1D occur in a ring between the peaks of the two Gaussian seamounts. These polar diagrams occur in the midst of very 3D structure, but again, some level of symmetry, other than radial, produces polar diagrams that are misleading.

Revisiting Figure 5.11, note the behavior in the corners of the plots. The values of apparent resistivity from Z_{xx} and Z_{yy} are significantly diminished along the edges of the model domain, especially in the corner. The phase plots show non-radially symmetric behavior in the corners as well. These are symptoms of the edge effects plaguing the use of a single model grid in the Fourier domain calculation. Similar edge effects exist in the Z_{xy} and Z_{yx} plots, but are much less visible. The model of a single seamount is relatively immune to edge effects because the conductance anomaly of the thin sheet is far from the edge of the grid. Nonetheless edge effects are visible in Figure 5.11; the would be much worse for a more realistic model with conductance anomalies throughout the grid.

To illustrate the effectiveness of the multi-grid method, we apply it to the original model of a single seamount. We will use two conductance grids: one large grid with low resolution, and one small grid with high resolution. The large conductance grid has dimensions 480×480 km, and is discretized into 512×512 cells, while the small conductance grid, which contains the area of interest has dimensions 120×120 km, with 512×512 cells. This multi-grid example uses 8 times less memory than a single grid approach with the large grid size at equivalent resolution. It was found, in practice, that the multi-grid calculations took about 7 times less computation time than the single grid analog. Figure 5.15 displays

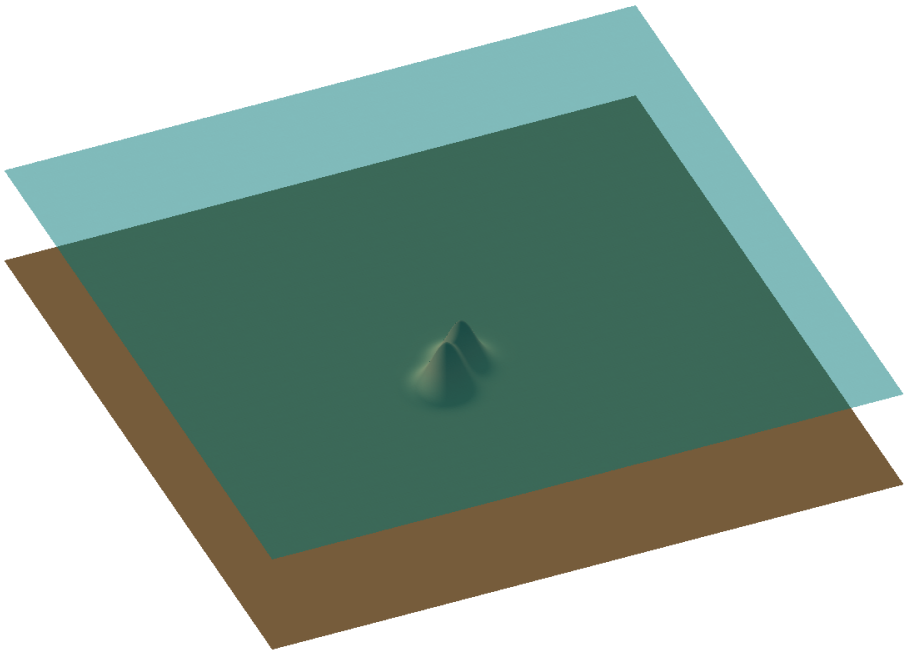

Figure 5.13: Illustation of the dual-Gaussian seamount on the 120 × 120 km square in a 4 km deep ocean.

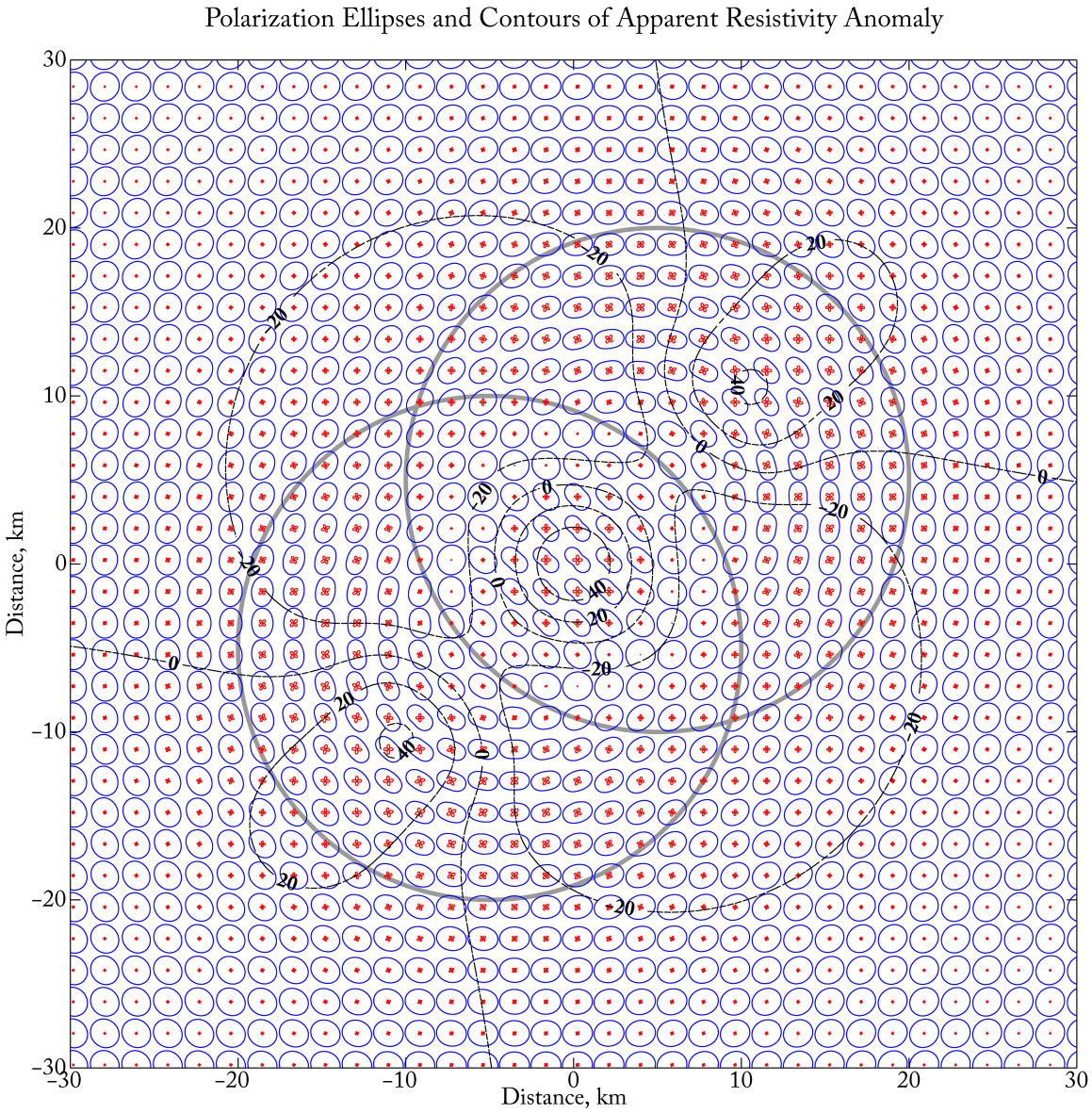

Figure 5.14: Polar diagrams around the dual-Gaussian seamount. The red lines represent the off-diagonal components of the impedance tensor as the tensor moves through one full rotation. The blue lines represent the diagonal components of the impedance tensor over the same rotation. The thick gray lines denotes the edge of the two Gaussian functions whose sum comprises the seamount. The black dashed lines are the labelled contours of the percentage apparent resistivity anomaly due to the seamount. These contours come from the same data that is portrayed in Figure 5.9.

the result of the multi-grid calculation. The edge effects seen in Figure 5.11 are no longer apparent as they have been moved to the edges of the large grid.

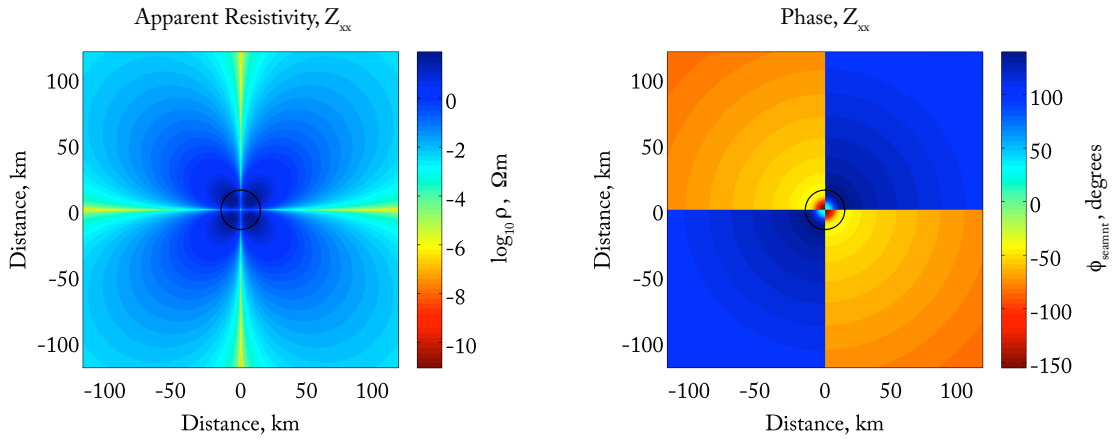

Figure 5.15: Apparent resistivity and phase of Z_{xx} for the Gaussian seamount calculated on an larger grid size of 480×480 km. The black line again outlines the edge of the seamount.

5.9 The Wavenumber-Impedance Tensor

We now revisit (5.40), rearranged here as,

$$\hat{\mathbf{B}}(\mathbf{k}) = i\bar{\mathbf{z}} \times \hat{\mathsf{L}}_l(\mathbf{k}) \cdot \hat{\mathbf{E}}(\mathbf{k}) = \hat{\mathsf{W}}(\mathbf{k}) \cdot \hat{\mathbf{E}}(\mathbf{k}). \tag{5.216}$$

We have introduced a 2×2 tensor, $\hat{\mathsf{W}}(\mathbf{k})$, which we will call the wavenumber impedance tensor. The spatial-domain MT impedance tensor is traditionally denoted with the letter Z and relates the electric and magnetic fields in the following way,

$$\mathbf{E}(\mathbf{r}) = \frac{1}{\mu_0}\mathsf{Z} \cdot \mathbf{B}(\mathbf{r}), \tag{5.217}$$

assuming, as we have throughout this work, there are no magnetic materials nearby. Since they are defined in different domains and relate the electric and magnetic fields in different ways, we make the distinction between the traditional impedance tensor and the wavenum-

ber impedance tensor by using a different character, $\hat{\mathsf{W}}$, for the wavenumber impedance. As should be apparent and will be expanded upon later in the current section, the wavenumber impedance tensor is inversely proportional to the wavenumber admittance tensor, the former in units of inverse length, and the latter in units of length. Such complementary definitions of admittance and impedance bestow semantic harmony, as opposed to the traditional definitions in the spatial domain where the admittance and impedance are directly related.

Examining (5.216), immediately we notice that the wavenumber impedance over a layered halfspace has no dependence on the currents within the overlying heterogeneous thin sheet. In fact, (5.216) implies that the wavenumber impedance is only ever sensitive to the structure below the plane of observation so long as it is layered. This conclusion has far-reaching repercussions. First, if one could make an estimate of the wavenumber impedance from an array of coplanar observations at the bottom of the ocean underlain by purely 1D structure, it would be unaffected by MT-induced electric currents in the ocean, even those of non-zero wavenumber, i.e. those that have been distorted by non-1D bathymetry; there would be no "coast-effect" apparent in data of this form. In addition, the plane wave assumption of the inducing magnetic field sourced from the ionosphere would no longer be necessary. All non-planar sources originating from above the plane of observation would be accounted for in the non-zero wavenumbers of the wavenumber impedance. Thus, non-planar ionospheric sources and two- or three- dimensional bathymetric distortions would have the same effect, that of providing the spectral diversity in the source fields needed to populate the wavenumber impedance. Naturally, this idea extends to controlled-source electromagnetics over a 1D earth. One major underlying goal of controlled-source surveying, albeit not always explicitly acknowledged in this language, is to provide richness in the wavenumber domain that is unavailable in the presumably planar MT source field; a more commonly advertised goal of controlled-source surveying is to provide stronger high-frequency signal. So long as the plane of observation lies below the depth of the controlled-source, the wavenumber impedance is insensitive to any source's size, shape, location, orientation, amplitude, and phase. In addition, the wavenumber impedance is insensitive to the conductivity of the material within which a source is embedded. In the wavenumber domain, the geometries

of sources are irrelevant because their effects cancel out in the wavenumber impedance. This means that uncontrolled sources, once considered noise, like overhead power-lines, are removed in wavenumber impedance estimation. Another consequence of the wavenumber impedance's insensitivity to all layers above the plane of measurement is that there is no "air-wave" in the wavenumber impedance measured on the seafloor, atop a stack of layers. The wavenumber impedance can be seen as the extension of the classical theory for the 1D MT impedance into the realm of all source fields, including those with non-zero k components.

By taking into account the components of $\hat{\mathsf{L}}_l$, we see that the the wavenumber impedance, as defined below the thin sheet by (5.216), is sensitive only to the layered structure below where it is measured, and ignorant of anything related to the source field or layered conductivity taking place above. Comparing (5.216) with (5.64) an apparent paradox is confronted. By (5.64), an impedance estimated by the electric and magnetic fields, as measured above the thin sheet, is instead only sensitive to the layered structure above, and ignorant of sources and layered structure below, except for $k = 0$ where we find that the primary fields carry sensitivity to the lower halspace. In other words, the impedance estimated for non-zero wavenumbers at, for example, the ocean floor (below a heterogeneous thin sheet) carries information about the layered structure below the seafloor, while the impedance estimated on the land side of the coast (above a heterogeneous thin sheet) is sensitive only to the layered structure of the atmosphere above. This at first sounds preposterous, as it is known that the impedance from land measurements, even near the coast and over an otherwise 1D earth, carries information about the subsurface. Nonetheless, the preceding statements are true and self-consistent; the key is in the location of the sources of energy at each wavenumber. For the wavenumber $k = 0$, we have our standard theory, which is that the source field originates from high up in the atmosphere, at the top of our model. Thus, impedances estimated below the $k = 0$ source fields are sensitive to the layered structure beneath them, regardless of whether they are measured above or below a thin sheet. On the other hand, the electric currents producing the non-zero wavenumber "source"-fields occur exclusively in the thin sheet, for the model we've described here. From this a consistent rule can be drawn: the wavenumber impedance of a

layered earth carries only the information about the conductivity structure in the opposite halfspace as that where the sources are contained, given a wholespace divided in two at the plane of observation. In the case of a seafloor observation, all source wavenumbers reside in the overriding halfspace and thus an impedance estimate there is sensitive only the the layered structure below. For the case of the land observation, non-zero wavenumber sources occur below, and therefore the non-zero wavenumber components of the impedance carry only information about the layered structure in the atmosphere. However, on land, the $k = 0$ wavenumber sources occur both above and below the plane of observation, at the top of our model as well as in the thin sheet. Thus the wavenumber impedance for $k = 0$ is sensitive to both the layers above and below the plane of observation. Keep in mind, this does not mean that the electric and magnetic fields themselves are not affected by the layers above and below the plane of observation; indeed, they are. It is merely a property specific to transfer functions such as the wavenumber impedance over a layered earth that filters out effects from the halfspace containing sources. See Sections 5.10 & 5.11 for other transfer functions that exhibit this property. Also, the MT model set forth in this chapter assumes only planar sources originate from the ionosphere, as is the traditional view. Yet, were it the case that the ionosphere produced non-zero wavenumber components in the source field, as is likely the truth, the equation (5.216) would define the impedance at the surface of a purely 1D earth (no 2D varying thin sheet).

How might we extend the traditional quantities of skin depth and apparent resistivity into the wavenumber domain? Both quantities relate to fields produced at the surface of an isotropic halfspace earth when induced by energy arriving from above. We enhance the old theory by now allowing the inducing energy to have a non-zero wavenumber, k. Harkening back to (5.25) we find that the electric field within the isotropic halfspace obeys,

$$\hat{E}_i(z) = \beta_i \exp\left[-\sqrt{\lambda} z\right], \tag{5.218}$$

where we have placed the top of the halfspace at z=0, and we see that the wavenumber-

enhanced skin depth, ${}^k\mathrm{d}$ is then defined by,

$$ {}^k\mathrm{d} = \frac{1}{\Re(\sqrt{\lambda})}. \tag{5.219} $$

Returning equation (5.21) to physical units, it gives for an isotropic halfspace conductivity, σ_0,

$$ {}^k\mathrm{d}_0 = \sqrt{\frac{2}{4\pi^2 k^2 + \sqrt{8\pi^4 k^2 + \omega^2 \mu_0^2 \sigma_0^2}}}. \tag{5.220} $$

Reassuringly, when $k = 0$ we retrieve the traditional form for skin depth. Recall that the traditional apparent resistivity can be expressed in terms of the admittance, $c(\omega)$, with the following,

$$ \rho_a(\omega) = \mu_0 \omega |c(\omega)|^2, \tag{5.221} $$

where the admittance is defined as,

$$ c(\omega) = -\frac{E(0)}{E'(0)}. \tag{5.222} $$

From equations (5.38) and (5.41), again restored to physical units, we find that by allowing non-zero k, we have a new admittance for the isotropic halfspace, which is the same for both polarizations of the electric field,

$$ c(\omega, k) = \frac{1}{\sqrt{4\pi^2 k^2 + i\omega\mu_0\sigma_0}}, \tag{5.223} $$

and thus we find that the traditional apparent resistivity is,

$$ \rho_a(\omega, k) = \frac{\mu_0 \omega}{\sqrt{8\pi^4 k^4 + \omega^2 \mu 0^2 \sigma_0^2}}. \tag{5.224} $$

When $k = 0$ we again find the property of ρ_a that bestowed it its name. However, when $k \neq 0$ the traditional ρ_a is not equivalent to the halfspace resistivity. Instead we must

introduce a new quantity, the wavenumber-enhanced apparent resistivity, ${}^{k}\rho_a$, which is given by,

$$ {}^{k}\rho_a(\omega, k) = \frac{\mu_0 \omega}{\sqrt{|c|^{-4} - 8\pi^4 k^4}} = \frac{1}{\sigma_0}, \tag{5.225} $$

and provides a true measure of the halfspace resistivity for energy of all wavenumbers. This new apparent resistivity is given in terms of the traditional definition of admittance, which does not change in the wavenumber domain. The admittance is a convenient quantity to work with in modeling and inversion when $k = 0$ because, for an isotropic earth, it is continuous across layer interfaces, and can be represented by a scalar multiplied by the identity matrix, i.e. the two orthogonal components of the admittance are independent and identical (see equations (5.38), (5.31), (5.36) and (5.21)); these properties of the admittance do not hold true with non-zero k. Furthermore, the admittance is difficult to estimate from observations because it requires the measurement of the vertical gradient of the horizontal electric field. Instead it is customary to make simultaneous measurements of the horizontal electric and magnetic fields and then estimate an impedance tensor, like the one in (5.216). This then broaches an important question: how does the admittance, and therefore our new standard of apparent resistivity, relate to the wavenumber impedance, $\hat{\mathsf{W}}$?

From (5.216) and (5.40) converted back to physical units, we find that,

$$ \hat{\mathsf{W}} = \frac{i}{\mathrm{d}_1} \bar{z} \times \hat{\mathsf{L}}_l = \frac{1}{\mathrm{d}_1} \mathsf{R} \cdot \mathsf{S}_1 \cdot \mathsf{C}_1^{-1}, \tag{5.226} $$

where: C_1 is the admittance above a stack of layers as defined in (5.38), but converted back to physical units by the factor $1/\mathrm{d}_1$;

$$ \mathsf{S}_1 = \left(\frac{4\pi^2}{4\pi^2 k^2 + i\omega\mu_0\sigma_1\nu_1} \mathbf{k}\mathbf{k} - \mathsf{I} \right); \tag{5.227} $$

and we have introduced R as,

$$ \mathsf{R} = \begin{bmatrix} 0 & -i \\ i & 0 \end{bmatrix}, \tag{5.228} $$

a transformation tensor which essentially rotates a vector a positive 90° in both the horizontal plane and the complex plane. Notice that $\mathsf{Ra} = i\bar{\mathbf{z}} \times \mathbf{a}$. Due to the form of S_1 we see that the transformation from $\hat{\mathsf{W}}$ to C_1 requires knowledge of the conductivity of the first layer below the plane of observation, except of course when $k = 0$. This fact makes the conversion of wavenumber impedance measurements into admittance impractical; we will have to model the impedance data directly. Let us derive the impedance of a homogeneous halfspace. From (5.223) and (5.226) we see that for a homogeneous halfspace conductivity σ_0, the impedance is given by,

$$\hat{\mathsf{W}} = \begin{bmatrix} -iH_0 \sin 2\phi & iH_0 \cos 2\phi - iG_0 \\ iG_0 + iH_0 \cos 2\phi & iH_0 \sin 2\phi \end{bmatrix}, \tag{5.229}$$

where G_0 and H_0 are versions of (5.149) and (5.150), respectively, which have been converted back to physical units. By solving each component of (5.229) for $1/\sigma_0$, and making use of the following identities,

$$\left|\frac{a+ib}{c+id}\right|^2 = \frac{a^2+b^2}{c^2+d^2}, \tag{5.230}$$

and,

$$|\sqrt{a+ib}|^2 = \sqrt{a^2+b^2}, \tag{5.231}$$

the apparent resistivity can then be extracted from the wavenumber impedance in the two following ways,

$${}^k\rho_a(\omega,k) = 2\mu_0\omega \left(4\pi^8 k^8 |\hat{W}_{ii}|^{-4} \sin^4 2\phi - 2\pi^4 k^4\right)^{-\frac{1}{2}}, \quad \text{for } k \neq 0,\ i = \{1,2\}, \tag{5.232}$$

and,

$${}^k\rho_a(\omega) = \mu_0\omega |\hat{W}_{ij}|^{-2} \quad \text{for } k = 0,\ i = \{1,2\},\ j = \{1,2\}, \,\&\, i \neq j. \tag{5.233}$$

There is an expression for apparent resistivity at non-zero k that uses $\hat{W}_{ij}$, but it has a

lengthy form and contains redundant information, so it is not presented here.

For an illustration of the wavenumber impedance, we turn to an example which can be developed analytically, that of an electric dipole in a wholespace of conductivity, σ_*. The formulae for both the electric and magnetic fields for such a model with the electric dipole at the origin and aligned with the x-axis, are found in Ward and Hohmann [1988]. We will use the forms found in equations (2.39) and (2.41) of that work. First we convert these equations into our dimensionless system of dipole-moment normalized units to find,

$$\mathbf{E} = \frac{1}{8\pi}\left[\left(-a^2 + \frac{\partial^2}{\partial x^2}\right)\bar{\mathbf{x}} + \frac{\partial^2}{\partial x \partial y}\bar{\mathbf{y}} + \frac{\partial^2}{\partial x \partial z}\bar{\mathbf{z}}\right]\frac{\mathrm{e}^{-aR}}{R}, \tag{5.234}$$

and

$$\mathbf{B} = \frac{1}{4\pi}\left[\frac{\partial}{\partial z}\bar{\mathbf{y}} - \frac{\partial}{\partial y}\bar{\mathbf{z}}\right]\frac{\mathrm{e}^{-aR}}{R}, \tag{5.235}$$

where $R^2 = x^2 + y^2 + z^2$, and $a^2 = 2i$. We then apply the 2D FT to all the field components. Starting with the x-directed electric field, the Fourier integral is simplified to,

$$\hat{E}_1 = \mathcal{F}_{xy}\left[\frac{1}{8\pi}\left(\frac{-a^2\exp(-aR)}{R} + \frac{\partial^2}{\partial x^2}\frac{\exp(-aR)}{R}\right)\right] \tag{5.236}$$

$$= \frac{1}{8\pi}\mathcal{F}_{xy}\left[\frac{-a^2\exp(-aR)}{R}\right] + \mathcal{F}_y\left[\mathcal{F}_x\left[\frac{\partial^2}{\partial x^2}\frac{\exp(-aR)}{R}\right]\right] \tag{5.237}$$

$$= \frac{1}{8\pi}\mathcal{F}_{xy}\left[\frac{-a^2\exp(-aR)}{R}\right] + \mathcal{F}_y\left[(-4\pi^2 k_x^2)\mathcal{F}_x\left[\frac{\exp(-aR)}{R}\right]\right] \tag{5.238}$$

$$= -\frac{1}{8\pi}\left(a^2 + 4\pi^2 k^2\cos^2\phi\right)\mathcal{F}_{xy}\left[\frac{\exp(-aR)}{R}\right]. \tag{5.239}$$

We find that we need the 2D FT of,

$$F(x,y) = \frac{\mathrm{e}^{-a\sqrt{x^2+y^2+z_0^2}}}{\sqrt{x^2+y^2+z_0^2}}. \tag{5.240}$$

The function F is the solution vanishing at infinity of the PDE

$$\nabla^2 G - a^2 G = -4\pi\delta(x)\delta(y)\delta(z+z_0) \tag{5.241}$$

on the plane $z = 0$; that is

$$F(x,y) = G(x,y,0). \tag{5.242}$$

We will first use the 3D FT of (5.241) to find $\hat{G}$, and then use the result that,

$$\mathcal{F}_{xy}\left[G(x,y,0)\right] = \int_{-\infty}^{\infty} dk_z \hat{G}(k_x,k_y,k_z). \tag{5.243}$$

The 3D FT of (5.241) is quickly found to be

$$-4\pi^2\kappa^2\hat{G} - a^2\hat{G} = -4\pi \mathrm{e}^{-2\pi i k_z z_0}, \tag{5.244}$$

where $\kappa^2 = k_x^2 + k_y^2 + k_z^2$. From (5.244) we have,

$$\hat{G}(k_x,k_y,k_z) = \frac{4\pi \mathrm{e}^{-2\pi i k_z z_0}}{4\pi\kappa^2 + a^2}. \tag{5.245}$$

Then, from (5.243) we get,

$$\mathcal{F}_{xy}\left[F\right] = \frac{1}{\pi}\int_{-\infty}^{\infty} dk_z \frac{\mathrm{e}^{-2\pi i k_z z_0}}{k_z^2 + (k_x^2 + k_y^2 + a^2/4\pi^2)} \tag{5.246}$$

$$= 2\pi \frac{\mathrm{e}^{-g|z_0|}}{g}, \tag{5.247}$$

where $g = \sqrt{2i + 4\pi^2 k^2}$, and the integral in (5.246) is a well-known Fourier transform.

Applying (5.247) to (5.239) we get,

$$\hat{E}_1 = -\frac{1}{4}\left(2i + 4\pi^2 k^2 \cos^2\phi\right)\left[\frac{\mathrm{e}^{-g|z|}}{g}\right]. \tag{5.248}$$

The other horizontal component is found in a similar fashion to be,

$$\hat{E}_2 = -\pi^2 k^2 \left[\frac{\mathrm{e}^{-g|z|}}{g}\right] \sin\phi\cos\phi. \tag{5.249}$$

The vertical component presents a minor modification:

$$\hat{E}_3 = \frac{1}{8\pi}(2\pi i k\cos\phi)\mathcal{F}_{xy}\left[\frac{\partial}{\partial z}\frac{\mathrm{e}^{-aR}}{R}\right]. \tag{5.250}$$

Yet we are able to couch the FT in (5.250) in a form that we already know by recognizing that the partial differential and the FT operators commute. Then we have,

$$\hat{E}_3 = \frac{1}{8\pi}(2\pi i k\cos\phi)\frac{\partial}{\partial z}\left(\mathcal{F}_{xy}\left[\frac{\mathrm{e}^{-aR}}{R}\right]\right) \tag{5.251}$$

$$= -\frac{\pi i z}{2|z|}\mathrm{e}^{-g|z|}k\cos\phi. \tag{5.252}$$

Due to the ratio $z/|z|$ in (5.252), $\hat{E}_3$ is undetermined at $z = 0$. However, we know E_3=0 at $z = 0$ and therefore $\hat{E}_3$=0 at $z = 0$ as well. To acknowledge this fact, we replace $z/|z|$ in (5.252) with the signum function, so that,

$$\hat{E}_3 = -\frac{\pi i}{2}\,\mathrm{sgn}(z)\mathrm{e}^{-g|z|}k\cos\phi. \tag{5.253}$$

Following the same procedure as for the electric field, the FT of the magnetic field yields the following:

$$\hat{B}_1 = 0, \tag{5.254}$$

$$\hat{B}_2 = -\frac{1}{2}\,\mathrm{sgn}(z)\mathrm{e}^{-g|z|}, \tag{5.255}$$

and

$$\hat{B}_3 = -\pi i k \frac{\mathrm{e}^{-g|z|}}{g} \sin\phi. \tag{5.256}$$

In order to solve for the wavenumber-impedance, $\hat{\mathsf{W}}$, which presents us with four unknowns, we need another independent source polarization to provide us with two more constraints. For this, we simply reorient the electric dipole along the y-axis, and by doing so get a new set of fields, denoted by the star superscript:

$$\hat{E}_1^\star = -\pi^2 k^2 \left[\frac{\mathrm{e}^{-g|z|}}{g}\right] \sin\phi\cos\phi, \tag{5.257}$$

$$\hat{E}_2^\star = -\frac{1}{4}\left(2i + 4\pi^2 k^2 \sin^2\phi\right)\left[\frac{\mathrm{e}^{-g|z|}}{g}\right], \tag{5.258}$$

$$\hat{E}_3^\star = -\frac{\pi i}{2}\,\mathrm{sgn}(z)\mathrm{e}^{-g|z|} k \sin\phi, \tag{5.259}$$

$$\hat{B}_1^\star = \frac{1}{2}\,\mathrm{sgn}(z)\mathrm{e}^{-g|z|}, \tag{5.260}$$

$$\hat{B}_2^\star = 0, \tag{5.261}$$

and

$$\hat{B}_3 = \pi i k \frac{\mathrm{e}^{-g|z|}}{g} \cos\phi. \tag{5.262}$$

It is easily shown that the solution for $\hat{\mathsf{W}}$ decouples into two sets of 2×2 matrix

systems:

$$\begin{pmatrix} \hat{B}_1^\star \\ \hat{B}_1 \end{pmatrix} = \mathrm{d}_* \begin{bmatrix} \hat{E}_1^\star & \hat{E}_2^\star \\ \hat{E}_1 & \hat{E}_2 \end{bmatrix} \begin{pmatrix} \hat{W}_{11} \\ \hat{W}_{12} \end{pmatrix}, \tag{5.263}$$

and,

$$\begin{pmatrix} \hat{B}_2^\star \\ \hat{B}_2 \end{pmatrix} = \mathrm{d}_* \begin{bmatrix} \hat{E}_1^\star & \hat{E}_2^\star \\ \hat{E}_1 & \hat{E}_2 \end{bmatrix} \begin{pmatrix} \hat{W}_{21} \\ \hat{W}_{22} \end{pmatrix}, \tag{5.264}$$

where the factor of d_* returns $\hat{\mathsf{W}}$ to its physical units of inverse length. The solutions of the two systems (5.263) and (5.264) result in the four equations for the four elements of $\hat{\mathsf{W}}$:

$$\hat{W}_{11} = (\hat{E}_2\hat{B}_1^\star - \hat{E}_2^\star\hat{B}_1)/(\Delta \mathrm{d}_*), \tag{5.265}$$

$$\hat{W}_{12} = (\hat{E}_1^\star\hat{B}_1 - \hat{E}_1\hat{B}_1^\star)/(\Delta \mathrm{d}_*), \tag{5.266}$$

$$\hat{W}_{21} = (\hat{E}_2\hat{B}_2^\star - \hat{E}_2^\star\hat{B}_2)/(\Delta \mathrm{d}_*), \tag{5.267}$$

$$\hat{W}_{22} = (\hat{E}_1^\star\hat{B}_2 - \hat{E}_1\hat{B}_2^\star)/(\Delta \mathrm{d}_*), \tag{5.268}$$

where,

$$\Delta = \hat{E}_1^\star\hat{E}_2 - \hat{E}_1\hat{E}_2^\star. \tag{5.269}$$

After some algebra we find,

$$\Delta = -\frac{i}{8}\mathrm{e}^{-2g|z|}. \tag{5.270}$$

Then by (5.265), (5.266), (5.267), and (5.268), for $z \geq 0$, we have,

$$\hat{W}_{11} = -i\frac{2\pi^2 k^2 \sin 2\phi}{\sqrt{i\omega\mu_0\sigma_* + 4\pi^2 k^2}} = -iH_* \sin 2\phi, \tag{5.271}$$

$$\hat{W}_{12} = i\frac{i\omega\mu_0\sigma_* + 2\pi^2 k^2}{\sqrt{i\omega\mu_0\sigma_* + 4\pi^2 k^2}} + i\frac{2\pi^2 k^2 \cos 2\phi}{\sqrt{i\omega\mu_0\sigma_* + 4\pi^2 k^2}} = iH_* \cos 2\phi - i\tilde{G}_*, \tag{5.272}$$

$$\hat{W}_{21} = -i\frac{i\omega\mu_0\sigma_* + 2\pi^2 k^2}{\sqrt{i\omega\mu_0\sigma_* + 4\pi^2 k^2}} - i\frac{2\pi^2 k^2 \cos 2\phi}{\sqrt{i\omega\mu_0\sigma_* + 4\pi^2 k^2}} = iG_* - iH_* \cos 2\phi, \tag{5.273}$$

and

$$\hat{W}_{22} = i\frac{2\pi^2 k^2 \sin 2\phi}{\sqrt{i\omega\mu_0\sigma_* + 4\pi^2 k^2}} = i\tilde{H}_* \sin 2\phi. \tag{5.274}$$

With no modification to (5.229), it is easily verified that these are the elements of the wavenumber-impedance in a homogeneous, isotropic wholespace, illuminated from above. We have proven that the elements of the wavenumber impedance are insensitive to the location and azimuthal orientation of the horizontal electric dipole within a homogeneous halfspace. Furthermore, due to the linear relationship between the wavenumber impedance and the transformed fields, we can say that the wavenumber impedance is insensitive to the locations and orientation of an arbitrary distribution of horizontal electric dipoles.

Does this result hold for vertical electric dipoles? Let us conduct the same wavenumber impedance estimation, but instead we make the second independent polarization a vertical electric dipole. The dimensionless fields due to a vertical dipole are given by,

$$\mathbf{E} = \frac{1}{8\pi}\left[\frac{\partial^2}{\partial z \partial x}\bar{\mathbf{x}} + \frac{\partial^2}{\partial z \partial y}\bar{\mathbf{y}} + \left(-a^2 + \frac{\partial^2}{\partial z^2}\right)\bar{\mathbf{z}}\right]\frac{\mathrm{e}^{-aR}}{R}, \tag{5.275}$$

and

$$\mathbf{B} = \frac{1}{4\pi}\left[\frac{\partial}{\partial y}\bar{\mathbf{x}} - \frac{\partial}{\partial x}\bar{\mathbf{y}}\right]\frac{\mathrm{e}^{-aR}}{R}. \tag{5.276}$$

Again employing (5.247), we quickly find the starred-fields:

$$\hat{E}_1^\star = -\frac{\pi i k}{2}\,\mathrm{sgn}(z)\mathrm{e}^{-g|z|}\cos\phi, \tag{5.277}$$

$$\hat{E}_2^\star = -\frac{\pi i k}{2}\,\mathrm{sgn}(z)\mathrm{e}^{-g|z|}\sin\phi, \tag{5.278}$$

$$\hat{E}_3^\star = \frac{\pi}{4}\left(-2i + g - \frac{2}{|z|}\right)\mathrm{e}^{-g|z|}, \tag{5.279}$$

$$\hat{B}_1^\star = -\pi i k\left[\frac{\mathrm{e}^{-g|z|}}{g}\right]\sin\phi, \tag{5.280}$$

$$\hat{B}_2^\star = -\pi i k\left[\frac{\mathrm{e}^{-g|z|}}{g}\right]\cos\phi, \tag{5.281}$$

and

$$\hat{B}_3^\star = 0. \tag{5.282}$$

For this new set of dipole polarizations,

$$\Delta = \frac{1}{4}\pi k\mathrm{e}^{-2g|z|}\sin\phi, \tag{5.283}$$

and after plugging the two sets of fields for $z \geq 0$ into (5.265), (5.266), (5.267), and (5.268), we again can recover all the components of the wavenumber impedance for a homogeneous, isotropic wholespace, illuminated from above. Thus, in the existence of a vertical electric

dipole, the wavenumber impedance has the same form as it does for horizontal electric dipoles. Any electric dipole, arbitrarily dipping out of the horizontal plane can be represented by a weighted sum of a horizontal and a vertical electric dipole. Therefore, we can say, so long as an estimate of the wavenumber impedance can be made from at least two independent polarizations of source fields, it is insensitive to the dip of a transmitter as well as its location and azimuth over a homogeneous halfspace.

Since actual magnetic dipoles are simply a distribution of electric current dipoles that form a closed loop, we offer without proof that the pre-described properties of the wavenumber impedance also hold in the presence of magnetic dipoles. This fact can easily be proven by applying the same transforms found in this section to the equations for the fields resulting from a point magnetic dipole, which are analogous to that of an electric dipole due to the duality between electric and magnetic point dipoles.

Finally, we close this section with a thought exercise which makes use of the following theorem put forth in this section:

> Given a 1D earth that is split into two halfspaces by a plane of measurement, the wavenumber impedance, estimated on that plane for a given wavenumber, is sensitive to the halfspace opposite from that which contains the driving sources for that wavenumber.

We then propose a hypothetical scenario. Imagine two independently-polarized asynchronous electric or magnetic sources are buried deep in the earth, say in a well. An dense array of electric and magnetic receivers is placed at the earth's surface, centered on the source-containing well so that the wavenumber impedance can be estimated over a broad survey area. If the earth were purely 1D, the theorem states that the wavenumber impedance depends only on the halfspace above the plane containing the receivers; for this example we will assert that the overriding halfspace is a homogeneous halfspace of air. The wavenumber impedance for a homogeneous halfspace of air is easy to compute. Would there be any reason for the measured wavenumber impedance to deviate from that calculated for a halfspace of air? The theorem requires the answer to be no if the earth is 1D. What would happen if the earth below the plane of measurement were not 1D? We could beak up any such conductivity into two parts, a background of 1D conductivity

and a residual distribution of 2D/3D conductivity anomalies. We have already determined that the 1D background will not contribute to any deviation of the wavenumber impedance from that of a halfspace of air. In the spatial domain, the anomalous scatterers can be represented by a distribution of electric source current proportional to the product of the primary electric field and the residual conductivity. This non-1D current distribution joins the controlled-source in the well in illuminating the upper halfspace, but the wavenumber impedance remains unchanged; it still is equal to the wavenumber impedance of a halfspace of air. Any distribution of current, controlled or induced, in an arbitrarily heterogenous halfspace will produce electric and magnetic fields on a plane of measurement whose interrelationship are exclusively dependent upon the opposing halfspace, so long as the opposing halfspace is layered and contains no additional driving sources. This is why we can express the wavenumber impedance below the heterogeneous thin sheet only in terms of the conductivity of the layers below it. So for the thought exercise at hand, the wavenumber impedance at the surface of the earth will always be equal to that of a halfspace of air, regardless of the distribution of controlled sources and heterogeneous conductivity below the surface.

There is one more intricacy. If the buried controlled source is wavenumber limited, within an earth that is strictly layered, the wavenumber impedance should only be estimable at the wavenumbers produced by that controlled source. However, if the earth is not strictly layered, dispersion will occur, just as it did in the heterogeneous thin sheet driven by an MT source field—only $k = 0$ wavenumbers drove the system, but the resulting fields were rich in wavenumber content. For a heterogeneous earth there will be more wavenumbers with energy to illuminate the overriding halfspace than there were originally in the controlled source alone. Thus, only for a non-1D earth structure will one be able to estimate the wavenumber impedance at wavenumbers of energy nonexistent in the controlled source. Nonetheless, we always know values of the wavenumber impedance to expect, that of a halfspace of air.

What happens when we place the controlled source above the earth, in the halfspace of air? With a layered earth below the plane of measurement, the theorem tells us that the wavenumber impedance is sensitive only to the layered structure of the earth. Now, if

the earth is non-1D, the previous scattering analogy tells us that we have sources above and below the plane of measurement. In this case, the wavenumber impedance depends upon both the halfspace of air above and the halfspace of heterogeneous conductivity below in an inextricable way.

5.10 Vertical Electric Transfer Functions over an Anisotropic 1D Earth

On the rare occasion that the vertical electric field is measured alongside the horizontal electric field, an estimate of the transfer function between the horizontal and vertical electric fields can be made; we call this the vertical electric transfer function, V. This type of measurement most likely pertains to the marine environment where the immersion in seawater facilitates electrical contact with the environment through vertically displaced sensors. In the marine case, the vertical electric transfer function is measured below the thin sheet of current which we use to represent the ocean; we will therefore write this case as V^+. Here we derive the theoretical value of $\hat{\mathsf{V}}^+$, the vertical electric transfer function in the wavenumber domain, over our earth model consisting of anisotropic layers. The short derivation makes use of equations already introduced in the preceding sections. Plugging (5.38) into (5.18), we quickly get what we seek,

$$\hat{E}_3^+ = \frac{2\pi i}{2i\sigma_n\nu_n + 4\pi^2 k^2}(\mathbf{k}\cdot\mathsf{C}_1^{-1})\cdot\hat{\mathbf{E}}^+ = \hat{\mathsf{V}}^+\cdot\hat{\mathbf{E}}^+. \tag{5.284}$$

Again we see that $\hat{\mathsf{V}}^+$ is independent of the currents within the thin sheet, as was $\hat{\mathsf{W}}$. In other words, $\hat{\mathsf{V}}^+$ is independent of the conductivity structure of the overriding halfspace from which source fields originate, and is sensitive only to the layered structure below the plane of measurement.

5.11 Vertical Magnetic Transfer Functions over an Isotropic 1D Earth

While vertical electric fields are not normally measured in practice (except in the marine environment where the electric sensor is easily embedded in a good conductor, see Section 5.10), vertical magnetic fields often are. A common quantity estimated from the vertical magnetic field measurement is the vertical magnetic transfer function, T, a 2-vector. This is the transfer function between the horizontal and vertical magnetic field, such that,

$$B_3 = \mathsf{T} \cdot \mathbf{B}. \tag{5.285}$$

The usefulness of T arises from the assumption of a horizontally polarized, planar magnetotelluric source. In that case, B_3 is entirely a result of non-planar currents induced in the earth, and thus T contains information about the earth's conductivity. The vertical magnetic transfer function is also commonly referred to as the tipper, as it describes how the horizontal magnetic source field is "tipped" upward by the conductivity structure of the earth. If earth's conductivity is 1D and the source field is planar, all induced currents are also planar, so B_3 and T are both zero. However the situation is different if the source field has non-zero wavenumber components; in that case, a non-zero T can be measured over 1D earth structure. We extend the definition of T into the wavenumber domain so that we may be shorn of the assumption of a horizontally polarized planar source. Here we derive the form $\hat{\mathsf{T}}$ takes over a layered earth. In order to do so, we must limit the conductivity of the earth to be isotropic, for reasons which will soon become apparent. We return to the dimensionless quasi-static Maxwell's equations (5.5) and (5.6). By taking the curl of an isotropic version of (5.6), inserting (5.5) and making use of (5.9) we can get,

$$\nabla^2 \mathcal{B} - \nabla(\nabla \cdot \mathcal{B}) - 2i\sigma_n \mathcal{B} = 0. \tag{5.286}$$

An isotropic σ_n makes it possible to make the substitution of (5.5) required to get (5.286). Moving (5.286) into the Fourier domain, just as was done before for the electric fields, we

find two equations:

$$-4\pi^2 k^2 \hat{\mathbf{B}} + \hat{\mathbf{B}}'' - 2\pi i \mathbf{k}(2\pi i \mathbf{k} \cdot \hat{\mathbf{B}} + \hat{B}_3') - 2i\sigma_n \cdot \hat{\mathbf{B}} = 0, \tag{5.287}$$

and,

$$-4\pi^2 k^2 \hat{B}_3 - 2\pi i \mathbf{k} \cdot \hat{\mathbf{B}}' - 2i\sigma_n \hat{B}_3 = 0. \tag{5.288}$$

Also, from (5.8) we have,

$$\hat{B}_3' = -2\pi i \mathbf{k} \cdot \hat{\mathbf{B}}. \tag{5.289}$$

Plugging (5.289) into (5.287), and after some cancellation, we find two uncoupled ordinary differential equations for the horizontal components of the magnetic field,

$$\hat{\mathbf{B}}'' - g_n^2 \hat{\mathbf{B}} = 0, \tag{5.290}$$

where $g_n = \sqrt{2i\sigma_n + 4\pi^2 k^2}$. By rearranging (5.288) we get,

$$\hat{B}_3 = -\frac{2\pi i}{2i\sigma_n + 4\pi^2 k^2}(\mathbf{k} \cdot \hat{\mathbf{B}}'). \tag{5.291}$$

Equation (5.291) is close to the form of the vertical magnetic transfer function we seek, we just need a substitution for $\hat{\mathbf{B}}'$ which depends upon $\hat{\mathbf{B}}$. For this we introduce another transfer function, D, which we define as,

$$\hat{\mathbf{B}}^+ = -\mathsf{D}\hat{\mathbf{B}}'^+. \tag{5.292}$$

Inserting (5.292) into (5.291) we arrive at the form we are looking for,

$$\hat{B}_3^+ = \frac{2\pi i}{2i\sigma_n + 4\pi^2 k^2}(\mathbf{k} \cdot \mathsf{D}^{-1}) \cdot \hat{\mathbf{B}}^+ = \hat{\mathsf{T}} \cdot \hat{\mathbf{B}}^+. \tag{5.293}$$

Equation (5.293) pertains to a plane of measurement at the top of a layer of uniform conductivity, like a measurement on the seafloor, below the thin sheet. The vertical magnetic field (normal to the layer interface) is always continuous, while the horizontal magnetic field (interface parallel) is only continuous if there is no free current at the interface. This is not true in the case of a thin sheet of current. Thus, $\hat{\mathsf{T}}$ is continuous across most interfaces except those occupied by thin sheets of current. A $\hat{\mathsf{T}}$ measured on the seafloor is independent of any currents induced in an ocean which can be represented by a thin sheet, while a $\hat{\mathsf{T}}$ measured on land, above such a thin sheet, is not independent of the currents within of the thin sheet.

We continue with the derivation of D for a layered isotropic earth. For this we borrow heavily from Section 5.1. Similar to (5.25), the general solution for (5.290) is,

$$\hat{B}_i(z) = \alpha_i \exp\left[g_n(z - z_n)\right] + \beta_i \exp\left[-g_n(z - z_n)\right], \tag{5.294}$$

$$z_{n-1} \leq z \leq z_n, \text{ and } i = \{1, 2\}. \tag{5.295}$$

Given a value of the horizontal magnetic field and its vertical derivative at the base of a layer, $\hat{B}_i^-$ and $\hat{B}_i'^-$, respectively, the corresponding values at the top of that layer are given by,

$$\hat{B}_i^+ = \hat{B}_i^- \cosh\left(g_n h_n\right) - \frac{\hat{B}_i'^-}{g_n} \sinh\left(g_n h_n\right), \tag{5.296}$$

and

$$\hat{B}_i'^+ = g_n \hat{B}_i^- \sinh\left(g_n h_n\right) - \hat{B}_i'^- \cosh\left(g_n h_n\right), \tag{5.297}$$

where h_n, the thickness of the n^{th} layer, is again defined as $h_n = z_n - z_{n-1}$.

At the base of the stack of layers below the plane of observation, we again set α_i to zero, thereby rejecting a model with energy originating from the center of the earth. We

therefore find,

$$\hat{B}_i(z) = -\frac{1}{g_n}\hat{B}_i'(z),\ z > z_N. \tag{5.298}$$

In order to propagate $\hat{\mathbf{B}}$ and $\hat{\mathbf{B}}'$ from the base of our layered model up to the plane of observation, we need boundary conditions for $\hat{\mathbf{B}}$ and $\hat{\mathbf{B}}'$ at layer interfaces. As was stated before, at conductivity interfaces containing no free charge or current,

$$\hat{\mathbf{B}}^+ = \hat{\mathbf{B}}^-, \tag{5.299}$$

and

$$\hat{B}_3^+ = \hat{B}_3^-. \tag{5.300}$$

The boundary condition for $\hat{\mathbf{B}}'$, perhaps as expected, takes more work. We start with a rearrangement of (5.6) in the Fourier domain. Extracting only the equation related to the horizontal electric field, we have within the n^{th} layer,

$$2\bar{\mathbf{z}} \times \hat{\mathbf{E}} = \frac{1}{\sigma_n}\left(2\pi i \mathbf{k}\hat{B}_3 - \hat{\mathbf{B}}'\right). \tag{5.301}$$

Noting boundary conditions (5.31), (5.299), and (5.300), the equation (5.301) affords us,

$$\hat{\mathbf{B}}'^- = \left[\frac{4\pi^2}{2i\sigma_{n+1} + 4\pi^2 k^2}\left(1 - \frac{\sigma_n}{\sigma_{n+1}}\right)\mathbf{kk} + \frac{\sigma_n}{\sigma_{n+1}}\mathsf{I}\right] \cdot \hat{\mathbf{B}}'^+, \tag{5.302}$$

the boundary condition for $\hat{\mathbf{B}}'$ at the bottom of the n^{th} layer, where $z = z_n$.

In order to calculate D, a problem with 4 unknowns, we start with two independent initial conditions of the horizontal magnetic field, which we can arbitrarily choose to be,

$$\mathbf{B}_N^+ \in \left\{\begin{bmatrix} 1 \\ 0 \end{bmatrix}, \begin{bmatrix} 0 \\ 1 \end{bmatrix}\right\}. \tag{5.303}$$

Then, starting with (5.303), we use (5.298), (5.296), (5.297), (5.299), and (5.302) to propa-

gate the horiztonal magnetic field and its vertical derivative up to the plane of measurement, where we then use them in (5.292) to solve for D. Finally, we are able so see that D is equivalent to C, the admittance tensor, for the case of an isotropic layered earth.

5.12 Wavenumber Domain Survey Design and Data Interpretation

Electromagnetic survey design along the time-axis is quite straightforward. A common path is to select a range in frequency of energy needed to sense a target, and then adjust the sampling rate and total measurement duration to best estimate those frequencies; as a rule of thumb, the sampling rate determines the highest estimable frequency in the data and the duration determines the lowest estimable frequency in the data. If there is a controlled source involved, the transmitted waveform is engineered to direct the highest power into a chosen set frequencies. The chosen set of frequencies can be determined by forward modeling the hypothetical conductivity of the survey's target and its environment. Alternatively, the frequencies are often chosen based on simpler arguments of the skin depth in a given background conductivity and how that relates to the hypothetical depth of burial of the target.

This chapter has laid the foundation for extending these preliminary survey design practices for both MT and controlled-source EM (CSEM) into the wavenumber domain. Section 5.9 introduced a new measure of skin depth which incorporates all wavenumbers of inducing energy. This skin depth can be used for survey design in the spatial plane in the same way that the skin depth at $k = 0$ has been used for survey design along the time axis. In addition, 1D forward modeling can determine which source wavenumbers are most sensitive to hypothetical targets. Once a set of wavenumbers are chosen, the spatial sampling "rate" as well as the survey aperture can be set to best estimate those wavenumbers. Also, the orientation and distribution of transmitters can be engineered to direct power into the wavenumbers of choice.

The estimation of the wavenumber impedance is in fact a type of array analysis like that of Egbert and Booker [1989] and Egbert [1997] (and, described in Chapter 3), yet

it has the advantage of taking into account a previously ignored piece of information, the spatial distribution of the observations. This removes the requirement that all sources be of $k = 0$. The inevitable corollary is a robust wavenumber impedance estimation procedure that involves a robust least-squares fitting to individual Fourier coefficients, frequency and wavenumber, of the electric and magnetic fields. This procedure could recycle much of the statistical machinery of Egbert and Booker [1986], but instead of the fitting a single line to the observations at a given frequency, it would fit a series of lines, one for each available wavenumber.

Care must be taken with the spatial Fourier transform of the electric and magnetic fields. It is highly unlikely that the observations will take place on a perfectly regularly-spaced grid, which would be ideal for the fast-Fourier transform techniques. In addition, edge effects will again be a problem. These issues have been dealt with before in the science of earth gravity. In that field, spatial arrays of measurements of the earths gravity are made and converted into the Fourier domain for modeling and interpretation. The only difference is that with gravity, only a single frequency, $f = 0$, is available. The 2D Fourier transformation of the electric and magnetic fields at each frequency can therefore borrow from the techniques borrowed for gravity studies.

Acknowledgments

Chapter 5, in part, derives from material published in the Geophysical Journal International. Parker, Robert L.; Wheelock, Brent, Blackwell Publishing Ltd., 2012. The dissertation author was the secondary investigator and author of this paper. The remainder of the text of Chapter 5 is currently being prepared for submission for publication of the material. Wheelock, Brent. The dissertation author was the primary investigator and author of this material.

Chapter 6

Modeling and Synthetic Inversion of Bathymetric Effects

In Chapter 4 it was found that the conductive anomaly below site 632, coined the Rinconada conductor, was required by the land data, predominantly the tipper portion of it, and rejected by much of the marine impedance data. Suspicion was raised that the conflict in sensitivity between the land and marine data was a result of some sort of coast effect. In this chapter, we pursue this suspicion first by comparing calculations with 2D and 3D bathymetry. Then we asses the effects of bathymetry on our inversion algorithm through the inversion of synthetic data.

6.1 3D Modeling of Bathymetry in Central California

We now apply the thin-sheet modeling technique, discussed at length in Chapter 5, to the 3D bathymetry surrounding the Estero MT profile. For estimates of bathymetry around the globe, we make use of both 1-minute and 2-minute resolution databases provided online at `http://topex.ucsd.edu` [Smith and Sandwell, 1997]. A grid about twice the size of the latitude/longitude extents of the Estero MT survey is selected from the 1-minute bathymetry database. This high-resolution bathymetry grid constitutes the inner-most grid in Figures 6.2 & 6.4, and will be the only grid from which the results of MT calculations

will be interpreted in subsequent plots. Figures 6.2 & 6.4 show multiple larger grids of progressively coarser bathymetry (originating from the 2-minute database) surrounding the inner grid; these are used to move the boundaries of our calculation far from the edges of our interpreted grid (see Section 5.5), as well as to incorporate the effects of distant, yet large-scale bathymetric features. Since only the increasingly longer wavelength features have an influence on the inner grid as their distance from it increases, the outer grids are increasingly smoothed and decimated towards the edge of the model. Figure 6.3 shows how the transition from the resolution of one grid to the next has been made smooth through interpolation to ensure no edge effects are produced with our Fourier-domain method.

The maximum seafloor depth of the inner-most grid defines the thickness of the thin sheet. The conductance of the thin sheet is calculated by integrating, over the thickness of the thin sheet, the resistivity-depth section below each cell in the conductance grid. Note that we include topography in the conductance integration, although its contribution is orders of magnitude smaller than that from bathymetry. Apart from the water layer, which varies in thickness over the horizontal plane, the earth's resistivity is represented with horizontal layers. The shallowest layers, comprising the crust, are assigned average resistivities drawn from Model 1. The uppermost layer is contained within the depth range represented by the thin sheet, so it is allowed to vary horizontally. Three values are used for the upper-most layer: 10 Ωm for oceanic material, 30 Ωm for continental material, and 3 Ωm for the sediments filling the GV basin (see Figure 6.1). Figure 6.5 displays the anomalous conductance associated with our GV analogue, corresponding to a maximum sediment thickness of 3 km with a resistivity of 3 Ωm; the bottom plot in Figure 6.22 illustrates how the GV conductance was produced by creating properly scaled pseudo-bathymetry. Below the upper-most layer in the models, all layers are horizontally uniform. While the crustal values for resistivities may vary from region to region (hence, we draw from our local inversion result), the upper oceanic mantle is assumed to be more uniform. Rather than select values for the upper mantle resistivity from our inversion model, where we have reason to suspect distortion, we utilize independent mantle resistivity estimates from Heinson and Constable [1992]. These estimates call for a more resistive oceanic lithosphere (30,000 Ωm) than was recovered in the inversion models (1,000 Ωm). We show in Section

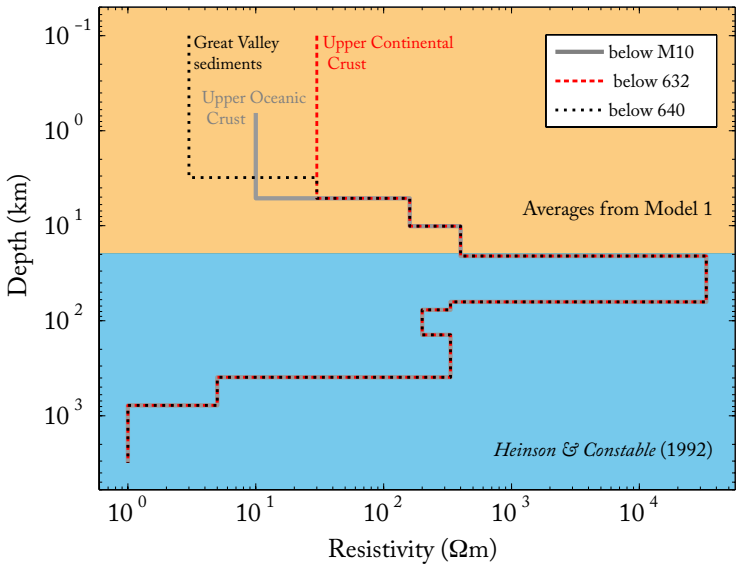

Figure 6.1: Resistivity-with-depth profiles for the three different regions in the thin-sheet model: the marine (e.g, below site M10), the continental (e.g., below site 632), and the GV basin (e.g., below site 640). The values in the upper part of the model (shaded orange) are derived from parameter averages from Model 1, while the values in the lower part of the model (shaded blue) are derived from a model described by Heinson and Constable [1992].

6.2, that a regularized MT inversion, with our given data and data errors, is unable to resolve such a high resistivity for the lithosphere.

To isolate the 3D effects of bathymetry from the 3D effects of the GV, we make calculations on two models, one described above which includes conductive sediments in the GV, and one without an anomalously conductive GV. For each model, 3D and 2D thin-sheet calculations will be made, with the 2D model constructed from the bathymetry along the Estero MT profile. As a benchmark for the accuracy of the thin-sheet calculations, we make a 2D finite element calculation on an equivalent model (Figure 6.6) using the Fortran code MARE2DEM [Key and Ovall, 2011]. The benchmark model does not include a more conductive GV. Figure 6.7 shows a comparison of our two 2D models, thin-sheet and MARE2DEM. The plot illustrates the extensiveness of the two models and the absence of bathymetric information throughout most of the MARE2DEM model. Note how the

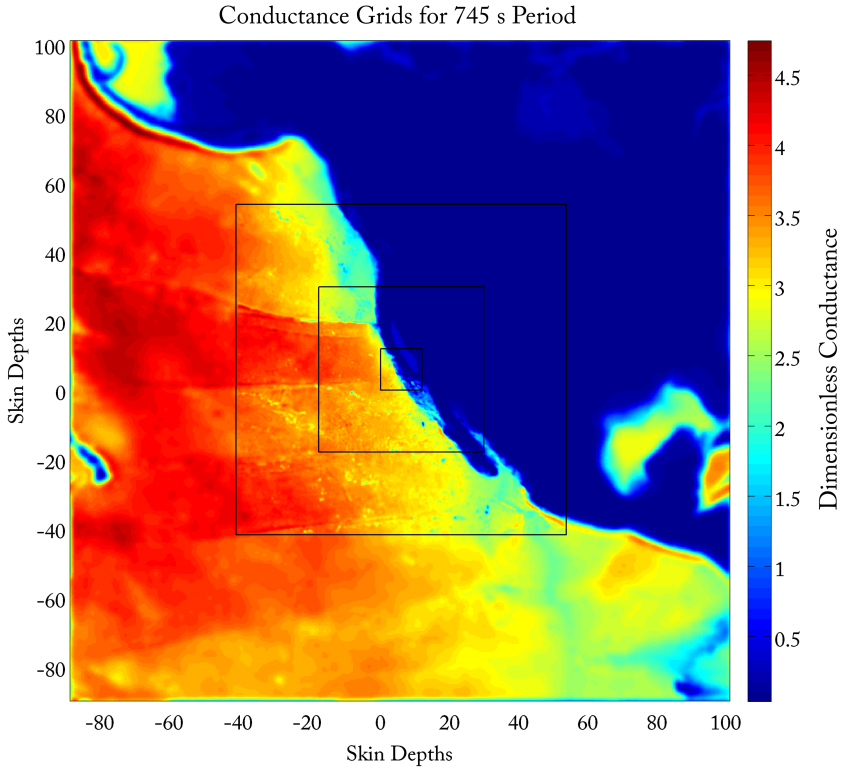

Figure 6.2: Three nested conductance grids used for a thin-sheet calculation at 745 s period. Black boxes demarcate the edges of the inset grids. Each inset grid is more finely sampled than the grid surrounding it. All units are dimensionless: distance is scaled by the skin depth in the upper-most layer, $z_0 = 43.43$ km, while conductance is scaled by the product of the upper-most conductivity, $\sigma_0 = 0.1$ S/m, and the skin depth.

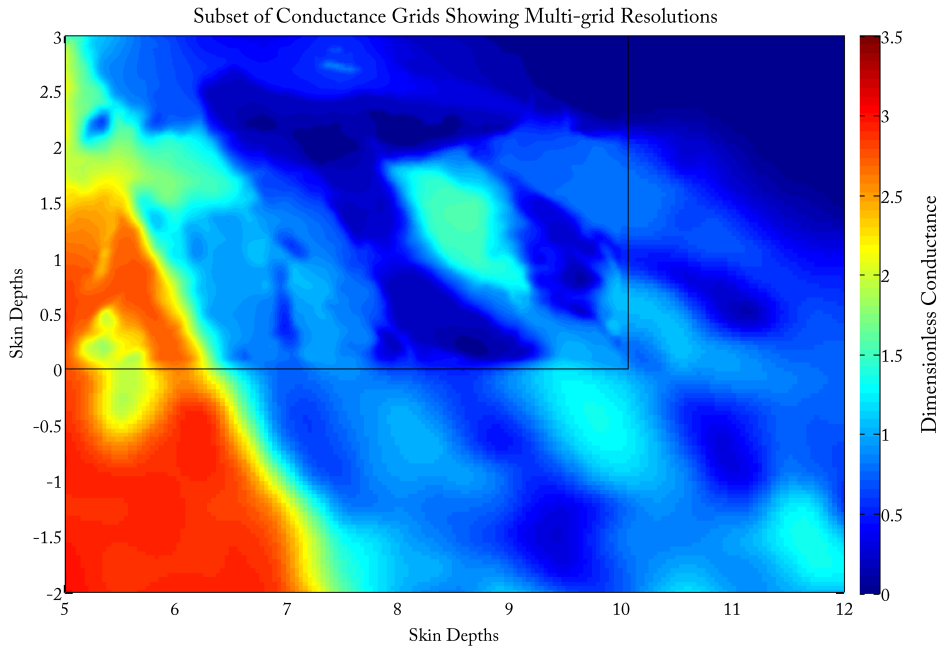

Figure 6.3: Image of the Southeast corner of the inner-most conductance grid in Figure 6.2, showing the smooth change in resolution between the coarse outer grid and finer inner grid. Units are the same as in Figure 6.2.

conductances on the very edges of the thin sheet model are bent to meet the value on the opposite side. This is done intentionally (to the conductance grids of 3D calculations as well) to avoid edge effects that would result from the periodic boundary conductions implicit in our Fourier treatment of the thin sheet.

The MT impedances and tipper vectors are calculated throughout each model at the nine longest periods found in the Estero MT data, where a total of 34 periods of data exist; subsequent plots will highlight only two of these periods, 745 s and 5460 s. The 2D models result in TE- and TM-mode impedance estimates and a TE tipper scalar, while the 3D models provide the full rank-2 impedance tensor and a 2-vector tipper. The full tensors/vectors from the 3D models are rotated into the reference frame of the line of instrument sites, and the appropriate elements are extracted so that they may be compared with the values from the 2D models. Recall from Chapter 5 that the thin-sheet method

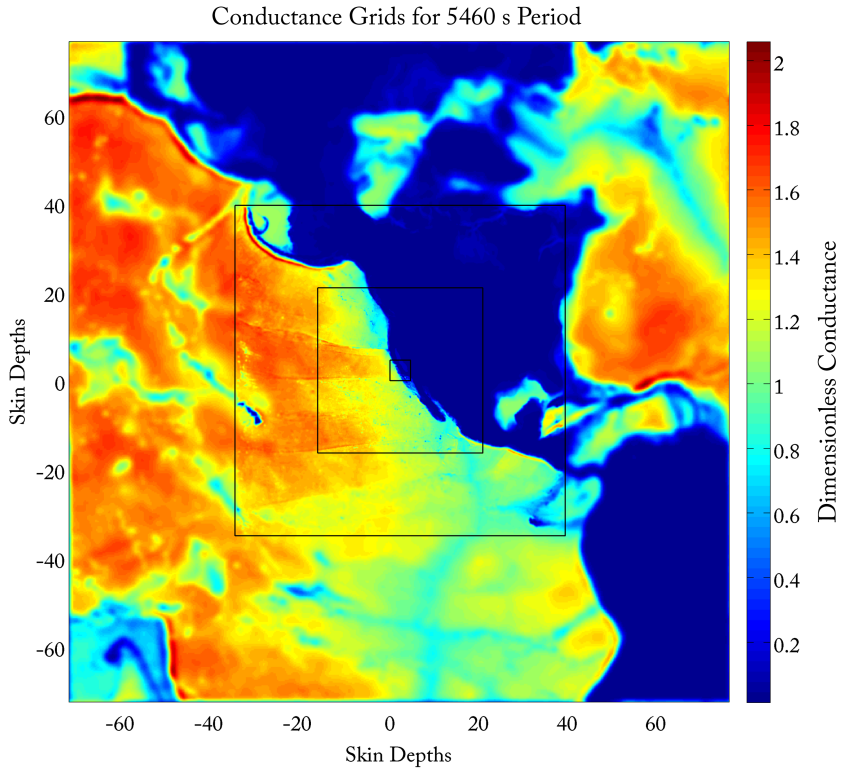

Figure 6.4: Three nested conductance grids used for a thin-sheet calculation at 5460 s period. Black boxes demarcate the edges of the inset grids. Each inset grid is more finely sampled than the grid surrounding it. All units are dimensionless: distance is scaled by the skin depth in the upper-most layer, $z_0 = 117.6$ km, while conductance is scaled by the product of the upper-most conductivity, $\sigma_0 = 0.1$ S/m, and the skin depth.

produces different values for impedance above and below the thin sheet; while the horizontal electric field is continuous across the sheet, the horizontal magnetic field is not. However, there is no way of recovering the impedance values at intermediate depths in the ocean from a thin-sheet model. We have only the values at the earth- or sea-surface, and at full ocean depth (or whatever depth interval is represented by the thin sheet). So, when comparing the thin-sheet results with the MARE2DEM results we use the values at the base of the thin sheet for all submarine measurements, and the values above the thin sheet for all subaerial measurements. Therefore an expected discrepancy between the two modeling methods arises at intermediate ocean depths, as will be evident in the first 100 km seaward

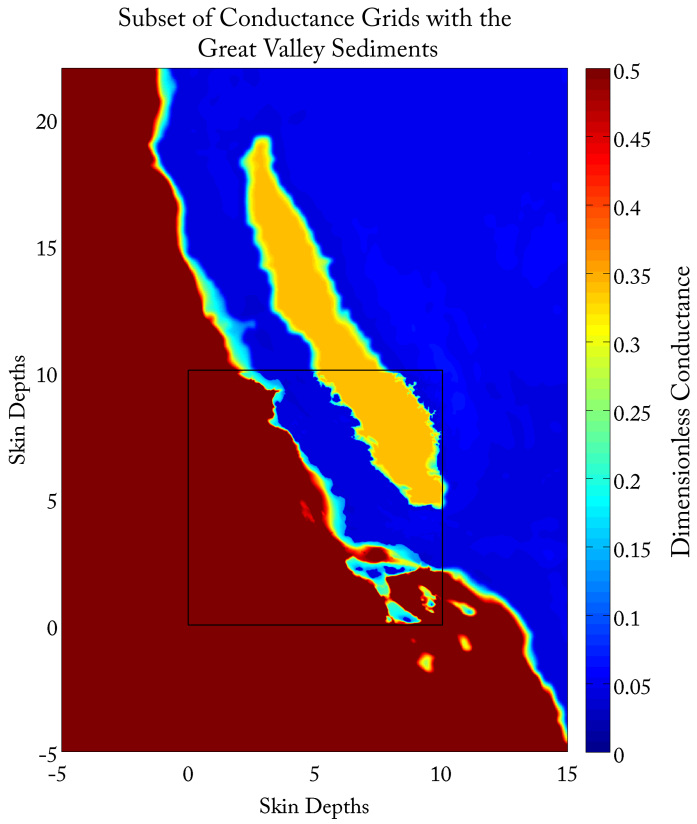

Figure 6.5: Image of the conductance grids of Figure 6.2 which incorporate a layer of 3 Ωm sediments in the GV (the golden basin enclosed in blue) that is 3 km thick at the maximum depth of the valley. Units are the same as in Figure 6.2.

of the coast in the upcoming plots, corresponding to the continental shelf and slope.

Figure 6.8 through 6.21 present the results from the 3D thin sheet calculations at the two selected periods of oscillation. The impedance results are presented in terms of the 3D anomaly relative to the expected 1D value in a given area of the plot. Since all of the models are 1D except for the upper-most layer, represented by the thin sheet, these plots may be interpreted as measure of distortion due to the coastline, bathymetry (including, to a lesser extent, topography), and, where applicable, conductive GV sediments. What these plots do not convey, however, is where a 2D model with the appropriate line of bathymetry installed would be sufficient to reproduce such distortions. Nonetheless,

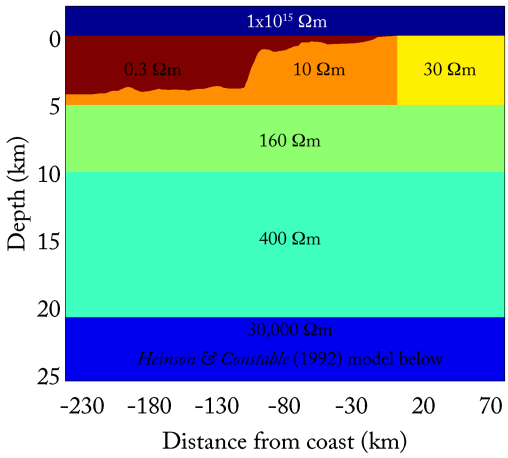

Figure 6.6: A subset of the 2D model used in MARE2DEM. The GV in this model is not made more conductive than the rest of the continent. The vertical exaggeration is 10 times.

wherever the anomalies are highly non-uniform in more than one horizontal direction, we may suspect that a 2D model is insufficient; we examine the veracity of these suspicions in upcoming plots. In Figures 6.12, 6.13, 6.18, and 6.19, we see that the Swift skew measure rarely reaches a significant (> 0.2) value; it does so only with the roughest of bathymetry, and more so with the shorter period calculation. Significant skews *are* found along the portion of the Estero MT profile which traverses the continental slope, coincident with sites M27-M19, whose data *do* exhibit elevated skew values (see Figure 6.22). The introduction of a conductive GV in the thin sheet also produces higher skews around its edges, near the eastern end of the Estero MT profile, where, again, higher skews are found in the data. Overall, however, the skew values produced by the thin-sheet calculations are much smaller than those encountered in the data. The data skews are also highly variable from site to site. Of course, we don't expect our thin-sheet model, which fills the whole continental margin down to a depth of 5 km with 10 Ωm resistivity, to be an exact replica of the earth as measured by our data, but the difference in magnitude and variance of the measured skews relative to the modeled skews suggests that there is more at work in the distortion of the data than simply 3D bathymetry. Two possible causes are broader 3D structures in the subsurface, or small-scale, near-surface, galvanic scatterers, which have been shown

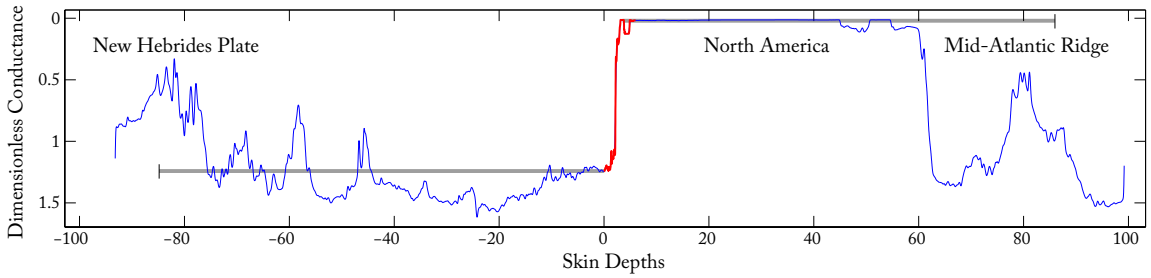

Figure 6.7: Conductance profiles, inner (red) and outer (blue), used in the 2D thin sheet calculations at 5460 s period (with a conductive GV). For reference, the conductance equivalent of the top-layer of the MARE2DEM model (Figure 6.6), is shown with thick gray lines, with thin vertical black lines denoting the edges of the MARE2DEM model.

to produce large skews even when the broader scale induction is 2D [Bahr, 1988]. The reproduction of these effects is beyond the capabilities of the thin-sheet approach. Along these same lines, the impedance polar diagrams, produced by the thin sheet model that includes a conductive GV (Figures 6.20 & 6.20), only roughly agree with those of the actual data (Figure 3.12).

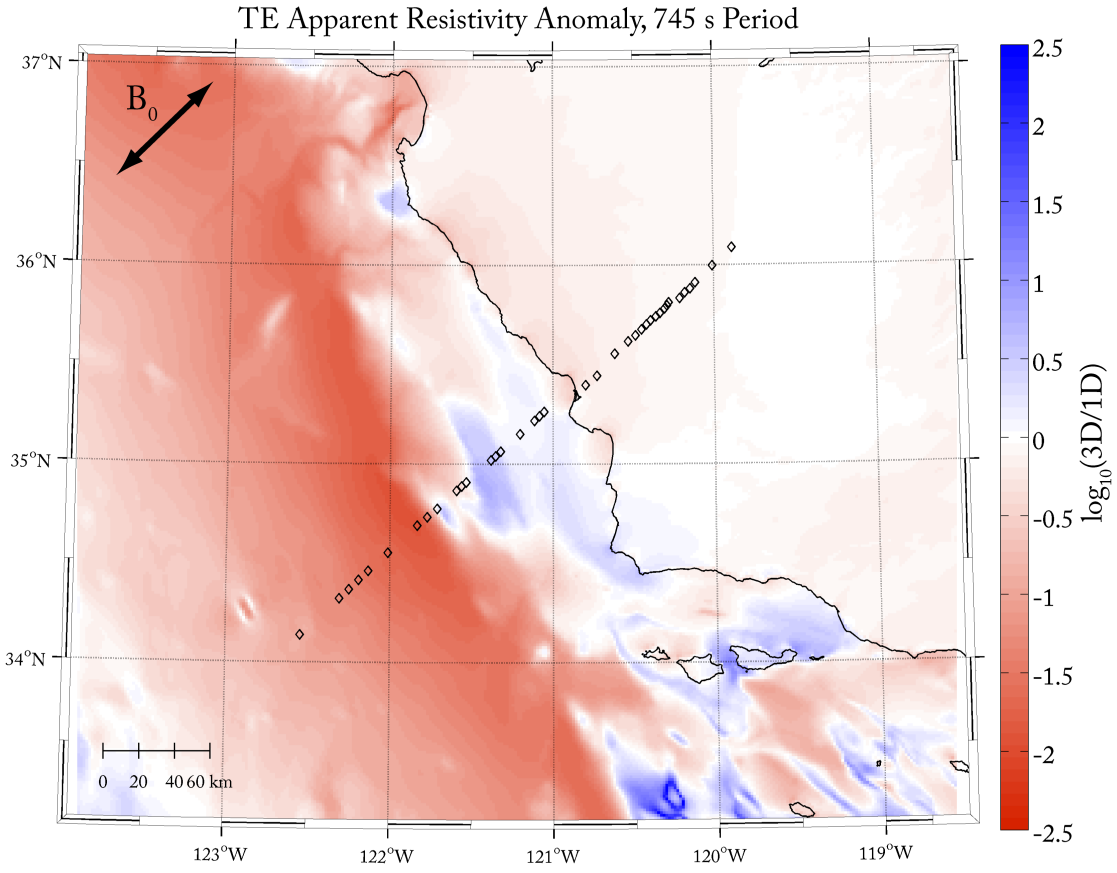

Figure 6.8: A map of TE-mode apparent resistivity anomaly from a thin sheet calculation at 745 s period (see Figure 6.2). Anomalies are plotted relative to the 1D value for the the layered structure below the thin sheet; for anomalies on land, the layered structure includes the top layer incorporated into the thin sheet. Estero MT sites are plotted with black diamonds. The direction of the driving magnetic field, B_0, denoted in the upper left corner.

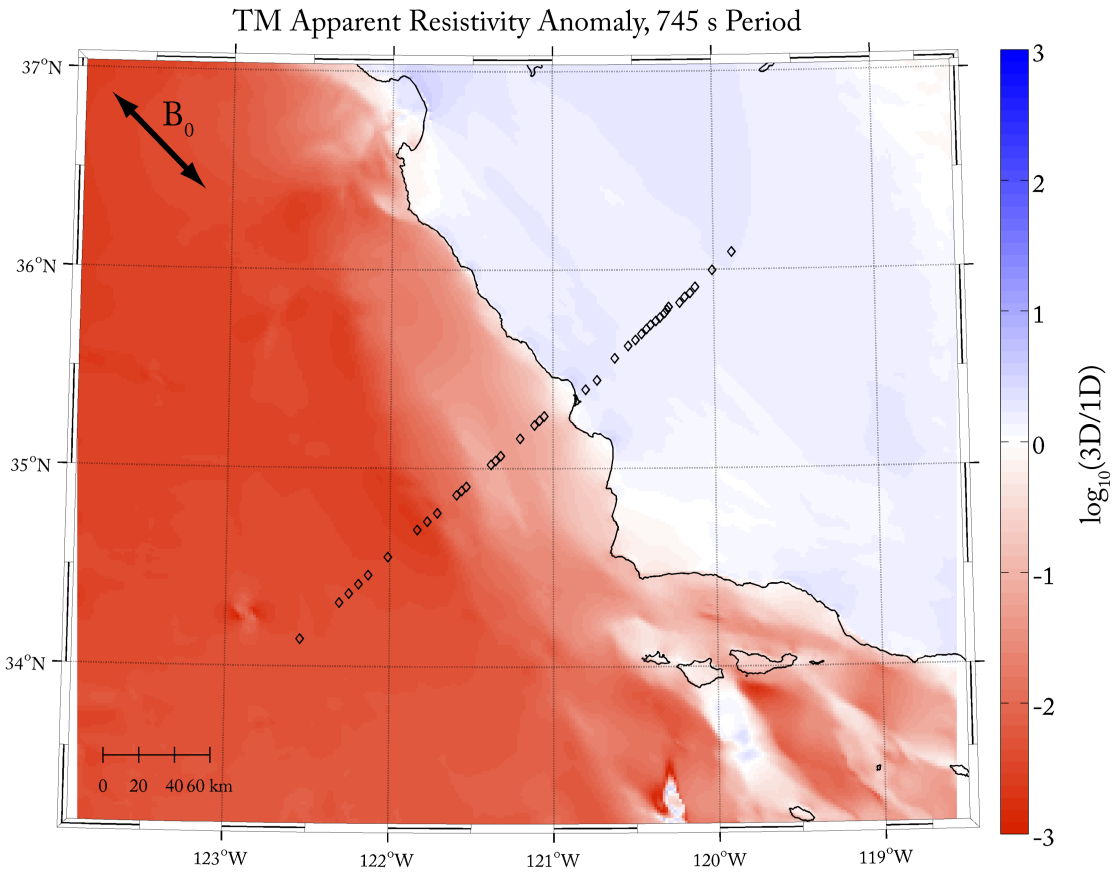

Figure 6.9: Same format as Figure 6.8, but for TM-mode apparent resistivity.

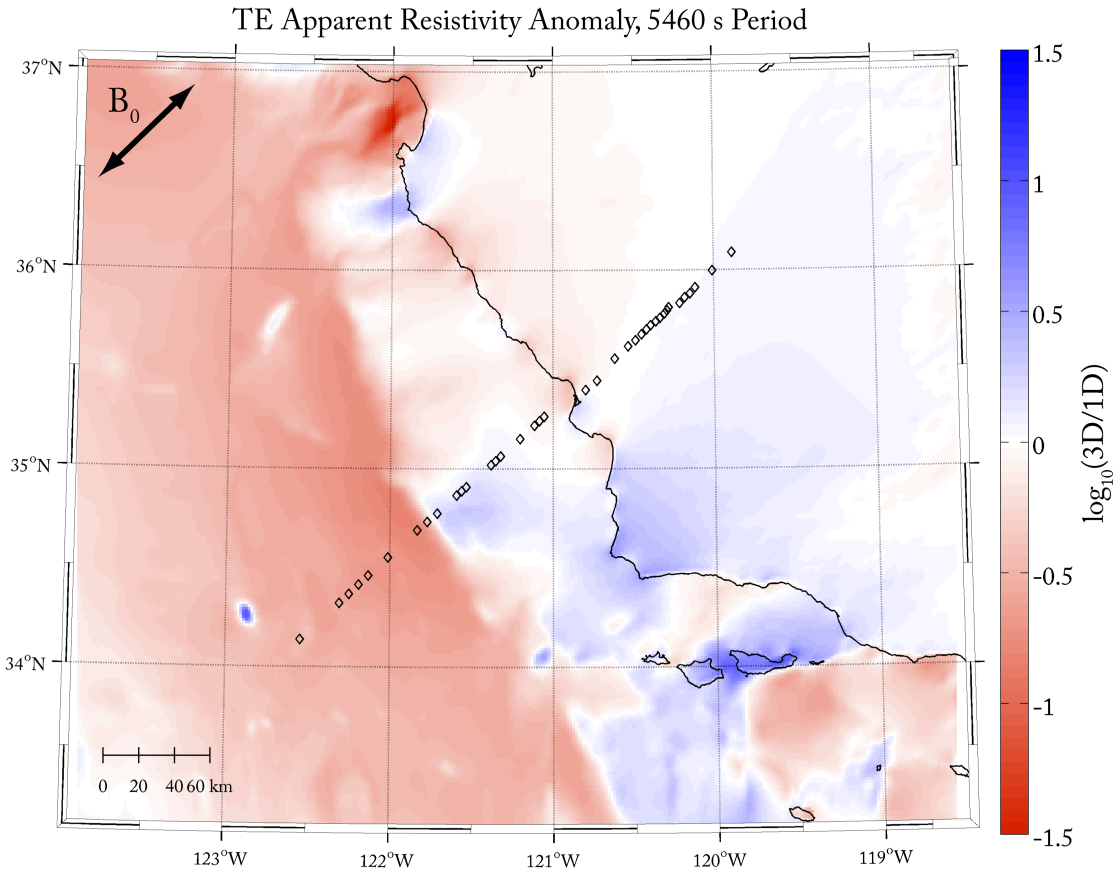

Figure 6.10: Same format as Figure 6.8, but for TE-mode apparent resistivity at 5460 s period (see Figure 6.4).

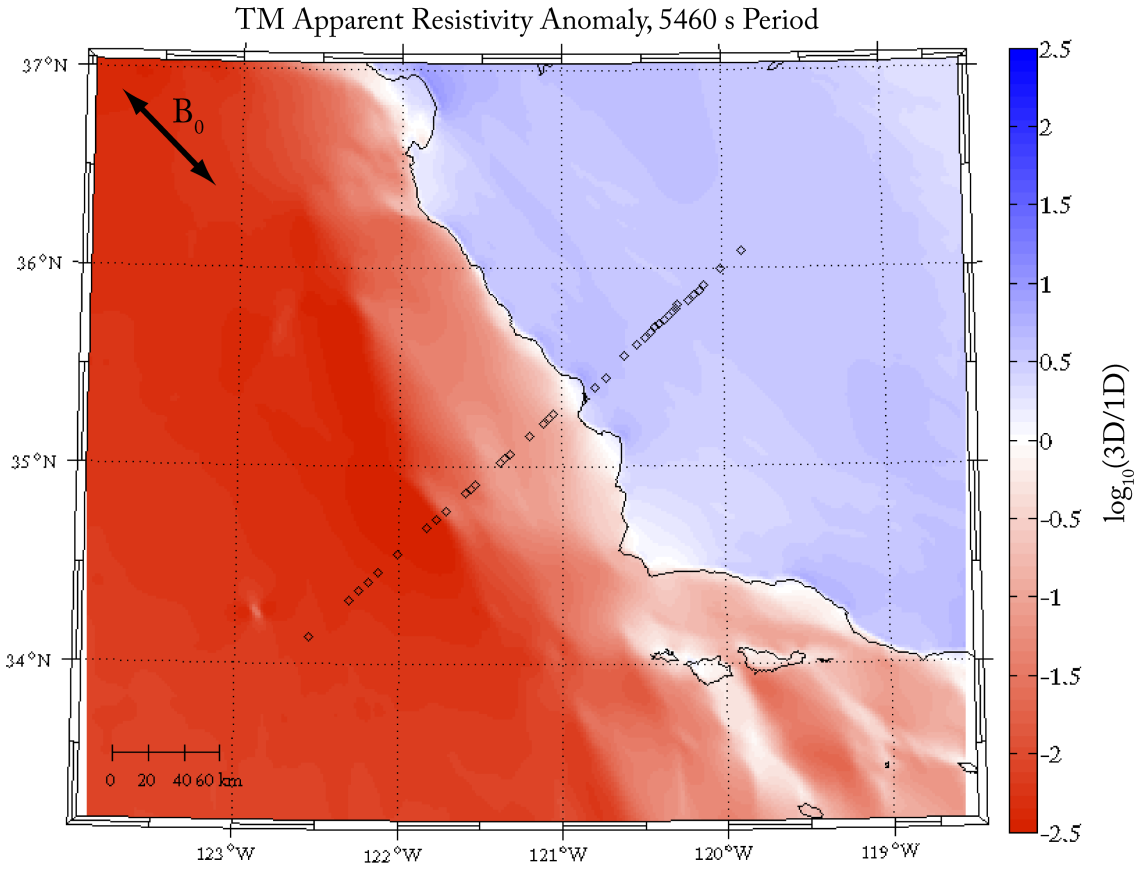

Figure 6.11: Same format as Figure 6.10, but for TM-mode apparent resistivity.

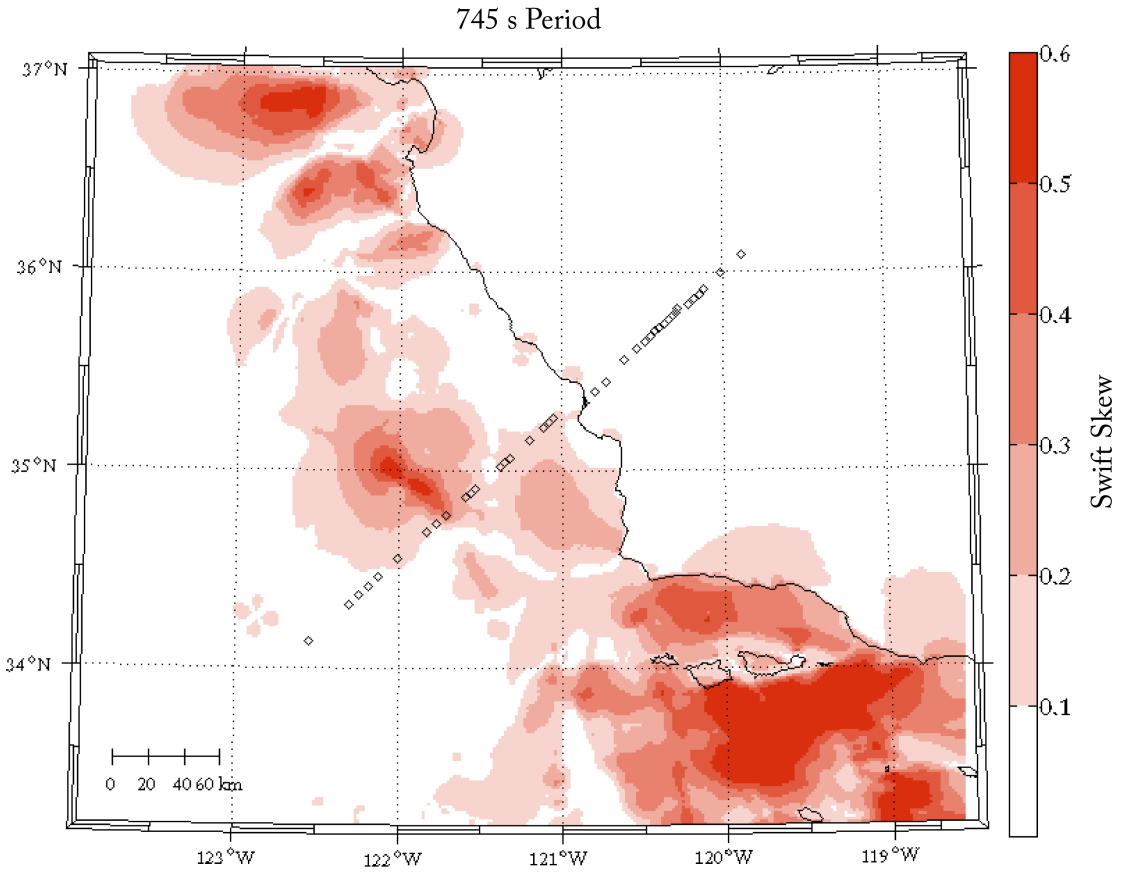

Figure 6.12: A map of the inner-grid Swift Skew from a thin sheet calculation at 745 s period. Estero MT sites are plotted with black diamonds.

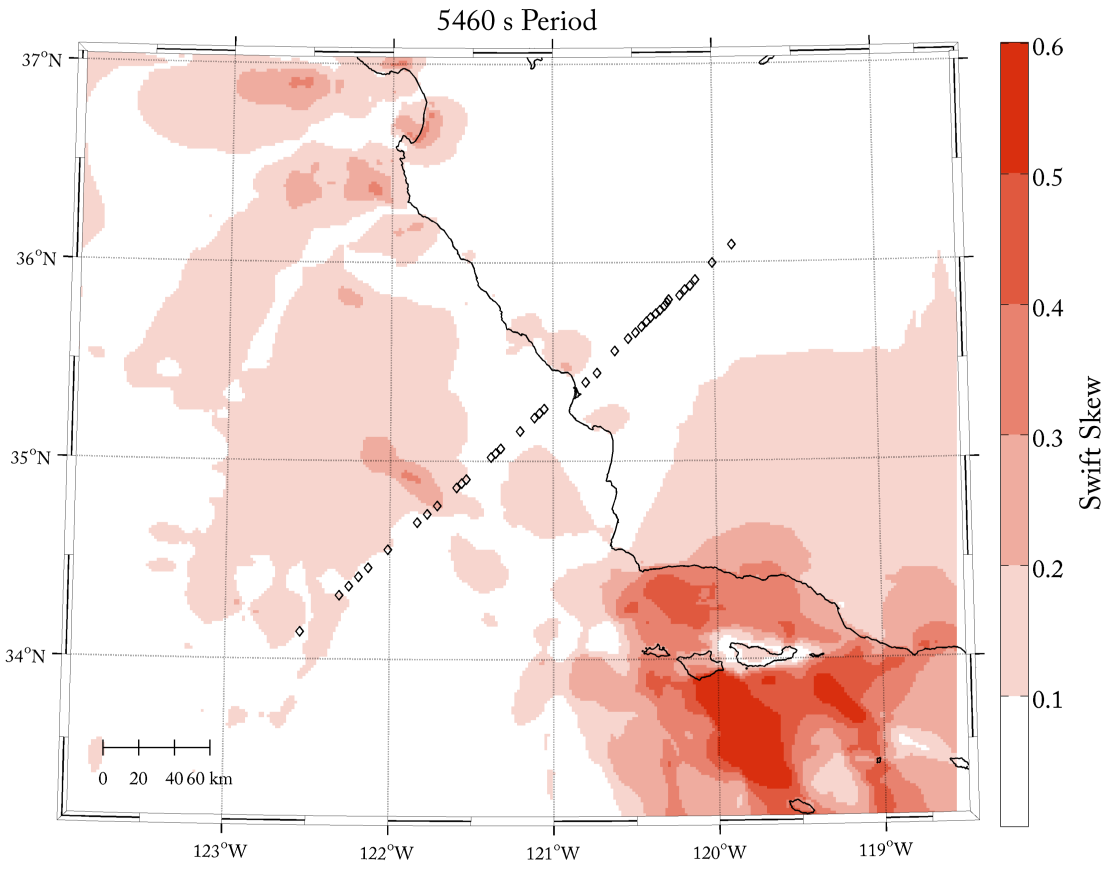

Figure 6.13: A map of the inner-grid Swift Skew from a thin sheet calculation at 5460 s period. Estero MT sites are plotted with black diamonds.

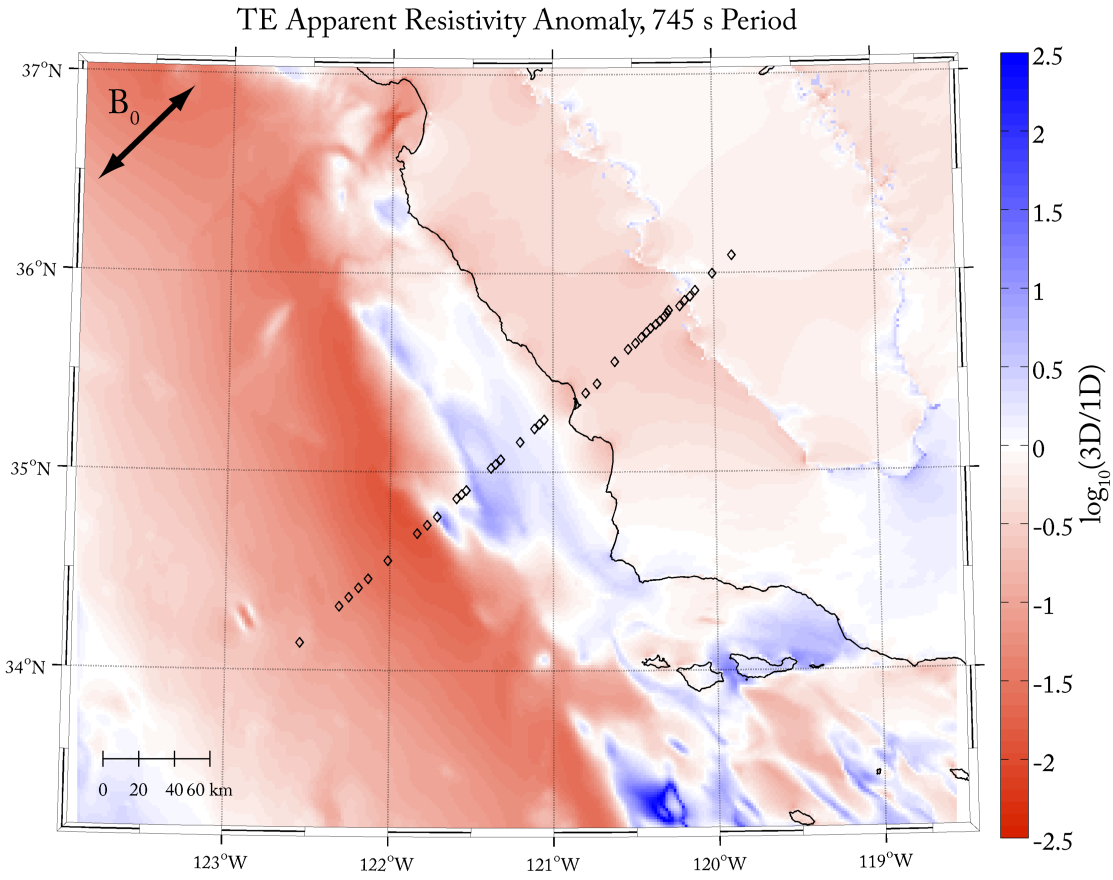

Figure 6.14: A map of the inner-grid TE-mode apparent resistivity anomaly from a thin sheet calculation that includes the GV sediments at 745 s period (see Figure 6.5). Anomalies are plotted relative to the 1D value for the the layered structure below the thin sheet; for anomalies on land, the layered structure includes the top layer incorporated into the thin sheet, which assumes a constant layer thickness (3 km) for the GV sediments. Estero MT sites are plotted with black diamonds. The direction of the driving magnetic field, B_0, denoted in the upper left corner.

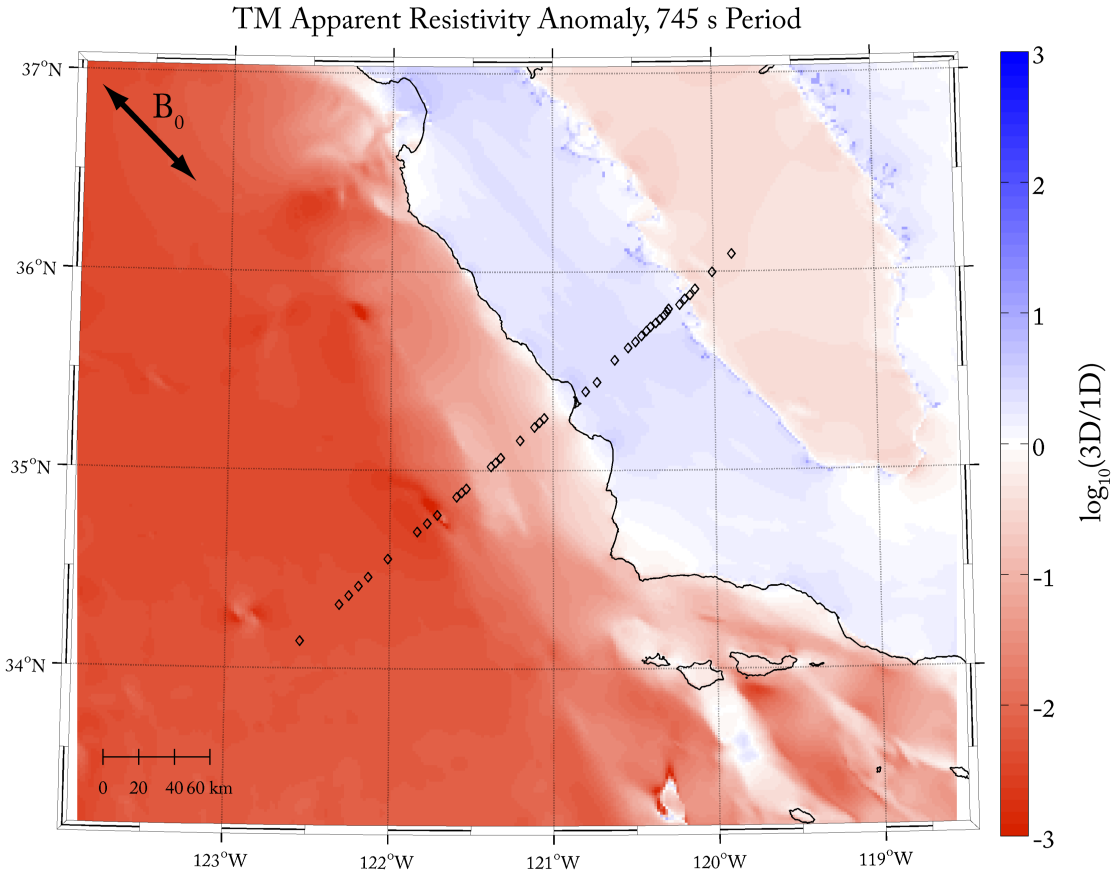

Figure 6.15: Same format as Figure 6.14, but for TM-mode apparent resistivity.

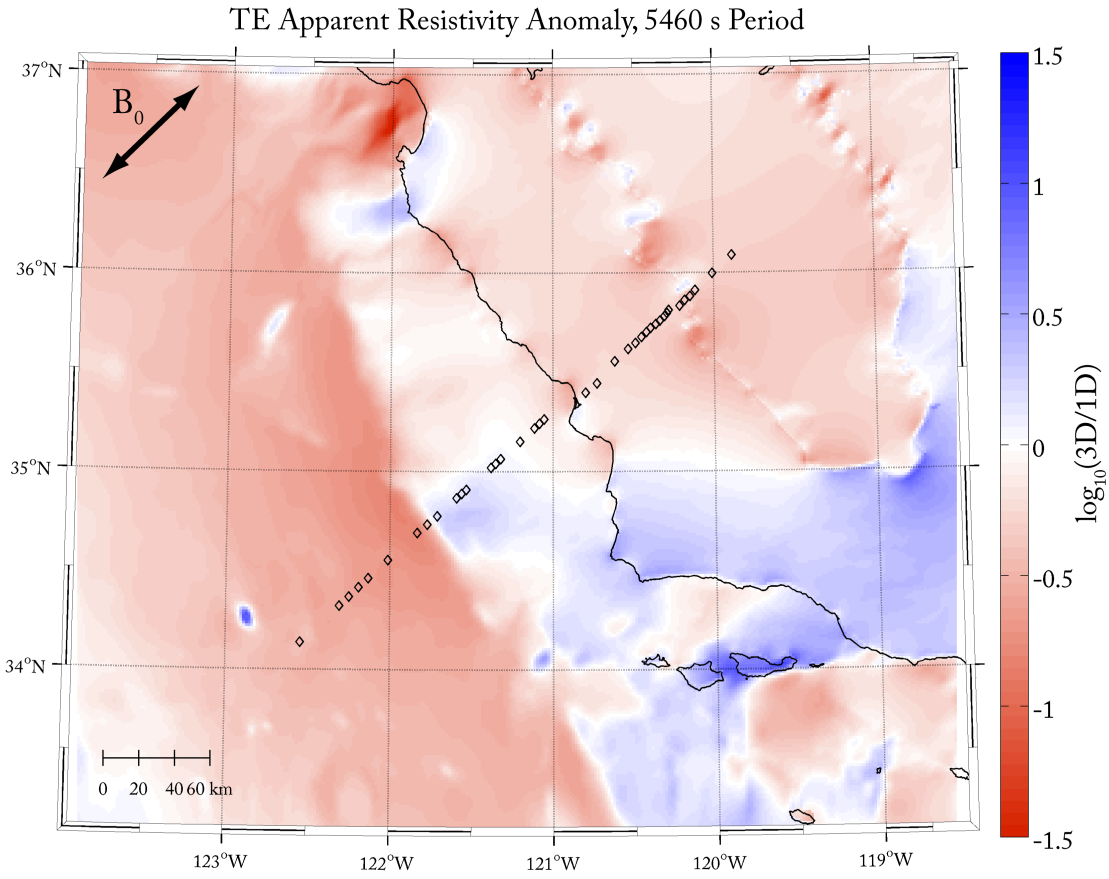

Figure 6.16: Same format as Figure 6.14, but for TE-mode apparent resistivity at 5460 s period (see Figure 6.4).

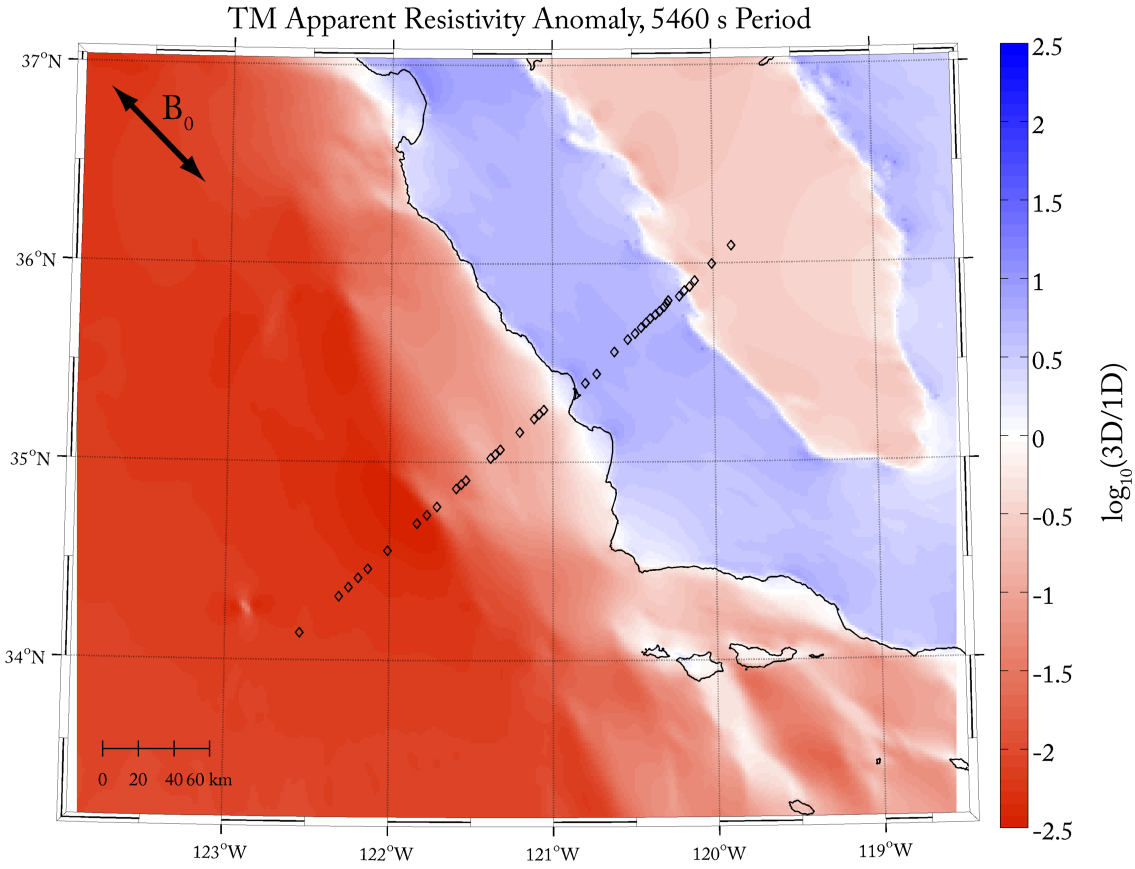

Figure 6.17: Same format as Figure 6.16, but for TM-mode apparent resistivity.

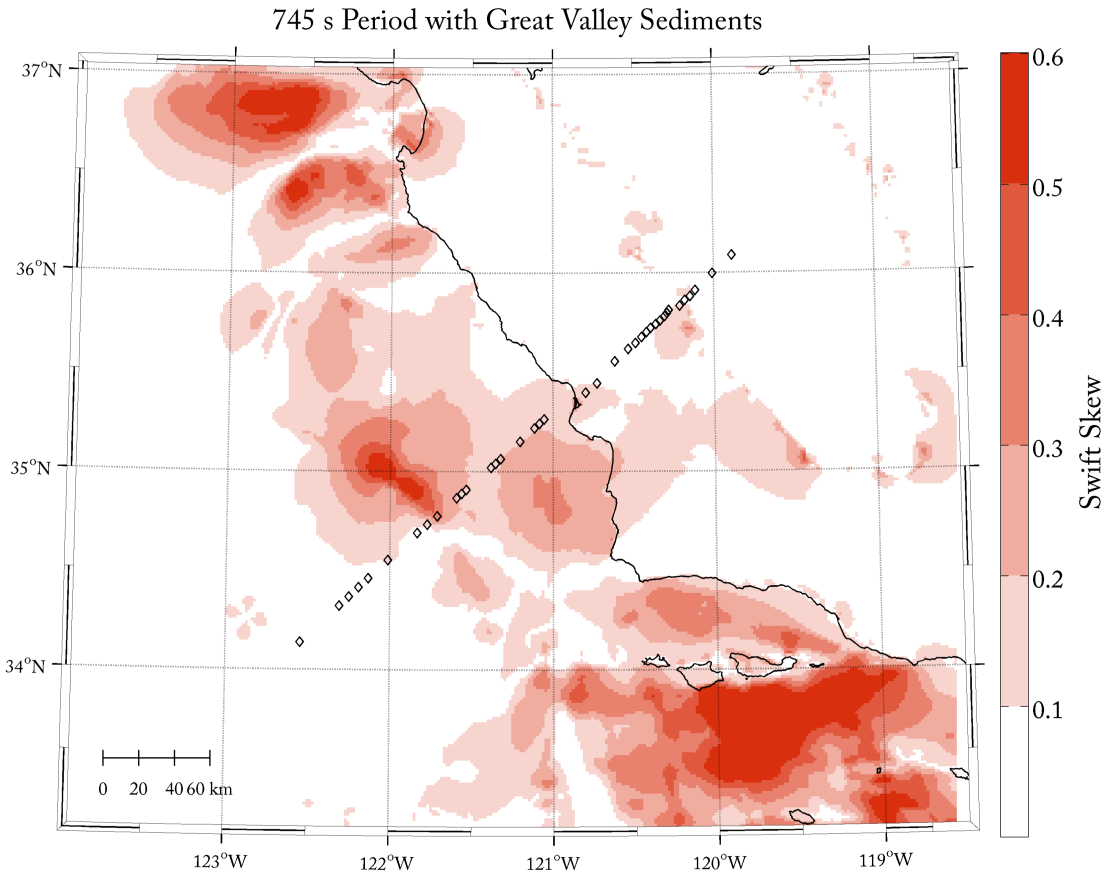

Figure 6.18: A map of the inner-grid Swift Skew from a thin sheet calculation at 745 s period. Estero MT sites are plotted with black diamonds.

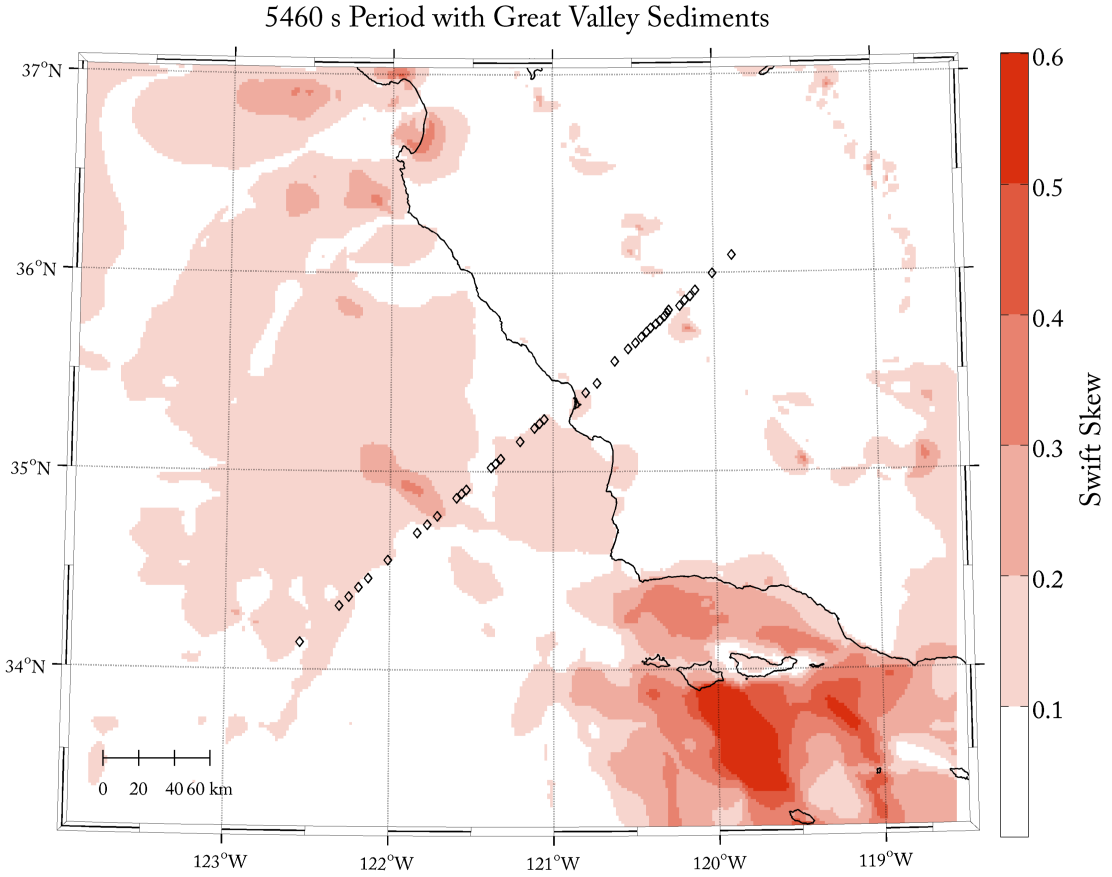

Figure 6.19: A map of the inner-grid Swift Skew from a thin sheet calculation at 5460 s period. Estero MT sites are plotted with black diamonds.

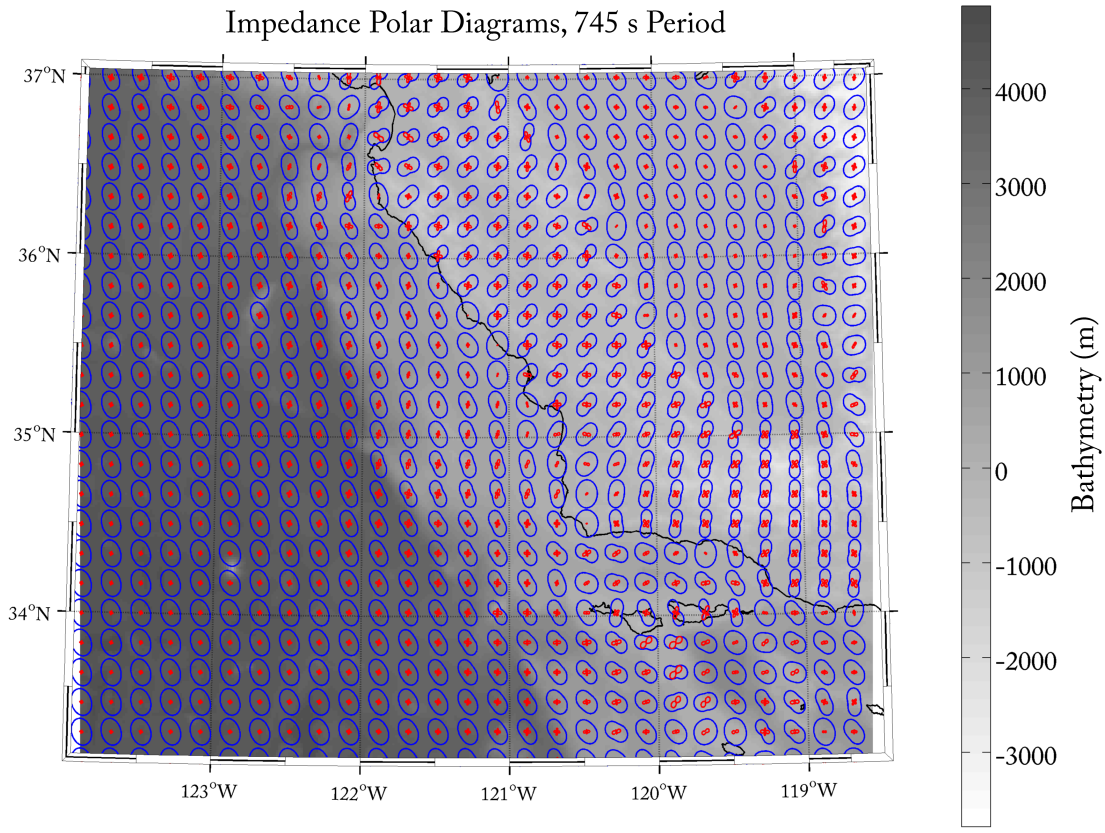

Figure 6.20: A map showing a sampling of impedance polar diagrams from a thin sheet calculation at 745 s period, plotted atop the bathymetry of the inner-grid. Blue lines are from P_{xy} (off-diagonals), and red lines are from P_{xx} (on-diagonals). Note, the displayed calculations included an anomalously conductive GV.

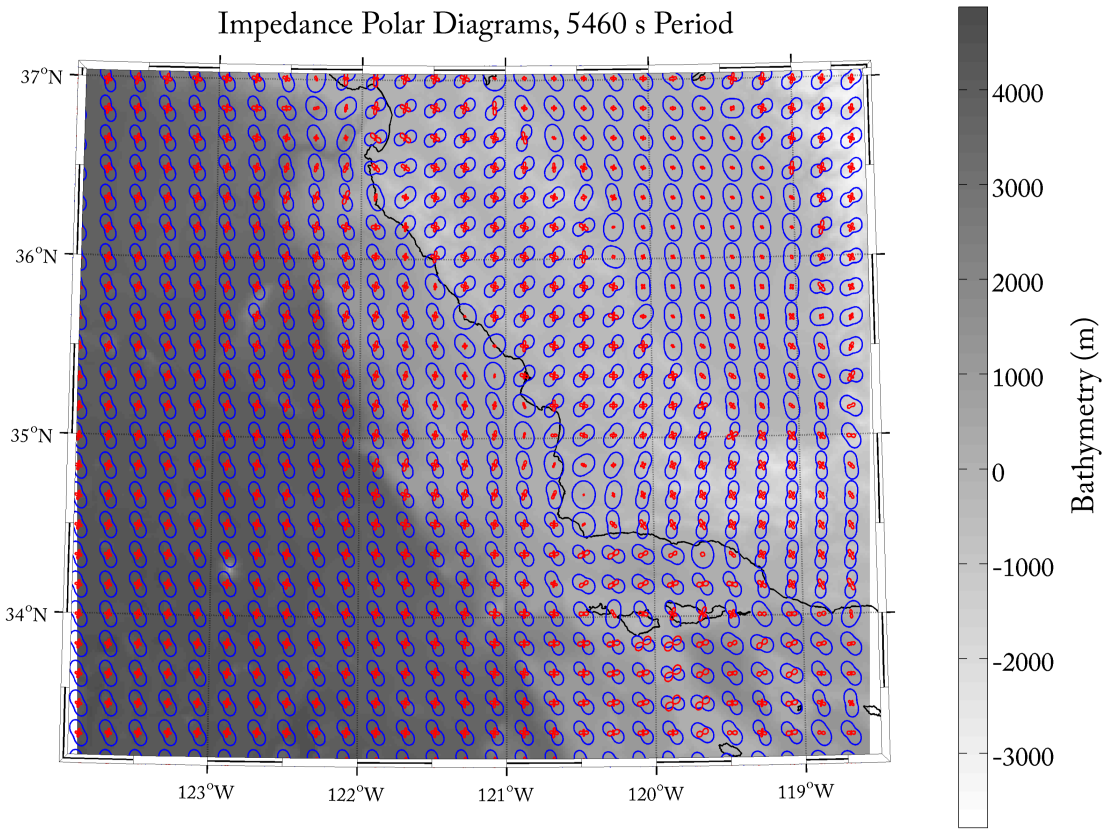

Figure 6.21: Same format as Figure 6.20, but for the thin sheet calculation at 5460 s period.

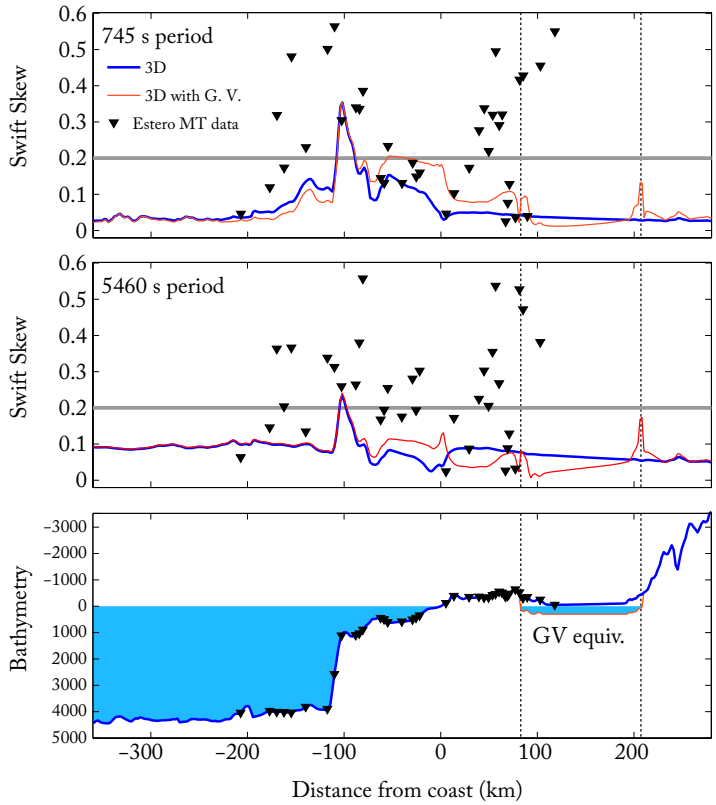

Figure 6.22: Swift skew values along the line projected by the Estero MT sites, taken from two thin-sheet model calculations: one without enhanced conductance in the GV, and one with relatively high conductance GV sediments (3 km thick of 3 Ωm). (Top) Swift skew values at 745 s period, and (middle) Swift skew values at 5460 s period. (Bottom) The bathymetry along the profile line illustrating the seawater integrated into the thin-sheet conductance, note the large vertical exaggeration. For the GV model, an analogous ≈ 300 m deep ocean was integrated to reproduce the conductance of the 3 km thick layer of sediments.

As stated before, plots of the thin sheet results referenced to the expected quantities for the 1D stack of layers below each model cell do not inform us as to whether a 2D inversion of bathymetry-affected data would suffice. To gain a better grasp on this matter, we compare the 3D thin-sheet results with the 2D calculations, first with Figures 6.23 through 6.26. The 3D results in these figures have been extracted from the line that best fits the formation of instrument sites in a Transverse Mercator projection, while the

2D results were calculated for the bathymetry along that same line.

Despite the period of 745 s being well below our predetermined threshold for thin sheet validity (see Section 5.6), the 2D thin-sheet results at that period match remarkably well with those of the benchmark MARE2DEM model. At a period of 5460 s, the thin sheet calculations agree with the benchmark very well. The greatest mismatch for all periods occurs between -100 km and 0 km from the coast, where the thin sheet returns values at $\approx$ 5 km depth whereas the MARE2DEM model returns values at shallower seafloor depths. With the TE-mode, in the areas distant from the coast, where the thin sheet and finite-element methods deliver the fields at close to the same depth, the differences between the two methods are well within the Estero data errors; examples of the data errors are shown in the corner of each figure. Note that the thin-sheet models include small-scale bathymetry throughout the model domain while the MARE2DEM calculation does not. Hence, there are small-wavelength undulations in the thin-sheet results that are non-existent in those from MARE2DEM. Also, notice that the TE-mode results meet the benchmark better than the TM-mode results. There is an unexplained near-constant shift between the TM-mode of the thin sheet calculations and its benchmark on the marine side of the model. We propose one possible explanation: the TM-mode is the most sensitive to the side boundary conditions in a 2D model. These boundary conditions differ significantly between the thin-sheet and finite-element methods; the thin-sheet method enforces periodicity, while the finite-element method enforces a match to the fields of a 1D background model, i.e., the fields resulting from an infinite ocean on one side, and the fields resulting from an infinite continent on the other. It is not immediately clear which condition is more applicable to the real earth. The real earth has neither infinitely wide oceans and continents, nor infinitely repeating clones of them. A serious discussion over which philosophy is superior must be limited, since both assume that the earth is flat; the correct solution for such vast models, of course, would be to proceed with modeling on a sphere. The observation however, is that such remote boundaries (see Figure 6.7) seem to matter, at least when given a lithosphere as resistive as has been proposed. The complication of the side boundary conditions may be the reason for anomalous conductivities that persistently appear just off the edge of spatial data coverage in inversion models.

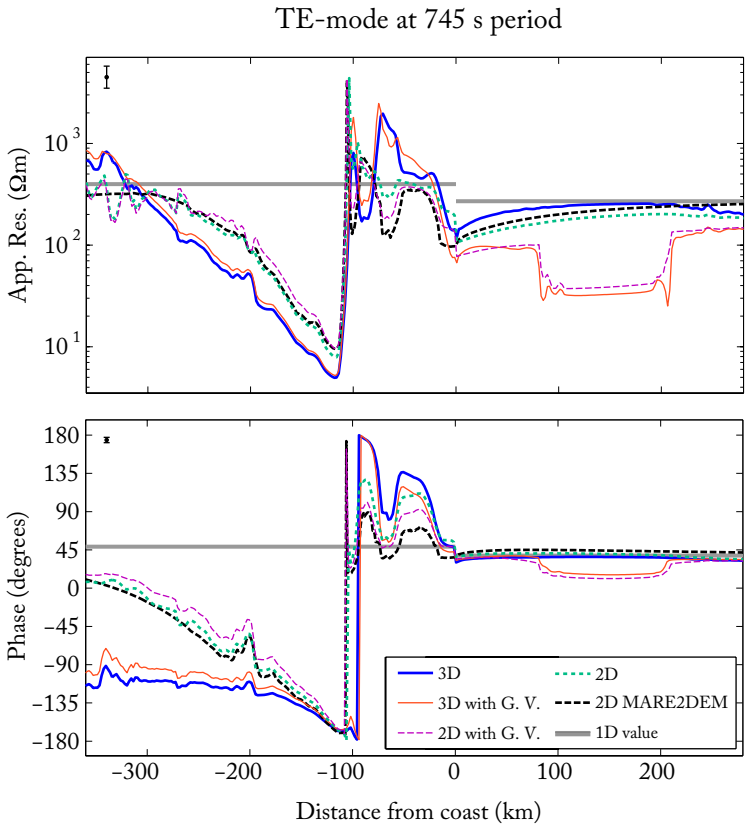

Figure 6.23: A comparison of the various model calculations for the TE-mode impedance at 745 s period, extracted along, and rotated into the reference frame of the Estero MT line of sites (see Figure 6.22 for bathymetry profile and site locations). 2D and 3D calculations are made with thin-sheet models unless otherwise stated (i.e., with MARE2DEM). Just as in Figures 6.8 through 6.21, submarine locations use the field values at the base of the thin sheet, while subaerial locations use field values atop the thin sheet. Likewise, 1D values pertain to the either the stack of layers below the thin sheet (submarine) or below the earth's surface (subaerial). In the upper-left of each of the two plots are sample data error bars showing the corresponding $\pm 1\sigma$ error floors used with inversion of the Estero MT data.

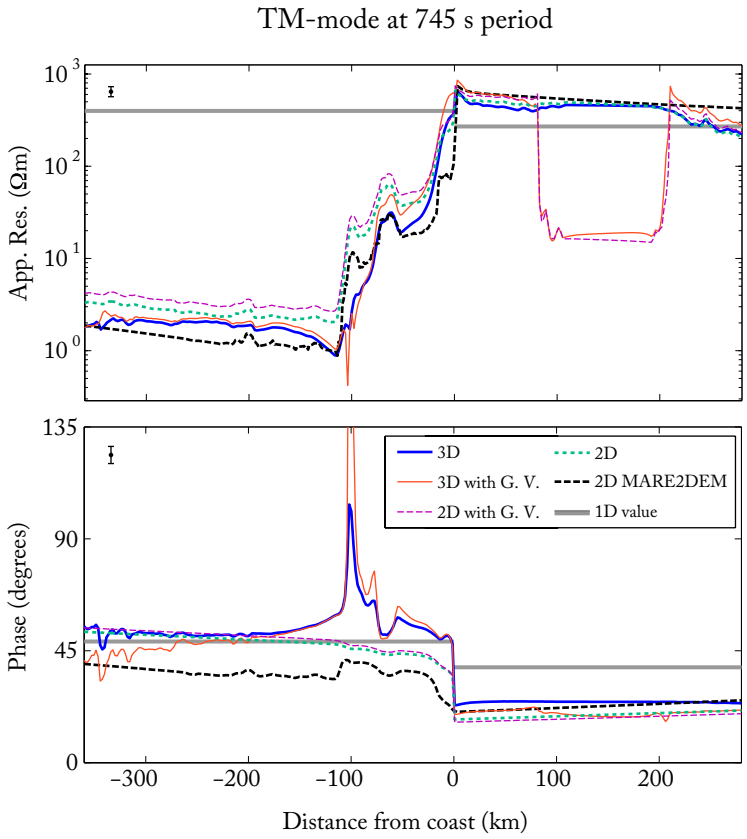

Figure 6.24: Same format as Figure 6.23 but for the TM-mode impedance.

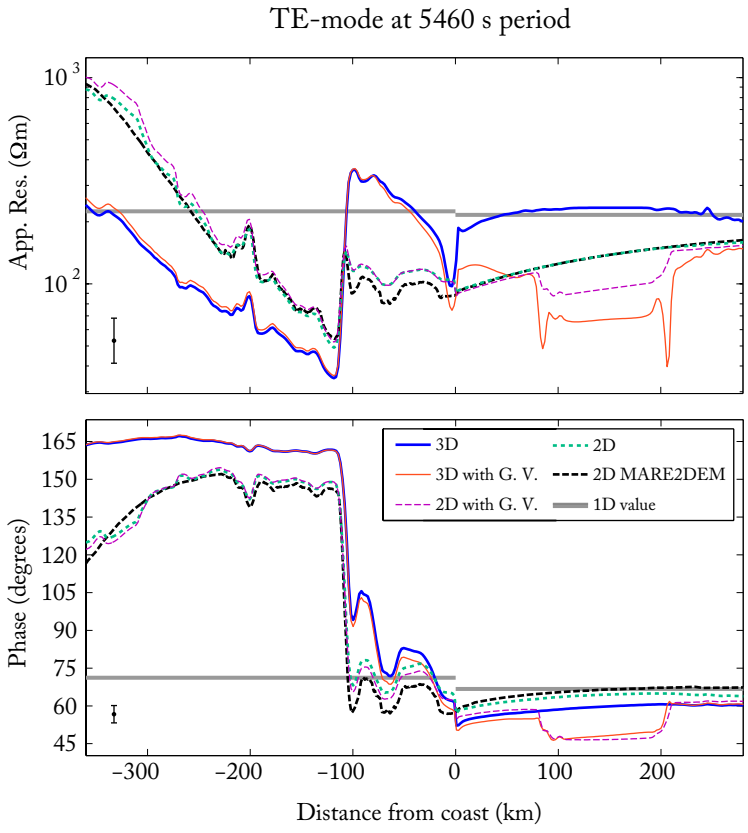

Figure 6.25: Same format as Figure 6.23 but for 5460 s period.

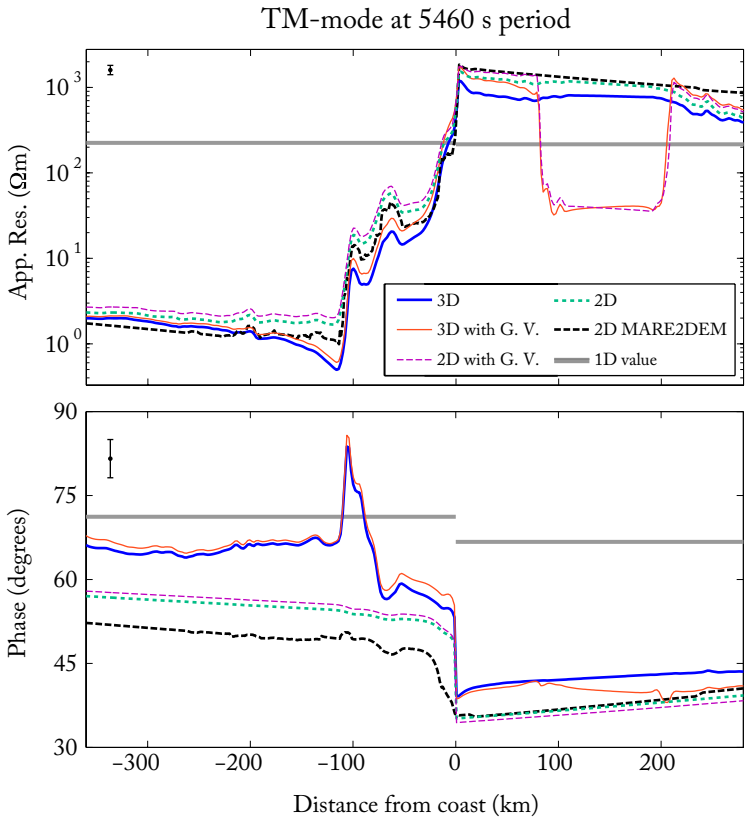

Figure 6.26: Same format as Figure 6.23 but for the TM-mode impedance at 5460 s period.

Despite the puzzling *long*-wavelength disparity between the TM-mode of the thin sheet and its benchmark, the short-wavelength results for both modes of the thin sheet match those of the benchmark very well. Next, we examine the differences between the short-wavelength behavior of the 3D thin-sheet results relative to those of the 2D thin sheet. Often where there is a bump in the 2D result the same bump is smoother in 3D, or in some cases, the 3D response takes the form of a depression instead. This is explained as the difference between a bathymetric high being interpreted as an infinite ridge in the 2D world whereas in the 3D world it may only be a local mound. To account for this, it may prove beneficial for 2D inversions to instead use as its fixed seafloor interface a local, cross-strike average of bathymetry rather than the exact bathymetry below a line a sites. Such a correction may remove the small conductive anomalies that appear localized below each marine data site in most inversion models.

Leaving the benchmark issue aside for now, let us address the differences between the middle- to long-wavelength behaviors of the 3D and 2D thin-sheet calculations. At these longer wavelengths, the 3D behavior indicates a mixing of the canonical behaviors of the two independent modes in 2D. The 2D TE-mode, some characteristic distance seaward of a coast, exhibits a steep depression in apparent resistivity at the base of the continental slope followed by its ascent with increasing distance from the coast, which eventually exceeds the value expected in the absence of a coast (1D); the 2D-TE phase either ascends or descends here, whichever direction brings it toward a 1D state. The 2D-TE phase may even go negative at shorter periods. On the contrary, the 2D TM-mode exhibits significant depressions in apparent resistivity and phase seaward of the coast which are nearly constant with distance and never exceed the expected 1D value. The 2D TM-phase never goes negative. In 3D, where the modes are inseparable, the TE-mode (we refrain from placing the 3D modes in quotation marks, yet, depending upon the conductivity distribution, they may lose much, if not all, of the connotation they carried in 2D) apparent resistivity is depressed relative to the 2D TE-mode, and, relative to the 2D TE-mode phase, the TE-mode phase in 3D is perturbed in the direction away from the 1D value. Conversely, the 3D TM-mode shows hints of the ascending curvature seen in the 2D TE-mode, and the 3D TM-mode is perturbed toward the 1D value, in some cases exceeding it. As for the more

conductive GV, the effect may be far-reaching in both 2D and 3D, and most noticeably in the shorter period TM-mode.

The long-wavelength mixing of modes is best illustrated with the map-view (e.g., Figure 6.16), where the distortions may be viewed relative to the local strike of the coastline. The longer-wavelength fields, as opposed to shorter-wavelengths, are still affected by the coast from a great distance away. When that distance becomes comparable to the radius of curvature of the coast, the prevailing induced electric current in the ocean is no longer exclusively parallel or exclusively perpendicular to the coast, as would be the case in a 2D world. This current, which intersect the coast obliquely, may be decomposed into a sum of coast-parallel and coast-perpendicular current, the independent currents induced by the 2D TE- and TM-modes, respectively. Since the 3D current distribution is a superposition of the two 2D modes of current, we naturally encounter mixing of these modes in the apparent resistivity and phase curves. What is more interesting is that the mixing of modes, as modeled here specifically for offshore central California, when viewed from the perspective of an inversion constrained by a 2D model for the world, either diminishes or increases the expected coast effect depending upon which type of data are to be analyzed, and where they are collected. We define the 2D coast-effect as the perturbation of the 2D model results away from their expected 1D value. If the 3D results trend closer to the 1D values than the 2D results, we consider the 2D coast effect to be diminished; likewise, the 2D coast effect is increased when the 3D results trend further away from the 1D values. Through careful analysis of the long-wavelength behavior of our collection of results at all nine periods, some generalized rules emerge: the 3D coastline increases the 2D coast effect in the TE-mode apparent resistivity and phase in the marine environment, and the only TE-mode phase on land, while diminishing the 2D coast effect in the TE-mode apparent resistivity on land; the 3D coastline increases the 2D coast effect in the marine TM-mode apparent resistivity, yet diminishes the 2D coast effect in the TM-mode phase, marine and terrestrial, and in the TM-mode apparent resistivity on land. There is an apparent symmetry in the 3D distortion, which must pull a 2D inversion in opposite directions, each with equal weight.

Next, we look to the 3D and 2D tipper results (Figures 6.27 - 6.30), for which the terrestrial and marine values are displayed separately. The marine results vary on a

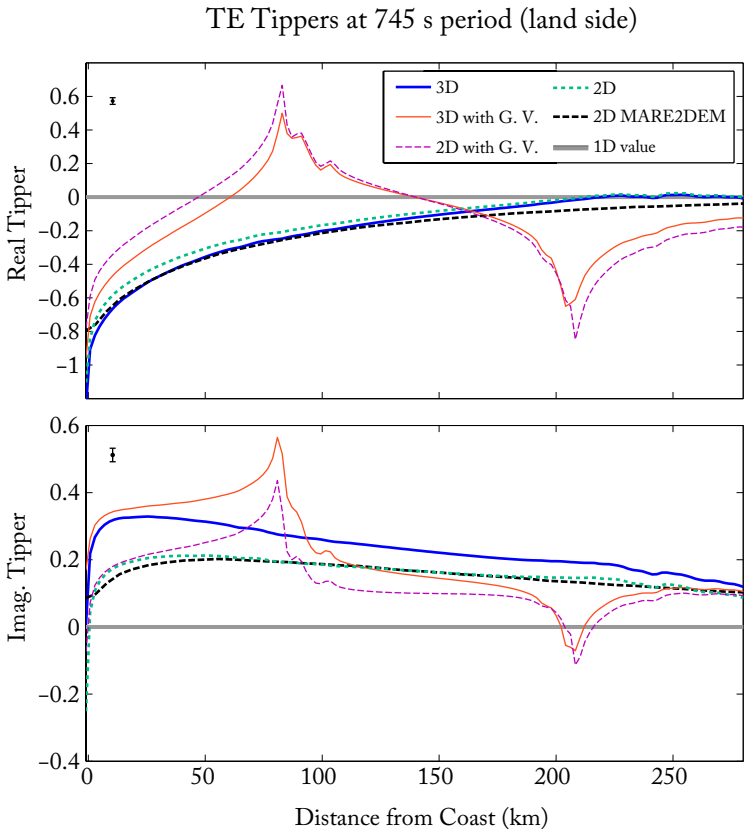

Figure 6.27: Same format as Figure 6.23 but for the TE-mode tipper.

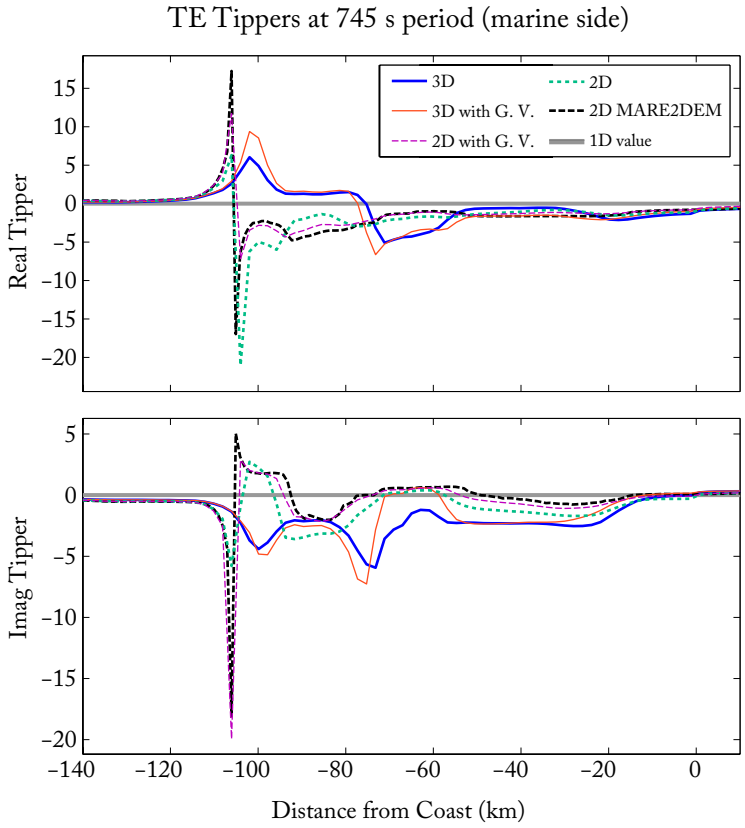

Figure 6.28: Same format as Figure 6.23 but for the TE-mode tipper. Note example data errors are not plotted because they would be too small to be visible.

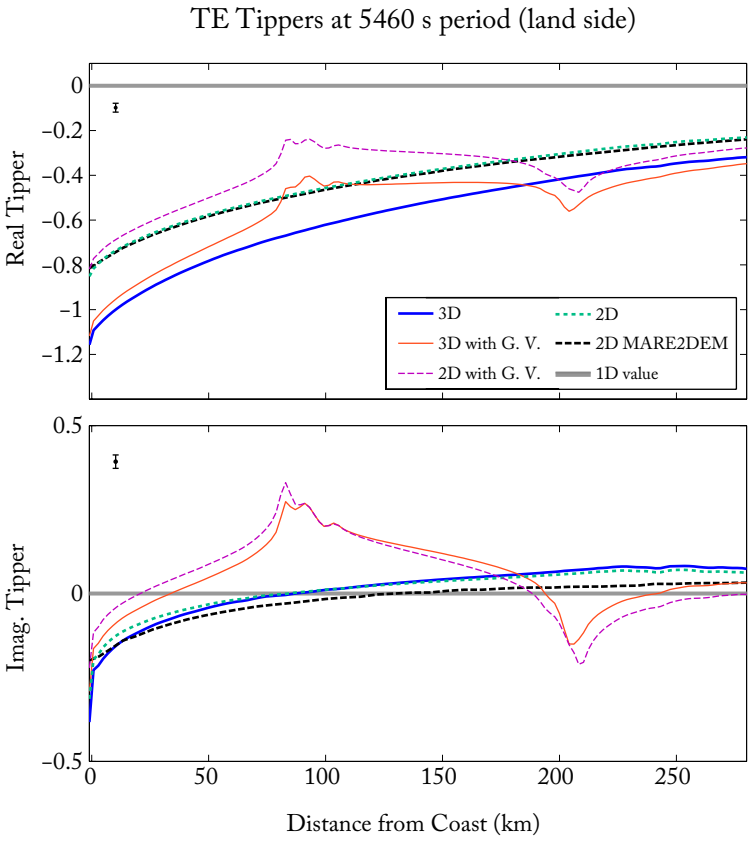

Figure 6.29: Same format as Figure 6.23 but for the TE-mode tipper at 5460 s period.

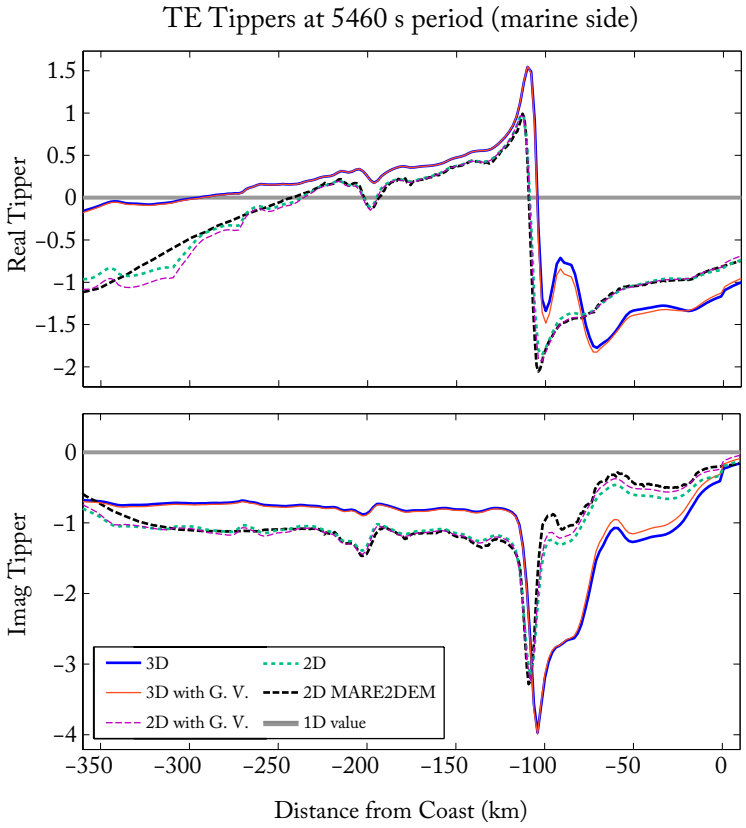

Figure 6.30: Same format as Figure 6.23 but for the TE-mode tipper. Note example data errors are not plotted because they would be too small to be visible.

scale that is an order of magnitude larger than the land side, and recall that such data do not exist in the Estero MT data set. The primary observation is that the differences between 3D and 2D for the tipper can be multiple times greater than the data errors, often greater than the relative differences in the impedance data. The difference between the 3D and 2D tipper in the marine environment is dramatic, hundreds of times greater than the tipper error floor used on land, and anti-correlated at shorter periods. This implies that collecting tipper data in the marine environment is especially futile unless accurate 3D modeling is available. The tipper disparity between 3D and 2D on land is large in the imaginary component at short periods, and large in the real component at long periods when compared with the data errors; the disparities in the real component at short periods, and the imaginary component at long periods are small enough to be within the data uncertainty. Furthermore, the difference between the 3D and 2D tipper are predominantly driven by the coast and not the more conductive GV; the effects of a conductive GV hardly differ between the 2D and 3D calculations. We conclude that within the area of Estero MT data coverage, and given the scale of the data error floors, the tippers are the most susceptible to 3D distortion from the coast. The same would have been resoundingly true in the marine environment had tipper data been collected there.

To visualize the effect that the distortion from 3D bathymetry and 3D GV sediments would have on a 2D inversion, Figure 6.31 presents distortions at a range of frequencies for positions along the line of Estero MT data in terms of the respective data error floors. The marine tipper results are withheld from these plots since they do not pertain to collected data, and are so far outside of the color-scale that they would be unintelligible in this format. Observe that the 3D perturbations to the impedance data are greater in amplitude on the marine side than on the land side. Keep in mind that in many areas the perturbations saturate the color scale; the color scale was capped to allow for the subtler effects on land to be visible. The perturbations to the tipper data on the land side are greater than all other forms of data. The sign of the perturbation changes both in period and space. The colormaps for the plots related to impedance data have been arranged so that warm colors correlate to perturbations that would, in a simple 1D sense, produce more conductive structure, while cooler colors correlate to perturbations that would pro-

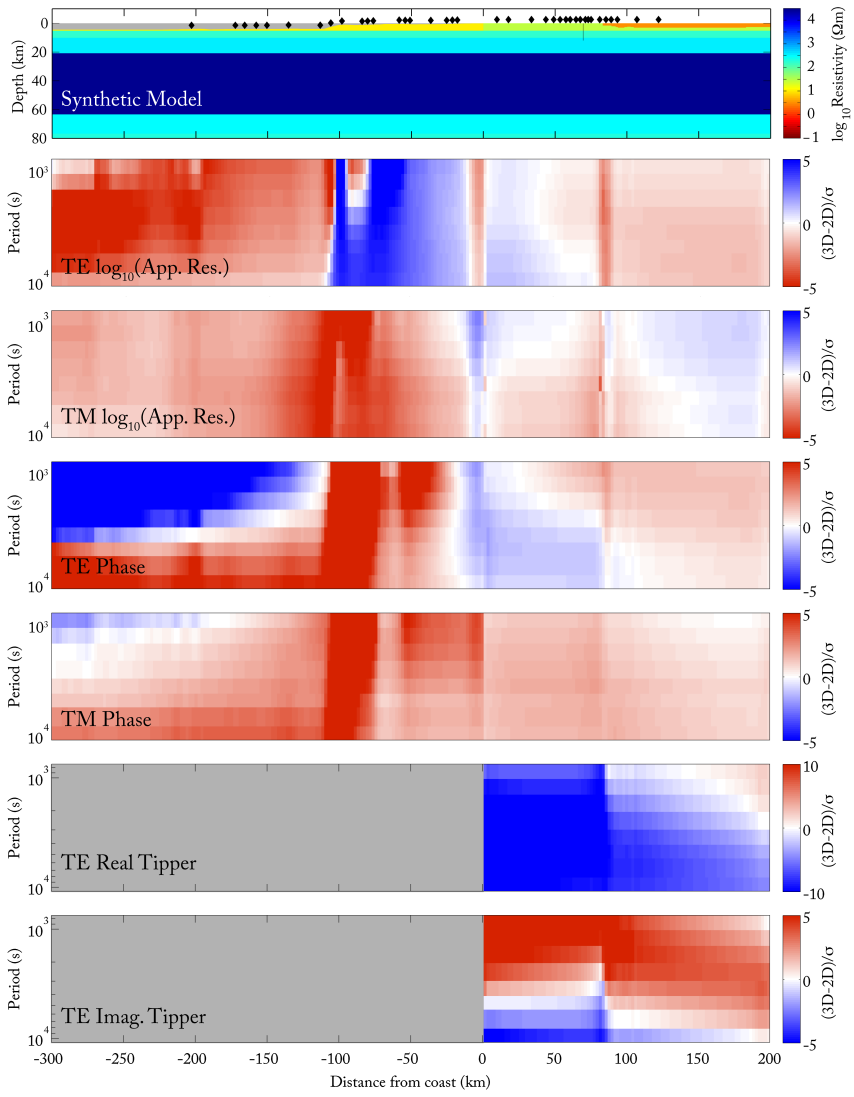

Figure 6.31: Scaled perturbations to hypothetical 2D MT data along the Estero line of sites due to 3D bathymetric variations. The hypothetical 2D data is taken from the 2D thin sheet calculation with a conductive GV, illustrated in the top plot. The perturbation is the difference in data between the 3D and 2D thin sheet calculations. The perturbations are provided in dimensionless units, having been normalized by the corresponding error-floor (σ) used in inversion of the actual Estero MT data. Thus, areas that are white, or within $\pm 1\sigma$, indicate data that have negligible distortion from 3D bathymetry from the perspective of 2D inversion. Note two irregularities: the color limits for the TE real tipper perturbations are twice the size of the others so as not to saturate the entire plot; and the colormaps of the two apparent-resistivity perturbation plots (App. Res.) are mirrored relative to the others. In a 1D sense, a positive perturbation in apparent resistivity indicates higher resistivities (cooler colors) at some depth, whereas a positive perturbation in phase indicates a decrease in resistivity (warmer colors) with depth.

duce more resistive structure; the behavior of the tipper does not furnish such a simplistic interpretation since it is always zero in 1D. We see that the perturbations to the two modes of apparent resistivity are generally in opposition except at a large distance seaward of the coast. The perturbations to the two modes of phase, however, are generally in agreement, except on the land side. The final observation is that the perturbations to the marine data do not exhibit extensive attenuation with decreasing period; in many areas they increase with period. We abstain from running our thin sheet calculations below a period of 745 s to avoid a breakdown in the thin-sheet approximation. Nonetheless, the results of the 745 s calculation agree surprisingly well with our benchmark. Since the perturbations in Figure 6.31 vary smoothly along the period axis, we expect an extrapolation to provide a reasonable predictions for shorter period behavior. Such an extrapolation of the results presented here would indicate that significant bathymetric distortions extend well into the shorter period range of MT measurements. This has important implications, as the exclusion of longer period data from inversion has been prescribed as a way to escape 3D bathymetric effects. Our results, catered to the bathymetry and resistivity structure of central California, predict that a short period inversion would still suffer from 3D distortion. Region specific studies of the sort presented in this chapter would need to be conducted for each survey before the results of a 2D inversion are to be trusted. Furthermore, high-resolution thin-sheet calculations of 3D bathymetry, like those presented here, may serve as a benchmark for accurate characterization of site-specific bathymetric effects in full 3D inversions of coastal and marine MT data in the future.

6.2 Synthetic Inversions of Coast-affected MT Data

Here we use the simplified model for the conductivity distribution below the Estero MT sites, developed in Section 6.1, to produce synthetic data which we test within our 2D inversion algorithm. We perform multiple tests to address the questions brought up on Chapter 4: How well do the marine data, the land data, and the full dataset resolve a hypothetical Rinconada conductor? Can a TM-mode-only inversion recover some semblance of the true resistivity model? Could the Rinconada conductor from Model 1 be an artifact

resulting from the way in which our inversion algorithm grapples with 2D or 3D bathymetry?

Inversion of synthetically produced data (synthetic inversion) that are identical in the data coverage, data weighting, model discretization, regularization settings, etc. to those used in the inversion of a real dataset constitutes a sound, albeit qualitative way to asses the resolution of an inverse process. For linear inverse problems, such resolution studies are often performed with discontinuous or highly-concentrated probing functions used for the distributions of model parameters (e.g., pseudo-delta functions or checker-board grids). The inversion of synthetic data produced by these extremely rough models will result in a smoothed version of them (assuming regularization is to be applied), called a resolving function in Parker [1994]. The width of the resolving function relative to the width of the probing function (which is made as close to zero as possible) provides a qualitative estimate of the scale of interpretable detail in a specific area of any inversion result (the specific area is determined by the probing function). What makes this process powerful for a linear problem, is that the resolving function will be the same regardless of the absolute size and distribution of all model parameters. In other words, the estimate of resolution will not depend upon the solution reached by the inverse process. This convenience is lost with non-linear problems. A checker-board probing function in a non-linear geophysical inverse problem will only provide the resolution scale for the same checker-board earth; the resolution scale for the real earth, which is unlikely to resemble a checker-board, may be completely different. Thus, resolution studies through synthetic *non-linear* inversion requires that the synthetic model be as close to the "truth" as possible. It is, of course, difficult to know what the true model should be, a quandary most geophysicists experience. The approach we are about to take is to derive an approximation from our inversion result and other geophysical knowledge. Resolution studies for non-linear inverse problems must be accepted with the caveat that they are, at best, a local measure (i.e., specific to the tested model), and sometimes, for example, in the case of 1D MT inversion, misleading [Parker, 1994].

We create 2D synthetic data, using the same 2D modeling code used by our inversion algorithm, that matches the coverage in site location, period, and data type of the Estero MT dataset. There is one important exception. We have restored the short period

range of apparent resistivity data at site 632 that had been omitted from the inversions of real data due to an irreparable glitch (see Figure 4.28). The intent here is to test structures analogous to those found in Model 1 that would occur regardless of the data gap at site 632. The same error floor weighting will be used in synthetic inversions as was used with the real data. Recall from Chapter 3 that the error floors used with the real data are much larger than the estimated error resulting from random variation. The inflated error floors, we explained, were to account for systematic errors in the data, an example of which was 3D distortion. To mimic this assertion, we add Gaussian noise to the synthetic data with a standard deviation linked to 10% of the apparent resistivity in either mode, such that the random variation has a smaller standard deviation than that conveyed by our error floors (12% TM-mode apparent resistivity, 25% TE-mode apparent resistivity). To complete the congruence, we set the tolerated level of misfit in the synthetic tests to match that used in the inversions of the actual data, so that the degree of fit, and therefore the model resolution from these tests should resemble those of inversions of real data.

First, we test the sensitivity of a 2D inversion to a hypothetical Rinconada conductor, when provided the Estero MT data coverage. The top plot in Figure 6.32 displays the upper portion of our synthetic model, which has a rectangular block of 1 Ωm resistivity added where the bulk of the Rinconada conductor occurs. The second plot from the top, is the final model achieved when the full Estero dataset is used in inversion. This inversion produces a downward smearing of the base of the block conductor, reminiscent of the comet tail of the Rinconada conductor in Model 1. This provides evidence that the base of the Rinconada conductor in Model 1 is very poorly resolved, as is assumed to be the case for most deep conductors in MT inversions. Note also that resistivity of the upper 10 km is recovered on average in these models. However, some spurious conductive basins appear at the surface in between marine sites. This behavior in the synthetics casts doubt on the veracity of the near-surface conductive anomalies found on the marine side in Model 1. Next, we note that the extremely resistive lithosphere is not recovered by any of the inversions; they place 1,000-5,000 Ωm where there should be 30,000 Ωm. The data contain little sensitivity to highly resistive layers, and the true stark increase in resistivity apparently requires too great of a roughness penalty to be allowed by this smooth inversion. For the same reason,

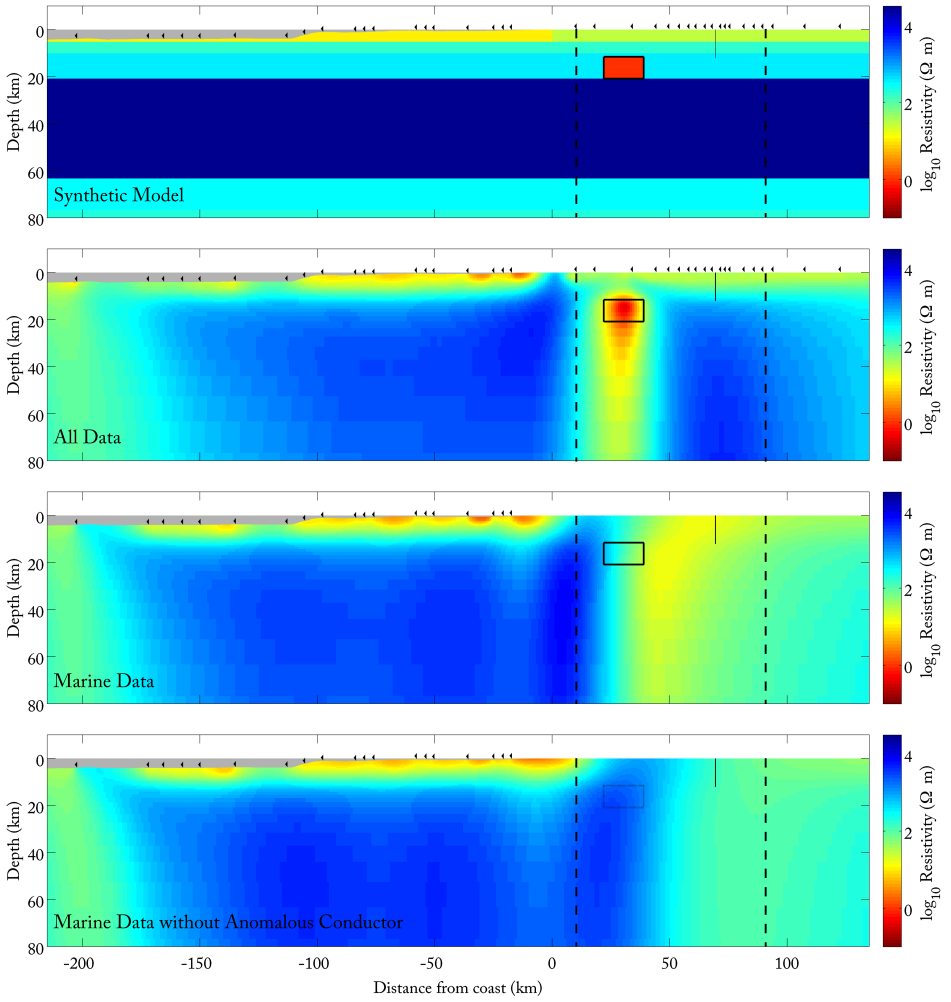

Figure 6.32: A synthetic test of the ability to resolve a conductive block similar to the Rinconada conductor in Model 1. From top to bottom: the model used to create the synthetic data; the final model result of an inversion of all data; the final model result of an inversion of just the marine data; the final model result of an inversion of just the marine data created from a synthetic model without the conductive block. Vertical long-dashed lines mark the horizontal boundaries (10 km-90 km from the coast) of the area used for the average conductivity calculation used in Figure 6.34.

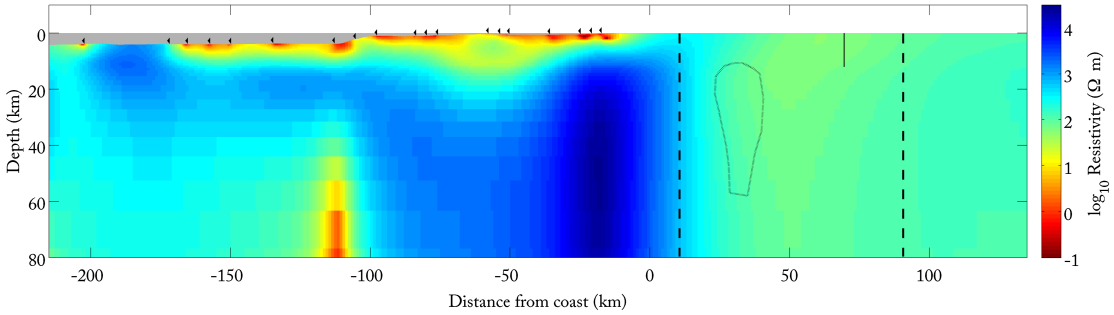

Figure 6.33: The final model result of the inversion result of just the marine portion of the Estero MT dataset. The boundary of the Rinconada conductor in Model 1 is shown with a dotted black line. Vertical long-dashed lines mark the horizontal boundaries (10 km-90 km from the coast) of the area used for the average conductivity calculation used in Figure 6.34.

the return to lower resistivities below lithosphere is not recovered. The inversion seems to compensate for its inaccurate and smooth layered structure by placing vertical anomalously conductive regions on either side of the models. In the bottom two plots of Figure 6.32 we test the sensitivity of just the marine data to the Rinconada conductor. When the conductive block exists, a marine data inversion does place a region of elevated conductivity whose vertical border coincides with the middle of the conductive block. However, the elevated conductivties are very diffuse with a maximum value over ten times less conductive than it should be (15 Ωm). When the conductive block does *not* exist, the inversion places the same background of resistive material (>1,000 Ωm) where the conductive block would otherwise be. Nonetheless, there remains a region of erroneously elevated conductivity (50 Ωm) in a large portion of the model beyond 50 km inland. It would seem that the marine data, on their own, do possess the ability to discern whether a highly conductive region exists as close to the coast as the Rinconada conductor does. Yet, the NE edge of the Rinconada conductor lies near the edge of the marine data's recoverable portion of the model. Other features such as the near-surface structure between marine sites, the resistive lithosphere below all sites, and the resistivity columns below the deepest-water sites are not resolved even when using the entire the dataset.

For comparison, we revisit the marine-data-only inversion of the actual Estero data

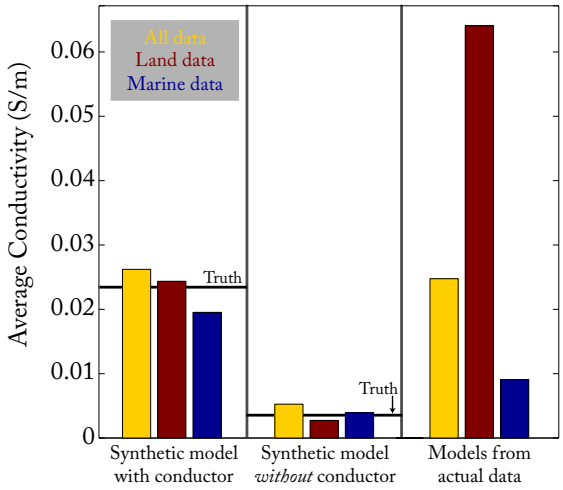

Figure 6.34: A comparison of average conductivity calculations over the area within 10 km-90 km from the coast and between 0 km and 100 km depths from a selection of the inversion models of actual and synthetic data. The area chosen encloses a broad region surrounding the Rinconada conductor of Model 1.

in Figure 6.33. While the foregoing findings from synthetic studies, such as the erroneously conductive basins between marine elicit clear correlation with the inversion of real marine data, the marine data's necessity for the Rinconada conductor is more ambiguous. On one hand, the marine data do not require quite as high of a conductivity in the location of the Rinconada conductor as found in the synthetic inversion with the block conductor; on the other hand, the inversion of real data does not place as highly resistive material as the synthetic inversion did when the block conductor was removed. For more concrete analysis of the necessity for the Rinconada conductor we look at a quantity that is more robustly conserved among inversions of different data subsets, total conductance. As was shown in Section 4.3, it is the TE-mode tipper and impedance data that almost exclusively require the Rinconada conductor. These data are entirely sensitive to the current running in the horizontal direction perpendicular to the line of sites, i.e., in and out of the page for the printed cross-sectional models. The total current running in this direction is much better constrained than the precise distribution of that current; as can be seen in the synthetic

inversions, a small region of high conductivity can often trade-off with a more diffuse region of lower conductivity, with a negligible affect on misfit. The quantity directly related to the total current running in and out of the page is conductance. Think of the current running perpendicular to the faces of each of our parameter blocks as the current contained in a linear circuit of parallel resistors driven by a constant voltage. With voltage conserved between different models, the total current is then a function of the sum of inverse resistances, or simply the total conductance. In Figure 6.34 we display a calculation of total conductance within a large region enclosing the Rinconada conductor for a selection of inversion models, both from the actual data and the synthetic data. The total conductance is found by taking the sum of the products of cross-sectional area and conductivity for each model block within the selected region; note the length parameter in the conversion from conductivity to conductance is immaterial in this calculation because it would be the same for every model block. The total conductance is expressed as an average conductivity, purely a matter of style as all conductance sums are normalized by the same total area, that of the selected region. The first observation drawn from Figure 6.34 is that both with and without the Rinconada-like block conductor, the synthetic inversions recover the total conductance in the area quite well, regardless of data subset; this confirms our previous statement that the total current is a well-constrained quantity. Also, note that the total conductance in the region for the synthetic model with the block conductor closely matches the total conductance found in Model 1 (see "all", "actual data", in Figure 6.34); this is by our design. Next, we see that the inversion of actual data differ from both of the synthetic studies in that the inversions the different data subsets all ask for wildly different conductances, when compared to the analogous variation found in the synthetic studies. The actual marine data predict a total conductance that is more in line with the synthetic study that does not have a block conductor. While still not conclusive, analysis of the better constrained total conductance implies that the marine data do not require a feature as extreme as the Rinconada conductor. Quite the opposite, the actual land data, on their own, seem to insist upon something far more extreme. Again we are faced a dichotomy between the demands of the marine data and those of the land data, a condition we suspect is the result of 3D bathymetric distortion, which, as we have shown, has opposing effects on the land and

marine side of the coast.

Figure 6.35 presents the final models from inversion of the synthetic model that does not contain a block conductor; the structure below the upper 5 Ωm of the synthetic model is entirely 1D. When all of the data are inverted, a curious artifact appears that is almost coincident with the Rinconada conductor. The artifact, with a minimum resistivity of 10 Ωm, is not nearly as conductive as the Rinconada conductor, and when only the TM-mode data are inverted, it vanishes. The TM-mode-only inversion drastically underestimates the resistivity of the crust and upper mantle below the deep-water sites, and is remarkably similar to the result of taking the same approach to the actual Estero MT data (see Figure 4.32). We conclude that a TM-mode-only inversion of severely coast-affected data is futile in the marine environment, even when the coast is perfectly 2D. The TE-mode is vital for diverting the inversion from satisfying the TM-mode depression due to the coast-effect with a more convenient wash of falsely conductive material. Let us return to the more disturbing column of higher conductivity below the coastal sites of 630-632, and reminiscent of the Rinconada conductor. This erroneous conductive anomaly, along with the one on the left side of the model below sites M40 and M36, seem to be coupled with the inversion's inability to recover the resistive lithosphere. The resistive lithosphere is critical in producing the coast effects in the tipper and TE-mode data which are most pronounced beyond the continental slope on the marine side and closest to the coast on the land side (as shown in Section 6.1). The smoothness constraint of the inversion, by nature of the model discretization, penalizes model roughness more in the vertical direction than it does in horizontal direction. Recall in Figure 4.9, that over an equivalent distance there are more model block boundaries in the horizontal directions than there are in the vertical direction. Thus, a gradient in resistivity may be spread over many boundaries in small jumps along the horizontal direction, whereas, along the vertical direction, the same gradient is spread over fewer boundaries necessitating larger jumps. Since the roughness measure in (4.2) is based on the 2-norm (a sum of squares) of model jumps at the boundaries, a few larger jumps are less favored by our inversion than many smaller jumps when describing the same average gradient. The use of a 1-norm (sum of absolute values) in the roughness measure would be more equitable given our non-uniform spacing of model boundaries, but it is algebraically

difficult to implement. Given the current setup, the anisotropic smoothing creates a preference for the placement of vertically-smooth conductors confined to the areas where the coast effect is greatest, rather than place the proper jump in resistivity along the vertical direction below the entire model. An alternative solution of using a uniform discretization of the model domain would create an isotropic measure of roughness, presumably preventing these artifacts, but with the given inversion software, such a discretization leads to models too large to be computationally tractable.

The easiest solution for correcting the anisotropic smoothing that results from a non-uniform model grid is to re-weight the roughness calculation. The matrix $\boldsymbol{\partial}$ in (4.2) is normally filled with 1's and -1's to represent the first difference between adjacent model blocks (such was the implementation used for all of the inversion models in this dissertation). In search of an unbiased alternative to this default implementation, we return to the continuous formulation of the roughness measure, the first term on the right hand side of (4.2); we write,

$$R_\Omega[m] = \int_\Omega ||\nabla m||^2 \, d^2s, \tag{6.1}$$

where $m(y, z)$ is the 2D function of the logarithm of resistivity, i.e. our model parameterization, over the domain Ω. Now moving back to the discrete case, we retain the forward first difference as an approximation of the model gradient, and evaluate the integral using a middle Riemann sum. For example, we analyze the effect of this new measure on the i^{th} model block with value m_i, width w_i, and height h_i. In the image of the model domain, the block directly to the right of the i^{th} we arrange to have the index $i + 1$, and the block directly below to have the index $i + 2$. Then, the terms of the roughness measure centered around the i^{th} model block are:

$$||R\mathbf{m}||^2 = \ldots + (m_{i+1} - m_i)^2 \frac{2h_i}{w_{i+1} + w_i} + (m_{i+2} - m_i)^2 \frac{2w_i}{h_{i+2} + h_i} + \ldots \, . \tag{6.2}$$

The new roughness matrix, R, in (6.2) is similar to $\boldsymbol{\partial}$, except that every first difference is weighted by the aspect ratio of each pair of connected blocks. In this way, the directional bias from a non-uniform mesh is neutralized. This correction for anisotropy in the roughness

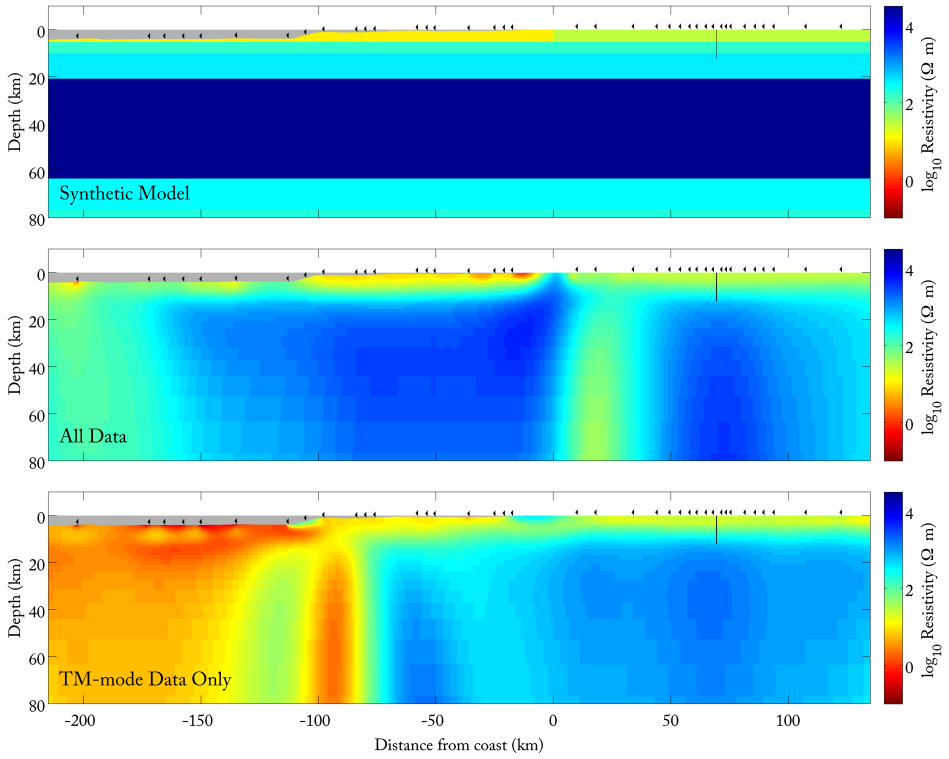

Figure 6.35: A synthetic test of the ability to resolve the resistive lithosphere in our simple model with 2D bathymetry. From top to bottom: the model used to create the synthetic data; the final model result of an inversion of all data; the final model result of an inversion of just the TM-mode data.

measure was discovered after the defense of the work in this dissertation, and thus is not used in any of the models presented throughout it. The author wishes to document the correction here for posterity's sake. Preliminary inversion trials with the new regularization have shown that, while the vertical bias in the regularization is removed, the other conclusions of this dissertation are unaffected. The issue of bias in regularization reminds us that over-parameterized, non-linear, gradient-based inversion is not an entirely objective exercise; the user has freedom to choose the regularization that best matches their expectations. Different choices made in that regard can often produce appreciably different models, each meeting the requirements of the data equally, for which the only remaining distinguishing factor is the prejudice of the appraiser.

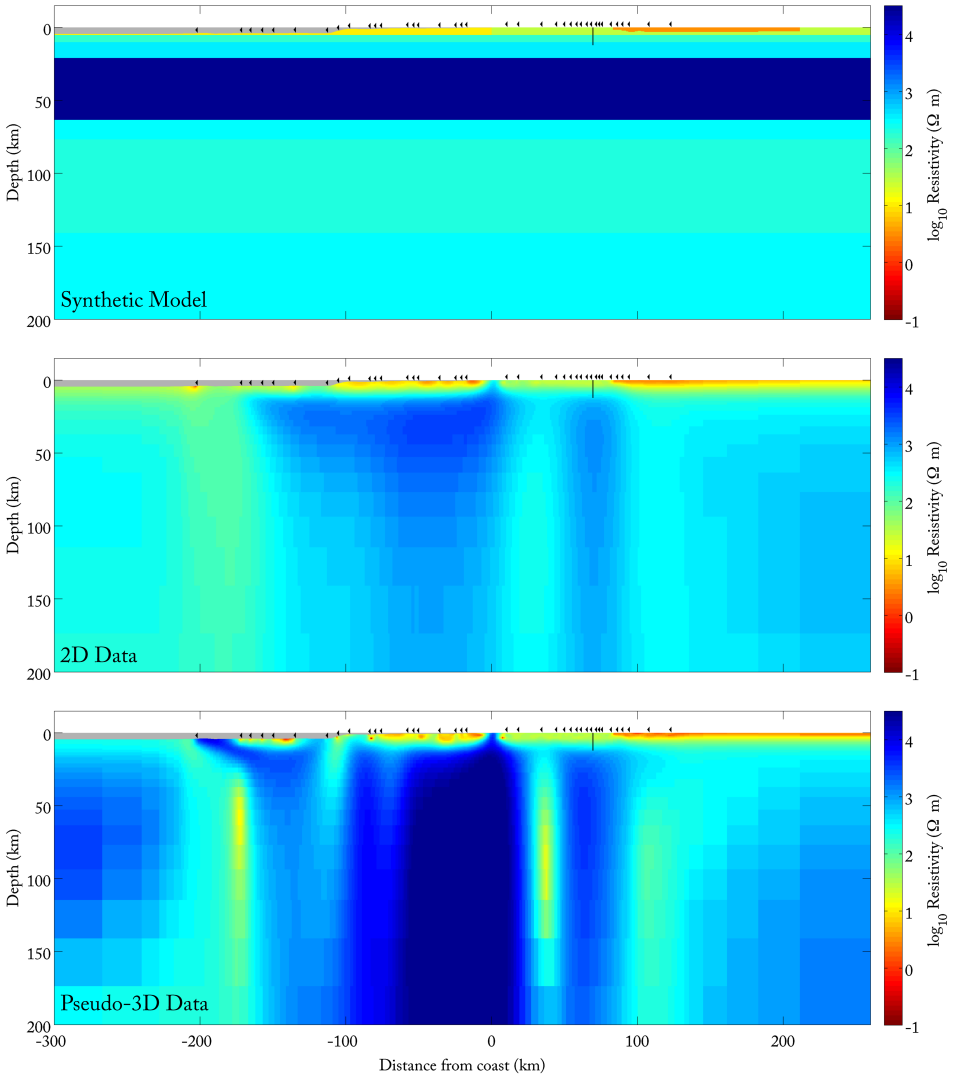

Figure 6.36: A synthetic test of the features introduced by 3D bathymetric distortion into a 2D inversion model. From top to bottom: the model used to create the synthetic data, which includes a conductive GV; the final model result of an inversion of 2D data; the final model result of an inversion of the 2D data with the perturbations of 3D bathymetry added to the nine longest periods of data (pseudo-3D).

Next, we take the synthetic data from a 2D model and apply the perturbations due to 3D bathymetry calculated in Section 6.1, and displayed in Figure 6.31. In this way we produce a pseudo-3D dataset, where the 3D distortions are entirely a product of bathymetry. We do not simply use the apparent resistivity and phase results from the 3D thin sheet model because, as we showed in 2D, they do not agree with the analogous finite element models at intermediate water depths. Nonetheless, we assume that the relative difference between the 2D and 3D results from the base of the thin sheet are a good approximation for the relative difference between 2D and 3D calculations at intermediate water depths. So, by starting from a 2D finite-element calculation at the true water depth of each instrument and adding the difference between the 2D and 3D thin sheet calculations, we arrive at a synthetic 3D dataset. However, we do this only for the nine longest periods in the dataset for which the thin sheet results were shown to be accurate. The shorter-period synthetic data are left in their original 2D form. Note that for this synthetic test, all of the models used include a conductive GV. We take the synthetic 3D data, which carry effects similar to those caused by the 3D bathymetry in the Estero dataset, and apply them in the same 2D inversion scheme that was employed with the Estero MT data. The resulting model should produce artifacts representative of the 3D bathymetric effects introduced into the 2D inversion of the Estero MT data, at least those affecting the nine longest periods. Figure 6.36 compares the synthetic model used to create the 2D data, the result of an inversion of the 2D data, and the result of an inversion of the pseudo-3D data. Again, the inversion of just the 2D data produces vertically smeared conductors below the two deepest-water sites, below the first three sites inland of the coast, and, now that the conductive GV has been added, below the two eastern-most sites. These vertical swaths of enhanced conductivities, while not nearly as resistive as they should be given the synthetic model, are not nearly as conductive as the anomalous conductors in Model 1; the conductors from the inversion of the synthetic 2D data are still above 300 Ωm. The inversion of the pseudo-3D data results in similar anomalous conductors, but their boundaries are sharper and their conductivities greater; the conductors below the deep-marine and coastal portion of the model fall below 20 Ωm, while the deep conductor below the GV remains just above 100 Ωm. The pseudo-3D model has become rougher overall, as the 2D inversion algorithm strains to meet aspects

of the data caused by 3D structure. Just below the coast a highly resistive wall appears in the model, similar to that found in Model 1. In summary, the inversion of the synthetic 2D data produces anomalous structures that hint at, but are much less extreme than those found in Model 1, the Rinconada conductor, the GV conductor, etc. It seems that the 2D algorithm, even with perfectly 2D data, is prone to the placement of vertically elongated conductors where they should not exist. Then, the addition of 3D distortions to only the nine longest periods sharpens each of these structures, bringing them even more in line with Model 1. We conjecture that if it were possible to create and invert data with 3D bathymetric distortions at *all* periods, these erroneous structures would become even more extreme, perhaps as extreme as the Rinconada and GV conductors in Model 1. In Figure 6.37, we compare the result of the inversion of the pseudo-3D data to the perturbations due to 3D bathymetry used to create those data. The comparison highlights the difficulty in predicting, based on the plots of the perturbations, how distortions from 3D bathymetry will affect the outcome of a 2D inversion. Synthetic inversions are vital to connecting input to outcome.

Finally, we compare the result of the inversion of the pseudo-3D data to Model 1, the result of the inversion of the actual Estero MT data. Each of the major artifacts introduced into the synthetic inversion model by bathymetry, both 2D and 3D, are labeled **A**-**E**. The structures similar to these that are found in Model 1 are given the same label. We do not expect the exact location, size, and resistivity of each of these structures to be equal to that of its counterpart. The simplistic model we used to create the synthetic data surely does not represent to the true complexity of the earth. However, the fact that very similar structures can be produced by an underlying model that was purely 1D below 5 km casts doubt on the interpretability of all the exciting features in Model 1. Clearly, some combination of the inversion algorithm and deficiency in the dimensionality in the forward model is capable of producing results that, while compelling, are mostly fictional. That is not to say that the entirety of Model 1 is false, but we have shown that without a more isotropic roughness penalty and 3D modeling, at least of bathymetry, we cannot discern with confidence what is true. The Rinconada conductor may exist, but it is apparently not required to.

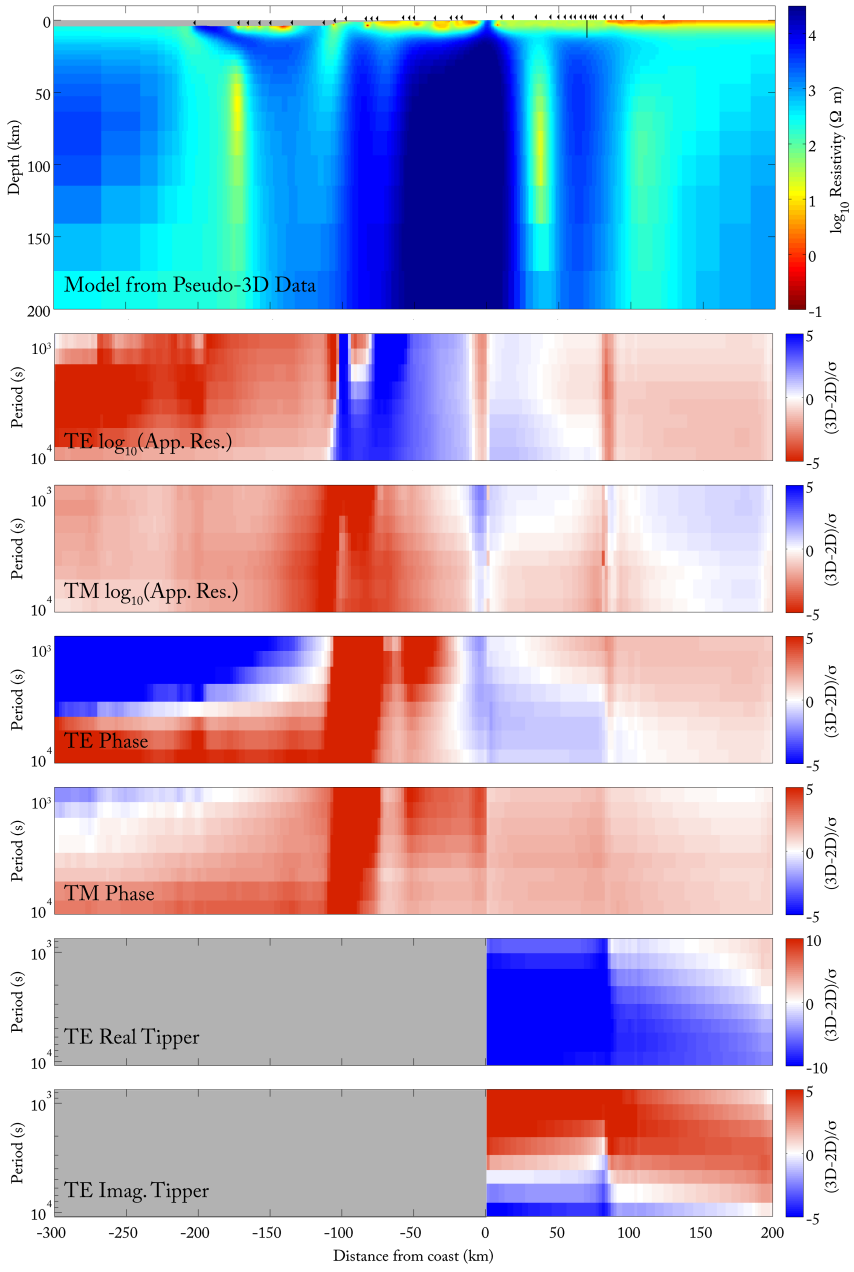

Figure 6.37: Same format as Figure 6.31, except that the top plot displays the result of inverting the pseudo-3D data.

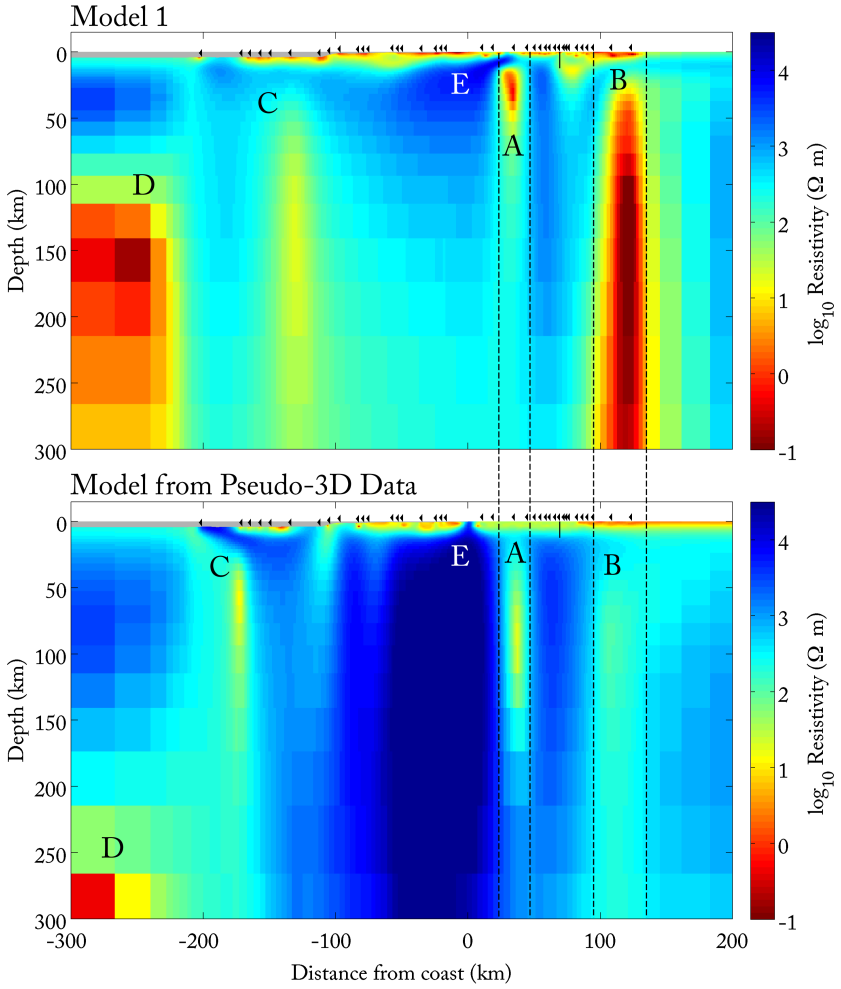

Figure 6.38: A comparison of the inversion result of the complete Estero MT dataset (Model 1) with the inversion result of the pseudo-3D synthetic data. Anomalous features akin to both models are labeled with letters **A**-**E**.

Chapter 7

Conclusions

In Chapter 4, I presented a 2D inversion model for the amphibious Estero MT dataset, which I call Model 1. In Figure 7.1 (**B** & **C**), the land portion of Model 1 is plotted alongside the inversion model for the same land data from Becken et al. [2011]. Both models maintain the existence of a large, deep, and high-conductive body southwest of the SAF (the Rinconada conductor). Nonetheless, the introduction of the marine data changes the land side of the model because the continental margin is no longer allowed to be filled with high conductivity material (see Figure 4.20). By adding the marine constraints, I find a sharpening of the Rinconada conductor and the emergence of a large conductor beneath the GV. In Chapter 4 I argued that the marine data do not call for the increase in conductance brought by the Rinconada conductor, and showed that the marine and land data express conflicting demands on the inverse model, which leads to very rough structure at the coast. I also found that both the Rinconada conductor and the conductor below the GV are driven predominantly by the TE-mode tipper data from land sites.

The best-fitting model predictions showed pervasive, systematic (not random) misfit to the data, despite a highly-parameterized model; I suspected the cause to be distortion from 3D bathymetry, which a 2D inversion cannot replicate. In Chapters 5 & 6 I developed a thin-sheet method to estimate the degree of distortion in the Estero MT data that is caused by the actual 3D bathymetry in the region in central California. From this, I found

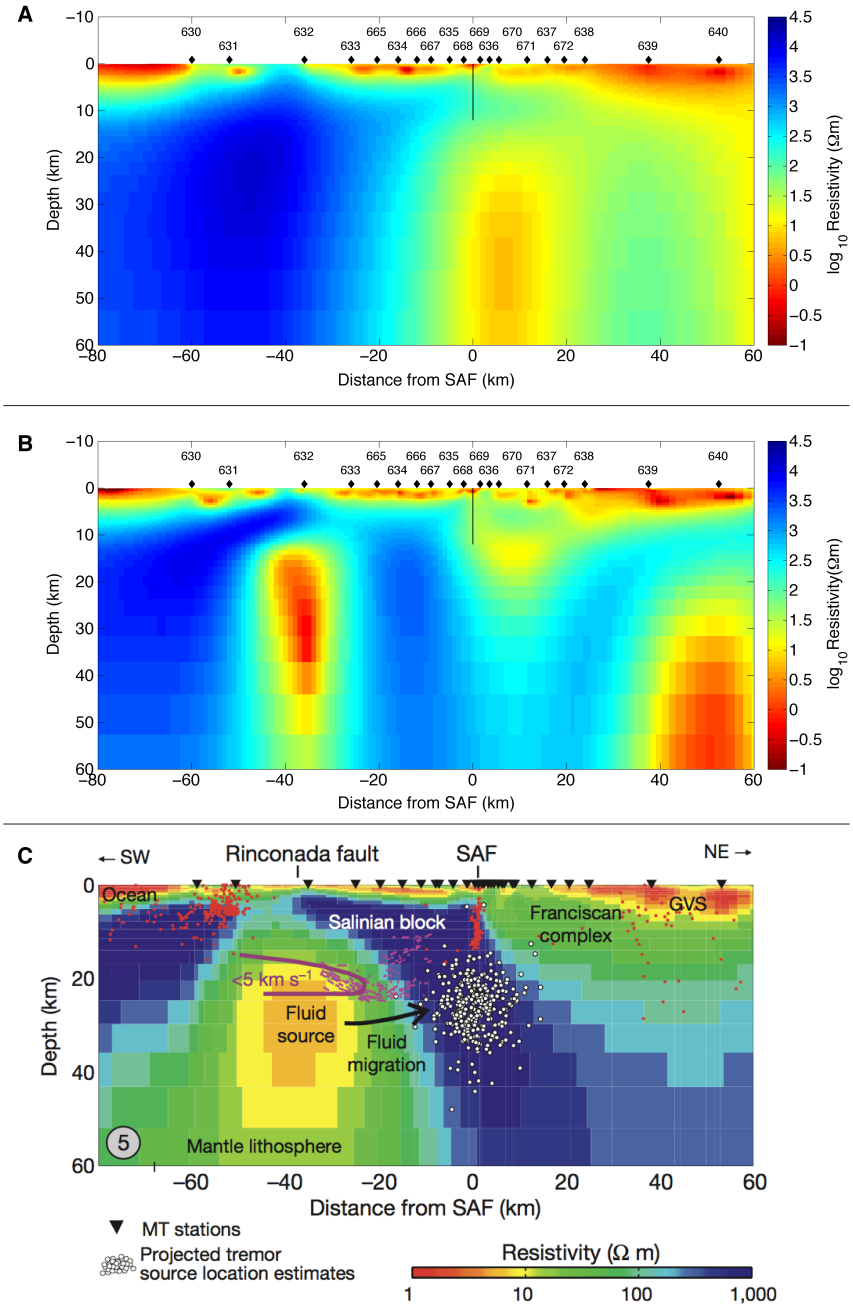

Figure 7.1: A comparison of the final models from: (**A**) inversion of the Estero MT dataset without tipper data; (**B**) inversion of the full Estero MT dataset; (**C**) inversion of the land data of the Estero MT dataset, as presented in Becken et al. [2011].

that the 3D bathymetric distortions are significant relative to the data errors used, and do not always produce overt symptoms of 3D-ness (high skew, etc.). The TE-mode tipper data were most affected by 3D-bathymetry. An inversion of the amphibious dataset with tipper data removed yielded a starkly different model on land, as seen in (**A**) of Figure 7.1. This result illustrates the tenuous existence of the Rinconada conductor. In Chapter 6 I composed a simplified model for the conductivity structure beneath the continental margin in central California. The synthetic model used average crustal conductivities drawn from Model 1, but, relative to Model 1, a much more resistive lithosphere, which is supported by multiple observations, independent of those involved in this dissertation. Below 5 km, the synthetic model is layered. Yet, synthetic inversions of data created from only 2D bathymetry in this simple model produced vertically-elongated, slightly-conductive anomalies coincident with the conductive anomalies of Model 1. When 3D distortions are added to a fraction of the data in synthetic inversions, these same conductive anomalies became sharper and more conductive, with greater resemblance to those of Model 1.

The fact that the synthetic studies with perfectly 2D bathymetry could not recover a smoothed version of the horizontally-layered synthetic model led me to question the inversion algorithm. The interplay between the model discretization and how roughness is computed is the likely source of the problem, the solution to which is left for future work. More disturbing is that the artifacts created in the 2D synthetic inversion model occur in nearly the same location as the extreme conductors in Model 1, albeit with much milder deviations from the background conductivity. The fact that the 2D inversion of 3D-distorted data produced even more extreme conductivities where they should not exist, confirms that 3D bathymetry is another important problem to contend with. The Rinconada conductor occurs at nearly the same distance from the coast in each of the 2D models in the Becken et al. [2011] study, yet its size and resistivity changes. I speculate that the change in character of the Rinconada conductor with distance along the coast may result from the 3D distortions produced by the ruggedness of the coast. These combined reasons lead me to conclude that the existence of the Rinconada conductor cannot be corroborated with the current set of tools. Instead, I suspect that this conductor is fictitious, an artifact of the inadequacy of the 2D inversions used both in my work and in the published work of Becken

et al. [2011]. Therefore, I suspend further geologic interpretation along the lines forged by Becken et al. [2011] until I have an inverse process that can be trusted. Full 3D modeling that accurately portrays bathymetric effects, and a better form of regularization which can reproduce the stark increase in resistivity that is expected at the crust/mantle boundary are needed before durable geological conclusions from the MT data of this dissertation may be drawn.

Since the tools for adequate 3D inversion of the amphibious Estero MT dataset are currently unavailable, I can only make broad conjectures about the geology below the survey line using the suite of 2D inversions presented in this dissertation. First, I note that none of the inversion models created with the use of the marine data show a conductive connection between the Rinconada conductor and the material below the continental margin. Thus, support for the hypothesis that the Rinconada conductor relates to a release of fluids from the subducted Monterrey plate was not found. Second, I was able to impugn the tipper data as those most corrupted by 3D bathymetric effects, relative to the respective data errors used, out of the land portion of the data set. So, perhaps the model (**A**) in Figure 7.1, which does not use tipper data, presents our best 2D model approximation of the actual electrical resistivity structure around the central Californian segment of the SAF. Entertaining this possibility, we see that the conductor below the SAF in (**A**) better aligns with the source locations of the recently discovered non-volcanic tremor shown in (**C**). Following the suggestion of Nadeau and Guilhem [2009] that tremor is associated with high pore-fluid pressures, one might expect the location of tremor production to be marked by a region of enhanced conductivity. This was not the case with the model from Becken et al. [2011] in (**C**), which *did* use the tipper data. Perhaps the 3D bathymetric distortions cause a *real* onshore conductor to be incorrectly mapped closer to the coast than it actually lies. Then a conductor directly below the seismogenic depth extent of the SAF, rather than offset to the southwest, would be the subject of geologic interpretation. The shallow section of the SAF (upper 3 km) has long been associated with a conductive zone attributed to fluids within a highly fractured damage zone [Ritter et al., 2005], but little has been discussed about the deep structure of the fault. If the deep incidence of tremor is the manifestation of slip on the sub-seismogenic extension of the fault [Shelly et al., 2009], then perhaps there

too a fault zone conductor has meaning. Such connections might be the subject of future work involving MT and the SAF.

Appendix A

Error Propagation in MT Data

In this appendix we derive the formulae for the linear (1st order) approximation in error propagation from one random quantity to another. We will assume the basic random measurement is a complex impedance tensor element or a complex tipper vector element. Then we wish to calculate the mean and variance of functions of these random variables. The real and imaginary parts of these measurements are each contaminated by independent, identically-distributed, Gaussian noise of zero mean and known variance, σ^2. For our impedance tensor element, $z = x + iy$, we write,

$$Z = (x + X) + i(y + Y), \tag{A.1}$$

where a capital letter signifies a randomly perturbed quantity, and a lower-case letter signifies the underlying true value. The probability density function (pdf) of the impedance noise is

$$\phi(X, Y) = \frac{\exp -(X^2 + Y^2)/2\sigma^2}{2\pi\sigma^2} \tag{A.2}$$

over the plane R^2; remember the integral of this function over the whole plane is equal to 1. We will use the symbol δ to signify the standard error of a quantity, such that,

$$\delta X = \sqrt{\mathrm{var}(X)} = \sigma. \tag{A.3}$$

We will derive the mean and variance of multiple quantities by using their definitions in terms of the expectation operator. The expectation of any function F of a random variable is found by integrating that function over the domain of the random variable, weighted by the pdf of the variable:

$$\mathrm{E}[F(\mathbf{X})] = \int F(\mathbf{X})\phi(\mathbf{X})d\mathbf{X}, \tag{A.4}$$

where the bold font represents a vector; in this way F may be a function of multiple random variables. Then the mean of F, $\bar{F}$, is given by,

$$\bar{F} = \mathrm{E}[F(\mathbf{X})]. \tag{A.5}$$

Note that since X and Y are zero-mean, we have

$$\mathrm{E}[Z] = z. \tag{A.6}$$

The variance of F is given by,

$$\mathrm{var}(F(\mathbf{X})) = \mathrm{E}[(F(\mathbf{X}) - \mathrm{E}[F(\mathbf{X})])^2] \tag{A.7}$$

$$= \mathrm{E}[F(\mathbf{X})^2] - \mathrm{E}[F(\mathbf{X})]^2. \tag{A.8}$$

Since X and Y are independent and zero mean,

$$\mathrm{E}[XY] = \mathrm{E}[X]\mathrm{E}[Y] = 0. \tag{A.9}$$

Using (A.6) and (A.9) we then have,

$$\delta Z^2 = \delta X^2 + \delta Y^2 = 2\sigma^2. \tag{A.10}$$

Now we move on to more complicated functions of Z. We wish to calculate the mean and variance of the apparent resistivity, R, given by,

$$R = \frac{1}{\mu\omega}((x+X)^2 + (y+Y)^2), \tag{A.11}$$

of the log of apparent resistivity, $L = \log_{10}(R)$, and of the impedance phase, P, given by,

$$P = \arctan((y+Y)/(x+X)), \tag{A.12}$$

in units of radians. A standard method of calculating the variance of functions of a random variable is called linear propagation of errors. It is founded upon approximating the function with its Taylor series. As the word "linear" in the title implies, only the first order terms in the Taylor series are uses. Thus returning to the arbitrary function, F, now a function of our two random variables, X and Y, we have,

$$F(x+X, y+Y) \approx f(x,y) + \frac{\partial f}{\partial x}X + \frac{\partial f}{\partial y}Y + O(X^2) + O(Y^2). \tag{A.13}$$

We quickly see,

$$\bar{F} = \mathrm{E}[F] = f. \tag{A.14}$$

Thus, to the first order of approximation, the mean of F is an unbiased estimator of f. Then for the variance we need,

$$\mathrm{E}[F^2] = \mathrm{E}[f^2 + 2f\frac{\partial f}{\partial x}X + 2f\frac{\partial f}{\partial y}Y + \left(\frac{\partial f}{\partial x}\right)^2 X^2 + \left(\frac{\partial f}{\partial y}\right)^2 Y^2] \tag{A.15}$$

$$= f^2 + \left(\frac{\partial f}{\partial x}\right)^2 \delta X^2 + \left(\frac{\partial f}{\partial y}\right)^2 \delta Y^2. \tag{A.16}$$

Combining (A.14) and (A.16) in (A.8) we recover the formula for linear propagation of errors:

$$\delta F^2 = \left(\frac{\partial f}{\partial x}\right)^2 \delta X^2 + \left(\frac{\partial f}{\partial y}\right)^2 \delta Y^2. \tag{A.17}$$

Applied to R, L, and P, we have the usual formulae for propagated variances:

$$\delta R^2 = \left(\frac{2x}{\mu\omega}\right)^2 \sigma^2 + \left(\frac{2y}{\mu\omega}\right)^2 \sigma^2 \tag{A.18}$$

$$= \frac{4r}{\mu\omega}\sigma^2, \tag{A.19}$$

which is commonly used in the fractional standard error form,

$$\frac{\delta R}{r} = \sqrt{\frac{4\sigma^2}{r\mu\omega}} = \frac{2\sigma}{|z|} = \sqrt{2}\frac{\delta Z}{|z|}, \tag{A.20}$$

then

$$\delta L = \frac{1}{\ln(10)}\left(\frac{2\sigma}{|z|}\right) = \frac{1}{\ln(10)}\left(\frac{\delta R}{r}\right), \tag{A.21}$$

and

$$\delta P^2 = \left(\frac{-y}{x^2+y^2}\right)^2 \sigma^2 + \left(\frac{x}{x^2+y^2}\right)^2 \sigma^2 \tag{A.22}$$

$$= \frac{\sigma^2}{|z|^2}, \tag{A.23}$$

which in standard error form becomes,

$$\delta P = \frac{\sigma}{|z|} = \frac{1}{2}\left(\frac{\delta R}{r}\right). \tag{A.24}$$

Following the preceding steps, we find that the 1st order approximation of the covariance

formula is given by,

$$\mathrm{cov}(F,G) = \frac{\partial f}{\partial x}\frac{\partial g}{\partial x}\delta X^2 + \frac{\partial f}{\partial y}\frac{\partial g}{\partial y}\delta Y^2. \tag{A.25}$$

Then, reusing the derivatives from before, we quickly find the reassuring fact that, at least to first order, $\mathrm{cov}(R,P) = \mathrm{cov}(L,P) = 0$. Thus, when we convert the real and imaginary parts of an impedance element to apparent resistivity and phase, the two resulting data remain independent.

Now we would like to asses the inaccuracy of the 1st order error propagation formulae. To do this exactly, we would need to calculate integrals of the form (A.4), for example,

$$\mathrm{E}[P^2] = \int_{\mathsf{R}^2} \arctan^2\left(\frac{y+Y}{x+X}\right)\frac{1}{2\pi\sigma^2}\mathrm{e}^{-(X^2+Y^2)/2\sigma^2}dXdY. \tag{A.26}$$

However, we are not interested in an exact method of error propagation, which would involve the solution of some difficult integrals. Instead we would just like to know, to an order of magnitude, the degree of failure of our linear approximation. To do so we may simply add the 2nd order terms to (A.13). So we have,

$$F(x+X,y+Y) \approx f(x,y) + \frac{\partial f}{\partial x}X + \frac{\partial f}{\partial y}Y + \frac{1}{2}\frac{\partial^2 f}{\partial x^2}X^2 + \frac{1}{2}\frac{\partial^2 f}{\partial y^2}Y^2 + \frac{\partial^2 f}{\partial x \partial y}XY \ldots$$
$$\ldots + O(X^3) + O(Y^3). \tag{A.27}$$

For the new mean, we have,

$$\mathrm{E}[F] = f + \frac{1}{2}\frac{\partial^2 f}{\partial x^2}\delta X^2 + \frac{1}{2}\frac{\partial^2 f}{\partial y^2}\delta Y^2. \tag{A.28}$$

Now, preparing for the variance calculations, we note that F^2 involves third- and fourth-order terms of X, and Y: X^3, Y^3, XY^2, YX^2, XY^3, YX^3, X^2Y^2, X^4, and Y^4. Only the terms involving all even powers of X and Y will have a non-zero expected value. First we address the non-zero expected values that are equal to the fourth central moment of a

Gaussian distribution,

$$\mathrm{E}[X^4] = \mathrm{E}[Y^4] = 3\sigma^4. \tag{A.29}$$

The other non-zero expected value is found by evaluating the integral,

$$\mathrm{E}[X^2Y^2] = \int_{\mathsf{R}^2} X^2Y^2 \frac{1}{2\pi\sigma^2} \mathrm{e}^{-(X^2+Y^2)/2\sigma^2} dX dY. \tag{A.30}$$

We do so by converting to polar coordinates:

$$\mathrm{E}[X^2Y^2] = \frac{1}{2\pi\sigma^2} \int_0^\infty d\rho\, \rho^5 \mathrm{e}^{-\rho^2/2\sigma^2} \int_0^{2\pi} d\theta \sin^2\theta \cos^2\theta \tag{A.31}$$

$$= \frac{1}{2\pi\sigma^2} \left(8\sigma^6\right) \left(\frac{\pi}{4}\right) = \sigma^4, \tag{A.32}$$

where the solution to the two integrals can be found in Gradshteyn and Ryzhik [1965]. Using the foregoing findings, we have,

$$\begin{aligned}\mathrm{E}[F^2] = f^2 + \left(\frac{\partial f}{\partial x}\right)^2 \sigma^2 + \left(\frac{\partial f}{\partial y}\right)^2 \sigma^2 + \frac{1}{2} f \frac{\partial^2 f}{\partial x^2} \sigma^2 + \frac{1}{2} f \frac{\partial^2 f}{\partial y^2} \sigma^2 + \frac{1}{2} \frac{\partial^2 f}{\partial x^2} \frac{\partial^2 f}{\partial y^2} \sigma^4 \ldots \\ \ldots + \left(\frac{\partial^2 f}{\partial x \partial y}\right)^2 \sigma^4 + \frac{3}{4} \left(\frac{\partial^2 f}{\partial x^2}\right)^2 \sigma^4 + \frac{3}{4} \left(\frac{\partial^2 f}{\partial y^2}\right)^2 \sigma^4.\end{aligned} \tag{A.33}$$

Finally, by inserting (A.28) and (A.33) into (A.8), we recover the second-order error propagation formula, given our jointly distributed random variables,

$$\delta F^2 = \left(\frac{\partial f}{\partial x}\right)^2 \sigma^2 + \left(\frac{\partial f}{\partial y}\right)^2 \sigma^2 + \frac{1}{2} \left(\frac{\partial^2 f}{\partial x^2}\right)^2 \sigma^4 + \frac{1}{2} \left(\frac{\partial^2 f}{\partial y^2}\right)^2 \sigma^4 + \left(\frac{\partial^2 f}{\partial x \partial y}\right)^2 \sigma^4. \tag{A.34}$$

We we return to our measured quantities. We will need all of the first- and second-order derivatives of our functions with respect to the basic random variables. For completeness we tabulate them all here:

$$\frac{\partial r}{\partial x} = \frac{2x}{\mu\omega}, \tag{A.35}$$

$$\frac{\partial r}{\partial y} = \frac{2y}{\mu\omega}, \tag{A.36}$$

$$\frac{\partial^2 r}{\partial x^2} = \frac{2}{\mu\omega}, \tag{A.37}$$

$$\frac{\partial^2 r}{\partial y^2} = \frac{2}{\mu\omega}, \tag{A.38}$$

$$\frac{\partial^2 r}{\partial x \partial y} = 0, \tag{A.39}$$

$$\frac{\partial l}{\partial x} = \frac{2x}{\ln(10)(x^2+y^2)}, \tag{A.40}$$

$$\frac{\partial l}{\partial y} = \frac{2y}{\ln(10)(x^2+y^2)}, \tag{A.41}$$

$$\frac{\partial^2 l}{\partial x^2} = \frac{2(y^2-x^2)}{\ln(10)(x^2+y^2)^2}, \tag{A.42}$$

$$\frac{\partial^2 l}{\partial y^2} = \frac{2(x^2-y^2)}{\ln(10)(x^2+y^2)^2}, \tag{A.43}$$

$$\frac{\partial^2 l}{\partial x \partial y} = \frac{-4xy}{\ln(10)(x^2+y^2)^2}, \tag{A.44}$$

$$\frac{\partial p}{\partial x} = \frac{-y}{x^2+y^2}, \tag{A.45}$$

$$\frac{\partial p}{\partial y} = \frac{x}{x^2 + y^2}, \tag{A.46}$$

$$\frac{\partial^2 p}{\partial x^2} = \frac{2xy}{(x^2 + y^2)^2}, \tag{A.47}$$

$$\frac{\partial^2 p}{\partial y^2} = \frac{-2xy}{(x^2 + y^2)^2}, \tag{A.48}$$

and,

$$\frac{\partial^2 p}{\partial x \partial y} = \frac{y^2 - x^2}{(x^2 + y^2)^2}. \tag{A.49}$$

By applying (A.28), we see there is a small upward bias in the mean estimate of apparent resistivity, given by,

$$\mathrm{E}[R] - r = \frac{2}{\mu\omega}\sigma^2. \tag{A.50}$$

Note that the second order taylor series expansion of R is exact since $\partial^3 r/\partial x^3 = \partial^3 r/\partial y^3 = 0$. Amazingly, there are no biases in the means of L or P, at least in the second-order approximation; one can verify that,

$$\mathrm{E}[L] = l, \tag{A.51}$$

and,

$$\mathrm{E}[P] = p. \tag{A.52}$$

Now, we calculate the variances. Again, looking at the relative forms of standard error in

apparent resistivity, we have,

$$\frac{\delta R}{r} = \frac{2\sigma}{|z|}\sqrt{1+\frac{\sigma^2}{|z|^2}}. \tag{A.53}$$

The first term on the right side of (A.53) is the linear approximation, and the second term represents the error in that approximation. The linearly approximated errors are underestimated by a very small amount. With 5% noise added to the real and imaginary components of z ($\sigma = 0.05|z|$), the linear propagation of errors would predict 10% noise in the apparent resistivity, whereas the true level of noise in the apparent resistivity would be 10.012%. Similarly, the standard errors in the log of apparent resistivity and phase, under the second order approximation, are,

$$\delta L = \frac{2\sigma}{\ln(10)|z|}\sqrt{1+\frac{(y^4-2x^2y^2+x^4)\sigma^2}{|z|^6}+\frac{4x^2y^2\sigma^2}{|z|^6}} \tag{A.54}$$

$$= \frac{2\sigma}{\ln(10)|z|}\sqrt{1+\frac{\sigma^2}{|z|^2}} = \frac{\delta R}{\ln(10)r}, \tag{A.55}$$

and,

$$\delta P = \frac{\sigma}{|z|}\sqrt{1+\frac{2x^2y^2\sigma^2}{|z|^6}+\frac{x^4\sigma^2}{|z|^6}+\frac{y^4\sigma^2}{|z|^6}} \tag{A.56}$$

$$= \frac{\sigma}{|z|}\sqrt{1+2\frac{\sigma^2}{|z|^2}\cos^2 p\sin^2 p+\frac{\sigma^2}{|z|^2}\cos^4 p+\frac{\sigma^2}{|z|^2}\sin^4 p} \tag{A.57}$$

$$= \frac{\sigma}{|z|}\sqrt{1+\frac{\sigma^2}{|z|^2}}, \tag{A.58}$$

respectively. In controlled-source electromagnetics, the amplitude of the transfer function between the source and the receiver is often used as a datum, which we will define as,

$$A = \sqrt{(x+X)^2+(y+Y)^2}. \tag{A.59}$$

Applying the same analysis as we did for apparent resistivity, we find the second-order

approximation formulae:

$$E[A] - a = \frac{\sigma^2}{2a}, \tag{A.60}$$

and

$$\frac{\delta A}{a} = \frac{\sigma}{a}\sqrt{1 + \frac{\sigma^4}{a^4}}. \tag{A.61}$$

The estimated mean amplitude is upward biased and a linearly-propagated error in amplitude is underestimated. Again, the mean of the log of amplitude is unbiased under the second-order approximation, and standard error in the log of amplitude differs from (A.55) only by a factor of 2.

With only a slight modification to the preceding development, we may derive the second order approximation to the covariance of two complex functions of random variables as such:

$$\mathrm{cov}(F, G) = \frac{\partial f}{\partial x}\frac{\partial g}{\partial x}\sigma^2 + \frac{\partial f}{\partial y}\frac{\partial g}{\partial y}\sigma^2 + \frac{1}{2}\frac{\partial^2 f}{\partial x^2}\frac{\partial^2 g}{\partial x^2}\sigma^4 + \frac{1}{2}\frac{\partial^2 f}{\partial y^2}\frac{\partial^2 g}{\partial y^2}\sigma^4 + \frac{\partial^2 f}{\partial x \partial y}\frac{\partial^2 g}{\partial x \partial y}\sigma^4. \tag{A.62}$$

By (A.62) we find that, even after applying a higher-order approximation, the pleasing properties, $\mathrm{cov}(R, P) = \mathrm{cov}(L, P) = 0$, still hold.

Bibliography

Karsten Bahr. Interpretation of the magnetotelluric impedance tensor: regional induction and local telluric distortion. *Journal of Geophysics*, 62:119–127, 1988.

M Becken and H Burkhardt. An ellipticity criterion in magnetotelluric tensor analysis. *Geophysical Journal International*, 2004.

M Becken, O Ritter, and H Burkhardt. Mode separation of magnetotelluric responses in three-dimensional environments. *Geophysical Journal*, 2008a.

M Becken, O Ritter, S K Park, P A Bedrosian, U Weckmann, and M Weber. A deep crustal fluid channel into the San Andreas Fault system. *Geophysical Journal International*, 173 (2):718–732, 2008b.

Michael Becken, Oliver Ritter, Paul A Bedrosian, and Ute Weckmann. Correlation between deep fluids, tremor and creep along the central San Andreas fault. *Nature*, 480(7375): 87–90, November 2011.

P A Bedrosian, M J Unsworth, G D Egbert, and C H Thurber. Geophysical images of the creeping segment of the San Andreas fault: implications for the role of crustal fluids in the earthquake process. *Tectonophysics*, 385(1-4):137–158, 2004.

M N Berdichevsky, V I Dmitriev, and E E Pozdnjakova. On two-dimensional interpretation of magnetotelluric soundings. *Geophysical Journal of the Royal Astronomical Society*, 133 (3):585–606, 1998.

H Bibby and T Caldwell. Determinable and non-determinable parameters of galvanic distortion in magnetotellurics. *Geophysical Journal*, 2005.

Florian Bleibinhaus, John A Hole, Trond Ryberg, and Gary S Fuis. Structure of the California Coast Ranges and San Andreas Fault at SAFOD from seismic waveform inversion and reflection imaging. *J. Geophys. Res.*, 112, 2007.

T Caldwell and H Bibby. The magnetotelluric phase tensor. *Geophysical Journal*, 2004.

A.D. Chave, D.J. Thomson, and M.E. Ander. On the robust estimation of power spectra, coherences, and transfer functions. *J. Geophys. Res.*, 92(B1):633–648, 1987.

Alan D Chave, Jean H Filloux, Douglas S. Luther, Lawrie K Law, and Antony White. Observations of Motional Electromagnetic Fields During EMSLAB. *J. Geophys. Res.*, 94 (B10):14153–14166, 1989.

Michael Commer and Gregory A. Newman. Three-dimensional controlled-source electromagnetic and magnetotelluric joint inversion. *Geophysical Journal of the Royal Astronomical Society*, 178(3):1305–1316, 2009.

S Constable, R Parker, and C Constable. Occam's inversion: A practical algorithm for generating smooth models from electromagnetic sounding data. *Geophysics*, 1987.

Steven Constable, Kerry Key, and Lisl Lewis. Mapping offshore sedimentary structure using electromagnetic methods and terrain effects in marine magnetotelluric data. *Geophysical Journal International*, 176(2):431–442, 2009.

C Cox. Electromagnetic Induction in the Oceans and Inferences on the Constitution of the Earth. *Geophysical Surveys*, pages 1–20, 1980.

T Dawson and J Weaver. Three-dimensional induction in a non-uniform thin sheet at the surface of a uniformly conducting earth. *Geophysical Journal of the Royal Astronomical Society*, 59(3):445–462, 1979.

C DeGroot Hedlin and S Constable. Occam's inversion to generate smooth, two-dimensional models from magnetotelluric data. *Geophysics*, 55(12):1613–1624, 1990.

Gary D Egbert. Robust multiple-station magnetotelluric data processing. *Geophysical Journal International*, 130(2):475–496, 1997.

Gary D Egbert. Processing And Interpretation Of Electromagnetic Induction Array Data. *Surveys in Geophysics*, 23(2):207–249, 2002.

Gary D Egbert and John R Booker. Robust estimation of geomagnetic transfer functions. *Geophysical Journal of the Royal Astronomical Society*, 87(1):173–194, 1986.

Gary D Egbert and John R Booker. Multivariate Analysis of Geomagnetic Array Data 1. The Response Space. *J. Geophys. Res.*, 94(B10):14227–14247, 1989.

Gary D Egbert and Anna Kelbert. Computational recipes for electromagnetic inverse problems. *Geophysical Journal International*, pages no–no, January 2012.

T D Gamble, W. M. Goubau, and J. Clarke. Magnetotellurics with a remote magnetic reference. *Geophysics*, 44(1):53–68, January 1979.

Leon Jay Gleser. Estimation in a Multivariate "Errors in Variables" Regression Model: Large Sample Results. *The Annals of Statistics*, 9(1):24–44, January 1981.

Gene H Golub and Charles F Van Loan. *Matrix computations*. Johns Hopkins University Press, 1983.

I. S. Gradshteyn and I. M. Ryzhik. *Table of Integrals, Series, and Products*. Academic Press, New York, NY, 1965.

R Groom and R Bailey. Decomposition of magnetotelluric impedance tensors in the presence of local three-dimensional galvanic distortion. *Journal of Geophysical Research*, 1989.

Graham Heinson and Steven Constable. The electrical conductivity of the oceanic upper mantle. *Geophysical Journal International*, 110(1):159–179, 1992.

Stuart A Henrys, Alan R Levander, and Anne S Meltzer. Crustal Structure of the Offshore Southern Santa Maria Basin and Transverse Ranges, Southern California, From Deep Seismic Reflection Data. *J. Geophys. Res.*, 98(B5):8335–8348, May 1993.

Stephen Hickman, Mark Zoback, and William Ellsworth. Introduction to special section: Preparing for the San Andreas Fault Observatory at Depth. *Geophys. Res. Lett*, 31(12): L12S01, January 2004.

Gerald Hohmann. Three-dimensional induced polarization and electromagnetic modeling. *Geophysics*, 40(2):309–324, March 1975.

John M Howie, Kate C Miller, and William U Savage. Integrated Crustal Structure across the South Central California Margin: Santa Lucia Escarpment to the San Andreas Fault. *J. Geophys. Res.*, 98:8173–8196, May 1993.

Roy D Hyndman and Simon M Peacock. Serpentinization of the forearc mantle. *Earth and Planetary Science Letters*, 212(3-4):417–432, 2003.

C. W. Jennings, R. G. Strand, and T. H. Rogers. Geologic map of California: California Division of Mines and Geology, 1977.

A. A. Kaufman and G. V. Keller. *The Magnetotelluric Sounding Method*. Elsevier Scientific Publishing Company, 1981.

K Key and S Constable. Coast effect distortion of marine magnetotelluric data: Insights from a pilot study offshore northeastern Japan. *Physics of The Earth and Planetary Interiors*, 2010.

Kerry Key and Jeffrey Ovall. A parallel goal-oriented adaptive finite element method for 2.5-D electromagnetic modelling. *Geophysical Journal International*, pages no–no, 2011.

Claude F Lafond and Alan Levander. Migration of wide-aperture onshore-offshore seismic data, central California: Seismic images of late stage subduction. *J. Geophys. Res.*, 100 (B11):22231–22243, 1995.

J. C. Larsen. Electric and Magnetic Fields Induced by Deep Sea Tides. *Geophysical Journal of the Royal Astronomical Society*, 16(1):47–70, 1968.

Peter Lonsdale. Structural patterns of the Pacific floor offshore of Peninsular California. *AAPG memoir*, 47:87–125, 1991.

Lucy MacGregor, Martin Sinha, and Steven Constable. Electrical resistivity structure of the Valu Fa Ridge, Lau Basin, from marine controlled-source electromagnetic sounding. *Geophysical Journal of the Royal Astronomical Society*, 146(1):217–236, 2001.

Randall L. Mackie and Theodore R Madden. Three-dimensional magnetotelluric inversion using conjugate gradients. *Geophysical Journal of the Royal Astronomical Society*, 115 (1):215–229, 1993.

P McGillivray, D Oldenburg, R Ellis, and T Habashy. Calculation of sensitivities for the frequency-domain electromagnetic problem. *Geophysical Journal International*, 116(1): 1–4, 1994.

D McKirdy, J Weaver, and T Dawson. Induction in a thin sheet of variable conductance at the surface of a stratified earth – II. Three-dimensional theory. *Geophysical Journal of the Royal Astronomical Society*, 80(1):177–194, 1985.

Gary McNeice and Alan Jones. Multisite, multifrequency tensor decomposition of magnetotelluric data. *Geophysics*, 66(1):158–173, 2001.

Anne S Meltzer and Alan R Levander. Deep crustal reflection profiling offshore southern central California. *J. Geophys. Res.*, 96(B4):6475–6491, April 1991.

Kate C Miller, John M Howie, and Stanley D Ruppert. Shortening Within Underplated Oceanic Crust Beneath the Central California Margin. *J. Geophys. Res.*, 97(B13):19961–19980, 1992.

W. H. Munk, G. R. Miller, F. E. Snodgrass, and N. F. Barber. Directional Recording of Swell from Distant Storms. *Philosophical Transactions of the Royal Society of London. Series A, Mathematical and Physical Sciences*, 255(1062):505–584, January 1963.

David Myer, Steven Constable, and Kerry Key. Broad-band waveforms and robust processing for marine CSEM surveys. *Geophysical Journal International*, 184(2):689–698, 2011.

Robert M Nadeau and David Dolenc. Nonvolcanic Tremors Deep Beneath the San Andreas Fault. *Science*, 307(5708):389, 2005.

Robert M Nadeau and Aurélie Guilhem. Nonvolcanic tremor evolution and the San Simeon and Parkfield, California, earthquakes. *Science*, 325(5937):191–193, 2009.

G A Newman and D L Alumbaugh. Three-dimensional massively parallel electromagnetic inversion—I. Theory. *Geophysical Journal of the Royal Astronomical Society*, 128(2): 345–354, 1997.

R Parker. The inverse problem of electromagnetic induction: existence and construction of solutions based on incomplete data. *Journal of Geophysical Research*, 1980.

R Parker. Numerical methods for establishing solutions to the inverse problem of electromagnetic induction. *Journal of Geophysical Research*, 1981.

R L Parker. *Geophysical Inverse Theory*. Princeton University Press, Princeton, New Jersey, 1994.

Robert Parker and Yi-Qaio Song. Assigning uncertainties in the inversion of NMR relaxation data. *Journal of Magnetic Resonance*, 174(2):314–324, 2005.

Robert L Parker and Brent Wheelock. Fourier domain calculation of terrain effects in marine MT. *Geophysical Journal of the Royal Astronomical Society*, 189(1):240–250, 2012.

William H. Press, Saul A. Teukolsky, William T. Vetterling, and Brian P. Flannery. *Numerical Recipes: The Art of Scientific Computing*. Cambridge University Press, New York, 3rd edition, 2007.

O Ritter, A Hoffmann-Rothe, P A Bedrosian, U Weckmann, and V Haak. Electrical conductivity images of active and fossil fault zones. *Geological Society, London, Special Publications*, 245(1):165–186, 2005.

Yutaka Sasaki. Full 3-D inversion of electromagnetic data on PC. *Journal of Applied Geophysics*, 46(1):45–54, January 2001.

David R Shelly, William L Ellsworth, Trond Ryberg, Christian Haberland, Gary S Fuis, Janice Murphy, Robert M Nadeau, and Roland Bürgmann. Precise location of San Andreas Fault tremors near Cholame, California using seismometer clusters: Slip on the deep extension of the fault? *Geophys. Res. Lett*, 36(L01303), 2009.

Weerachai Siripunvaraporn, Gary Egbert, Yongwimon Lenbury, and Makoto Uyeshima. Three-dimensional magnetotelluric inversion: data-space method. *Physics of The Earth and Planetary Interiors*, 150(1–3):3–14, January 2005.

Walter H F Smith and David T Sandwell. Global Sea Floor Topography from Satellite Altimetry and Ship Depth Soundings. *Science*, 277(5334):1956–1962, January 1997.

C M Swift. A magnetotelluric investigation of an electrical conductivity anomaly in the southwestern United States. *Ph.D Thesis, Massachusetts Institute of Technology*, 1967.

A. N. Tikhonov and V. Y. Arsenin. *Solution of Ill-posed Problems.* Winston & Sons, Washington, 1977.

Sam C Ting and Gerald W Hohmann. Integral equation modeling of three-dimensional magnetotelluric response. *Geophysics*, 46(2):182–197, February 1981.

Anne Tréhu. Tracing the Subducted Oceanic Crust Beneath the Central California Continental Margin: Results From Ocean Bottom Seismometers Deployed During the 1986 Pacific Gas and Electric EDGE Experiment. *J. Geophys. Res.*, 96(B4):6493–6506, 1991.

Anne M Trehu and Walter H Wheeler. Possible evidence for subducted sedimentary materials beneath central California. *Geology*, 15(3):254–258, 1987.

Martyn Unsworth and Paul A Bedrosian. Electrical resistivity structure at the SAFOD site from magnetotelluric exploration. *Geophys. Res. Lett*, 31, 2004.

Martyn Unsworth, Gary Egbert, and John Booker. High-resolution electromagnetic imaging of the San Andreas fault in Central California. *J. Geophys. Res.*, 104(B1):1131–1150, 1999.

Martyn Unsworth, Paul Bedrosian, Markus Eisel, Gary Egbert, and Weerachai Siripunvaraporn. Along Strike Variations in the Electrical Structure of the San Andreas Fault at Parkfield, California. *Geophys. Res. Lett*, 27(18):3021–3024, 2000.

Martyn J Unsworth, Peter E Malin, Gary D Egbert, and John R Booker. Internal structure of the San Andreas fault at Parkfield, California. *Geology*, 25(4):359–362, 1997.

G Vasseur and P Weidelt. Bimodal electromagnetic induction in non-uniform thin sheets with an application to the northern Pyrenean induction anomaly. *Geophysical Journal of the Royal Astronomical Society*, 51(3):669–690, 1977.

P E Wannamaker and G W Hohmann. Electromagnetic modeling of three-dimensional bodies in layered earths using integral equations. Technical report, Historical Energy Database, January 1982.

Philip E Wannamaker, Gerald W Hohmann, and Stanley H Ward. Magnetotelluric responses of three-dimensional bodies in layered earths. *Geophysics*, 49(9):1517–1533, September 1984.

Philip E Wannamaker, John A Stodt, and Luis Rijo. A stable finite element solution for two-dimensional magnetotelluric modelling. *Geophysical Journal of the Royal Astronomical Society*, 88(1):277–296, 1987.

Stanley H Ward and Gerald W Hohmann. *Electromagnetic theory for geophysical applications*, volume 1 of *Electromagnetic Methods in Applied Geophysics–Theory*. Society of Exploration Geophysicists, 1988.

Michael S Zhdanov, Sheng Fang, and Gábor Hursán. Electromagnetic inversion using quasi-linear approximation. *Geophysics*, 65(5):1501–1513, 2000.